Technische Universität München

Max-Planck-Institut für Astrophysik

Astrophysical magnetohydrodynamics and radiative transfer: numerical methods and applications

Martin Obergaulinger

Vollständiger Abdruck der von der Fakultät für Physik der Technischen Universität München zur Erlangung des akademischen Grades eines

Doktors der Naturwissenschaften (Dr. rer. nat.)

genehmigten Dissertation.

Vorsitzender: Univ.-Prof. Dr. R. Krücken

Prüfer der Dissertation:

1. Priv.-Doz. Dr. E. Müller
2. Univ.-Prof. Dr. H. Friedrich

Die Dissertation wurde am 8. November 2007 bei der Technischen Universität München eingereicht und durch die Fakultät für Physik am 9. Januar 2008 angenommen.

ED AL MAGNETICO
SIGNOR DOTTORE
RENDO L'ONORE
CHE MERITÒ!

Ferrando e Guglielmo a Despina

Così fan tutte ossia la scuola degli amanti
di Lorenzo da Ponte e Wolfgang Amadeus Mozart

Contents

Chapter 1

Introduction

> WHAT THE DEUCE IS THE SOLAR SYSTEM TO ME? YOU SAY THAT WE GO ROUND THE SUN. IF WE WENT ROUND THE MOON IT WOULD NOT MAKE A PENNYWORTH OF DIFFERENCE TO ME OR MY WORK.
>
> Sherlock Holmes, *A Study in Scarlet*

1.1 Astrophysical magnetohydrodynamics

The evolution of many astrophysical systems is strongly influenced by magnetic fields. Examples of such systems can be found on all astrophysically relevant scales, from stellar interiors and atmospheres to accretion discs around black holes, extragalactic jets and the gas in galaxy clusters. Important issues in the study of such systems can be summarised as follows:

1. How is the magnetic field built up and maintained against dissipative losses?
2. How does the magnetic field affect the dynamics, the interaction of matter and radiation, and the observables?

In some situations both questions can be addressed independently of each other, but usually the amplification of the magnetic field and the dynamics of the fluid are tightly coupled and one cannot consider any of these questions without taking into account the other one. This tight coupling makes the full problem fairly complex and limits the applicability of analytic methods. Thus, numerical simulations are an indispensable tool in the investigation of magnetised systems in astrophysics.

One case in which this is particularly true is the study of instabilities and turbulence in a magnetised fluid. The reason for this is deeply related to the basic properties of magnetic turbulence. Important quantities characterising turbulent magnetic and velocity fields are the respective energies and the so-called helicities. The evolution of these quantities is dominated by the *direct* and *inverse cascades*. A quantity following a direct cascade is created or injected to the fluid at large length scales (*integral scale*), from which it is transferred down to ever smaller scales where it ultimately is dissipated (*viscous scale*). An inversely cascading quantity, on the other hand, has its source at small length scales and is transferred to the integral scale. In the intervening *inertial range* of length scales, its distribution with wave number typically follows a power law scaling. In a turbulent magnetised fluid, different scaling laws and different cascade directions exist for different quantities. As a consequence, even if the magnetic field may be negligible on one length

scale, e.g., the integral one, it still can – and in many cases will – dominate the dynamics of the fluid on a different scale. Thus, simplifications of the coupling between magnetic fields and the fluid may be particularly inappropriate for turbulent fluids, making turbulent dynamics a topic in which numerical simulations are of particular importance.

In many cases, the dynamics of these objects can be modelled very well using the assumptions of *magnetohydrodynamics (MHD)*. The theory of MHD describes the joint evolution of an electrically conducting fluid and a magnetic field permeating the fluid. Based on the equations of *hydrodynamics (HD)* for the fluid flow, the Maxwell equations for the evolution of the electromagnetic fields, and the description of the fluid-field interaction by Lorentz's law for the electromagnetic force and Ohm's law for the current density, the MHD system constitutes of conservation laws for mass, momentum, energy, and magnetic flux. As a continuum theory, it neglects kinetic phenomena and its applicability is limited to collisional systems and to length and time scales much larger than the Larmor radius and the gyration time of the particles. Though extensions such as two-fluid MHD and Hall MHD exist, in most astrophysical applications one can safely apply the simpler one-fluid MHD model which does not treat the electronic and ionic components of the fluid separately.

The success of the application of MHD in many fields of astrophysics is a relatively recent development, due in large part to the increasing performance of supercomputers and the development of stable and accurate numerical schemes. Well resolved multidimensional simulations of turbulent or highly dynamic systems have become possible only in the last decades, and, still, there are many open physical questions as well as a strong need for technical and numerical improvements. Thus, we focus on the implementation of new numerical methods which allow us to study the dynamics of magnetised matter in the dynamic final stages of stellar evolution. The numerical code we design has to follow the – potentially turbulent – evolution of the magneto-fluid in smooth flow regions with high accuracy while robustly dealing with the strong discontinuities that may ensue where the flow is supersonic. Furthermore, it has to be both modular and efficient to allow for simple adaptation to a given physical system and for a detailed investigation of interesting phenomena using extensive parameter studies or highly resolved simulations.

1.2 Supernovae and gamma-ray bursts

The prime targets we want to apply our code to are the explosive events at the end of the evolution of a massive star and the accretion system around a *neutron star (NS)* or a *black hole (BH)*. In the following, we will provide a short introduction to the physics of these systems.

1.2.1 Core-collapse supernovae

General considerations

The commonly accepted model of a *core-collapse supernova (SN)* is the *convectively supported neutrino-driven* explosion mechanism which we will briefly explain in the following.

The stability of a massive star ($M \gtrsim 8M_\odot$) is the result of the balance between its own gravitational force and forces directed outwards such as pressure gradients and the centrifugal force. As long as a main-sequence star maintains the energy-producing nuclear reactions in its central regions, the large thermal pressure provided by these reactions can counteract the gravitational pull, and, as a result, the star remains in a state of hydrostatic equilibrium during most phases of

its life. As soon as it has consumed its nuclear fuel, these reactions cease. This happens, when, after successive stages of hydrogen, helium, carbon, oxygen, and silicon burning, the inner core of the star consists mainly of iron-group elements, the most tightly bound nucleus from which no energy can be gained by nuclear reactions.

Suffering a decrease of the the main forces that balance gravity, the core starts to collapse from an initial central density of $\rho \sim 10^{10}$ g cm^{-3}. Due to deleptonisation reactions, the electron fraction of the core, Y_e, decreases from about 0.5 in the pre-collapse core to about 0.2 in the collapsed core. As the core deleptonises, a large number of neutrinos is produced to which most of the gravitational binding energy liberated in the collapse is transferred. Despite the tiny reaction cross sections of neutrinos and matter, the neutrinos eventually are trapped within the core as densities above $\rho \sim 10^{12}$ g cm^{-3} are reached. Rather than leaving the core freely streaming, neutrinos diffuse out on timescales that are comparable to or even larger than the hydrodynamic (infall) time.

Within less than a second, the central density of the core reaches and exceeds nuclear-matter density, $\rho_{\rm nuc} \sim 2 \times 10^{14}$ g cm^{-3}, forming a *proto-neutron star (PNS)*. At this point in evolution, the pressure of the innermost regions increases strongly with density due to the near incompressibility of nuclear matter, and, consequently, a strong shock wave forms at the boundary of the subsonically collapsing inner core. Propagating outwards through the supersonically infalling outer core, the shock looses a large amount of its energy due to the endothermic dissociation of shock-heated heavy nuclei. The shock wave stalls and turns into a standing accretion shock.

The shock wave can be revived by the energy that is transferred to the fluid by the neutrinos still present in the core and diffusing outwards. The transfer of a few percent of the neutrino energy is sufficient to unbind the gas behind the shock surrounding the PNS and revert the accretion into an explosion. Whether or not interactions such as scattering, emission, and absorption processes provide a sufficiently tight coupling of neutrinos and matter has to be studied in detail. At least for the stars above a mass of $M \sim 11 M_\odot$, an additional ingredient appears to be crucial: the development of hydrodynamic instabilities such as convection or the *standing accretion shock instability*. Overturn motions caused by these instabilities enhance the efficiency of the neutrino heating of the gas. According to detailed simulations (e.g., Scheck et al. 2006), a flow pattern dominated by low-order modes, characterised by only a small number of outflows and downdrafts, evolves. In two- and three-dimensional numerical simulations, this flow pattern is found to be particularly efficient in triggering the explosion and to provide a natural explanation for the asymmetries observed in many SNe as well as the large spatial velocities of newly born NS.

The physics of core-collapse SNe is very rich and complex, involving the theory of the state of matter at high densities, the radiative transfer of neutrinos, the interactions of neutrinos with matter and of nucleons and nuclei among each other, general relativity, and (magneto-)hydrodynamics. Moreover, investigations of SNe assuming spherical symmetry prove to be incapable of explaining the explosion phenomenon. Instead, two-dimensional (axisymmetric) or, preferably, unconstrained three-dimensional simulations are required for this purpose. Putting all these ingredients adequately and accurately together into an explosion model still exceeds current computational capabilities. Thus, one cannot avoid assumptions and approximations concerning the physical content of the model. Various authors have made approximations at different levels, or have even neglected some physical aspects entirely. A large number of studies completely ignore neutrino transport and employ a very simplified nuclear *equation of state (EOS)*, whereas others treat these microphysical aspects in great detail and with great accuracy, e.g., by solving the Boltzmann equation of radiative transport. The latter approach usually leads to extremely time-consuming simulations which do not allow for a comprehensive exploration of the large parameter space of

possible progenitor stars.

In this work, we will present a numerical method which falls between these two extremes: it solves the equations of classical MHD in one, two, or three dimensions, uses a detailed microphysical EOS, and treats the neutrino transport with a method of intermediate complexity and accuracy. This approach is well suited for investigating the explosion in 2d or 3d in a parametric way.

Rotation and magnetic fields

If the pre-collapse core rotates or is endowed with a magnetic field, the basic mechanism described above may be subject to some modifications, which are, however, are not yet understood fully.

During collapse, the angular momentum of a fluid element changes only little. Thus, the rotational energy of the core increases, both in absolute number and relative to the gravitational energy from which it is diverted. Furthermore, the homologous infall profile (i.e., the infall velocity is proportional to the radius) leads to an increasing degree of differential rotation, which enhances possible effects of the rotation strongly. An important effect may come from the centrifugal force helping the matter to overcome the gravitational force; a further, more uncertain, possibility is that the post-collapse core is unstable against rotational instabilities.

The magnetic field of the core can become dynamically important, if its energy reaches equipartition with the internal energy. In this case, it can influence the dynamics of the core in several ways:

1. By virtue of its Lorentz stress, the magnetic field can transport angular momentum from the PNS outwards along open field lines. Thus, the decreasing rotational support will enforce changes in the PNS structure. Potentially, the PNS can undergo a phase of secular contraction leading to higher densities.
2. The rotational energy lost in such a process can be transferred to the layers surrounding the PNS. Thus, leading to additional energy input, the magnetic field may help to unbind these layers and thus facilitate the explosion.
3. Magnetic fields, in concurrence with rotation, may trigger the formation of jet-like outflows up to Lorentz factors of a few. Even if the magnetic field is not initiated magneto-centrifugally, the field can alter the shape of the explosion, inducing a bipolar geometry of the ejecta.
4. The evolution of hydrodynamic instabilities such as convection can be modified significantly in the presence of a strong magnetic field. Since these are crucial for the explosion mechanism, this effect may be important.
5. Additionally, the microphysical state of the gas and its interactions with neutrinos can be subject to modifications in a strong magnetic field, e.g., by the coupling of the magnetic moments of elementary particles to the field, or by leading to anisotropies of microscopic transport coefficients such as heat conduction or viscosity.

To lead to such effects, however, the magnetic field must be strong, i.e., in equipartition with the internal energy. Since its typical pre-collapse strength is far below such values, it has to grow by several orders of magnitude. A number of processes exist by which such a growth is feasible. In the following, these processes will be reviewed.

The magnetic field of the initial core will be amplified during collapse by flux-conserving compression. This process works irrespective of and without any influence on the seed field geometry. It can be viewed as the $P_{\mathrm{mag}}\ \mathrm{d}\mathcal{V}$ work the infalling matter does against the (isotropic) magnetic

pressure $P_{\rm mag}$ as its volume $\mathcal{V}$ decreases. Hence, the kinetic energy of the infall mediates the conversion of gravitational binding energy into magnetic energy.

If the core rotates differentially, a poloidal[1] magnetic field component can act as a seed for the process of *linear winding*, also known as Ω-*effect*. Creating a toroidal component, this process increases the field strength linearly with time at the cost of the rotational energy.

The occurrence of these two amplification processes (compression and winding) is well established by the results of several numerical simulations (e.g., Bisnovatyi-Kogan et al. 1976; Meier et al. 1976; Müller & Hillebrandt 1979; Symbalisty 1984; Yamada & Sawai 2004; Kotake et al. 2004; Ardeljan et al. 2005; Obergaulinger et al. 2006b,a; Cerdá-Durán et al. 2007; Burrows et al. 2007). However, most simulations agree that, given the rotation rates and magnetic fields of pre-collapse progenitors, they fail to produce dynamically important field strengths on hydrodynamic time scales, i.e., within the time required for collapse or for the delayed explosion. Only for very rapidly rotating models, accounting for merely a small fraction of progenitors, the conditions may be favourable for strong amplification.

The post-collapse core is subject to several hydrodynamic instabilities, which can give rise to a *turbulent dynamo*. In the so-called α *effect*, a turbulent velocity field creates a poloidal field from a toroidal component, which then can act as the seed field for the Ω effect. Both processes together constitute a $\alpha - \Omega$ *dynamo*; even without rotation, a so-called α^2 *dynamo* can develop in a turbulent layer.

A potentially very important field amplification mechanism is the *magneto-rotational instability (MRI)*, a local linear MHD instability that operates if the angular velocity Ω decreases with radius. A particularly important feature of the MRI is that it represents a *weak-field instability*, i.e., it operates on any given initial field no matter how weak. Thus, even if the initial field is negligible compared to the local internal or kinetic energy, it may nevertheless impact the dynamics significantly via the MRI.

The MRI was first discovered by Velikhov (1959); Chandrasekhar (1960). Although Acheson (1978) studied the MRI and related instabilities in stars, the MRI did not attract much attention from astrophysicists until Balbus and Hawley, in a series of papers (Balbus & Hawley 1991; Hawley & Balbus 1991, 1992; Balbus & Hawley 1992a), identified it as a promising candidate for the solution of a longstanding problem in high-energy astrophysics, viz. the creation of turbulence in accretion discs (for a comprehensive review of this topic, see Balbus & Hawley 1998). To accrete onto the central object, gas orbiting in an accretion disc has to lose its angular momentum. Already Shakura & Syunyaev (1973) suspected turbulence to be responsible for the required transport of angular momentum, but it was not clear what physical mechanism could excite it. Following the initial suggestion by Balbus & Hawley (1991), a great number of studies, both analytical and numerical, confirmed that indeed the MRI can provide a viable physical mechanism for this effect.

In recent years, additional interest in the MRI has grown in SN theory, after Akiyama et al. (2003) demonstrated that post-collapse cores are likely to fulfil the instability criterion. This, as a consequence, may open up similar possibilities as in accretion disc systems, e.g., the development of turbulence and enhanced transport of angular momentum, even if the initial magnetic field is weak. Although this does not imply that the magnetic field will be dynamically important, it certainly indicates that one cannot safely exclude any magnetic influence on the evolution *a priori*. Recently, MHD instabilities in PNSs, including the MRI were studied analytically by Masada et al.

[1] In spherical coordinates r, θ, ϕ, the components B_r and B_θ of the magnetic field $\vec{B}$ constitute the *poloidal* field, wheras the component B_ϕ is called the *toroidal* field.

(2006, 2007). These authors pointed out the importance of the non-axisymmetric MRI of toroidal fields.

A problem of the subject is, however, the lack of detailed, more quantitative investigations of the evolution of the MRI in SN cores, in particular of its nonlinear evolution. For accretion discs, several authors have studied the instability numerically using different techniques. On the one hand, well-resolved local simulations (Hawley & Balbus 1991, 1992; Hawley et al. 1995; Brandenburg et al. 1995; Hawley et al. 1996; Stone et al. 1996; Sano et al. 2004; Fromang & Papaloizou 2007; Fromang et al. 2007,e.g.) of a small part of an accretion disc allow for a detailed exploration of the onset of the instability and the transition to turbulence under well controlled conditions. These simulations have to assume simplified initial and boundary conditions, and thus, they are usually performed in the frame of a more or less comprehensive parameter study attempting to cover the space of possible conditions in an accretion disc. Global simulations of the entire accretion disc (Hawley 2000; Stone & Pringle 2001; Arlt & Rüdiger 2001; Hawley et al. 2001; Hawley & Balbus 2002,e.g.,), on the other hand, allow to study the effect of the overall disc geometry and the interaction with the surrounding medium as well as the accretor while be unable to accurately resolve the growth of the instability on small spatial scales. Though the combination of results from these two kinds of simulations provides valuable insight into the physics of the MRI, its transfer from accretion discs to stars in general, and SNe, in particular is restricted by the different physical conditions in the two systems:

1. Accretion discs are supported almost entirely by Keplerian rotation, whereas stars, including post-collapse cores, are mainly stabilised by pressure, with a small or modest contribution due to rotation. The growth time of the instability is of the order of the rotational period, whereas the fundamental timescales of the system to which the growth of the instability has to be compared are set for accretion discs by the rotational velocity and for stars by the sound speed. Thus, in a star, the growth competes with, e.g., sound waves which are considerably faster. Thus, the reactions of the two systems to MRI may differ significantly. If the MRI develops in a highly dynamical background, as is the case in a SN, more and even shorter timescales (e.g., related to fast accretion flows, explosion, radiation-matter reactions) may be set by the characteristic times on which the background evolves. One of the big uncertainties concerning MRI in SNe, e.g., is whether or not it grows fast enough to play a role in the very rapid evolution of the explosion.
2. The larger importance of internal w.r.t. kinetic energy entails additional physics, viz. buoyancy, and thus convection. In a star, in contrast to an accretion disc, a convectively stable stratification may hinder the growth of MRI, whereas in a layer already convectively unstable, the MRI will evolve substantially different than in discs, gradually forming into magnetoconvection. Since the envelope of a PNS can be unstable to various hydrodynamic instabilities, this implies a considerable uncertainty.

Very much like in discs, the MRI in stars and SN cores can be investigated using global and local simulations. In global computations, though using (over-)simplified physics, MRI was identified by Obergaulinger et al. (2006b,a). These authors, however, pointed out a crucial problem of global MRI simulations: the fastest growing unstable modes typically have wavelengths of the order of a few meters or less, and with current computers, one cannot resolve these scales and at the same time evolve the whole core. Local simulations, on the other hand, have not been performed so far. Thus, there is a need for closing this gap by a parametrised investigation of the local growth and nonlinear evolution of the MRI. One of the aims of this thesis is to present a newly developed code able to perform such simulations and report on a parametric study of the MRI in SN cores.

1.2.2 Gamma-ray bursts

The observational appearance of *gamma-ray bursts (GRBs)* is characterised by a short (up to several seconds) outburst of radiation in the hard X-ray and soft gamma-ray bands from several 100 kev up to a few MeV. Two subclasses are distinguished according to the duration of the gamma-ray emission: short and long bursts last for less than and more than about 2 seconds, respectively. For both types, optical afterglows have been discovered which are delayed by several minutes w.r.t. the gamma emission. For a recent review on GRBs, we refer the reader to, e.g., Zhang & Mészáros (2004) and the references therein.

Commonly accepted characteristics of both classes are their extragalactic origin, the connection to ultra-relativistic jet-like outflows, and the compactness of their central engine. These characteristics suggest a common explanation by a short phase of intense accretion with accretion rates of the order of $0.1\ M_\odot/\mathrm{s}$ onto a stellar-mass BH. The favoured models for the two classes differ in the physical system in which the BH is embedded:

1. The *collapsar* model for long bursts assumes that the rapidly rotating core of a massive star collapses in a SN-like event to a BH which starts to accrete matter from the surrounding stellar envelope. Due to its large angular momentum, the accreting gas forms an accretion disc, and a jet is launched by magneto-centrifugal forces and/or anisotropic neutrino emission. The jet then drills through the overlying stellar layers into the interstellar medium.
2. Short GRBs are believed to originate from the merger of two compact objects, either a BH and a NS, or two NSs. Due to the orbital angular momentum prior to merger, the post-merger BH is surrounded by an accretion torus. The gravitational energy liberated in the accretion is partially transferred to a jet which escapes basically into empty space.

The physics of a collapsar is fairly similar to that of a regular core-collapse SN, and it is suggestive to think of a continuous sequence of massive star collapse ranging from ordinary SNe to collapsars. In this view, the main factor determining the place of a collapsing star on this sequence is its structure, in particular its amount of rotation. As a consequence, our code, if suited for SN, can be used for studying aspects of collapsar-type explosions as well, with, of course, the limitation that the correct treatment of the nascent BH requires general relativistic gravity.

Mergers leading to short gamma-ray bursts, in contrast, differ considerably from SNe concerning the importance of various physical effects, and thus, most numerical studies of their evolution use methods quite different from the ones employed for SNe, e.g., *smoothed particle hydrodynamics (SPH)* codes. The SPH method is a Lagrangian scheme for the solution of the HD equations which is inherently adaptive in resolution; SPH is known to have problems in accurately following the evolution of fluid instabilities (Agertz et al. 2007). Recently, it has been extended to general-relativistic HD (e.g., Oechslin et al. 2002) and to MHD (Price & Monaghan 2004a,b, 2005; Rosswog & Price 2007) and successfully used in merger simulation (Rosswog et al. 2000; Rosswog & Davies 2002; Rosswog & Liebendörfer 2003; Rosswog et al. 2003; Price & Rosswog 2006; Oechslin et al. 2002; Oechslin & Janka 2006; Oechslin et al. 2007).

Before the formation of a BH in the merger of two NSs, the two NSs are strongly deformed by tidal forces. When they first touch each other, these deformations lead to the formation of a rather broad contact surface. Matter from each of the two stars streams along this surface with a tangential velocity given approximately by the rotation of the NS. Generically, the two stars rotate rapidly, and, in many cases, the spins are aligned. Consequently, the tangential velocities of fluid elements on either side of the contact surface differ by a large amount. The velocity difference is maximum, viz. the sum of the two rotational velocities, for aligned rotators. It is well known that

a jump in tangential velocity across a thin transition layer is unstable to the *Kelvin-Helmholtz (KH)* instability (e.g., Chandrasekhar 1961). The KH instability amplifies any perturbation of the layer, smoothing out the transition and leading to enhanced mixing and dissipation of kinetic into thermal energy. If the fluid is endowed with a magnetic field, the field will be amplified as the perturbations grow. Eventually, it will become strong enough to react back on the instability and modify its evolution. Whether with or without magnetic fields, the emergence of the KH instability can have significant impact on the global evolution of the merger remnant by, e.g., mixing and heating.

The existence of the KH unstable sheet in mergers is well established by various global merger simulations. However, the exact properties of the instability, and in particular the magnetic field structure, may be subject to uncertainties due to numerical issues. Additionally, local simulations of the KH instability with or without magnetic field exist, albeit with parameters that are not appropriate for mergers. Thus, it is another goal of this thesis to present results of local simulations of the KH instability using a high-resolution code that is particularly well suited to compute the evolution of unstable turbulent media.

1.3 Plan of this thesis

The plan of this thesis is as follows: we will introduce the basic physical model which our code is based and discuss some properties important for numerical applications on in Chapter 2. We then proceed to discuss the numerical algorithms we implemented in Chapter 3. After presenting a set of test calculations (Chapter 4), we will show the results of our simulations of the KH instability and the MRI in Chapter 5. The final chapter, Chapter 6, will contain a short summary of the work as well as some concluding remarks and an outlook on further research.

Chapter 2

The physical model

> WENN MAN THEORETISCHER PHYSIKER WERDEN WILL, MUSS MAN SICH AUCH FÜR LOKOMOTIVEN INTERESSIEREN.
>
> Werner Heisenberg[1]

Our goal is to develop a numerical code that allows us to simulate the evolution of magnetised matter in stellar interiors and high-density accretion systems. To this end, the code has to cover a wide range of physics. The theory of MHD provides a good description for the coupled evolution of the magnetic field and the gas, which has to be complemented by an EOS characterising the behaviour of the gas under the given physical conditions; we will elaborate on these in sections 2.1.1 and 2.1.2, respectively. Additionally, neutrino radiation can be of principal importance in such systems. We will describe the relevant processes, assumptions, and equations of *radiative transfer (RT)* and of neutrino-matter interactions in sections 2.2.1 and 2.2.2, respectively.

2.1 Magnetohydrodynamics of stellar interiors

2.1.1 Equations of magnetohydrodynamics

We seek to study the coupled evolution of an electrically conducting fluid permeated by a magnetic field by solving the MHD system. The MHD equations are based on

1. the equations of HD for a non-magnetised fluid,
2. the Maxwell equations for the electromagnetic fields,
3. and the description of the interaction of the fluid and the field components by Lorentz' law for the electromagnetic force and Ohm's law for the current density.

Under the assumption of sufficiently large electric conductivity and sufficiently small velocities, the electric field entirely drops out of the system. Thereby, purely electromagnetic waves are eliminated, and the current density can be computed solely from the magnetic field and the conductivity.

[1] in Anita Ehlers, *Liebes Hertz! Physiker und Mathematiker in Anekdoten*, 1994, Birkhäuser Verlag

The equations of classical MHD result as follows

$$\partial_t \rho + \nabla_j \left[\rho v^j\right] = 0, \tag{2.1a}$$
$$\partial_t p^i + \nabla_j \left[p^i v^j + P_\star \delta^{ij} - b^i b^j - \mathfrak{T}^{ij}\right] = f^i, \tag{2.1b}$$
$$\partial_t e_\star + \nabla_j \left[\left(e_\star + P_\star\right) v^j - b^i v_i b^j - \mathfrak{T}^{ij} v_j\right] = f_j v^j, \tag{2.1c}$$
$$\partial_t \vec{b} = -c\, \vec{\nabla} \times \vec{E}, \tag{2.1d}$$
$$\nabla_j b^j = 0, \tag{2.1e}$$

where $c = 2.998 \times 10^{10}$ cm s^{-1} is the vacuum speed of light and Einstein's summation convention applies.

symbol	definition	variable	dimension
t		time	s
ρ		gas density	g cm^{-3}
$\vec{p}$		momentum density	g cm s^{-1} cm^{-3}
$\vec{v}$	$\vec{p}/\rho$	velocity	cm s^{-1}
$\mathfrak{T}$	$\mathfrak{T}(\vec{v},...)$	(viscous) stress tensor	g cm^2 s^{-2}
$\vec{B}$		magnetic field	G
$\vec{b}$	$\frac{\vec{B}}{\sqrt{4\pi}}$	magnetic field	G
$\vec{E}$	$\vec{E}(\vec{b},\vec{v},...)$	electric field	G
$\vec{j}$	$\frac{c}{\sqrt{4\pi}}\vec{\nabla}\times\vec{b}$	electric current density	
ε		internal energy density	erg cm^{-3}
e_{kin}	$\frac{1}{2}\rho\vec{v}^2$	kinetic energy density	erg cm^{-3}
e_{mag}	$\frac{1}{2}\vec{b}^2$	magnetic energy density	erg cm^{-3}
$e_\star$	$\varepsilon + e_{\rm kin} + e_{\rm mag}$	total energy density	erg cm^{-3}
P	$P(\rho,\varepsilon,...)$	gas pressure	erg cm^{-3}
P_{mag}	$\frac{1}{2}\vec{b}^2$	magnetic pressure	erg cm^{-3}
$P_\star$	$P + P_{\rm mag}$	total pressure	erg cm^{-3}
ν, η, ζ		general, shear, bulk viscosity	
σ		scalar conductivity	
R	$\frac{1}{\sigma}$	scalar resistivity	
$\nu_{\rm m}$	$\frac{c^2}{4\pi\sigma}$	magnetic viscosity	
$\vec{f}$		external force density	dyn cm^{-3}
φ		gravitational potential	cm^2 s^{-2}

Table 2.1: Summary of MHD variables. We give the symbols used throughout the thesis, the definition of the variable, and its dimension in cgs units. For some of the variables, viz. $\vec{E}, \mathfrak{T}, P$, no general definition can be given. Instead, a particular model has to be assumed; the reader is referred to the main text for a more thorough discussion of such models.

The definitions of the symbols used in equations Eqns. (2.1) and in the following equations are summarised in Tab. 2.1. A few comments are in order regarding the variables and equations:

1. We will denote a *partial differential equation (PDE)* of one of the general forms

$$\partial_t u + \vec{\nabla} \cdot \vec{F} = S, \tag{2.2a}$$
$$\partial_t \vec{u} + \vec{\nabla} \times \vec{F} = \vec{S} \tag{2.2b}$$

a *conservation law*. In Eqn. (2.2a), the variable u can be a scalar, vector, or in general a tensor of rank r; S and $\vec{F}$ are tensors of rank r and $r+1$, respectively. In contrast, Eqn. (2.2b) is necessarily a vector equation. For both equations, the variable u is conserved, i.e., its integral over a given domain (a volume for Eqn. (2.2a) or an area for Eqn. (2.2b)) only changes due to fluxes $\vec{F}$ across the boundary of the volume or along the boundary of the domain and due to sources S generating or destroying u within this domain. If the sources vanish, the integral of u over the entire space is constant. We will refer to Eqn. (2.2a) and Eqn. (2.2b) as Gauss and Stokes equations, respectively.

2. If we integrate the conservation laws, Eqn. (2.2) over volume $\mathcal{V}$ or surface $\mathcal{A}$, we can transform them using the Gauss or Stokes theorems, getting

$$\int_{\mathcal{V}} \mathrm{d}\mathcal{V}\, \partial_t u + \oint_{\partial_\mathcal{V}} \overrightarrow{\mathrm{d}\mathcal{A}} \cdot \vec{F} = \int_{\mathcal{V}} \mathrm{d}\mathcal{V}\, S, \tag{2.3a}$$

$$\int_{\mathcal{A}} \mathrm{d}\mathcal{A}\, \partial_t \vec{u} + \oint_{\partial_\mathcal{A}} \mathrm{d}\mathcal{L}\, \vec{F} = \int_{\mathcal{A}} \mathrm{d}\mathcal{A}\, \vec{S}. \tag{2.3b}$$

3. The MHD equations constitute a system of conservation laws. If external forces and losses through the surfaces $\partial\mathcal{V}$ of a volume $\mathcal{V}$ can be ignored, then the following integral quantities of the system will be conserved:
   - mass, $\mathscr{M} = \int_\mathcal{V} \rho \, \mathrm{d}\mathcal{V}$,
   - momentum, $\vec{\mathscr{P}} = \int_\mathcal{V} \vec{p} \, \mathrm{d}\mathcal{V}$,
   - total energy, $\mathscr{E} = \int_\mathcal{V} e_\star \, \mathrm{d}\mathcal{V}$,

   and, analogously, if losses through the boundary $\partial\mathcal{A}$ can be ignored, the magnetic flux through a surface $\mathcal{A}$, $\Phi_\mathcal{A} = \int_\mathcal{A} \vec{B} \cdot \, \mathrm{d}\vec{\mathcal{A}}$, will be conserved. The variables $\rho, \vec{p}, e_\star, \vec{b}$ form the set of *conserved variables* of the system, as opposed to the *primitive variables* $\rho, \vec{v}, P, \vec{b}$ which determine the thermodynamic state of the gas.
4. A model of the thermodynamical properties of the gas is required for determining the EOS, i.e., the dependence of the gas pressure as a function of the conserved variables. We will discuss the models implemented in our code in Sect. 2.1.2.
5. The shear viscosity η and the bulk viscosity ζ of a gas give rise to a *viscous stress tensor*

$$\mathfrak{T}^{\mathrm{vis}}_{ik} = \eta \left(\nabla_k v_i + \nabla_i v_k - \frac{2}{3} \delta_{ik} \vec{\nabla} \cdot \vec{v} \right) + \zeta \, \delta_{ik} \vec{\nabla} \cdot \vec{v}. \tag{2.4}$$

   For ideal MHD, $\eta = 0$ and $\zeta = 0$, and the viscous stress tensor vanishes. Otherwise, the importance of viscous stresses w.r.t. ideal terms such as advection can be quantified by the dimensionless *hydrodynamic Reynolds number* (or Reynolds number for short)

$$\mathsf{Re} = \frac{LU}{\nu}, \tag{2.5}$$

   where L and U are typical length and velocity scales, and ν is short-hand for η or ζ. If $\mathsf{Re} \gg 1$, the dynamics is dominated by the ideal terms. The dynamics of many systems is influenced strongly by small-scale fluctuations of their velocity or magnetic field, e.g., due to turbulence. Quite commonly, numerical simulations fail to resolve properly these fields due to limitations of their spatial accuracy. In such a situation, a *turbulent stress tensor* $\mathfrak{T}^{\mathrm{tur}}$ may account for the macroscopic transport properties of the small-scale fields.
6. The electric field $\vec{E} = \vec{E}^{\mathrm{id}} + \vec{E}^{\mathrm{nonid}}$ comprises an ideal contribution and a resistive contribution due to the finite conductivity of the gas. The ideal field can be determined from first principles, but the non-ideal field requires a model of the electromagnetic properties of the

conducting medium. In Eqn. (2.6b), we assume the simplest model, viz., an isotropic (i.e., scalar) conductivity σ:

$$\vec{E}^{\text{id}} = -\frac{\vec{v}}{c} \times \vec{b}, \tag{2.6a}$$

$$\vec{E}^{\text{nonid}} = \frac{c}{4\pi\sigma} \vec{\nabla} \times \vec{b}. \tag{2.6b}$$

For future reference, we define the resistivity $R = \frac{1}{\sigma}$ and the magnetic viscosity $\nu_{\text{m}} = \frac{c^2}{4\pi\sigma}$. For infinite conductivity, only the ideal field has to be considered. If $\sigma < \infty$, the *magnetic Reynolds number*

$$\mathsf{Re}_{\text{m}} = \frac{Lb}{\nu_{\text{m}}} \tag{2.7}$$

is a measure of the relative importance of ideal and resistive terms: for $\mathsf{Re}_{\text{m}} \gg 1$, the ideal ones dominate. Analogously to a turbulent stress tensor, a *turbulent electric field* can be used to model the influence of the small-scale dynamics on the macroscopic magnetic field.

7. The electric current of the gas can be computed from the magnetic field by

$$\vec{j} = \frac{c}{\sqrt{4\pi}} \vec{\nabla} \times \vec{b}. \tag{2.8a}$$

It does not depend on the conductivity. For a given σ, its connection to the electric field follows from Eqns. (2.6) and (2.8a):

$$\vec{j} = \sigma \left(\vec{E} + \frac{\vec{v}}{c} \times \vec{b} \right). \tag{2.8b}$$

8. The most relevant external force, $\vec{f}$, in our applications is gravity,

$$\vec{f}_{\text{G}} = -\rho \vec{\nabla} \varphi, \tag{2.9a}$$

where the potential φ can be given externally or result from the self-gravity of the gas. In Newtonian theory, φ can be computed from the density of the gas according to Poisson's law,

$$\vec{\nabla}^2 \varphi = 4\pi\rho. \tag{2.9b}$$

To achieve a better approximation of general relativistic gravity, the Newtonian potential can be modified by several correction terms following Marek et al. (2006).

9. The specification of the EOS, the models for $\mathfrak{T}$ and $\vec{E}$, and the external force close the MHD system Eqn. (2.1) and allow for a solution.
10. We can recover the Navier-Stokes equations of non-magnetic HD from Eqns. (2.1) by setting the magnetic field equal to zero. If we additionally disregard $\mathfrak{T}$, we arrive at the Euler equations.

The HD and magnetic Reynolds numbers depend on material properties of the fluid, viz. the viscosities and the resistivity, as well as on its dynamical state, i.e., characteristic length scale and characteristic velocities or magnetic fields. Since they are a function of the length scales of interest, the Reynolds numbers are large ($\gg 1$) for the longest length scales in the system but become increasingly small for ever smaller scales.

A flow with a sufficiently large Reynolds number can undergo a transition to turbulence. In this case, it develops a turbulent cascade in which kinetic (and magnetic) energy is transferred from

the integral scale to ever smaller scales. The cascade terminates at the scale where the Reynolds number becomes unity, $L \sim \nu/U$, at which the turbulent energy is dissipated into heat.

Under the conditions we are interested in, i.e., the dense interior of compact objects such as NSs, ν and ν_m are fairly small: Thompson & Duncan (1993) estimate typical values in neutron stars as $\nu_\nu \sim 10^8\,\mathrm{cm^2\,s^{-1}}$, $\nu_\mathrm{e} \sim 1\,\mathrm{cm^2\,s^{-1}}$ for the viscosity due to neutrinos and electrons and $\nu_\mathrm{m} \sim 10^{-4}\,\mathrm{cm^2\,s^{-1}}$ for the magnetic viscosity. The viscosities due to neutrinos and electrons differ by several orders of magnitude, but, as Thompson & Duncan (1993) argue, both viscosities may be important in NS, albeit in different regimes. The Reynolds numbers following from these estimates are of the orders $\mathrm{Re}_\nu \sim 10^4$, $\mathrm{Re}_\mathrm{e} \sim 10^{10}$, and $\mathrm{Re}_\mathrm{m} \sim 10^{17}$. The values cited here refer to the innermost hot, dense regions of the core. In the surrounding regions, the values may be even higher; furthermore, the viscosity is dominated by electrons in these regions, and, hence, the higher value for Re applies. As a consequence, we neglect hydrodynamic and magnetic viscosity, but we have to treat turbulence correctly. Unfortunately, we will not be able to resolve the full turbulent cascade due to its huge range of spatial scales demanding unattainable computational resources. Thus, we potentially have to consider turbulence models such as turbulent stress tensors and electric fields. However, in the first place, we will focus on ideal MHD.

2.1.2 Matter models

We shortly describe the implemented EOS, the physical model behind them, and their applicability in our study.

Ideal-gas EOS

For an ideal non-degenerate gas, the pressure is a function of the internal energy only,

$$P = (\Gamma - 1)\varepsilon, \tag{2.10}$$

with the adiabatic index Γ. Two important limiting cases can be distinguished according to the mean kinetic energy of the gas particle: non-relativistic and relativistic particle velocities correspond to $\Gamma = \frac{5}{3}$ and $\Gamma = \frac{4}{3}$, respectively. Temperature T and entropy S of the gas are given by:

$$T = kn\,\varepsilon, \tag{2.11a}$$
$$S = kn\,\varepsilon, \tag{2.11b}$$

and the sound speed is

$$c_\mathrm{s}^2 = \frac{\Gamma P}{\rho}. \tag{2.12}$$

Here, $k = 1.38 \times 10^{-16}\,\mathrm{erg\,K^{-1}}$ is the Boltzmann constant and n is the number density of gas particles.

Barotropic EOS

For a fully degenerate gas, pressure and internal energy decouple, and P is a function of ρ only:

$$P = \kappa\rho^\Gamma. \tag{2.13}$$

In the simplest case, κ and Γ are constants, but they may as well be functions of ρ. If we set these functions to

$$\Gamma = \begin{cases} \Gamma_{\text{subnuc}} & \text{if } \rho < \rho_{\text{nuc}}, \\ \Gamma_{\text{nuc}} & \text{if } \rho > \rho_{\text{nuc}}, \end{cases} \qquad \kappa = \begin{cases} \kappa_{\text{subnuc}} & \text{if } \rho < \rho_{\text{nuc}}, \\ \kappa_{\text{nuc}} & \text{if } \rho > \rho_{\text{nuc}}, \end{cases} \tag{2.14a}$$

we can use the EOS as a rough approximation of nuclear matter. To account for degenerate matter composed of symmetric nuclei at subnuclear densities and for the stiffening of the EOS at nuclear densities, the constants will be set to

$$\Gamma_{\text{subnuc}} \lesssim \frac{4}{3}, \qquad \Gamma_{\text{nuc}} \approx 2..2.5, \qquad \kappa_{\text{subnuc}} \approx 4.897 \times 10^{14}\ [\text{cgs}]. \tag{2.14b}$$

The remaining constant κ_{nuc} follows from the requirement that the pressure is continuous at $\rho = \rho_{\text{nuc}}$.

The gas is characterised by vanishing temperature and entropy, $T = 0$ and $S = 0$. Thus, this EOS cannot account for heating of the gas, e.g., due to shock waves. It nevertheless can provide a simple approximation of the state of the matter in cold NS and white dwarfs.

The thermodynamics of the gas does not depend on the internal energy; on the contrary, it is possible to compute the value of the internal energy from the pressure:

$$\varepsilon^{\text{pol}} = (\Gamma - 1)^{-1} P, \tag{2.15a}$$

$$\varepsilon^{\text{pol}}_{\text{subnuc}} = (\Gamma_{\text{subnuc}} - 1)^{-1} P, \qquad \varepsilon^{\text{pol}}_{\text{nuc}} = (\Gamma_{\text{nuc}} - 1)^{-1} P - \hat{\Gamma}\rho. \tag{2.15b}$$

Eqn. (2.15a) is the general expression for a constant Γ, whereas Eqn. (2.15b) holds for the nuclear-matter approximation Eqn. (2.14). In the latter case, the term linear in ρ is a consequence of the continuity of ε at ρ_{nuc}, and the constant $\hat{\Gamma}$ can be determined from this condition. For the sound speed, a relation equivalent to Eqn. (2.12) holds.

Hybrid EOS

Combining the barotropic and the ideal-gas EOS, a simple analytic hybrid EOS can be derived. We add a barotropic pressure P_{b}, given by Eqns. (2.13) and (2.14), and a thermal pressure P_{t} given by an ideal-gas law. The exact form of the EOS can be derived from the constraint that the sum of the internal energies associated with the barotropic and the ideal-gas partial pressures, cf. Eqns. (2.15) and (2.10), must equal the total internal energy of the gas. Defining a thermal part of the internal energy,

$$\varepsilon^{\text{th}} = \varepsilon - \varepsilon^{\text{pol}}, \tag{2.16a}$$

where ε^{pol} is given by Eqn. (2.15), we find the total pressure

$$P = P^{\text{th}} + P^{\text{pol}}, \tag{2.16b}$$

$$P^{\text{th}} = (\Gamma^{\text{th}} - 1)\varepsilon^{\text{th}}, \qquad P^{\text{pol}} = \kappa\rho^{\Gamma_{\text{pol}}}. \tag{2.16c}$$

With the barotropic parameters of Eqn. (2.14) and $\Gamma^{\text{th}} = \frac{4}{3}...\frac{5}{3}$, this EOS can serve as a simple matter model for NS and SNe. It was used in a number of parametric studies of selected aspects of SNe (e.g., Zwerger & Müller 1997; Dimmelmeier et al. 2002; Obergaulinger et al. 2006b,a). The sound speed can be computed from the sound speeds due to the barotropic and the ideal parts:

$$c_{\text{s}}^2 = \frac{\Gamma^{\text{pol}} P^{\text{pol}} + \Gamma^{\text{th}} P^{\text{th}}}{\rho}. \tag{2.17}$$

For later use, we define an entropy-like variable for this EOS,

$$S = \frac{P^{\mathrm{th}}}{P^{\mathrm{pol}}}. \tag{2.18}$$

Shen's microphysical EOS

As a common characteristic, the EOS discussed so far share their simplicity, being given by simple analytic formulae. Their applicability, in contrast, is quite different: the ideal-gas EOS provides a very good description of stellar matter under a wide range of conditions, whereas the barotropic and hybrid EOS are only rough approximations for the specialised case of a high-density gas. A more realistic EOS for matter around and above ρ_{nuc} requires a detailed modelling of the interactions of hadrons at high densities, and of the properties of nuclei, free baryons, and potentially asymptotically free quarks.

Since the thermodynamical conditions under interest here are difficult to probe experimentally, only comparably weak constraints can be put on theoretical models. Moreover, the many-body problem with hadronic interaction is inherently complex and requires substantial approximations. Different approaches can be chosen for such an approximation, leading to a number of different EOS. Though lab experiments together with astrophysical observations can rule out several models, it is currently not possible to identify a single EOS as the most realistic – or even the correct – one. Consequently, the nuclear EOS is still somewhat uncertain.

In our code, we opted for one particular model, viz. the EOS of Shen et al. (1998) provided to us by courtesy of A. Marek who used this EOS in SN simulations (Marek 2007). In the following, we will shortly list the main physical properties of the Shen model:

1. For $\rho < 10^{12}$ g cm^{-3}, the gas is composed of the non-interacting Boltzmann gases of nuclei and nucleons.
2. For higher densities, $10^{12}\,\mathrm{g\,cm^{-3}} < \rho < 1.58 \times 10^{14}$ g cm^{-3}, and low temperature, $T <$ 15 MeV, the gas is assumed to consist of a cubic lattice of heavy nuclei and a vapour of nucleons and α particles. The exact state of the matter is determined by minimising a free-energy functional derived from a Thomas-Fermi approximation.
3. At even higher densities or temperatures, the nuclei dissociate into free nucleons described by a relativistic mean field model.

The complexity of the EOS prohibits us from solving the basic equations at code runtime. Instead, the thermodynamic properties are tabulated in advance as a function of a few basic variables. During a simulation, we interpolate in this look-up table. Our choice of basic variables is the combination of density, temperature, and electron fraction. For Y_e, we solve an additional evolutionary equation,

$$\partial_t \rho Y_e + \vec{\nabla} \cdot \rho Y_e \vec{v} = S_{Y_e}, \tag{2.19}$$

where the source term S_{Y_e} describes the change of the electron fraction due to charged-current interactions with neutrinos. To ensure the consistency of ρY_e and ρ, we solve Eqn. (2.19) together with an analogous equation for $\rho(1-Y_e)$ using the *sCMA* scheme due to Plewa & Müller (1999). We do not obtain the gas temperature from the MHD equations directly; instead, they give us the internal energy $\varepsilon = e_\star - (e_{\mathrm{kin}} + e_{\mathrm{mag}})$. Thus, we have to invert the monotonic relation between ε and T to determine the temperature.

Given the input variables ρ, T, and Y_e, the thermodynamic variables we obtain from the EOS table are

1. the gas pressure P,
2. the adiabatic index Γ,
3. properties of the nucleonic and nuclear components of the gas such as the fractions of neutrons, protons, α particles and a representative heavy nucleus, and their respective chemical potentials.

Γ and P are used to compute the sound speed

$$c_{\mathrm{s}}^2 = \frac{\Gamma P}{\rho}. \tag{2.20}$$

2.2 Radiative transfer

2.2.1 Basic equations

Boltzmann equation

Like the equations of HD, the equations of RT can be derived from the equations governing the dynamics of the distribution of an ensemble of N individual particles – in this case radiation quanta, e.g., photons or neutrinos – in phase space. In $6N$-dimensional phase space ("Γ phase space"), each point $(\vec{r}_1,...,\vec{r}_N;\vec{p}_1,...,\vec{p}_N)$ represents a possible state of the ensemble characterised by the positions $\vec{r}_i$ and momenta $\vec{p}_i$ of all quanta. The particles are assumed to obey the equations of motion for a given Hamiltonian functional, e.g., the equations of classical mechanics.

The distribution function of a large ensemble of identical quanta without internal degrees of freedom (such as spin), $\mathscr{F}(\vec{r}_1,...;\vec{p}_1,...;t)$, describes the probability density of finding the ensemble at time t at phase space point $(\vec{r}_1,...;\vec{p}_1,...)$. An ensemble of non-interacting particles can be described in one-particle phase space $(\vec{r},\vec{p})$ by the one-particle distribution function $\mathcal{F}_i(\vec{r};\vec{p};t)$, $i = 1,...,N$; in this case, the ensemble distribution is given by the product of the distribution functions of all individual particles:

$$\mathscr{F}(\vec{r}_1,...;\vec{p}_1,...;t) = \prod_{i=1,...,N} \mathcal{F}_i(\vec{r};\vec{p};t). \tag{2.21}$$

The evolution equation for $\mathscr{F}$ follows from the *Liouville theorem* stating that the phase-space volume occupied by the ensemble is constant in time. In terms of the distribution functions, this means that the integrals over the entire phase space remain constant (the constant, by normalisation, can be set to 1). This requirement yields the *Liouville equation* for $\mathscr{F}$

$$0 = \frac{\mathrm{d}\mathscr{F}}{\mathrm{d}t} = \partial_t \mathscr{F} + \sum_{i=1}^{N} \left(\partial_{\vec{r}_i} \mathscr{F} \cdot \partial_t \vec{r}_i + \partial_{\vec{p}_i} \mathscr{F} \cdot \partial_t \vec{p}_i \right). \tag{2.22a}$$

and the *Vlasov equation* for $\mathcal{F}$

$$0 = \frac{\mathrm{d}\mathcal{F}}{\mathrm{d}t} = \partial_t \mathcal{F} + \partial_{\vec{r}} \mathcal{F} \cdot \partial_t \vec{r} + \partial_{\vec{p}} \mathcal{F} \cdot \partial_t \vec{p}. \tag{2.22b}$$

From these basic equations, we can derive several theories making additional assumptions on the interactions of individual particles by the so-called *BBGKY hierarchy* (Born, Bogoljubov, Green,

Kirkwood, Yvon). The case we are interested in here is that of short-range interactions within sufficiently dilute systems. We assume that the interactions between particles are restricted to n-particle collisions.

If we integrate the Liouville equation over all but one particle, we get the equation for the distribution function of one particle. The resulting equation is an integro-differential equation, in which the two-particle distribution function appears under a phase-space integral. This function describes the probability density of finding two particles at phase-space points $(\vec{r}_1, \vec{p}_1)$ and $(\vec{r}_2, \vec{p}_2)$. This quantity is not known *a priori*, but we can find an evolutionary equation for it by integrating the Liouville equation over $N-2$ particles. The result, again, is an integro-differential equation, with the three-particle distribution function appears under a phase-space integral. Repeating that process, we can derive integro-differential equations for ever higher moments of the Liouville equation. Instead of carrying out this process *ad inifintum*, we can truncate the series of *radiation-moments equations (RMEs)* at some point by making an assumption (a *closure relation*) on the form of the phase-space integral of a particular multi-particle distribution function.

For RT, we restrict ourselves to two-body collisions which do not depend on any variables but the particle positions. Thus, we can truncate the series of equations after the first one, and we get the *Boltzmann equation*:

$$\partial_t \mathcal{F} + \dot{\vec{r}} \cdot \partial_{\vec{r}} \mathcal{F} - \dot{\vec{p}} \cdot \partial_{\vec{u}} \mathcal{F} = [\partial_t \mathcal{F}]_{\mathrm{C}} \,. \tag{2.23}$$

The second term on the left-hand side describes the spatial advection of $\mathcal{F}$ with the particle velocity $\dot{\vec{r}}$. The third term describes the reaction of $\mathcal{F}$ to the presence of particle accelerations. The *collision integral* $[\partial_t \mathcal{F}]_{\mathrm{C}}$ parametrises how two-body interactions redistribute $\mathcal{F}$ in phase space.

For radiation quanta moving at the speed of light, i.e., $\dot{\vec{r}} = \vec{n}c$, where $|\vec{n}| = 1$, and not subject to external forces, i.e., $\dot{\vec{p}} = 0$, we recover the Boltzmann equation of RT (or the *radiative-transfer equation (RTE)*)

$$\frac{1}{c}\partial_t \mathcal{F} + \vec{n} \cdot \vec{\nabla} \mathcal{F} = \mathcal{B}, \tag{2.24a}$$

$$\frac{1}{c}\partial_t \mathcal{I} + \vec{n} \cdot \vec{\nabla} \mathcal{I} = \mathcal{S}. \tag{2.24b}$$

Here, we introduced the *monochromatic specific intensity*

$$\mathcal{I} = \left(\frac{\omega}{hc}\right)^3 c\mathcal{F}, \tag{2.25}$$

where $h = 6.626 \times 10^{-27}\,\mathrm{erg\,s}$ and $c = 2.9979 \times 10^{10}\,\mathrm{cm\,s^{-1}}$ are the Planck constant and the speed of light, respectively. Furthermore, $\omega = c|\vec{p}|$ is the energy of a quantum of momentum $\vec{p}$. We introduced the source terms $\mathcal{B}$ and $\mathcal{S}$ summarising the emission, absorption and scattering of radiation quanta.

Moments of the intensity

The distribution function $\mathcal{F}$ lives in a seven-dimensional space: four space-time components and three coordinates in momentum space (compare this to the usual HD fields which are functions only of space-time coordinates). This high dimensionality makes the equation very hard to solve, and, thus, we strive to reduce the complexity by considering angular moments of $\mathcal{F}$. We define the

monochromatic n^{th} *moment* of the radiation field by integrating $\mathcal{F}$ and a *n*adic tensorial product of the direction of radiation propagation, $\vec{n}$, over angular directions in momentum space,

$$\mathfrak{M}^{(n)}(\vec{r};\omega;t) = \int \mathrm{d}\Omega \left(\prod_{i=0}^{n} \vec{n}\right) \cdot \mathcal{I}(\vec{r};\vec{p};t). \tag{2.26a}$$

This quantity is a tensor of *n*th rank. If we additionally integrate over energy ω, we get the energy-integrated or *grey* specific intensity

$$\bar{\mathfrak{M}}^{(n)}(\vec{r};t) = \int \mathrm{d}\omega \int \mathrm{d}\Omega \left(\prod_{i=0}^{n} \vec{n}\right) \cdot \mathcal{I}(\vec{r};\vec{p};t). \tag{2.26b}$$

We will need only the first three *radiation moments (RM)*. The 0^{th} moment,

$$\mathfrak{E}(\vec{r};\omega;t) = \frac{4\pi}{c}\mathfrak{J}(\vec{r};\omega;t) = \frac{1}{c}\int \mathrm{d}\Omega\, \mathcal{I}(\vec{r};\vec{p};t), \tag{2.27a}$$

$$\bar{\mathfrak{E}}(\vec{r};t) = \frac{4\pi}{c}\bar{\mathfrak{J}}(\vec{r};t) = \frac{1}{c}\int \mathrm{d}\omega \int \mathrm{d}\Omega\, \mathcal{I}(\vec{r};\vec{p};t), \tag{2.27b}$$

here given both in the monochromatic and grey version, is the *radiation energy density* $\mathfrak{E}, \bar{\mathfrak{E}}$. The variables $\mathfrak{J}, \bar{\mathfrak{J}}$ defined in Eqn. (2.27) are the 0^{th} *Eddington moments*. Likewise, we define the 1^{st} moments, i.e., the radiation flux density $\vec{\mathfrak{F}}, \bar{\vec{\mathfrak{F}}}$ and the associated 1^{st} Eddington moment

$$\vec{\mathfrak{F}}(\vec{r};\omega;t) = 4\pi\vec{\mathfrak{H}}(\vec{r};\omega;t) = \int \mathrm{d}\Omega\, \vec{n}\, \mathcal{I}(\vec{r};\vec{p};t), \tag{2.28a}$$

$$\bar{\vec{\mathfrak{F}}}(\vec{r};t) = 4\pi\bar{\vec{\mathfrak{H}}}(\vec{r};t) = \int \mathrm{d}\omega \int \mathrm{d}\Omega\, \vec{n}\, \mathcal{I}(\vec{r};\vec{p};t). \tag{2.28b}$$

The momentum density of the radiation field is given by $1/c^2\vec{\mathfrak{F}}$. The 2^{nd} moment

$$\mathfrak{P}_{ij}(\vec{r};\omega;t) = \frac{4\pi}{c}\mathfrak{K}_{ij}(\vec{r};\omega;t) = \frac{1}{c}\int \mathrm{d}\Omega\, n_i n_j \mathcal{I}(\vec{r};\vec{p};t), \tag{2.29a}$$

$$\bar{\mathfrak{P}}_{ij}(\vec{r};t) = \frac{4\pi}{c}\bar{\mathfrak{K}}_{ij}(\vec{r};t) = \frac{1}{c}\int \mathrm{d}\omega \int \mathrm{d}\Omega\, n_i n_j \mathcal{I}(\vec{r};\vec{p};t). \tag{2.29b}$$

is the radiation pressure tensor $\mathfrak{P}$; the corresponding Eddington moment is $\mathfrak{K}$. We will denote the third moment by $\mathfrak{Q}$ and $\bar{\mathfrak{Q}}$ where necessary.

We finally introduce the occupation density, i.e., the 0^{th} moment of the distribution function, a measure of the momentum-space volume the radiation quanta occupy:

$$\mathfrak{e}(\vec{r};\omega;t) = \frac{1}{4\pi c}\int \mathrm{d}\Omega\mathcal{F} = \mathfrak{E}(\vec{r};\omega;t)\left(\frac{\omega}{hc}\right)^{-3}, \tag{2.30a}$$

$$\bar{\mathfrak{e}}(\vec{r};t) = \frac{1}{4\pi c}\int \mathrm{d}\omega \int \mathrm{d}\Omega\mathcal{F}. \tag{2.30b}$$

We can give a simple relation between the monochromatic zeroth moments $\mathfrak{e}(\vec{r};\omega;t)$ and $\mathfrak{E}(\vec{r};\omega;t)$, but a similar relation for the grey variables can only be obtained by carrying out the integrals for an assumed dependence of $\mathscr{F}$ on ω. For most spectra, e.g., Fermi-Dirac or Bose-Einstein, the integral will become quite complicated. Hence, in practice, we can approximate the mean occupation density $\langle e \rangle$ in an energy-integrated scheme by $\langle \mathfrak{e} \rangle \sim \bar{\mathfrak{E}}/\langle\omega\rangle^4$, where we define the mean energy of radiation $\langle\omega\rangle = \bar{\mathfrak{E}}/\bar{n}$ ($\bar{n}$ is the total particle number). Plugging in the values of constants, we can evaluate the relation: $\langle \mathfrak{e} \rangle \sim 4.65 \times 10^{-13}(\bar{n}/\mathrm{cm}^{-3})^4(\bar{\mathfrak{e}}/(\mathrm{erg}/\mathrm{cm}^{-3}))^{-3}$.

Moments equations

To derive evolutionary equations for the radiation moments, we have to integrate the RTE, Eqn. (2.24), over angle. The result is a hierarchy of RMEs, the first two of which are

$$\frac{1}{c}\partial_t \mathfrak{J} + \nabla \cdot \vec{\mathfrak{H}} = \mathfrak{S}^{(0)}, \tag{2.31a}$$

$$\frac{1}{c}\partial_t \vec{\mathfrak{H}} + \nabla \cdot \mathfrak{K} = \vec{\mathfrak{S}}^{(1)}, \tag{2.31b}$$

$$\dots$$

The source terms $\mathfrak{S}^{(n)}$ are defined as the n^{th} moments of $\mathcal{S}$.

These equations form an infinite series of equations for ever higher moments. The equation for the n^{th} moment has a similar form as the ones explicitly listed in Eqns. (2.31) have (of course for a tensor of n^{th} rank), and involves the divergence of the $(n+1)^{\text{th}}$ moment. At some rank, we have to truncate the series, evolving only the first $n+1$ equations. In our scheme, we choose $n = 1$; the consequences of this choice will be discussed in a later paragraph. If we preferred $n = 0$, we would end up with the diffusion equation. Since this equation is also of importance to our scheme, we will discuss some related aspects there, too.

Solving the moments equations

Independent of the rank of truncation, we get a system which is not closed: the first two equations, Eqns. (2.31a) and (2.31b), e.g., consist of one scalar and one vector equation but have – apart from the source terms – one scalar, one vector, and one 2^{nd}-rank tensor variable. Thus, to solve for $\mathfrak{J}$ and $\vec{\mathfrak{H}}$, we require a closure – either an additional evolutionary equation for $\mathfrak{K}$ or relations specifying a dependence of $\mathfrak{K}$ on $\mathfrak{H}$ and $\vec{\mathfrak{J}}$.

The first technique, providing an independent evolutionary equation for $\mathfrak{K}$, was applied, e.g., by Rampp (2000); Rampp & Janka (2002) in spherical symmetry. They obtain the pressure tensor from a formal solution of the Boltzmann equation using the method of *variable Eddington factors (VEFs)*. Since this is not the direction we are heading, we will not go into detail here but rather refer the reader to Rampp (2000); Rampp & Janka (2002).

In our attempt to solve the RME, we use the second technique: we assume a fixed local (both in space and time) form of the *closure relation* between the first three moments. This can be a simple analytic function or it may be given by an implicit relation. Such a relation is the RT analogue to the EOS of HD. The method of closure relation is very common in solving the RT equations. Most previous work has closed the RM equations on the level of the energy equation by specifying a function $\vec{\mathfrak{F}}(\mathfrak{E})$. Depending on the function $\vec{\mathfrak{F}}(\mathfrak{E})$ applied, the result can be, e.g., a diffusion scheme, valid in optically thick regions, or a free-streaming scheme, valid in optically thin regions, or – most sophisticated – a *flux-limited diffusion (FLD)* scheme attempting at equally good performance in either of the two limiting cases.

Only a few authors have truncated the system at the first moments equation by a closure relation $\mathfrak{K}(\mathfrak{E}, \vec{\mathfrak{F}})$. Cernohorsky & van Weert (1992) explored this possibility, but afterwards, most efforts in the development of RT codes have shifted either to the simpler diffusion approximation of the more sophisticated Boltzmann schemes such as the one by Rampp & Janka (2002). Recently, however, Pons et al. (2000); Balsara (1999a,b); Audit & González (2006) pointed out a particular merit of the first-rank system: the resulting system is of hyperbolic type and can, thus, be handled with

highly developed techniques for hyperbolic PDEs, similarly to the HD system. Hence, we opted for the 1st-rank moments equations.

Source terms

Before further elaborating on the first-moment system, we will briefly discuss the source term $\mathcal{S}$ and its moments $\mathfrak{S}^{(0,1)}$ which are a major source of complication for the solution of the RT equations. These terms describe:

1. The generation of radiation intensity, energy, and momentum in emission reactions, e.g., by radiative cooling of matter. We shall parametrise the emission by the *emissivity* η. This will typically be a function of both the radiation intensity and the thermodynamical state of the matter.
2. The loss of intensity, energy, and momentum to matter in various absorption processes. We will assume that the loss of intensity has the form $-\kappa\mathcal{I}$ with the *opacity* κ depending on the intensity as well as on the thermodynamical state of the matter. The opacity is the inverse mean free path of a radiation quantum.
3. The redistribution of intensity, energy, and momentum between different radiative channels (i.e., between different radiation energies and directions, or radiation species) by means of scattering off matter or direct quantum-quantum reactions. As a simplification, these processes can be treated as absorption of one quantum and subsequent re-emission of another quantum in the new state. Thus, we need not introduce additional functions to describe scattering, but rather can describe scattering by a *scattering opacity* σ (to distinguish it from κ, it is often referred to as *true opacity*).

Hence, the source term $\mathcal{S}$ becomes

$$\mathcal{S} = \eta - \chi\mathcal{I}, \tag{2.32}$$

where η and $\chi = \kappa + \sigma$ include emission and absorption as well as scattering contributions.

In the limiting case of thermal equilibrium between radiation and matter, no net transfer occurs between these two subsystems, and $\mathcal{S} = 0$. Thus, the emissivity is determined by the absorption,

$$\eta = \chi\mathcal{I}. \tag{2.33}$$

An important concept related to absorption is the (dimensionless) *optical depth* τ along a path $\vec{r}(s)$ (s being a variable parametrising the path)

$$\mathrm{d}\tau = \chi \mathrm{d}|\vec{r}|. \tag{2.34}$$

If we consider a static (i.e., $\partial_t = 0$) system, we can rewrite the RTE as an *ordinary differential equation (ODE)* using the definition of τ:

$$\mu\partial_\tau\mathcal{I} = -\mathcal{I} + \frac{\eta}{\chi}, \tag{2.35a}$$

where μ is the cosine of the angle between the path and the direction of radiation. If we now set $\mu = 1$, neglect emission, $\eta = 0$, we can integrate Eqn. (2.35a), yielding

$$\mathcal{I} = \mathcal{I}_0 e^{-\tau}, \tag{2.35b}$$

where $\mathcal{I}_0$ is the intensity at $\tau = 0$, and get the important result that the optical depth of a system gives the number of e-foldings of the decrease of the intensity. In terms of the opacity, $\frac{1}{\chi}$, is the characteristic decay length of $\mathcal{I}$. If we consider instead a spatially homogeneous but temporally varying system, we conclude that $\frac{1}{c\chi}$ is the characteristic decay time of the intensity.

Solutions – free streaming and diffusion

Depending on the optical depth, the RTE allows for two limiting cases: if no source terms are present, i.e., at low τ (the transparent regime), the intensity will stream freely, whereas in the opposite case of high τ (the opaque regime), the diffusion approximation will be valid. Both limits can be described well by the 0^{th} RME.

For radiation streaming freely in direction $\vec{n}$, the RME simplify to

$$\partial_t \mathfrak{E} + c\vec{\nabla}\cdot\vec{n}\mathfrak{E} = \mathfrak{S}^{(0)}. \tag{2.36}$$

Apart from the source term, this is a simple linear advection equation, hence hyperbolic.

For very high optical depth, the diffusion approximation holds, and

$$\partial_t \mathfrak{E} - \vec{\nabla}\cdot\vec{D}\nabla\mathfrak{E} = \mathfrak{S}^{(0)}, \tag{2.37}$$

where the diffusion constant $D = \frac{c}{3\chi}$ follows from the opacity. Apart from the source term, this equation is parabolic, thus violating causality.

First- and second-order closure system

The system of first-moment equations of RT together with a closure relation forms the so-called *two-moment transport (TMT)*

$$\partial_t \mathfrak{E} + \vec{\nabla}\cdot\vec{\mathfrak{F}} = \mathfrak{S}^{(0)}, \tag{2.38a}$$

$$\frac{1}{c^2}\partial_t\vec{\mathfrak{F}} + \vec{\nabla}\cdot\mathfrak{P} = \frac{1}{c}\mathfrak{S}^{(1)}, \tag{2.38b}$$

$$\mathfrak{P} = \mathfrak{P}(\mathfrak{E},\vec{\mathfrak{F}}), \tag{2.38c}$$

which is a hyperbolic system of PDEs, similar to the HD equations. Because the directions of radiation propagation have been integrated out, the complexity of the system Eqn. (2.38) is greatly reduced compared to the original RTE.

A further reduction of complexity is reached when we consider the first-order closure system (*one-moment transport*)

$$\partial_t \mathfrak{E} + \vec{\nabla}\cdot\vec{\mathfrak{F}} = \mathfrak{S}^{(0)}, \tag{2.39a}$$

$$\vec{\mathfrak{F}} = \vec{\mathfrak{F}}(\mathfrak{E}). \tag{2.39b}$$

This system, widely used in astrophysical applications, can be derived from Eqn. (2.38) by neglecting the time derivative of the fluxes in Eqn. (2.38b). Thus, there is a close correspondence between the choice of $\mathfrak{P}$ (represented by the VEF) and the choice of $\vec{\mathfrak{F}}$ (represented by the *flux limiter*).

Depending on this choice, we may reproduce with good accuracy the two limiting cases of RT, viz. diffusion and free streaming. We will here consider only 1d Cartesian systems with the radiation propagating in x direction. Then, both the flux vector and the pressure tensor both have only one independent component. We will define a few variables: the *flux factor* $\mathfrak{f} = \frac{\mathfrak{F}_x}{c\mathfrak{E}}$, and the VEF $\mathfrak{p} = \frac{P_{xx}}{\mathfrak{E}}$. In the free-streaming limit, we have to set

$$\mathfrak{f} = 1, \qquad \mathfrak{F} = c\mathfrak{E}, \qquad \mathfrak{p} = 1, \qquad \mathfrak{P} = E. \tag{2.40a}$$

We note that the value $c\mathfrak{E}$ represents an upper bound to the flux: larger values would correspond to radiation propagating at a speed larger than c, thus violating causality. In the highly opaque limit, the diffusion equation can be recovered by setting

$$\mathfrak{f} = -\frac{c}{3\chi\mathfrak{E}}\nabla\mathfrak{E}, \qquad \mathfrak{F} = -\frac{c}{3\chi}\nabla\mathfrak{E}, \qquad \mathfrak{p} = \frac{1}{3}, \qquad \mathfrak{P} = \frac{\mathfrak{E}}{3}. \tag{2.40b}$$

The relation for the diffusion flux is known as *Fick's law*.

Both 1st- and 2nd-order closure method have to reproduce these two cases, as well as to guarantee a good approximation in the intermediate regime of semi-transparent media. Both methods use different yet related approaches to deal with this case:

1. When applying a diffusion scheme in the limit $\chi \to 0$, the flux can become acausal. As a consequence, FLD schemes are used, in which the flux is given by

$$\mathfrak{F} = c\mathfrak{E}\Lambda(R)R, \tag{2.41}$$

where we introduced the *Knudsen number* $R = |\nabla\mathfrak{E}|/\chi\mathfrak{E}$ and the *flux limiter* Λ. A number of flux limiters has been proposed, all of which have to respect the two limiting cases, i.e.,

$$\lim_{R\to\infty} R\Lambda(R) = 1, \tag{2.42a}$$

$$\lim_{R\to 0} R\Lambda(R) = \frac{1}{3}. \tag{2.42b}$$

2. In TMT, we use the flux factor $\mathfrak{f}$, satisfying $|\mathfrak{f}| \leq 1$, and the VEF $\mathfrak{p}(\mathfrak{e},\mathfrak{f})$ to provide an interpolation between the two limits. The consistency requirements become

$$\lim_{\mathfrak{f}\to 1}\mathfrak{p}(\mathfrak{e},\mathfrak{f}) = 1, \tag{2.43a}$$

$$\lim_{\mathfrak{f}\to 0}\mathfrak{p}(\mathfrak{e},\mathfrak{f}) = \frac{1}{3}. \tag{2.43b}$$

A further constraint relates $\mathfrak{f}$ and $\mathfrak{p}$,

$$\mathfrak{f}^2 \leq \mathfrak{p} \leq 1. \tag{2.43c}$$

It follows from the definition of $\mathfrak{f}$ and $\mathfrak{p}$ as normalised averages of a distribution function.

A tight relation exists between flux limiters Λ and the Eddington flux factor $\mathfrak{f}$; furthermore, from a VEF, one can compute a flux limiter

$$\Lambda(R) = \mathfrak{p} - \mathfrak{f}^2 > 0. \tag{2.44}$$

Closure relations

Hyperbolicity requirements We will now list a few properties we require from a closure relation. We will still work, for simplicity, in one-dimensional Cartesian coordinates. We will, additionally, use units in which $c = 1$.

We rewrite the TMT system, neglecting sources:

$$\partial_t\vec{U} + \nabla\vec{F} = 0, \tag{2.45a}$$

where the vectors of conserved variables and fluxes are

$$\vec{U} = (\mathfrak{E}, \mathfrak{F}), \tag{2.45b}$$

$$\vec{F} = (\mathfrak{F}, \mathfrak{p}\mathfrak{E}). \tag{2.45c}$$

The TMT system, Eqn. (2.45), is hyperbolic if the Jacobi matrix of the fluxes, $\mathfrak{J} = \partial_{\vec{U}}\vec{F}$, has real eigenvalues and a complete set of eigenvectors.

We can derive the Jacobian (Pons et al. 2000)

$$\mathfrak{J} = \begin{pmatrix} 0 & 1 \\ \mathfrak{p} - \mathfrak{f}\partial_{\mathfrak{f}}\mathfrak{p} + \mathfrak{e}\partial_{\mathfrak{e}}\mathfrak{p} & \partial_{\mathfrak{f}}\mathfrak{p} \end{pmatrix}. \tag{2.46}$$

Here, $\mathfrak{e} = \mathfrak{E}/\omega^3$ is the zeroth moment of the distribution function. The eigenvalues of the Jacobian, and hence the characteristic velocities, read

$$\lambda_{\pm} = \frac{\partial_{\mathfrak{f}}\mathfrak{p} \pm \sqrt{(\partial_{\mathfrak{f}}\mathfrak{p} - 2\mathfrak{f})^2 + 4(\mathfrak{p} - \mathfrak{f}\partial_{\mathfrak{f}}\mathfrak{p} + e\partial_{\mathfrak{e}}\mathfrak{p})}}{2}. \tag{2.47}$$

We will specialise to the case that $\mathfrak{p}$ only depends on $\mathfrak{f}$, i.e., $\partial_{\mathfrak{e}}\mathfrak{p} = 0$. Taking into account Eqn. (2.43c) and computing the discriminant of Eqn. (2.47), we can conclude that the TMT system is hyperbolic for all $\mathfrak{p}$. The diffusion and free-streaming limits transform into the constraints Eqns. (2.43b) and (2.43a), and the characteristic velocities in the diffusion and free-streaming limits have to be $\lambda_{\pm} = \frac{1}{3}$ and $\lambda_{+} = 1, \lambda_{-} = \partial_{\mathfrak{f}}\mathfrak{p} - 1$, respectively; in the latter limit, we must have $0 \leq \partial_{\mathfrak{f}}\mathfrak{p} \leq 2$.

Multi-dimensional generalisation The TMT system is a system of tensor equations. Thus, its generalisation to multi-dimensional situations is straightforward. The only complication is the formulation of the pressure tensor. Following Audit et al. (2002), we use

$$\mathfrak{P} = \left(\frac{1-\mathfrak{p}}{2}\mathfrak{1} + \frac{3\mathfrak{p}-1}{2}\vec{n}\otimes\vec{n} \right) \mathfrak{E}, \tag{2.48}$$

where $\mathfrak{1}$ is the unit tensor.

Closures Several authors have proposed VEFs. We consider a few different choices. Possibly the most general and accurate one is the *maximum-entropy* VEF (Cernohorsky & Bludman 1994), which is given as an implicit function of $\mathfrak{e}$ and $\mathfrak{f}$. In this *ansatz*, the VEF is obtained from a maximisation of the entropy of all angular distributions of the specific intensity consistent with given $\mathfrak{e}$ and f. As our work focuses on the principle viability of TMT in *radiation hydrodynamics (RHD)* in stellar explosions, we deferred the implementation of this more complex VEF to a later time. Instead, we implemented two limiting cases of the maximum-entropy VEF, and a few further closures:

1. The $M1$ model (Audit et al. 2002)

$$\mathfrak{p} = \frac{3+4\mathfrak{f}^2}{5+2\sqrt{4-3\mathfrak{f}^2}} \tag{2.49}$$

was used by Audit et al. (2002); Audit & González (2006) in photon transport. Similar to the maximum-entropy closure, it is based on an extremisation of the entropy, but is an explicit function and depends only on $\mathfrak{f}$.

2. We implemented a function consistent with the requirements listed above,

$$\mathfrak{p} = \frac{1}{3}(1 + a_1\mathfrak{f}^m + a_2\mathfrak{f}^n), \tag{2.50}$$

similar to a closure devised by Janka (1991) based on fits to Monte-Carlo simulations of neutrino transport. We set $a_1 = 16/30, a_2 = 2 - a_1, m = 1.9, n = 3.4$. These parameters differ slightly from the original ones which do not give the correct eigenvalues in the free-streaming limit.

3. The maximum-entropy closure allows for two simple limiting cases.
   (a) One is the *maximum-packing* closure, in which all radiation propagates in a cone of minimal opening angle around $\vec{n}$. It is given by

$$\mathfrak{p} = \frac{1}{3}(1 - 2\mathfrak{f} + 4\mathfrak{f}^2). \tag{2.51}$$

   (b) The opposite limiting case of the maximum-entropy closure is given by the Minerbo closure

$$\mathfrak{p} = 1 - 2\mathfrak{f}/q(\mathfrak{f}), \tag{2.52}$$

   where $q(x)$ is given implicitly by the Langevin function $x = \coth q - 1/q$. This function can be approximated by a polynomial,

$$q(x) \approx x^2(3 - x + 3x^2)/5. \tag{2.53}$$

4. The Kershaw closure

$$\mathfrak{p} = \frac{1}{3}(1 + 2\mathfrak{f}^2). \tag{2.54}$$

All of these closures satisfy the requirements listed above.

Cernohorsky & Bludman (1994) pointed out that the maximum-entropy closure admits a fairly analytic approximation $p(e, f)$

$$\mathfrak{p} = \frac{1}{3} + \frac{2}{3}(1 - \mathfrak{e})(1 - 2\mathfrak{e})\, q\left(\frac{\mathfrak{f}}{1 - \mathfrak{e}}\right). \tag{2.55}$$

Implementing this formula (for grey systems together with the approximation for $\langle\mathfrak{e}\rangle$) allows us to approximate the maximum-entropy closure without inverting the full implicit relation.

Moving media

If the medium through which the radiation propagates is not at rest, the RTEs need to be extended. To formulate the modifications, we have to select a frame of reference, i.e., a frame in which the various radiation quantities (energies, fluxes, ...) are measured. Since the RMEs are Lorentz-covariant tensor equations, the transformation between different frames follow from the Lorentz transformations. The transformations involve the standard transformations of tensors such as the velocity or the radiation moments, but also the blue- or redshift of the energy of radiation quanta. They are straightforward but tedious; we do not list them here but refer the reader to, e.g., Mihalas & Weibel Mihalas (1984). Due to the complexity of the transformations, usually only terms up to an order of 1 or 2 in (v/c) are retained.

We have the following basic choices at hand:

1. an inertial frame in which the fluid moves at velocity $\vec{v}$,
2. the co-moving frame, in which the fluid is at rest, and
3. the mixed frame, in which different parts of the equations are treated in different frames of reference.

Some terms explicitly depend on the energy of radiation quanta; in particular, source terms often have a fairly complicated spectral dependence. Typically, this dependence is simplest (in particular isotropic) in the rest frame of the matter. Thus, the evaluation of these terms is cumbersome in the inertial frame. In this frame, on the other hand, the left-hand sides of the system tends to be simplest, consisting only of standard flux-conservative terms. In contrast, the co-moving frame necessitates the introduction of non-conservative terms coupling different radiation moments.[2] Since we will try to employ standard methods for hyperbolic conservation laws, these extra terms might be considered problematic. Recently, however, Audit et al. (2002) demonstrated that these terms can be treated seperately from the hyperbolic part of the system. Thus, they do not conflict with Riemann-solver based methods. Because of this property, we selected the co-moving frame of reference to solve the RMEs.

The frame of reference is not to be confused with the coordinate system, i.e., Cartesian, spherical, ..., and the Eulerian or Lagrangian description. The coordinates only label space-time events; whether or not these labels are allowed to change in time has little to do with the values of tensor components at a certain space-time point governed by the frame of reference chosen. In principle, any combination between a reference frame and a Eulerian or Lagrangian description can be chosen. Not all of these are relevant for practical applications. One of most commonly employed combinations is, e.g., to describe the radiation field in a co-moving frame while using fixed Eulerian coordinates to refer to the spatial and temporal locations at which the field is measured – by a locally co-moving observer whose coordinates are subject to change as the fluid moves.

We list here the first moments equations in the co-moving frame as derived by Munier & Weaver (1985a,b). In these papers, expressions are given in general covariant form as well as specialised to different coordinates and symmetries. Because the equations are conceptionally most simple in covariant form, we will only list this form here. The equations are valid to first order in v/c.

$$\begin{aligned}\partial_t \mathfrak{E} + \nabla_i \mathfrak{F}^i + \nabla_i(\mathfrak{E} v^i) + \frac{v^i}{c^2}\partial_t \mathfrak{F}_i + \frac{a_i}{c^2}\mathfrak{F}^i \\ - \omega \frac{a_i}{c^2}\partial_\omega \mathfrak{F}^i - \omega(\nabla_i v_j)\partial_\omega \mathfrak{P}^{ij} = \frac{1}{c}\mathfrak{S}^0,\end{aligned} \tag{2.56a}$$

$$\begin{aligned}\frac{1}{c}\partial_t \mathfrak{F}^i + c\nabla_j \mathfrak{P}^{ij} + \nabla_j(\mathfrak{F}^i \frac{v^j}{c}) + \mathfrak{F}^j \nabla_j \frac{v^i}{c} + \frac{v_j}{c}\partial_t \mathfrak{P}^{ij} + \frac{a^i}{c}\mathfrak{E} \\ - (\nabla_j \frac{v_k}{c})\mathfrak{Q}^{ijk} - \omega \frac{a_j}{c}\partial_\omega \mathfrak{P}^{ij} - \omega(\nabla_j \frac{v_k}{c})\partial_\omega \mathfrak{Q}^{ijk} = \frac{1}{c}\mathfrak{S}^{1,i},\end{aligned} \tag{2.56b}$$

and the corresponding grey system consists of

$$\partial_t \bar{\mathfrak{E}} + \nabla_i \bar{\mathfrak{F}}^i + \nabla_i(\bar{\mathfrak{E}} v^i) + \frac{v^i}{c^2}\partial_t \bar{\mathfrak{F}}_i + \frac{a_i}{c^2}\bar{\mathfrak{F}}^i + \frac{a_i}{c^2}\bar{\mathfrak{F}}^i + (\nabla_i v_j)\bar{\mathfrak{P}}^{ij} = \frac{1}{c}\bar{\mathfrak{S}}^0, \tag{2.57a}$$

$$\frac{1}{c}\partial_t \bar{\mathfrak{F}}^i + c\nabla_j \bar{\mathfrak{P}}^{ij} + \nabla_j(\bar{\mathfrak{F}}^i \frac{v^j}{c}) + \bar{\mathfrak{F}}^j \nabla_j \frac{v^i}{c} + \frac{v_j}{c}\partial_t \bar{\mathfrak{P}}^{ij} + \frac{a^i}{c}\bar{\mathfrak{E}} + \frac{a_j}{c}\bar{\mathfrak{P}}^{ij} = \frac{1}{c}\bar{\mathfrak{S}}^{1,i}. \tag{2.57b}$$

The terms can be characterised as follows:

[2] In the mixed frame approach, one tries to combine both frames by evaluating each term in the frame in which it assumes its simplest form: conservative terms in the inertial frame, and source terms in the co-moving frame.

1. the standard terms present without fluid motion (blue);
2. terms describing the advection of the radiation with the fluid (green; these and the standard terms form the hyperbolic subsystem we try to address using standard methods for hyperbolic systems);
3. the source terms (light blue)
4. temporal derivatives of the higher moments (orange); these terms are often ignored, although Mihalas & Weibel Mihalas (1984); Rampp & Janka (2002); Buras et al. (2006) pointed out their significance. We will not include them in the first step;
5. acceleration ($\vec{a} = \partial_t \vec{v}$) terms (brown). According to Mihalas & Weibel Mihalas (1984) (§95), these terms can be dismissed;
6. blue- and redshift terms (violet) coupling different quantum energies and involving higher-order moments. In the grey system, the ω derivatives can be transformed using the fundamental theorem of calculus;
7. further terms involving the covariant derivative of the velocity (light green). In the grey system, the light green and violet terms involving $\mathfrak{Q}$ in the momentum equation cancel. Consequently, the grey momentum equation does not depend on moments higher than $\mathfrak{P}$, which is a further simplification.

In this exploratory study, we do not aim at a fully realistic description of the radiation field and RT. Thus, we will restrict ourselves to the grey system, Eqn. (2.57), and we will retain only the most important terms, viz. the hyperbolic part (blue and green terms), the transformation terms (violet and light green), and the source terms. In their §95, Mihalas & Weibel Mihalas (1984) point out that, in order to solve the RMEs correctly to order v/c, we can neglect all velocity-dependent terms in Eqn. (2.57b). Nevertheless, we will retain these terms except for the ones involving the fluid acceleration. To summarise, we attempt to solve the same system as Audit et al. (2002) do,

$$\partial_t \bar{\mathfrak{E}} + \nabla_i \bar{\mathfrak{F}}^i + \nabla_i (\bar{\mathfrak{E}} v^i) + (\nabla_i v_j) \bar{\mathfrak{P}}^{ij} = \frac{1}{c} \bar{\mathfrak{S}}^0, \tag{2.58a}$$

$$\frac{1}{c} \partial_t \bar{\mathfrak{F}}^i + c \nabla_j \bar{\mathfrak{P}}^{ij} + \nabla_j (\bar{\mathfrak{F}}^i \frac{v^j}{c}) + \bar{\mathfrak{F}}^j \nabla_j \frac{v^i}{c} = \frac{1}{c} \bar{\mathfrak{S}}^{1,i}. \tag{2.58b}$$

The generalisation to non-grey transport would require us to discretise the moments also in energy and to solve a system like Eqn. (2.58) for each *energy bin*, including the ω derivatives (and potentially further coupling terms in the sources).

As mentioned above, the RMEs have a hyperbolic part accounting for higher moments as well as advection by the fluid. Thus, the eigensystem is modified compared to the case discussed previously with the fluid at rest: to find the eigenspeeds of the full system, it is sufficient to add the fluid velocity to the eigenvalues of the pure RME (Audit et al. 2002).

We want to note furthermore that the left-hand sides of the grey RMEs do not make any reference to the spectrum of the moments, i.e., their dependence on ω. This only enters into the source terms.

Neutrino transport

The most important differences between photon and neutrino transport come from the fermionic character of neutrinos, the presence of three flavours of neutrinos and antineutrinos, and the conservation of the lepton numbers associated with each flavour.

Since neutrinos are fermions, they obey the Pauli principle and their spectra are given by the Fermi-Dirac distribution. From a technical point of view, we have to take this into account when

computing spectral averages. Furthermore, the Pauli principle has very important implications for neutrino-matter reactions.

The multi-flavour nature of the quanta can be accounted for by solving one transport system for each flavour. Since μ and τ (anti)neutrinos behave very similarly, e.g., in terms of reactions with matter, they are in most simulations treated as one flavour. Thus, typically, three flavours are present: e neutrinos, $\bar{e}$ neutrinos and "X" (i.e., $\mu, \bar{\mu}, \tau, \bar{\tau}$) neutrinos. We will simplify even further and disregard X neutrinos.

The second issue can be treated differently in energy-dependent and in grey simulations. In the energy-dependent case, both total radiation energy and total lepton number follow from the spectral distribution of the intensity and, hence, of the moments. Thus, one has to find a way to evolve the general, energy-dependent system under the constraint of conserving both energy and lepton number. We will not go into details further here. Solving the grey system, we, instead, treat two RME systems for each flavour: one of the systems describing the transport of energy, and the other one describing the transport of lepton number. Both systems can be coupled via the source terms and, potentially, the closure relation.

We will now explain some basics of the two systems. We start from the distribution function $\mathcal{F}(\vec{r};\vec{p};t)$. From this, we can compute the specific intensity $\mathcal{I}$ following Eqn. (2.25) by multiplying with ω^3. The result is the energy radiated at a given space-time point $(\vec{r};t)$ per energy interval into a given direction $\vec{n}$. If we, instead, multiply the distribution function by ω^2, we get the number of radiation quanta propagating at a given space-time point $(\vec{r};t)$ per energy interval into a given direction $\vec{n}$ (we call this intensity-like variable the "number intensity"). Therefore, if we interpret the RMEs, Eqn. (2.58), in terms of these number intensities rather than in terms of standard energy intensities, we can apply the very same RT system to both variables with only the source terms demanding adjustment. In the following, we will denote the 0^{th} (number density), 1^{st} (number flux), and 2^{nd} number moments by $\mathfrak{n}$, $\vec{\mathfrak{N}}$, and $\mathfrak{D}$, respectively.

Radiation hydrodynamics

Our goal is to investigate the coupled evolution of the radiation field and the fluid, i.e., to solve the full RHD problem. The terms coupling the radiation and the fluid subsystems follow from the conservation of total (i.e., fluid plus radiation) lepton number, energy, and momentum. They have been summarised, e.g., by Mihalas & Weibel Mihalas (1984). Within our approximations, they

read (e.g., Audit et al. 2002)

$$\partial_t \rho + \vec{\nabla}\cdot[\rho\vec{v}] = 0, \tag{2.59a}$$

$$\partial_t(\rho Y_e) + \vec{\nabla}\cdot[\rho Y_e\vec{v}] = -\frac{1}{c}\vec{\tilde{\mathfrak{S}}}^1_n, \tag{2.59b}$$

$$\partial_t \rho\vec{v} + \vec{\nabla}\cdot[\rho\vec{v}\otimes\vec{v} + P\mathbb{1}] = -\frac{1}{c}\vec{\tilde{\mathfrak{S}}}^1_E, \tag{2.59c}$$

$$\partial_t e + \vec{\nabla}[(e+P)\vec{v}] = -\frac{1}{c}\tilde{\mathfrak{S}}^0_E - \frac{1}{c}\vec{\tilde{\mathfrak{S}}}^1_E\cdot\vec{v}, \tag{2.59d}$$

$$\partial_t \bar{\mathfrak{E}} + \nabla_i(\tilde{\mathfrak{F}}^i + \bar{\mathfrak{E}}v^i) + (\nabla_i v_j)\bar{\mathfrak{P}}^{ij} = \frac{1}{c}\tilde{\mathfrak{S}}^0_E, \tag{2.59e}$$

$$\frac{1}{c}\partial_t\vec{\tilde{\mathfrak{F}}}^i + \nabla_i(c\bar{\mathfrak{P}}^{ij} + \tilde{\mathfrak{F}}^i\frac{v^j}{c}) + \tilde{\mathfrak{F}}^j\nabla_j\frac{v^i}{c} = \frac{1}{c}\tilde{\mathfrak{S}}^{1,i}_E. \tag{2.59f}$$

$$\partial_t \bar{\mathfrak{n}} + \nabla_i(\bar{\mathfrak{V}}^i + \bar{\mathfrak{n}}v^i) + (\nabla_i v_j)\bar{\mathfrak{O}}^{ij} = \frac{1}{c}\tilde{\mathfrak{S}}^0_n, \tag{2.59g}$$

$$\frac{1}{c}\partial_t\vec{\bar{\mathfrak{V}}}^i + \nabla_i(c\bar{\mathfrak{O}}^{ij} + \bar{\mathfrak{V}}^i\frac{v^j}{c}) + \bar{\mathfrak{V}}^j\nabla_j\frac{v^i}{c} = \frac{1}{c}\tilde{\mathfrak{S}}^{1,i}_n, \tag{2.59h}$$

and have to be augmented by the closure relations for HD pressure and for $\mathfrak{P}$ and $\mathfrak{O}$. For simplicity, we ignore the magnetic field and external forces such as gravity here. They simply add to the HD subsystem and do not provide any modifications to the RT subsystems or the coupling of the subsystems. We wrote down only the grey RT equations; even for non-grey transport, it is the energy-integrated variables $\bar{\mathfrak{E}}$ and $\vec{\bar{\mathfrak{F}}}$ that appear in the source terms of the HD equations. Furthermore, we only listed the RMEs for one neutrino flavour; if we evolve a system in which more species play a role, we will have to add a RT system for each of them, and to construct the radiative source terms in the HD equations from the summation of the contributions of each species.

Audit et al. (2002) demonstrated that Eqn. (2.59) decomposes into independent hyperbolic systems, viz. the hyperbolic parts of the HD and of the systems of radiative number and energy transport, and that the coupling terms do neither affect the hyperbolic character nor the set of eigenvalues of either system. Thus, they argued, the subsystems can be treated independently using *high-resolution shock-capturing (HRSC)* methods, under the constraint, however, that the solver for the RT system correctly reproduces the parabolic diffusion limit. Treating a diffusive system numerically by a TMT scheme amounts to applying a hyperbolic solver in the parabolic limit. As we will see later, this can be a major complication and requires certain modifications of the hyperbolic scheme. Finally, the source terms form a third building block of the system that can be tackled independently of the other two parts.

2.2.2 Radiation-matter interaction

Here, we will briefly list the source terms playing a role in SN neutrino transport and shortly describe how we implemented them. For a more detailed description, we refer the reader to, e.g., Burrows & Lattimer (1986); Cernohorsky & van Weert (1992); Keil et al. (1996); Rampp & Janka (2002); Burrows & Thompson (2002); Scheck et al. (2006), from which we adopted emission, absorption, and scattering rates.

Basics Typically, the rates of neutrino-matter reactions depend on both

1. the thermodynamical state of the matter, e.g., the gas temperature T, electron fraction Y_e, and the abundances and chemical potentials of different components of the gas such as electrons, protons, neutrons, and nuclei,
2. the energy spectrum of the neutrinos.

To compute the source terms, we have to perform an integral of the differential reaction rates $\sigma(\omega)$ over neutrino energy, either ranging from $\omega = 0$ to $\omega = \infty$ (for grey transport) or from $\omega = \omega_-$ to $\omega = \omega_+$ (for multi-energy-group transport, where ω_- and ω_+ are the lower and upper bounds of a particular energy bin).

The matter thermodynamics can be determined using a sufficiently sophisticated EOS, but for the spectral integral, we have to add a few considerations:

1. In energy-dependent transport, we have a numerical approximation to the neutrino energy spectrum. We, thus, can evaluate the integral in question numerically up to a desired accuracy.
2. In grey transport, lacking any spectral information, we only know the integral energy and number densities. Tom compute the source terms, we have to integrate the reaction rates depending on ω over neutrino energy. To perform such spectral integrals, we must assume a mock spectrum. For this, we can make different choices which we will describe in the next paragraph.

The source terms for the different moments can be found by the appropriate integration of the differential reaction rates over the angle of radiation propagation. Only anisotropic emission processes act as a source for $\vec{\mathfrak{F}}$, and isotropic scattering does not affect $\bar{\mathfrak{E}}$ at all. Absorption reactions, in contrast, appear as a sink of both $\mathfrak{E}$ and $\vec{\mathfrak{F}}$.

In the important case of *local thermodynamic equilibrium (LTE)*, the sources for E assume a relaxation form:

$$\mathfrak{S}^0 = -c\chi(\mathfrak{E}^{\mathrm{eq}} - \mathfrak{E}), \tag{2.60}$$

where $\mathfrak{E}^{\mathrm{eq}}$ is the equilibrium energy density consistent with the thermodynamic state of the matter, e.g., given by the Planck spectrum for photons. As we can see, when the source term is dominant (i.e., for large optical depth), $\mathfrak{E}$ will quickly approach $\mathfrak{E}^{\mathrm{eq}}$.

Mock neutrino spectra The simplest possible assumption for the neutrino energy spectrum is that all particles have the same energy $\bar{\omega}$, independent of the actual values of $\mathfrak{E}$ and $\mathfrak{n}$. We can evaluate all source terms for a given energy which, in spectral simulations, is found to be representative for the neutrinos in the system we study.

A second choice is to compute, for given $\mathfrak{E}$ and $\mathfrak{n}$, a representative particle energy $\bar{\omega} = \mathfrak{E}/\mathfrak{n}$ and assume that all quanta have an energy of $\bar{\omega}$.

The most sophisticated approach to mock spectra is to assume a pre-defined non-constant spectrum – e.g., Fermi-Dirac for neutrinos or Planck for photons – characterised by a few *radiation thermodynamics* parameters such as radiation temperature T_{R} and chemical potential μ_{R}. To compute these parameters from E and n, we have to invert the relation $\left(\frac{\mathfrak{E}}{\mathfrak{n}}\right) = \left(\frac{\mathfrak{E}}{\mathfrak{n}}\right)(T_{\mathrm{R}}, \mu_{\mathrm{R}})$. Depending on their complexity, we can then apply analytic expressions for the integral reaction rates as a function of T_{R} and μ_{R}, or integrate the rates numerically. In many cases, this approach will give the most accurate results. It is, however, subject to a possible limitation: there is no guarantee that the radiation field can always be described by the pre-selected spectrum. It may as well assume a completely different spectrum, and, in this case, the inversion yielding $(T_{\mathrm{R}}, \mu_{\mathrm{R}})$ may become ill-defined.

Relevant reactions Emission, absorption, and scattering rates have been computed for several neutrino-matter reactions relevant to SNe. We will list a few of the most important ones for which we have implemented approximative expressions based on the mock spectra described above. The reaction rates implemented follow mainly the formulae given by Rampp (2000); Cernohorsky & van Weert (1992).

1. Neutrinos of all flavours scattering off electrons, nucleons, and nuclei:

$$\nu + \begin{pmatrix} \mathrm{e}^{\pm} \\ \mathrm{N} \\ \mathrm{A} \end{pmatrix} \rightleftharpoons \nu + \begin{pmatrix} \mathrm{e}^{\pm} \\ \mathrm{N} \\ \mathrm{A} \end{pmatrix}, \tag{2.61}$$

   where $\mathrm{N} = \mathrm{n}, \mathrm{p}$, and A stand for nucleons and nuclei. The neutral-current versions of these reactions are allowed for neutrinos of all flavours. Additionally, electron-flavour neutrinos can scatter in charged-current reactions. A particularly important detail about the scattering off nuclei is the possibility of coherent scattering which enhances the reaction rates significantly.
2. Absorption and emission by free nucleons,

$$\nu_{\mathrm{e}} + \mathrm{n} \rightleftharpoons \mathrm{e}^{-} + \mathrm{p}^{+}, \tag{2.62a}$$
$$\bar{\nu}_{\mathrm{e}} + \mathrm{p}^{+} \rightleftharpoons \mathrm{e}^{+} + \mathrm{n}, \tag{2.62b}$$

   converting charged into neutral leptons and vice versa.
3. Absorption and emission by nucleons inside nuclei,

$$\nu_{\mathrm{e}} + \mathrm{A} \rightleftharpoons \mathrm{e}^{-} + \mathrm{A}'. \tag{2.63}$$

4. Thermal pair processes

$$\nu + \bar{\nu} \rightleftharpoons \mathrm{e}^{+} + \mathrm{e}^{-}, \tag{2.64}$$

   by which all can flavours of neutrinos be produced.

Chapter 3

Numerical methods

A CONJURER GETS NO CREDIT WHEN ONCE HE HAS EXPLAINED HIS TRICK; AND IF I SHOW YOU TOO MUCH OF MY METHOD OF WORKING, YOU WILL COME TO THE CONCLUSION THAT I AM A VERY ORDINARY INDIVIDUAL AFTER ALL.

Sherlock Holmes, *A Study in Scarlet*

3.1 Magnetohydrodynamics

3.1.1 Methods for hyperbolic equations

Hyperbolic conservation laws

The MHD equations form a hyperbolic PDE system, similar to, e.g., the equations of non-magnetic hydrodynamics. Hyperbolic systems share many properties which are important for numerical analysis. In the following, we will briefly review some of these (see, e.g., LeVeque 1992, 1998).

For simplicity, we start with the homogeneous, i.e., source-less version of the conservation law (2.2) in one spatial dimension,

$$\partial_t u + \partial_x f(u) = 0 \tag{3.1}$$

where $u = (u^i)$, $f = (f^i)$ are the conserved variables and the fluxes, respectively, and $i = 1, ..., m$ numbers different variables such as mass density, momentum components, or energy density[1]. Its simplest special case is the linear system describing the advection of $\vec{u}$ along x with a constant velocity c,

$$\partial_t u + \partial_x cu = 0. \tag{3.2}$$

For this equation, the state of $u(t_0, x_0)$ at a given point (t_0, x_0) is simply propagated along a space-time curve $\mathcal{C} : x - ct = x_0 - ct_0$. This curve of information propagation is called the *characteristic* of the system, and the velocity of information propagation is called the *characteristic velocity*.

[1] Please note that this short-hand notation only serves to conveniently summarise all equations of the system, and does not imply any tensorial character. In fact, the HD system consists of equations of different tensorial rank: the continuity equations for mass and energy are scalar equations whereas the momentum equation is a vectorial one.

Equation (3.1) can be linearised, yielding

$$\partial_t u + \mathfrak{J}\partial_x u = 0, \tag{3.3a}$$

where we define the Jacobi matrix $\mathfrak{J}$ of the flux vector f:

$$\mathfrak{J}^{ij} = \frac{\partial f^i}{\partial u^j}. \tag{3.3b}$$

The system (3.1) is called *hyperbolic* if $\mathfrak{J}$ can be diagonalised with real eigenvalues λ^i, $i = 1...m$, and correspondingly has a set of linearly independent left and right eigenvectors (l^i) and (r^i), respectively (the so-called eigenvalues and eigenvectors of the ith wave family). The system is *strictly hyperbolic* if all eigenvalues are distinct, else it is called *weakly hyperbolic*. In the following, we will denote by $\mathfrak{R}$ the matrix whose columns are r_i.

We will now focus on the characteristics and characteristic velocities of the non-linear system. As we will see, the characteristic velocities are finite, given by the eigenvalues of the Jacobian. First, we transform Eqn. (3.1) into the eigensystem of the Jacobi matrix. The transformation matrix can be described in terms of the matrix of right eigenvectors $\mathfrak{R}$. We can write the system in terms of the *characteristic variables* v, for which $\mathrm{d}v = \mathfrak{R}^{-1}\mathrm{d}u$. The flux will be given by the matrix of eigenvalues $\mathfrak{E} = \mathrm{diag}(\lambda^i)$, for which $\mathfrak{J} = \mathfrak{R}\mathfrak{E}\mathfrak{R}^{-1}$:

$$\mathrm{D}_t^{\mathcal{C}^i} v^i = \partial_t v^i + \lambda^i \partial_x v^i = 0. \tag{3.4}$$

Here, we define the integral curve $\mathcal{C}^i$ of the eigenvalue λ_i, i.e., the trajectory $x(t)$, for which $\dot{x} = \lambda_i$. The total derivative along this curve is given by $\mathrm{D}_t^{\mathcal{C}_i} = \partial_t + \dot{x}\partial_x$.

Comparing the last equation with the other representations of the hyperbolic system and the linear advection system, we may note a few important points:

1. When written in terms of conserved variables, all m equations of the system couple through the dependence of the flux f on u, whereas the system decomposes into m independent equations in terms of the characteristic variables.
2. The characteristic equations bear a striking resemblance to the linear advection system with the advection velocity c_x replaced by λ^i. The similarity is limited by the fact that the eigenvalues are not constants but depend on u. The eigenvalues are only approximately constant in the vicinity of a given point (t,x) in space-time.
3. The hyperbolic system can be transformed locally into a system of advection equations by virtue of which the characteristic variables are advected independently of each other. The characteristics of the system are the integral curves $\mathcal{C}^i$, and the characteristic velocities are the eigenvalues λ^i.
4. Hence, if we know the state $u(t,.)$ at any given time, and if we are able to decompose it into eigenstates (components v^i), we can compute the temporal evolution locally by advecting each characteristic variable v_i with its eigenspeed λ_i.
5. For the advection equation, the value of u^i is constant along the ith characteristic. This no longer holds for the conserved variables of a non-linear system. Instead, the characteristic component v^i is constant on $\mathcal{C}^i$, since $\mathrm{D}_t^{\mathcal{C}^i} v^i = 0$.
6. Due to the finite eigenspeeds, a state $v_i(t_0,x_0)$ can only affect a limited space-time domain of influence, and it can only be affected from points within a limited domain of dependence.
7. For non-linear systems, the eigenvalues vary in space and time. Thus, the characteristics of one particular family i are not in general parallel, but they can cross. At a crossing (t_c,x_c), two different values of the characteristic variable v^i are at hand, and thus, $v^i(t_c,x_c)$ is not

fixed uniquely. In such a case, the linearisation meets its limitations. The two linear states interact non-linearly, and the solution of the system may become discontinuous.

8. While the procedure described so far can be applied to a large number of system, the diagonalisation required is very tedious or even unknown for many other systems. In such a case, simplifying approximations have to be made.

Physically, the eigenvectors correspond to wave-like solutions of the linearised equations. We now consider the one-dimensional Euler equations. For a gas with fluid velocity $v_x(x,t)$ and sound speed $c_s(x,t)$, the eigenvectors correspond to two sound waves, travelling at $v_x \pm c_s$, and an entropy wave, travelling at v_x. Thus, the evolution of an Eulerian fluid can be described in terms of travelling sound and entropy waves. Examples for the non-linear waves developing in characteristic crossings are (supersonic) shock and rarefaction waves.

For the numerical solution of the system, a particularly important step is the consideration of the *Riemann problem*, i.e., the evolution of two constant states $u^{\mathrm{L,R}}$ (left, right state) separated by a discontinuity. The discontinuity decays into a number of waves travelling to the left or right, the so-called *Riemann fan*. For HD, these waves may be different combinations of shocks or rarefaction waves, whereas for MHD considerably more combinations of waves are possible.

Numerical methods for hyperbolic conservation laws

Spatial Discretisation A class of very powerful methods for the numerical solution of hyperbolic systems consists of the HRSC schemes. These schemes will be explained in the following. For a review on the numerics of hyperbolic conservation laws, including HRSC schemes, we recommend the books by LeVeque (1992, 1998); Toro (1997) as well as the reviews by Tadmor (1998); Martí & Müller (2003); Font (2003).

In this subsection, we will be concerned primarily with conservation laws of the Gauss form (2.2a) and will defer the discussion of the peculiarities of the Stokes equation (2.2b) to the next subsection.

To evolve the hyperbolic system for a given set of initial data numerically, we have to decompose a continuous region of space and time properly into discrete elements. Belonging to the so-called *Eulerian* schemes, HRSC follow the evolution of the fluid in a mesh which is fixed in space, as opposed to the so-called *Lagrangian* methods tracking the motion of individual fluid elements.

More specifically, we divide the physical domain into a finite number of disjoint volumes (grid zones) $\mathcal{Z}_i$ and approximate the conserved variable $u(\vec{x})$ by its volume averages

$$u_i = \frac{1}{\int_{\mathcal{Z}_{i-\frac{1}{2}}} \mathrm{d}\mathcal{V}} \int_{\mathcal{Z}_i} \mathrm{d}\mathcal{V}\, u. \tag{3.5}$$

This volumetric discretisation contrasts to a point-value formulation which approximates $u(\vec{x})$ by its value at the centre of each cell, $u_i = u(\vec{x}_0)$. We will focus mainly on the volumetric form. The temporal evolution of u_i is governed by the discretised conservation law

$$\partial_t u_i + \frac{1}{\int_{\mathcal{Z}_{i-\frac{1}{2}}} \mathrm{d}\mathcal{V}} \int_{\mathcal{Z}_i} \mathrm{d}\mathcal{V}\, \vec{\nabla}\cdot\vec{F} = \frac{1}{\int_{\mathcal{Z}_{i-\frac{1}{2}}} \mathrm{d}\mathcal{V}} \int_{\mathcal{Z}_i} \mathrm{d}\mathcal{V}\, S_i. \tag{3.6a}$$

Ignoring source terms and applying Gauss' law (Eqn. (2.3a)), we find the *flux-conservative* form of (3.6a)

$$\partial_t u_i + \frac{1}{\int_{\mathcal{Z}_{i-\frac{1}{2}}} \mathrm{d}\mathcal{V}} \int_{\partial\mathcal{Z}_i} \overrightarrow{\mathrm{d}\mathcal{A}}\cdot\vec{F} = 0. \tag{3.6b}$$

We will simplify the discussion in the following by limiting our considerations to one-dimensional equations and discuss the generalisation to multi-dimensional systems later. We will assume that zone $\mathcal{Z}_i$ extends from $x_{i-\frac{1}{2}}$ to $x_{i+\frac{1}{2}}$, and we will denote the volume of the zone and the areas of the surfaces at the left (interface $\mathcal{I}_{i-\frac{1}{2}}$ at $x_{i-\frac{1}{2}}$) and right (interface $\mathcal{I}_{i+\frac{1}{2}}$ at $x_{i+\frac{1}{2}}$) zone boundaries by $\mathcal{V}_i$ and $\mathcal{A}_{i\pm\frac{1}{2}}$, respectively. The exact definition of these geometry elements, but not the general form of the equations, will depend on the coordinate system chosen (e.g., Cartesian, spherical, or cylindrical coordinates). The location of the zone centre will be denoted x_i.

Using these definitions, we can reformulate (3.6b), yielding

$$\partial_t u_i + \frac{1}{\mathcal{V}_i}\left(\mathcal{A}_{i+\frac{1}{2}}\bar{F}_{i+\frac{1}{2}} - \mathcal{A}_{i-\frac{1}{2}}\bar{F}_{i-\frac{1}{2}}\right) = 0, \tag{3.7}$$

where $\bar{F}_{i\pm\frac{1}{2}}$ is the surface-average flux through $\mathcal{A}_{i\pm\frac{1}{2}}$. Thus, to solve the conservation law numerically, we have to determine discrete approximations to $\bar{F}_{i\pm\frac{1}{2}}$. Denoting such approximations by $F_{i\pm\frac{1}{2}}$, we get an ODE,

$$\partial_t u_i + \frac{1}{\mathcal{V}_i}\left(\mathcal{A}_{i+\frac{1}{2}}F_{i+\frac{1}{2}} - \mathcal{A}_{i-\frac{1}{2}}F_{i-\frac{1}{2}}\right) = 0. \tag{3.8}$$

In deriving this equation, we treated the temporal and the spatial operators of the original equation independently of each other and did not apply a discretisation in time, only in space; Therefore, (3.7) is called the *semi-discrete* form of the conservation law. Given the numerical fluxes $F_{i\pm\frac{1}{2}}$, it can be treated using a standard ODE solver such as multi-step Runge-Kutta schemes. We will consider this issue later, after a brief discussion of techniques for the computation of the fluxes.

Since the flux is a function of the conserved variables, $F = F(u)$, we have to find a method of computing the zone-interface fluxes from the zone averages u_i. Furthermore, we want to take advantage of the characteristic properties of hyperbolic systems described above. These two constraints give rise to a decomposition of the full task into two separate ones: the *reconstruction* of zone-interface variables from zone averages, and a *flux function* to obtain the flux from the reconstructed variables.

Before going into the details of the reconstruction process, we want to note that two basic schemes can be distinguished, which we will classify according to Zhang & MacFadyen (2006) as *finite difference (FD)* and *finite volume (FV)* schemes:

1. FD schemes first compute the fluxes in each zone, and then reconstruct the fluxes to zone interfaces (for applying the flux function, they also need to reconstruct the conserved variables); afterwards, they apply the flux function to the reconstructed fluxes,
2. FV schemes reconstruct the conserved variables to zone interfaces and, after computing the interface fluxes from the interface values of u, apply the flux function to these fluxes.

Whereas our previous code exclusively used the first kind of schemes, the new one can employ both. Most tests and all applications were carried out using FV schemes.

Reconstruction We want to compute the value $\phi(x)$ of a variable ϕ at a given location x on the grid, e.g., at the zone interfaces $\mathcal{I}_{i\pm\frac{1}{2}}$, from the zone averages f_i. For each zone $\mathcal{Z}_i$, we will determine a function $\phi^i(x)$ locally approximating f around $\mathcal{Z}_i$. This procedure, hence, yields two distinct values for $\phi(x_{i-\frac{1}{2}})$, viz. $\phi^{i-1}(x_{i-\frac{1}{2}})$ and $\phi^i(x_{i-\frac{1}{2}})$. With these two values of fluxes and/or conserved variables at hand, we can construct unique interface values using flux functions. We will elaborate on this in the next paragraph.

We define the interpolating functions ϕ^i from the zone averages $\phi_j, j \in \{i-n,...,i+n\}$ (these zones are called the reconstruction *stencil*). They have to fulfil three basic requirements:

1. *Consistency*: for each zone in the stencil, the zone average of ϕ^i has to equal the original zone average, $\int_{\mathcal{Z}_j} \mathrm{d}\mathcal{V}\, \phi^i = \phi_j$. This is the volumetric form of the constraint. In a point-value discretisation, we would instead demand that $\phi^i(x_j) = \phi_j$. For uniform Cartesian grids, both forms coincide, but they may differ for more general geometries.
2. *Accuracy*: the ϕ^i have to approximate the "true" function f accurately, i.e., the error $\left|\phi^i - f\right|$ has to be of a high order in the zone width.
3. *Stability*: the reconstruction must not lead to an unstable numerical scheme.

Piecewise-constant reconstruction Typically, the functions ϕ^i are constructed from polynomials, giving rise to the family of *piecewise-polynomial methods*. The simplest choice is the *piecewise-constant method (PCM)* employing a one-zone stencil:

$$\phi^i(x) = \phi_i,\ x \in [x_{i-\frac{1}{2}}, x_{i+\frac{1}{2}}]. \tag{3.9}$$

This method is only first order accurate, i.e., the truncation error scales linearly with the grid resolution. It turns out to be the least accurate yet most stable reconstruction.

Piecewise-linear reconstruction To gain accuracy, we may construct the interpolant function from a larger stencil using higher-order polynomials. We will illustrate this for the second-order *piecewise-linear method (PLM)*. To find the reconstructing function in zone $\mathcal{Z}_i$, ϕ^i, we first construct two linear polynomials from the one-sided linear approximations to the zone averages,

$$\phi^i_+(x) = \frac{2(\phi_{i+1}-\phi_i)}{x_{i+\frac{3}{2}} - x_{i-\frac{1}{2}}} x + \frac{\phi_i(x_{i+\frac{3}{2}} + x_{i+\frac{1}{2}}) - \phi_{i+1}(x_{i+\frac{1}{2}} + x_{i-\frac{1}{2}})}{x_{i+\frac{3}{2}} - x_{i-\frac{1}{2}}}, \tag{3.10a}$$

$$\phi^i_-(x) = \frac{2(\phi_i-\phi_{i-1})}{x_{i+\frac{1}{2}} - x_{i-\frac{3}{2}}} x + \frac{\phi_{i-1}(x_{i+\frac{1}{2}} + x_{i-\frac{1}{2}}) - \phi_i(x_{i+\frac{1}{2}} + x_{i-\frac{3}{2}})}{x_{i+\frac{1}{2}} - x_{i-\frac{3}{2}}}. \tag{3.10b}$$

We note that both linear functions agree in their value at the zone centre, $\phi^i_+((x_{i+\frac{1}{2}} + x_{i-\frac{1}{2}})/2) = \phi_i = \phi^i_-((x_{i+\frac{1}{2}} + x_{i-\frac{1}{2}})/2)$, and, away from extrema or discontinuities, the individual slopes $m^i_{+,-}$ (i.e., the coefficients of x in the first terms on the right-hand sides of Eqn. (3.10)) will be very similar as well. Furthermore, each linear combination is a consistent approximation to ϕ.

Owing to the linear approximation, we can construct a second-order method from these two polynomials. Thus, the consistency and the accuracy constraints are readily fulfilled. A problem arises, however, if we take into account the stability criterion. Near a discontinuity, an approximation of the function $\phi(x)$ by one-sided gradients can result in significant overshooting, creating additional extrema. In a dynamic situation, the ensuing spurious oscillations will degrade the overall accuracy and eventually lead to unphysical values of the variables. To account for this observation, we demand that the total variation

$$TV[\phi] = \sum_i |\phi_{i+1} - \phi_i| \tag{3.11}$$

does not increase with time, which forbids the development of new extrema. The so-called *total variation diminishing (TVD)* constraint is an exact property of linear advection equations. Though

no longer exact for more general hyperbolic systems, it still provides a very valuable stability criterion for these systems.

As a remedy, we are thus forced to abandon the use of one-sided gradients in the reconstruction and rather construct a TVD combination of ϕ^i_+ and ϕ^i_- by applying a TVD *slope limiter* to the slopes $m_{+,-}$,

$$m^i = SL(m^i_+, m^i_-). \tag{3.12}$$

This function allows to determine the final slope m^i, yielding the final stable second-order interpolant

$$\phi^i(x) = \phi_i \left(x - \frac{x_{i+\frac{1}{2}} - x_{i-\frac{1}{2}}}{2} \right) + mx. \tag{3.13}$$

Various TVD slope limiters $SL(m_-, m_+)$ have been given by different authors; all of them have to lie within the TVD region of the (m_1, m_2) plane identified by Sweby (1984). This region defines the range of admissible values of the interpolant. If both slopes have the same sign, the limited slope will be a combination of m_- and m_+. The exact form of this combination depends on the limiter and determines its accuracy and stability properties. We implemented the *minmod*, the *van Leer*, and the *monotonised central* limiters. For different signs, on the other hand, all limiters have to return 0 thus reverting to the stable PCM reconstruction in order to avoid spurious oscillations near discontinuities. Unfortunately, this leads to a degradation of the accuracy also near smooth extrema since TVD limiters, based only on local first derivatives, cannot distinguish an extremum from a discontinuity.

Higher-order reconstruction This is the point where some of the more recently developed higher-order reconstruction methods come into play. Common to them is the use of higher-order polynomials (typically parabolae or higher) and larger ($n \geq 5$) stencils. In our code, we implemented the *weighted essentially non-oscillatory (WENO)* and the *monotonicity preserving (MP)* methods, which we will describe in the following briefly.

We reconstruct the interpolant $\phi^i(x)$ according to the *essentially non-oscillatory (ENO)* (Harten et al. 1987) or WENO (Liu et al. 1994) methods. During the last years, various implementations of WENO (and related *convex-ENO*) schemes for HD (e.g., Shu & Osher 1989; Levy et al. 1999, 2000, 2002; Del Zanna & Bucciantini 2002; Rahman & Moore 2005a,b; Tchekhovskoy et al. 2007) and MHD (e.g., Jiang & Wu 1999; Del Zanna et al. 2003) were proposed which differ in several details of the reconstruction. Of these, our implementation follows most closely the one by Levy et al. (1999). For a review on ENO and WENO schemes, see, e.g., Shu (1997).

We first define a set of consistent "candidate" polynomials[2] $\phi_j(x)$ of order m centred at cells $\mathcal{Z}_j$, $j = i-m, ..., i+m$. The stencil of each candidate polynomial is $p = m+1$; thus, each one is consistent with $\mathcal{Z}_i$. In our implementation, we use parabolae, i.e., $m = 2$, $p = 3$ which do not suffer from the inability to distinguish between smooth extrema and discontinuities. From these candidate polynomials, we construct the final interpolant by a weighting procedure. This procedure is not unique; of the many different possible choices, we use the definitions by Jiang & Shu (1996), implemented by Levy et al. (1999). The reconstruction scheme is approximately of 4^{th} order; thus, it will be called WENO-4.

The *smoothness indicators*

$$SI_j = \sum_{l=1}^{2} \int_{\mathcal{Z}_j} \mathrm{d}\mathcal{V} (\Delta x)^{2l-1} (\partial^l_x \phi_j)^2, \tag{3.14a}$$

[2]here and in the following, we omit the superscript ^{i} to avoid the formulae getting cluttered with indices

depending on the the 1st and 2nd numerical derivatives of the candidate polynomials, provide us with an estimate of the amplitude of short-wavelength oscillations, and thus of possible sources of instability, in the data. The ENO method selects the least oscillatory candidate polynomial, i.e., the one having the smallest smoothness indicator, $\phi(x) = \phi_j(x)$, and discards the rest. The WENO methods, in contrast, do not surrender the additional information contained in these functions. Instead, it computes the final interpolant using a weighted sum of all candidate polynomials. The weights are defined as functions of the smoothness indicators. We set them to

$$w_j = \frac{\alpha_j}{\sum_k \alpha_k}, \tag{3.14b}$$

where

$$\alpha_j = \frac{C_k}{(\varepsilon + SI_k)^p}, \tag{3.14c}$$

and C_k, ε, and p are constants which we set to the values from Levy et al. (1999) generalised to non-equidistant volumetric coordinates. For smooth data, all weights will be of comparable order, and thus, the accuracy benefits from a very large stencil equal to the union of the candidate stencils. At discontinuities, WENO meets the stability requirements by assigning the largest weights to the smoothest polynomials and virtually no weight to the more oscillatory ones. Near such points, the order of the method degrades to 1, but WENO schemes with an arbitrary high order in smooth flow regions can be devised.

For MP reconstruction (Suresh & Huynh 1997), we first construct a consistent high-order function. In our code, we use polynomials of 5th, 7th, or 9th order (the resulting schemes will be refered to as MP-5, MP-7, MP-9, respectively). Similar to TVD limiting, we then limit the interpolant to a region of admissible values. The definition of this region involves stability as well as accuracy constraints, which, compared to TVD, are less restrictive, allowing for a closer reproduction of smooth extrema and maintaining an exact reconstruction of smooth flows, while efficiently suppressing spurious oscillations near discontinuities. Recently, MP reconstruction has been used by Del Zanna et al. (2007) for the general relativistic MHD.

Evaluating the interpolant Having constructed an interpolant fulfilling the consistency, accuracy, and stability constraints, we can finally obtain the interface value. Again, we have two different possibilities:

1. in a point-value formulation, we would simply evaluate this function at the given location $x_{i\pm\frac{1}{2}}$,
$$\phi^{\mathrm{P}}_{i\pm\frac{1}{2}} = \phi^i(x_{i\pm\frac{1}{2}}), \tag{3.15a}$$
2. in a volumetric formulation, we have to compute the volume average over the zones $\mathcal{Z}_{i-\frac{1}{2}}$ (ranging from $x_{i-1} \in [x_{i-\frac{3}{2}}, x_{i-\frac{1}{2}}]$ to $x_i \in [x_{i-\frac{1}{2}}, x_{i+\frac{1}{2}}]$) staggered w.r.t. to $\mathcal{Z}_i$,
$$\phi^{\mathrm{V}}_{i\pm\frac{1}{2}} = \frac{1}{\mathcal{V}_i} \int_{\mathcal{Z}_{i-\frac{1}{2}}} \mathrm{d}\mathcal{V}\, \phi^i(x). \tag{3.15b}$$

Both forms differ only for higher-order reconstruction in some geometric terms, with the point-value reconstruction being more straightforward to implement. Recently, however, Del Zanna & Bucciantini (2002) pointed out a peculiarity of FV schemes: while we can reconstruct the interface values of the conserved variables $u^{\mathrm{P}}_{i\pm\frac{1}{2}}$ using, e.g., WENO or MP schemes, up to a very high

order, this high accuracy does not necessarily carry over to the derivatives of the interface fluxes $f^{\mathrm{P}}(u^{\mathrm{P}}_{i\pm\frac{1}{2}})$. To maintain the high order of accuracy also for these, the authors use a second reconstruction step to convert the reconstructed point values to volumetric averages over staggered zones. To this end, they compute new interpolants $\{\tilde{f}_{i-\frac{1}{2}}(x)\}$ based on the point values $\{f^{\mathrm{P}}(u^{\mathrm{P}}_{i-\frac{1}{2}})\}$ and compute the staggered averages of these interpolants. To avoid this second reconstruction step, we propose to use the volumetric formula (3.15b) instead of the point-value version. We tested our reconstruction method against the corrector step due to Del Zanna & Bucciantini (2002) and found very similar results. Hence, we use the volumetric approach in our simulations.

Flux functions After the reconstruction step, we know the interface values of the conserved variables. When using a FD scheme, we have also reconstructed the interface fluxes; in a FV scheme, we instead compute the interface fluxes from the conserved variables. In any case, the physics at each interface $\mathcal{I}_{i-\frac{1}{2}}$ can be described in terms of two independent states resulting from the reconstruction centred at $\mathcal{Z}_{i-1}$ and $\mathcal{Z}_i$, the so-called *left* and *right* states, respectively. We will denote these states using supersripts, e.g., $u^{L,R}$. The interface represents a discontinuity separating these states. Thus, at each interface, we have to solve a Riemann problem. Exploiting the properties of the Riemann problem and the upwind properties of hyperbolic system, we can derive methods to compute a unique final interface flux by following all waves within the Riemann fan explicitely.

The situation is fairly straightforward for linear advection equations. In this case, a well-defined upwind direction can be identified according to the sign of the advection velocity v, and we can set the flux equal to the upwind one:

$$f_{i-\frac{1}{2}} = \begin{cases} f^L_{i-\frac{1}{2}} & \text{if} \quad v \geq 0 \quad \text{(advection to the right)}, \\ f^R_{i-\frac{1}{2}} & \text{if} \quad v < 0 \quad \text{(advection to the left)}. \end{cases} \tag{3.16}$$

To compute the fluxes of more complex non-linear systems exactly, we could transform the system locally to characteristic variables, obtaining a system of decoupled linear advection equations. For each of the equations we then would apply the recipe given in (3.16), i.e., advect each eigenstate with the corresponding eigenspeed, independently of the other eigenstates. The scheme thus described is the basic building block of an exact *Riemann solver (RS)*. These methods introduce a small amount of numerical diffusion to the solution which is required for a stable evolution. The corresponding numerical viscosity for each eigenstate can be expressed in terms of the absolute value of the characteristic eigenspeed and the gridwidth.

Approximate solvers The drawback of this procedure is the necessity to compute the characteristic variables, i.e., the eigenvectors of the flux Jacobian. For many systems, this is fairly complicated or even unknown. Thus, we rather use *approximate RS* which rely only on a limited subset of the full characteristic information.

Instead of the full characteristic decomposition, the minimal amount of information required by the simplest approximate solvers is the fastest eigenspeed. More sophisticated solvers can be constructed based on more than only one eigenvalue, but still not requiring the more tedious (and expensive) computation of the eigenvectors. Common to all of these methods is that they do not "open" the Riemann fan, i.e., they do not follow all waves explicitely, but rather describe them by a few representative waves. The exact Riemann fan can be embraced, e.g., by one wave moving to

the right at least as fast as the fastest right-moving exact wave and one moving to the left at least as fast as the fastest left-moving exact wave.

Discarding the detailed information on the waves, these methods are much faster and simpler, at the expense, however, of accuracy. Typically, they introduce a larger amount of numerical diffusion w.r.t. exact solvers.

We consider as an example the *Lax-Friedrichs (LxF)* solver (e.g. LeVeque 1992). We note that the maximum velocity of information propagation is given by the maximum of the absolute values of all eigenspeeds, $\lambda_{\max}$. Hence, if we base our numerical viscosity on this velocity (or an upper bound to it), and the corresponding approximate waves, we will obtain a stable yet rather diffusive solver. The LxF flux is given by

$$f_{i-\frac{1}{2}} = \frac{1}{2}\left(f^{\mathrm{R}}_{i-\frac{1}{2}} + f^{\mathrm{L}}_{i-\frac{1}{2}}\right) + \frac{\lambda_{\max}}{2\delta x}\left(u^{\mathrm{R}}_{i-\frac{1}{2}} - u^{\mathrm{L}}_{i-\frac{1}{2}}\right), \tag{3.17}$$

where $f^{\mathrm{L,R}}_{i-\frac{1}{2}} = f(u^{\mathrm{L,R}}_{i-\frac{1}{2}})$ are the right and left states of the fluxes. Only requiring the maximum characteristic velocity, this solver is quite simple, fast, and can be used for a large number of equation systems.

The LxF solver is particularly inaccurate when all characteristic velocities have the same sign: if, e.g., all waves are moving to the right, LxF will nevertheless compute the flux symmetrically from both left and right contributions. This can be avoided in a quite simple way by using two eigenvalues, viz. the maximum and the minimum ones, $\lambda_{\max}$ and $\lambda_{\min}$, rather than only one. This procedure is applied to construct the *Harten-Lax-van Leer (HLL)* (e.g. LeVeque 1992) flux defined by

$$f_{i-\frac{1}{2}} = \frac{\lambda^{+}_{i-\frac{1}{2}} f^{\mathrm{L}}_{i-\frac{1}{2}} - \lambda^{-}_{i-\frac{1}{2}} f^{\mathrm{R}}_{i-\frac{1}{2}} + \lambda^{+}_{i-\frac{1}{2}}\lambda^{-}_{i-\frac{1}{2}}(u^{\mathrm{R}}_{i-\frac{1}{2}} - u^{\mathrm{L}}_{i-\frac{1}{2}})}{\lambda^{+}_{i-\frac{1}{2}} - \lambda^{-}_{i-\frac{1}{2}}}. \tag{3.18a}$$

Here, we denote by $\lambda^{+,-}_{i-\frac{1}{2}}$ functions of the eigenvalues:

$$\lambda^{+}_{i-\frac{1}{2}} = \max(0, \lambda^{\mathrm{L}}_{i-\frac{1}{2};\max}, \lambda^{\mathrm{R}}_{i-\frac{1}{2};\max}), \tag{3.18b}$$

$$\lambda^{-}_{i-\frac{1}{2}} = \min(0, \lambda^{\mathrm{L}}_{i-\frac{1}{2};\min}, \lambda^{\mathrm{R}}_{i-\frac{1}{2};\min}). \tag{3.18c}$$

This solver represents a more accurate approximation to the exact Riemann fan than LxF, in particular in the situation described above. In such a case, the HLL flux will be one-sided in accordance with the upwind properties of the flow.

In our code, we implemented these two approximate solvers and the recently developed GFORCE solver (Titarev & Toro 2005; Toro & Titarev 2006), a symmetric solver with a very low numerical diffusivity. The GFORCE solver uses a composite scheme: a convex average of the LxF flux and a two-step *Lax-Wendroff (LxW)* flux. The LxW flux is defined as follows

$$f_{i-\frac{1}{2}} = f(u^{\mathrm{LxW}}_{i-\frac{1}{2}}), \tag{3.19a}$$

$$u^{\mathrm{LxW}}_{i-\frac{1}{2}} = \frac{1}{2}\left(u^{\mathrm{L}}_{i-\frac{1}{2}} + u^{\mathrm{R}}_{i-\frac{1}{2}}\right) - \frac{1}{2}\frac{1}{c_{\max}}\left(f(u^{\mathrm{R}}_{i-\frac{1}{2}}) - f(u^{\mathrm{L}}_{i-\frac{1}{2}})\right). \tag{3.19b}$$

Here, $c_{\max}$ is (an upper bound of) the maximum characteristic speed at the interface. In the *FORCE* solver (see Toro & Titarev 2006), both (i.e., LxF and LxW) fluxes are summed with equal weights, whereas for the GFORCE (generalised FORCE) solver, the weights depend on the CFL number: they are $1/(1+CFL)$ and $1-1/(1+CFL)$ for the LxF and LxW fluxes, respectively, where CFL is the *Courant-Friedrichs-Levy (CFL)* number of time stepping (see below).

Multi-stage fluxes Recently, the *multi stage (MUSTA)* method was developed to improve the accuracy of approximate solvers (Titarev & Toro 2005; Toro & Titarev 2006). MUSTA provides a framework which can be combined with any of the solvers listed above to reduce the numerical diffusivity considerably. The basic idea behind the method is to open up the Riemann fan even without an exact solver. We will explain this here briefly; for the technical details of this scheme, the reader is referred to Appendix B.

Having reconstructed the interface states, we seek to solve the Riemann problem at each interface. An exact solver provides us with the solution in terms of the characteristic waves obtained from the solution of the eigenvector problem. In the MUSTA framework, we try to recover these waves by an approximate solver. In this context, it is important to note that even an approximate solver will return the correct waves of the Riemann problem at the interface, albeit with an accuracy worse than an exact one. In particular, the approximate solver will allow us to identify the Riemann waves originating from the discontinuity only after a few time steps, whereas the exact one has this knowledge built in.

Therefore, to compute the fluxes by solving the Riemann problem, we open up the Riemann fan by evolving each of the interface Riemann problems one (or a few) "virtual" time step(s) using an approximate solver. The result will provide us with predictor values of the characteristic waves. We then use these predictor states to compute the final fluxes.

Since MUSTA-based schemes do not explicitely attempt to compute the costly characteristic decomposition, they are much simpler and significantly faster than exact solvers. Nevertheless, we find in numerical experiments that their accuracy is comparable to the one achieved with exact solvers. Thus, in most of our simulations, we use a one-stage MUSTA scheme with the HLL solver as a building block.

In the following, we will refer to a scheme with n MUSTA predictor steps using the XXX solver as building block to as MUSTA(n)-XXX.

Zone update Having constructed the interface fluxes $f^{(0)}_{i-1/2}$ from the flow variables $u^{(0)}_i$ at a given time $t^{(0)}$, we can now advance the solution over a small time step δt. We seek to compute the state $u^{(1)}$ at time $t^{(1)} = t^{(0)} + \delta t$. In a volumetric discretisation (Eqn. (3.5)), we can now apply Gauss' theorem (Eqn. (3.6b)), to get, e.g., the simplest form of an explicit time integration scheme, viz. the *forward Euler method*:

$$\frac{u^{(1)}_i - u^{(0)}_i}{\delta t} = \frac{\mathcal{A}_{i+\frac{1}{2}} f^{(0)}_{i+\frac{1}{2}} - \mathcal{A}_{i-\frac{1}{2}} f^{(0)}_{i-\frac{1}{2}}}{\mathcal{V}_i}. \tag{3.20}$$

An analogous formula can be derived for a conservation law in Stokes form. Eqn. (3.20) defines a scheme of only 1st order accuracy, but which can be used as the building block of more accurate schemes such as higher-order Runge-Kutta methods. Since it is explicit (i.e., the r.h.s. of the Eqn. (3.20) contains only terms at the old time, $t^{(0)}$), it is stable only for sufficiently small time steps. We will discuss both issues later briefly.

Boundary conditions We implemented various boundary conditions in our code using the standard method of *ghost zones*. We pad the computational grid by additional n_{gh} zones in each direction, with n_{gh} larger than the stencil of our reconstruction. These zones are then set according to the boundary conditions chosen. To simulate, e.g., transmissive (outflow) boundaries, we copy

the values of the conserved variables from inside the computational domain into the adjacent ghost zones.

Since the methods implemented in our code are standard, we do not go into any detail here but refer the reader to, e.g., LeVeque (1998). If applications demand non-standard boundary conditions, e.g., shearing disk boundaries, we will elaborate on these in the corresponding sections of this thesis later.

General coordinate systems Our code solves the MHD equations in Cartesian, spherical, or cylindrical coordinates. All of these coordinate systems are orthogonal ones, which greatly eases the formalism. To derive the equations in either of these systems, we start with the general covariant form, and transform the covariant derivatives into partial ones, obtaining additional geometric source terms. The resulting equations are well known (e.g., Mihalas & Weibel Mihalas 1984, appendix A); we list them in Appendix A.

We will discuss here only one aspect concerning the reconstruction. In orthogonal coordinates (ξ_1, ξ_2, ξ_3), the volume element is given by

$$\mathrm{d}\mathcal{V} = \mathrm{d}f_1(\xi_1)\,\mathrm{d}f_2(\xi_2)\,\mathrm{d}f_3(\xi_3), \tag{3.21}$$

with some functions f_i depending only on one of the three coordinates (e.g,. in spherical coordinates $\mathrm{d}\mathcal{V} = \mathrm{d}\frac{r^3}{3}\,\mathrm{d}(-\cos\theta)\,\mathrm{d}\phi$). This suggests to use *volumetric coordinates* in, e.g., the volume integrals required for the definition of the consistent reconstruction interpolants. Hence, we perform the reconstruction in volumetric rather than standard coordinates, i.e., the generic coordinate x as used in the reconstruction formulae listed above does not represent ξ_i, but $f_i(\xi_i)$.

Source terms The MHD equations may be augmented by physical source terms, such as the gravitational force; additionally, in general orthogonal coordinate systems, they will feature geometric source terms. We discretise them in a standard way by integrating them over grid cells. As an example, the pressure term P/r present as a source in the spherical momentum equations becomes

$$\int_{r_-}^{r_+} \mathrm{d}\frac{r^3}{3}\frac{P}{r} = \frac{r_+^2 - r_-^2}{2} P_0, \tag{3.22}$$

with the zone-average pressure P_0.

Time integration The techniques described above only concern the spatial discretisation of the conservation systems, but still leave the time coordinate unmodified. Thus, they lead to *semi-discrete* equations of the general form

$$\partial_t u_i = \mathscr{L}(u_i), \tag{3.23}$$

where $\mathscr{L}$ is an operator acting on the spatially discretised variables u_i. This equation can be treated by standard time integrators. We use 2nd and 3rd order *Runge-Kutta (RK)* schemes. We list here the two schemes we implemented. The RK integration of 2nd order (RK2, for short) uses one intermediate time step. If we denote the known solution at time $t^{(0)}$ by $u^{(0)}$ (omitting spatial and component indices), we can compute the solution at time $t^{(1)} = t^{(0)} + \delta t$ by the following procedure:

$$w^{(1)} = u^{(0)} + \frac{1}{2}\delta t \mathscr{L}(u^{(0)}), \tag{3.24a}$$

$$u^{(1)} = u^{(0)} + \delta t \mathscr{L}(w^{(1)}). \tag{3.24b}$$

The 3rd-order analogue of this scheme, RK3, uses two intermediate steps. It can be formulated in different ways. We use the form given by Shu & Osher (1989) enjoying the TVD property:

$$w^{(1)} = u^{(0)} + \delta t \mathscr{L}(u^{(0)}), \tag{3.25a}$$

$$w^{(2)} = \frac{3}{4}u^{(0)} + \frac{1}{4}\left(w^{(1)} + \delta t \mathscr{L}(w^{(1)})\right), \tag{3.25b}$$

$$u^{(1)} = \frac{1}{3}u^{(0)} + \frac{2}{3}\left(w^{(2)} + \delta t \mathscr{L}(w^{(2)})\right). \tag{3.25c}$$

An important issue in the solution of conservation laws is the time step control. This is governed by the CFL condition (e.g., LeVeque 1992): to prevent numerical instabilities, no information is allowed to propagate more than one grid cell during one time step. Since the speed of information propagation is given by the eigenvalues, the CFL condition translates into a requirement for the time step δt

$$\delta t \leq (\delta t)^{\max} = \frac{(\delta \xi)_i}{c_i^{\max}} \quad \forall i, \tag{3.26}$$

where $(\delta\xi)_i$ and $c_i^{\max}$ are the width of and the maximum eigenvalue in cell i. We take $\delta t = CFL(\delta t)^{\max}$ with the CFL number $CFL \leq 1$.

Multi-dimensional problems Based on the scheme described above, we build our multi-dimensional code by *dimensional splitting*. We apply the one-dimensional algorithm successively to the two or three dimensions of our physical domain using the *method of lines* (e.g., Shu 1997). In contrast to the so-called Strang-type splitting (e.g., LeVeque 1992), we use for each of the one-dimensional *sweeps* of a particular time step the same initial data, viz. the values of the conserved variables at the beginning of the time step. Strang-type splitting would demand us to use the results of one sweep as an input for the following one.

3.1.2 MHD schemes

The MHD system

The MHD equations fulfil the basic properties of hyperbolic systems as described above, but their specific structure entails modifications of these properties as well as a very important additional constraint not present for ordinary hyperbolic systems, viz. the divergence-free conditions. We will shortly describe these peculiarities in the following.

Non-strict hyperbolicity and eigenproblem The MHD equations are considerably more complex than the non-magnetic HD ones. They admit 7 characteristic waves instead of the 3 waves of ordinary HD (e.g., Kulikovskii et al. 2001). The number of possible combinations of waves in a Riemann problem, consequently, is much larger. Additionally, the system is not strictly hyperbolic, since various degeneracies of the eigenvalues are possible. These facts make the design of an exact RS much more complex for MHD than it is for HD. Thus, we did not make any attempts to devise an exact solver, but instead use approximate ones within the MUSTA framework.

Divergence constraint One of the crucial properties of the MHD system is the condition that the divergence of the magnetic field vanishes. A numerical scheme has to obey this constraint in order to guarantee an accurate evolution both of the magnetic field and the Lorentz forces acting on the fluid. Artifical magnetic monopoles as a result of a non-zero divergence may lead to unphysical fluid acceleration in the direction of the magnetic field (Brackbill & Barnes 1980).

Numerical MHD

When applying them to the full system Eqn. (2.1), standard HRSC schemes have to be modified to account for the peculiarities of the MHD equations. The most important modifications are the more complex eigenstates and the divergence constraint. Since our schemes, based on approximate RS does not treat the characteristic waves explicitely, we only consider the second point in the following.

The divergence constraint is usually not fulfilled by the discretised fields unless the scheme is carefully designed to respect it. Several methods exist for this purpose:

1. The *8-wave*, or *hyperbolic divergence cleaning method* (Powell 1994) adds to the MHD system an evolutionary equation for the $\operatorname{div}\vec{b}$. These methods do not prevent $\operatorname{div}\vec{b}$ from developing, but instead transport an eventually produced divergence away from the place where it is created by an 8^{th} characteristic wave in addition to the 7 waves of standard MHD.
2. *Projection schemes* (Brackbill & Barnes 1980) enforce $\operatorname{div}\vec{b} = 0$ by projecting the solution after each time step onto a divergence-free field. To this end, elliptic equations have to be solved.
3. The class of *constraint transport (CT)* schemes (Evans & Hawley 1988) achieves a divergence-free solution (up to round-off errors) by a discretisation of the field respecting the Stokes form ((2.2b)) of the induction equation. As a consequence, CT deals with staggered discretisations of HD variables and magnetic field components.

The first two methods discretise the magnetic field as an volume average over grid cells and treat the induction equation with the same methods as a Gauss-type conservation law ((2.2a)). In contrast, CT methods evolve the magnetic fluxes, i.e., the integrals of the field components over cell surfaces. The x component of the field, e.g., will be represented by the magnetic flux through the surfaces orthogonal to the x direction. As a consequence, we have to discretise the fluxes $\vec{F}$ of (2.2b), i.e., the electric field components, as line averages over cell edges.

We formulate the semi-discrete induction equation,

$$\partial_t b^x_{i-\frac{1}{2},j,k} = -c\frac{1}{\mathcal{A}^x_{i-\frac{1}{2},j,k}}\left[\begin{array}{l}\left(\mathcal{L}^z_{i-\frac{1}{2},j+\frac{1}{2},k}E^z_{i-\frac{1}{2},j+\frac{1}{2},k} - \mathcal{L}^z_{i-\frac{1}{2},j-\frac{1}{2},k}E^z_{i-\frac{1}{2},j-\frac{1}{2},k}\right)\\ -\left(\mathcal{L}^y_{i-\frac{1}{2},j,k+\frac{1}{2}}E^y_{i-\frac{1}{2},j,k+\frac{1}{2}} - \mathcal{L}^y_{i-\frac{1}{2},j,k-\frac{1}{2}}E^y_{i-\frac{1}{2},j,k-\frac{1}{2}}\right)\end{array}\right], \tag{3.27a}$$

$$\partial_t b^y_{i,j-\frac{1}{2},k} = -c\frac{1}{\mathcal{A}^y_{i,j-\frac{1}{2},k}}\left[\begin{array}{l}\left(\mathcal{L}^x_{i+\frac{1}{2},j-\frac{1}{2},k}E^x_{i+\frac{1}{2},j-\frac{1}{2},k} - \mathcal{L}^x_{i-\frac{1}{2},j-\frac{1}{2},k}E^x_{i-\frac{1}{2},j-\frac{1}{2},k}\right)\\ -\left(\mathcal{L}^z_{i,j-\frac{1}{2},k+\frac{1}{2}}E^z_{i,j-\frac{1}{2},k+\frac{1}{2}} - \mathcal{L}^z_{i,j-\frac{1}{2},k-\frac{1}{2}}E^z_{i,j-\frac{1}{2},k-\frac{1}{2}}\right)\end{array}\right], \tag{3.27b}$$

$$\partial_t b^z_{i,j,k-\frac{1}{2}} = -c\frac{1}{\mathcal{A}^z_{i,j,k-\frac{1}{2}}}\left[\begin{array}{l}\left(\mathcal{L}^y_{i+\frac{1}{2},j,k-\frac{1}{2}}E^y_{i+\frac{1}{2},j,k-\frac{1}{2}} - \mathcal{L}^y_{i-\frac{1}{2},j,k-\frac{1}{2}}E^y_{i-\frac{1}{2},j,k-\frac{1}{2}}\right)\\ -\left(\mathcal{L}^x_{i,j-\frac{1}{2},k-\frac{1}{2}}E^x_{i,j+\frac{1}{2},k-\frac{1}{2}} - \mathcal{L}^x_{i,j-\frac{1}{2},k-\frac{1}{2}}E^x_{i,j-\frac{1}{2},k-\frac{1}{2}}\right)\end{array}\right]. \tag{3.27c}$$

and the discretised version of the divergence constraint,

$$\left(\operatorname{div}\vec{b}\right)_{i,j,k} = \mathcal{V}_{i,j,k}\left[\begin{array}{ccccc} & \mathcal{A}^x_{i+\frac{1}{2},j,k} b^x_{i+\frac{1}{2},j,k} & - & \mathcal{A}^x_{i-\frac{1}{2},j,k} b^x_{i-\frac{1}{2},j,k} \\ + & \mathcal{A}^y_{i,j+\frac{1}{2},k} b^y_{i,j+\frac{1}{2},k} & - & \mathcal{A}^y_{i,j-\frac{1}{2},k} b^y_{i,j-\frac{1}{2},k} \\ + & \mathcal{A}^z_{i,j,k+\frac{1}{2}} b^z_{i,j,k+\frac{1}{2}} & - & \mathcal{A}^z_{i,j,k-\frac{1}{2}} b^z_{i,j,k-\frac{1}{2}} \end{array}\right], \tag{3.28}$$

Here, we introduced the discretised magnetic fields, for which, e.g., the x component is defined as the surface mean over the cell surface orthogonal to the x direction,

$$b^x_{i-\frac{1}{2},j,k} = \frac{1}{\mathcal{A}^x_{i-\frac{1}{2},j,k}} \int_{\mathcal{A}^x_{i-\frac{1}{2},j,k}} \mathrm{d}\mathcal{A}\, b^x(\vec{r}); \tag{3.29}$$

$\mathcal{L}^x_{i,j-\frac{1}{2},k-\frac{1}{2}}$ etc. denote the length of the zone edge at $y = y_{j-\frac{1}{2}}$ and $z = z_{k-\frac{1}{2}}$. We note that the divergence is conserved, if we use consistent electric field components in the evolution equations for all three field components, i.e., if, e.g., the electric field $E^y_{i+\frac{1}{2},j,k+\frac{1}{2}}$ is the same in both (3.27a) and (3.27c), and analogously for the other components. In particular, the divergence will remain zero if it vanishes in the beginning.

Two important issues have to be taken into account when constructing a CT scheme:

1. Since the line averages of the electric fields have to be obtained from the surface averages of the magnetic fields and the volume averages of the momenta and the density, there is no unique method to compute them.
2. On the other hand, to compute the Lorentz forces, we need products of different field components ($b_i b_j$) that are defined as averages over different surfaces of the cells. Again, there is no unique recipe for this step.

Different kinds of CT schemes can be distinguished by the way in which they perform these constructions.

It is possible to construct the electric fields from the zone-surface values of the velocities obtained using a suitable reconstruction method and the field components collocated at the same surfaces by interpolation and averaging. First, the zone averages of the electric fields to the zone edges, obtaining two pairs of fields there. Then, we apply a simple arithmetic average there. Methods of this type have been used successfully (e.g., Ryu et al. 1998). However, we can improve on them by taking into account upwind considerations.

A step into this direction is the scheme devised by Pen et al. (2003). These authors decompose the field into *advection* and *constraint partial fields*. In this nomenclature, the advection field is the partial field $b_\perp v_\parallel$ composed of the magnetic field orthogonal to the given surface and a velocity component parallel to the surface. An important symmetry is inherent in these two classes of fields: the advection field of one velocity direction is the constraint field w.r.t. the other direction. Pen et al. (2003) apply the reconstruction procedure to the advection parts in the velocity direction only. At each zone edge, they, thus, obtain two pairs of advection fields. Instead of an average of these fields, Pen et al. (2003) now apply an upwind RS, obtaining a unique advection field along each direction. Finally, they add these fields to compute the full electric field. This is one of the methods implemented in our code.

In both classes of schemes described above, the Lorentz forces are typically computed from the zone averages of the fields. These usually are obtained using an averaging step, either arithmetic or volumetric, but one can as well use a high-order reconstruction method. Londrillo & del Zanna (2004) pointed out that a slight modification of this method provides a better realisation of the

divergence constraint in the Lorentz force, in particular for higher-order reconstruction: for computing the fluxes in, say, the x direction, they do not average the b_x field over the zone volume and then reconstruct it back to zone interfaces, where it is used to compute the magnetic stress tensor components $b_x b_i$. Instead, they compute these stresses from the original b_x field as defined on the zone surface $\mathcal{A}^x$. Of course, the normal field components b_y, and b_z still require both the averaging and the reconstruction step. In our code, we use this new method rather than the more traditional one. See Londrillo & Del Zanna (2000) for a detailed discussion of divergence-free higher-order reconstruction; here, we only note that a clear distinction between point values and geometrical averages (over lines, surfaces, and volumes) of variables is key.

Recently, the class of *upwind constraint transport (UCT)* schemes has been developed (Londrillo & Del Zanna 2000; Londrillo & del Zanna 2004; Gardiner & Stone 2005). The schemes have then been applied by Fromang et al. (2006); Del Zanna et al. (2007). These schemes attempt to compute electric fields and Lorentz forces in a way consistent with the characteristics of the full MHD Riemann problem. To this end, these schemes usually are combined with an exact Riemann solver. We try to apply a similar scheme, based, however, on approximate solvers and MUSTA schemes. Following Gardiner & Stone (2005), we evolve the induction equation for the volume averaged magnetic field together with the fluid equations. After solving the Riemann problem for this extended system by MUSTA solvers, we can obtain zone-surface values of the electric fields from MHD variables of the approximate Riemann solution. We do, however, not evolve the "original", zone-surface magnetic field in this step. We note that we can formulate versions of the scheme that use here the advection, or the constraint, or the full field. For simplicity, we assume here a scheme based on the advection field. In the next step, we apply an upwind solver to the zone-surface electric fields to get two pairs of advection fields on the adjacent zone edge. We then treat these fields similarly to the scheme by Pen et al. (2003) describe above. Having constructed the full edge-centred electric fields, we then evolve the original magnetic fields according to the induction equation. Before the next time step, we reset the zone-centre fields used in the RS step to the volume averages of the original fields. As in most CT schemes, the zone-centre fields are, thus, only secondary variables we need for constructing the solution to the full MHD Riemann problem, but they are not a set of additional evolutionary variables. For computing them, we use either a simple averaging or a high-order reconstruction. The technical details of our implementation will be discussed in Appendix C.

3.1.3 Our MHD code: overview and supplementing issues

Overview Here, we will list the different physical systems and numerical schemes we implemented. For a more thorough discussion of these issues, the reader is referred to the corresponding sections.

The MHD equations are discretised in 1d, 2d,or 3d Cartesian, spherical, or cylindrical coordinates. The gravitational force acting on the fluid can be given by a pre-defined potential; alternatively, we can compute the self-gravity of the fluid from the solution of the Poisson equation. In spherical coordinates, we use the Poisson solver of Müller & Steinmetz (1995) based on a multipole expansion of the density field and the potential. To mimic general relativistic effects, we can include the correction terms due to Rampp & Janka (2002); Marek et al. (2006).

We use either FD or FV schemes. Within the FV schemes, we employ MUSTA fluxes based on the global or the local versions of LxF, HLL, or GFORCE, or MUSTA-UCT schemes based on the global or the local versions of LxF, or HLL. Reconstruction can be performed using PCM, PLM, or

high-order methods (WENO-4, MP-5, MP-7, MP-9). For interpolating between the staggered grids of magnetic field and HD variables, we use volume averages or high-order interpolation.

For multi-dimensional systems, we use a dimensionally split method of lines approach. Time evolution is performed using 2nd or 3rd order RK methods.

We conclude with a few technical notes concerning the code: it is written in Fortran 90 and makes use of common F90 features such as modules and dynamic memory allocation. Different settings for physical and numerical parameters (such as the choice of the physics evolved, the Riemann solver, or the reconstruction method) can be made either by preprocessing using the C preprocessor or by input from parameter files. For testing, initial data for all of the problems discussed in Chapter 4 are included. The code is parallelised for shared-memory and distributed-memory computers using the OpenMP and the MPI standard, respectively. It was used for tests and simulations on a number of different system architectures such as IBM regatta systems, and AMD and Intel Linux machines. Depending on the problem size, we made efficient use of up to 256 CPUs in simulations.

Treatment of unphysical solutions Many numerical MHD codes are beset with problems in regions where the internal energy is only a small fraction of the conserved total energy. In such cases, it becomes increasingly difficult to maintain the positivity of the internal energy. Since our schemes evolve the total energy density e, we have to subtract the kinetic energy density $e_{\rm kin} = \frac{1}{2}\rho\vec{v}^2$ and the magnetic energy density $e_{\rm mag} = \frac{1}{2}\vec{b}^2$ from e to obtain the internal energy density ε. In regions of large velocity or strong fields, where ε makes up for only a small fraction of e, the positivity of the internal energy can be violated by this procedure, leading to an unstable evolution. Several methods exist to overcome the limitations imposed by this issue.

One of the methods we employ is specific to MUSTA schemes. We note that the schemes least prone to such problems are the very stable PCM methods. As a consequence, we try to replace the accurate yet less stable high-order reconstruction by PCM. Thus, whenever the predictor step of the MUSTA solver yields an unphysical MHD state (e.g., one with negative internal energy), we replace this state by a PCM reconstructed non-MUSTA state. This procedure is fully consistent with the conservative MHD equations, only reducing the order of accuracy at certain points. It allows us to avoid unphysical results in most cases.

In some extreme situations, e.g., involving magnetic pressures many orders of magnitude greater than the gas pressure, this simple recipe is not sufficient to avoid unphysical solutions, and we have to rely to more fundamental modifications of the scheme. It is very common to evolve the equation for the internal energy,

$$\partial_t \hat{\varepsilon} + \vec{\nabla}\cdot(\hat{\varepsilon}\vec{v}) = -P\vec{\nabla}\cdot\vec{v}, \tag{3.30a}$$

as an additional evolutionary equation (the hat ˆ serves to distinguish the internal energy as an additional evolutionary variable from the internal energy ε computed from the total energy). Whenever the positivity of ε is violated by the standard scheme, we can resort to the value given by (3.30a) to replace the negative internal energy.

Apart from the internal-energy scheme, we also adopted a method similar to one devised by Mignone & Bodo (2006). We evolve the evolutionary equations for the kinetic and magnetic energies together with the total energy:

$$\partial_t \hat{e}_{\rm kin} + \vec{\nabla}\cdot(\hat{e}_{\rm kin}\vec{v}) = (P + \frac{1}{2}\vec{b}^2)\vec{\nabla}\cdot\vec{v} - \vec{B}\vec{\nabla}(\vec{B}\cdot\vec{v}), \tag{3.30b}$$

$$\partial_t \hat{e}_{\rm mag} + \vec{\nabla}\cdot(\hat{e}_{\rm mag}\vec{v}) = -\frac{1}{2}\vec{b}^2\vec{\nabla}\cdot\vec{v} + \vec{B}\vec{\nabla}(\vec{B}\cdot\vec{v}). \tag{3.30c}$$

Additional terms may be present when, e.g., gravity is included. To stably evolve systems with an extreme ratio of magnetic to internal energy, we apply the following procedure in each time step:

1. At the beginning of each time step, we compute the magnetic and kinetic energies $e^t_{\mathrm{mag,kin}}$ from the velocity and magnetic field.
2. We evolve all MHD variables, including the additional partial energies $\hat{e}_{\mathrm{mag,kin}}$, to the new time step $t' = t + \Delta t$.
3. We compute the magnetic and kinetic energies $e^{t'}_{\mathrm{mag,kin}}$ from the kinetic and magnetic fields at the new time step.
4. We then correct the temporal change of the total energy density $\Delta e = e^{t'} - e^t$ by the change of the kinetic and magnetic energies:
$$\Delta e = \Delta e + \left(\Delta \hat{e}_{\mathrm{mag}} - (e^{t'}_{\mathrm{mag}} - e^t_{\mathrm{mag}})\right) + \left(\Delta \hat{e}_{\mathrm{kin}} - (e^{t'}_{\mathrm{kin}} - e^t_{\mathrm{kin}})\right). \tag{3.31a}$$
5. Finally, we update all energies:
$$e^{t'} = e^t + \Delta e, \tag{3.31b}$$
$$e^{t'}_{\mathrm{mag}} = \frac{1}{2}(\vec{b}^{\,t'})^2, \tag{3.31c}$$
$$e^{t'}_{\mathrm{kin}} = \frac{1}{2}\rho^{t'}(\vec{v}^{\,t'})^2. \tag{3.31d}$$
In this step, we override the partial energies by the corresponding values consistent with the velocity and magnetic fields.

Four remarks concerning this scheme are in order before presenting results:

1. The correction steps can be used in each time step and each grid cell, or only in those time steps and grid cells in which unphysical states are present. As a compromise, we may select to apply the correction in all zones adjacent to a cell of unphysical state.
2. We may, of course, use this procedure with both partial energies, or with only one of them, e.g., $\hat{e}_{\mathrm{mag}}$.
3. This scheme is non-conservative, introducing a violation of the conservation of e. However, we find these errors typically only minor.
4. Our scheme deviates from the one by Mignone & Bodo (2006) in that it evolves the partial energies whereas their scheme introduces the field components $\hat{b}^2_{x,y,z}$ as additional variables. The Mignone & Bodo (2006) version discretises these additional variables as volume averages over grid cells (as our partial energies are discretised) instead of averages over grid surfaces. Thus, our version is, in essence, equivalent to theirs summed over the three (squared) component-wise equations.

3.2 Radiative transfer

As we noted above, the RME system we solve consists of a hyperbolic part, non-hyperbolic terms due to fluid motion, and source terms accounting for emission and absorption of radiation. We will shortly describe our treatment of these three groups of terms in this section.

Before going into detail, we point out that the inclusion of the RT system does not change the basic strategy of our scheme. Because of the separation of the full RHD system into hyperbolic subsystems and non-hyperbolic, but local coupling terms, we solve each of the parts independently of each other using operator splitting. Furthermore, we still use explicit time stepping for most parts.

3.2.1 Transport

Hyperbolic subsystem

The hyperbolic part of the RME can be treated analogously to the HD equations. We employ the same basic method of reconstruction algorithm, approximate Riemann solver based on the characteristic velocities, and an explicit Runge-Kutta solver for time integration.

As Pons et al. (2000); Audit et al. (2002); Audit & González (2006) pointed out, there is, however, an important limitation we have to account for when applying the scheme in the diffusion limit. Unless we enforce the correct parabolic limit, it is bound to fail in this case.

To understand the reason for this failure, we consider the stationary (i.e., $\partial_t = 0$) one-dimensional RME. We assume that only isotropic scattering is present, giving rise to an opacity χ. Hence, the system becomes

$$\partial_t \mathfrak{E} + \nabla_x \mathfrak{F} = 0, \tag{3.32a}$$

$$\partial_t \mathfrak{F} + c^2 \nabla_x \mathfrak{P} = -c\chi \mathfrak{F}. \tag{3.32b}$$

We assume that we are, due to a dominant sink (or relaxation) term $-c\chi\mathfrak{F}$, at large optical depth, i.e., in the diffusion limit. We note that the time scale associated with the sink is $\tau = (c\chi)^{-1}$. In the diffusion limit, the pressure tensor is $\mathfrak{P} = \frac{1}{3}\mathfrak{E}$, and the flux can be expressed by Fick's law

$$\mathfrak{F}_\mathrm{D} = -\frac{c}{3\chi}\nabla\mathfrak{E}, \tag{3.33}$$

which limit we should recover when solving the TMT numerically.

Using an explicit time integration scheme, this is not a problem as long as the time step δt is small w.r.t. the relaxation time τ. For longer time steps, the stiff source term makes the explicit scheme numerically unstable, thus requiring a costly implicit solver instead.

In our numerical scheme, δt is given by the CFL time step, which is of the order $\delta t \sim \frac{c}{\delta x}$, where δx is the zone width. Thus, the stability constraint $\delta t < \tau$ translates into a condition for the *Peclet number*

$$\mathrm{Pe} = \chi\,\delta x, \tag{3.34}$$

i.e., the product of the hyperbolic (CFL) time step and the source time scale or the optical depth per grid cell. Stability requires $\mathrm{Pe} < 1$; otherwise, the relaxation term becomes stiff.

To cure this problem without the need for an implicit solver for the entire system, we implemented two schemes:

1. In the first scheme, we modify the 1st moment equation using an *ansatz* similar to the one proposed by Jin et al. (2000) and implemented by Audit et al. (2002). We replace Eqn. (3.32b) by

$$\partial_t \mathfrak{F} + c^2 \nabla_x \mathfrak{P} = -c\chi\left[\mathfrak{F} - (1 - \Xi(\mathrm{Pe}))\,\mathfrak{F}_\mathrm{D}\right], \tag{3.35a}$$

where Ξ is a function of the Peclet number satisfying the limits

$$\Xi(\mathrm{Pe}) = \begin{cases} 1 & \text{for } \mathrm{Pe} < \mathrm{Pe_c} \\ 0 & \text{for } \mathrm{Pe} \to \infty \end{cases}, \tag{3.35b}$$

with the critical Peclet number $\mathrm{Pe_c}$ of the order of 1. We choose an interpolation, e.g., by an exponential or tanh law. We found that the exact form of $\Xi(\mathrm{Pe})$ is only of minor importance

as long as it drops sufficiently quickly for $\mathrm{Pe} \gtrsim \mathrm{Pe}_\mathrm{c}$. Eqn. (3.35a) is solved implicitly. Additionally, we multiply the characteristic velocities by Ξ to avoid excess numerical diffusion by the approximate Riemann solver, and – for MUSTA schemes – decrease the time step of the MUSTA predictor step by the same amount.

2. The second method draws from the scheme devised by Jin & Levermore (1996) and implemented by Pons et al. (2000). We use the same diffusive flux and the same function of the Peclet number as before. Different from the first scheme, we enforce the diffusion limit in the energy equation:
$$\partial_t \mathfrak{E} + \nabla_x [\Xi \mathfrak{F} + (1-\Xi)\mathfrak{F}_\mathrm{D}] = \mathfrak{S}^0. \tag{3.35c}$$
We can apply the multiplication operation $\cdot(1-\Xi)$ to the diffusion flux either before or after the Riemann solver. In the previous case, we have to additionally reduce the characteristic velocities as described above to avoid excess numerical diffusion. Additionally, we have to apply the relaxation procedure to the flux (Eqn. (3.35a)) as described above.

The effect of these extra terms is:

1. In the limit of small Pe, when the hyperbolic system is stable, the modifications are switched off, and we evolve the standard system.
2. For large Pe, when the original system is unstable, we relax the flux to the diffusive one on a time scale $(c\chi)^{-1}$, i.e., within one time step. We are, thus, fully consistent with the diffusion limit, and we do not encounter any numerical instability.

Non-hyperbolic terms

The additional terms present in the TMT system do not require special treatment as the time scale associated with them is given by the fluid velocity and, thus, is less than the eigenspeeds.

3.2.2 Interaction with matter

The interaction source terms neither modify the hyperbolic systems of neither radiation nor fluid. Thus, we treat them separately from the other terms in an operator-splitting way. Local in space, they couple radiation with matter, and different radiation species (i.e., neutrino flavours as well as energy bins) with each other. Thus, our main task when computing their contribution is an accurate and stable time integration. As they can be very stiff for large optical depths, we employ implicit time stepping for their solution.

Chapter 4

Code validation

HOWEVER BEAUTIFUL THE STRATEGY, YOU SHOULD OCCASIONALLY LOOK AT THE RESULTS.

Winston Churchill

4.1 Magnetohydrodynamics

4.1.1 One-dimensional problems

A number of one-dimensional tests served us as a test bench for verifying the correctness of our MHD algorithm. We simulated purely hydrodynamic as well as MHD tests.

Hydrodynamic shock tubes

We will present a selection of results from various HD Riemann problems commonly used as test problems for code validation. All of these tests assume an ideal gas; the adiabatic index is $\gamma = 1.4$ unless stated otherwise. Outflow *boundary conditions (BCs)* are assumed in most tests.

Sod shock tube The *Sod shock tube* is defined by a jump in density and pressure in the middle of the grid. The initial velocity and the magnetic field vanish. Specifically, the HD variables are given by $u(x) = u^{\mathrm{L}}$ if $x < 0.5$ and $u(x) = u^{\mathrm{R}}$ if $x > 0.5$, where

$$\rho^{\mathrm{L}} = 1, \qquad \rho^{\mathrm{R}} = 0.125, \tag{4.1a}$$

$$P^{\mathrm{L}} = 1, \qquad P^{\mathrm{R}} = 0.1. \tag{4.1b}$$

This initial state decays into a right-moving shock wave, a contact discontinuity in the middle and a left-moving rarefaction wave.

The result of this test, computed with MP-5 reconstruction and the MUSTA(1)-HLL solver are displayed in the top two rows of Fig. 4.1. We, furthermore, compare the results of this test for different methods, including MUSTA and non-MUSTA versions of the LxF solver and different reconstruction algorithms in the bottom panels of the same figure. The results demonstrate that a

stable evolution using high-order reconstruction schemes such as MP-5 or WENO-4 and the novel Riemann solvers is possible. They indicate, however, certain differences regarding the accuracy and stability: PCM reconstruction is least prone to overshooting near discontinuities but introduces the largest amount of smearing. The highest-order schemes, on the other hand, in combination with the MUSTA scheme, may produce small short-wavelength oscillations close to the shock and at the tip of the rarefaction wave. These oscillations turn out to be much less pronounced with the non-MUSTA solver. Even when they are present, they do not grow above an uacceptable level.

Lax shock tube The *Lax shock tube* starts from a discontinuity in density and pressure as the Sod test does, but it additionally involves a velocity towards the discontinuity:

$$\rho^{\mathrm{L}} = 0.445, \qquad \rho^{\mathrm{R}} = 0.5, \tag{4.2a}$$

$$v_x^{\mathrm{L}} = 0.698, \qquad v_x^{\mathrm{R}} = 0, \tag{4.2b}$$

$$P^{\mathrm{L}} = 3.528, \qquad P^{\mathrm{R}} = 0.571. \tag{4.2c}$$

The conclusions we draw from our results are similar: we are able to simulate this test with most of the high-order schemes and all Riemann solvers without running into stability problems. The level of overshooting for, e.g., MP-5, is similar to TVD-PLM with the MC limiter. However, the differences between the reconstruction schemes come out more clearly in this test than in the previous one: methods of a very high order, such as MP-9, show significantly stronger post-shock oscillations.

Interacting blast waves This tests, originally proposed by Woodward & Colella (1984), involves two strong discontinuities in pressure, located at $x = 0.1$ and $x = 0.9$, in a gas of constant density $\rho = 1$ and zero velocity. The pressure in the background state is $P_{\mathrm{mid}} = 0.01$, whereas P at the left and right boundary is $P^{\mathrm{L}} = 1000$ and $P^{\mathrm{R}} = 100$, respectively. To confine the gas within the numerical grid, we assume reflecting BC at both ends. The two discontinuities decay into blast waves heading towards each other. After a short time, they interact and a complex pattern of shocks, contact discontinuities, and rarefaction waves forms.

This is a quite demanding test for the HD scheme. Hence, we expect to see considerable differences between the schemes, both regarding stability and accuracy.

We compare different Riemann solvers. We performed simulations using PCM reconstruction but different solvers, viz. LxF, GFORCE, and HLL, both with and without MUSTA steps with $m_x = 3000$ zones. Lacking an exact solution, we compared the results with a simulation of $m_x = 9000$ zones, standard HLL solver and MC reconstruction. They show that, as expected, the GFORCE and HLL are much less viscous than LxF. They track the "exact" solution significantly better than the LxF simulation. We note also that the accuracy of all of the schemes, but in particular of the most viscous ones, greatly benefits from the use of the MUSTA method. With the corresponding MUSTA versions, results of the HLL and GFORCE solvers do not change strongly. The MUSTA(1)-LxF simulation, in contrast, exhibits a much better accuracy than the non-MUSTA variant, coming closest to the reference solution. The MUSTA(1) versions of GFORCE and HLL give nearly indistinguishable results.

Concerning the reconstruction, we find in simulations with a given solver (HLL with one MUSTA step)) a strong increase in accuracy when using high-order schemes. We note the appearance of a certain amount of oscillations, in particular near the "shoulder" near $x \approx 0.7$ and at the left contact discontinuity ($x \approx 0.61$) in the bottom right panel of Fig. 4.3 for some of the high-order schemes.

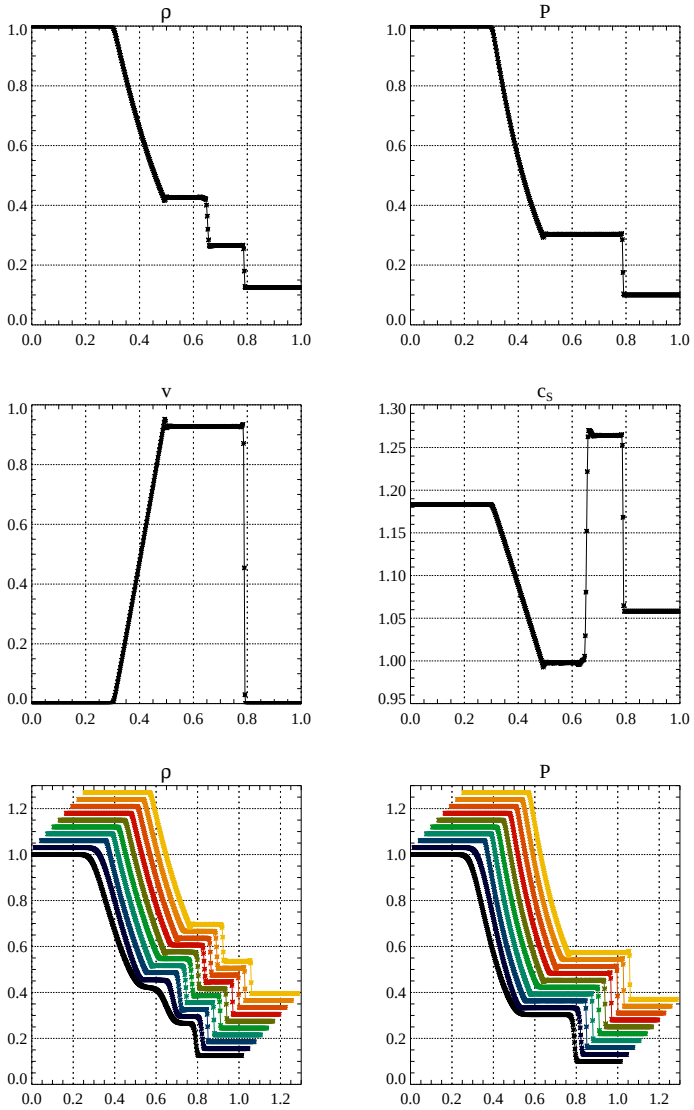

Figure 4.1: The result of the Sod shock tube at $t = 0.1644$. The plots show the density (top left panel), the gas pressure (top right panel), the fluid velocity (middle left panel), and the sound speed (middle right panel). We used 3rd-oder Runge-Kutta time stepping, MP-5 reconstruction and the MUSTA(1)-HLL solver. The grid size was $m_x = 400$ zones, and the CFL factor was CFL $= 0.8$. The flow shows a rarefaction wave, a contact discontinuity, and a shock wave.
The bottom panels show a comparison of the density (left panel) and gas pressure (right panel) computed with different solvers: the lines represent (from bottom to top) the solution obtained using 1. PCM reconstruction and LxF solver, 2. PCM reconstruction and MUSTA(1)-LxF solver, 3. MC reconstruction and LxF solver, 4. MC reconstruction and MUSTA(1)-LxF solver, 5. WENO-4 reconstruction and LxF solver, 6. WENO-4 reconstruction and MUSTA(1)-LxF solver, 7. MP-5 reconstruction and LxF solver, 8. MP-5 reconstruction and MUSTA(1)-LxF solver, 9. MP-9 reconstruction and LxF solver, 10. MP-9 reconstruction and MUSTA(1)-LxF solver. For clarity, the curves are shifted w.r.t. each other both in horizontal and vertical direction by a small amount.

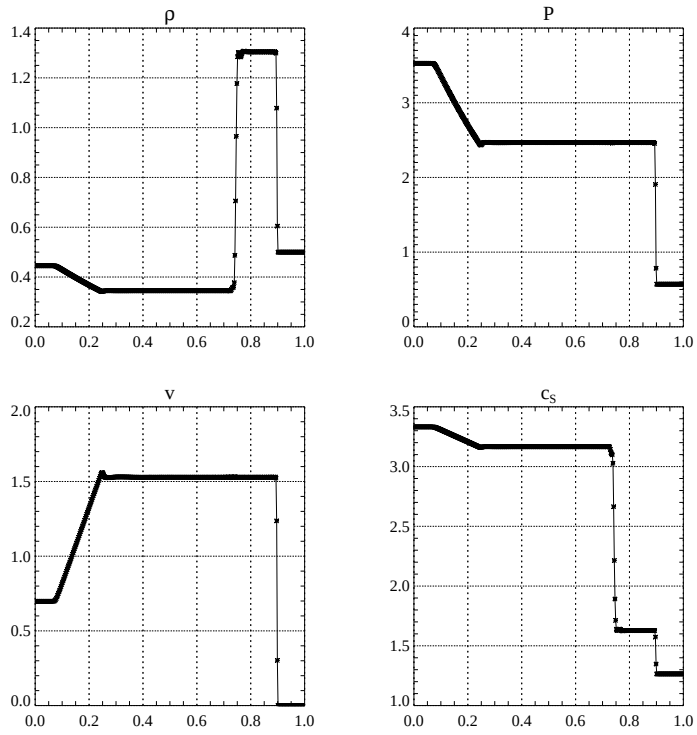

Figure 4.2: The result of the Lax shock tube at $t = 0.16$. The plots show the density (top left panel), the gas pressure (top right panel), the fluid velocity (bottom left panel), and the sound speed (bottom right panel). We used 3^{rd}-oder Runge-Kutta time stepping, MP-5 reconstruction and the MUSTA(1)-HLL solver. The grid size was $m_x = 400$ zones, and the CFL factor was CFL $= 0.8$. The flow shows a rarefaction wave, a contact discontinuity, and a shock wave.

We regard the oscillations, though not leading to a degradation of the accuracy in other regions and vanishing with better resolved grids, as an indication of a beginning numerical instability. We find in this test MP-5 reconstruction (the green line) a good choice w.r.t. accuracy and stability. Hence, in production simulations, we use primarily this scheme.

Interaction of a shock and a density wave As last of the non-magnetic shock tubes, we want to discuss the results of the test proposed by Shu (1990). A shock waves runs from the left side of the grid into an oscillating density profile given by

$$\rho(x) = 1 + 0.2\sin(50x) \tag{4.3a}$$

When the shock passes over the oscillations, they are squeezed and amplified, leading to a pattern of short and violent oscillations.

The results, computed with MP-5 reconstruction and a grid size of $m_x = 400$, are displayed in Fig. 4.4. We find that the post-shock density profile is quite sensitive to the numerical accuracy. Thus, we compare different schemes on this test. The results can be found in the bottom panel of Fig. 4.4. Clearly, the higher-order schemes succeed in providing a much more accurate solution than even the most accurate of our PLM schemes, viz. MC reconstruction.

Magnetohydrodynamic shock tubes

We will present a few 1d MHD shock tubes to assess the performance of our code in Riemann problems involving magnetic fields. The tests are taken from the paper by Ryu & Jones (1995). Following these authors, we use a grid of 512 zones for our tests. The tests use outflow BC on the left and right side of the grid. The EOS is that of an ideal gas with $\gamma = 5/3$. We compute all of these tests, unless stated else, using 3rd-order Runge-Kutta time stepping, MP-5 reconstruction with the original parameters, and the MUSTA(1)-HLL Riemann solver. The CFL factor is set to CFL = 0.95.

MHD Riemann problem 1a – MHD shocks We start with the shock tube presented in their Fig. 1a. The initial conditions, $u(x) = u^{\mathrm{L}}$ for $x < 0.5$ and $u(x) = u^{\mathrm{R}}$ for $x > 0.5$ with

$$(\rho, v_x, v_y, v_z, P, b_x, b_y, b_z)^{\mathrm{L}} = (1, 10, 0, 0, 20, 5/\sqrt{4\pi}, 5/\sqrt{4\pi}, 0), \tag{4.4a}$$

$$(\rho, v_x, v_y, v_z, P, b_x, b_y, b_z)^{\mathrm{R}} = (1, -10, 0, 0, 1, 5/\sqrt{4\pi}, 5/\sqrt{4\pi}, 0), \tag{4.4b}$$

define a discontinuity across which the tangential field component b_y is continuous. It decays into a two fast shocks, a slow rarefaction wave moving to the left, a slow shock moving to the right, and a contact discontinuity.

Our simulations used 3rd-order Runge-Kutta time stepping, MP-5 reconstruction, and the MUSTA(1)-HLL Riemann solver. We resolve the Riemann structure well. The diffusive smearing of discontinuities is small, with typically at most two cells in the fast shocks. We note some overshooting near jumps and oscillations in v_y. The level of these numerical artifacts is comparable to or better than with the TVD-PLM reconstruction with MC limiter.

MHD Riemann problem 1b – MHD rarefactions This problem is described by the initial state

$$(\rho, v_x, v_y, v_z, P, b_x, b_y, b_z)^{\mathrm{L}} = (1, 0, 0, 0, 1, 3/\sqrt{4\pi}, 5/\sqrt{4\pi}, 0), \tag{4.5a}$$

$$(\rho, v_x, v_y, v_z, P, b_x, b_y, b_z)^{\mathrm{R}} = (0.1, 0, 0, 0, 10, 3/\sqrt{4\pi}, 2/\sqrt{4\pi}, 0). \tag{4.5b}$$

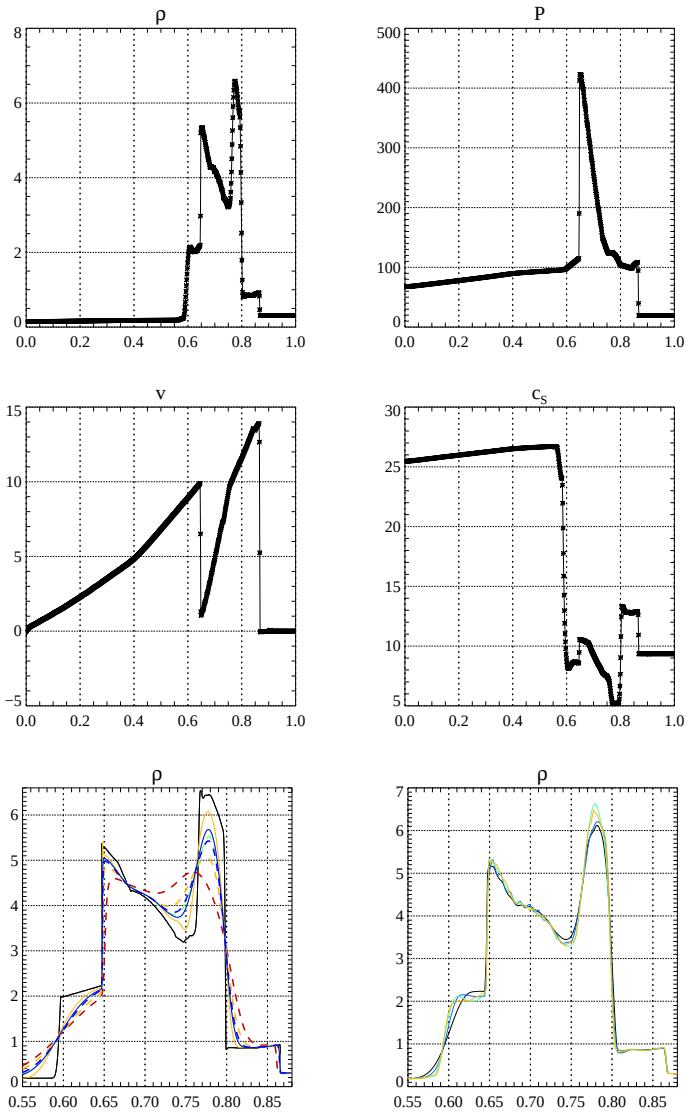

Figure 4.3: The interaction of two oppositely travelling blast waves at $t = 0.038$. The plots show the density (top left panel), the gas pressure (top right panel), the fluid velocity (middle left panel), and the sound speed (middle right panel). We used 3rd-oder Runge-Kutta time stepping, MP-5 reconstruction and the MUSTA(1)-HLL solver. The grid size was $m_x = 800$ zones, and the CFL factor was CFL $= 0.8$.

The bottom left panel displays a comparison of the density in the region $x \in [0.55, 0.88]$ for different Riemann solvers. The time stepping in this test was Runge-Kutta of 2nd order, the reconstruction was PCM, the grid had $m_x = 3000$ zones, and the CFL factor was CFL $= 0.95$. The thin black line represents a reference solution computed with a finer resolution.For the other lines, the colours distinguish between different basic solvers (red, yellow, green, and blue show the global LxF, the local LxF, the HLL, and the GFORCE solver), and line styles distinguish between non-MUSTA (dashed) and MUSTA (solid) simulations. Please note that the blue and green solid lines lie nearly on top of each other.

The bottom right panel shows the same results for different reconstruction schemes. Here, we use 3rd-order time integration, $m_x = 600$, and CFL $= 0.8$. The black, blue, green, and yellow lines display MC, WENO-4, MP-5, and MP-9 reconstruction, respectively.

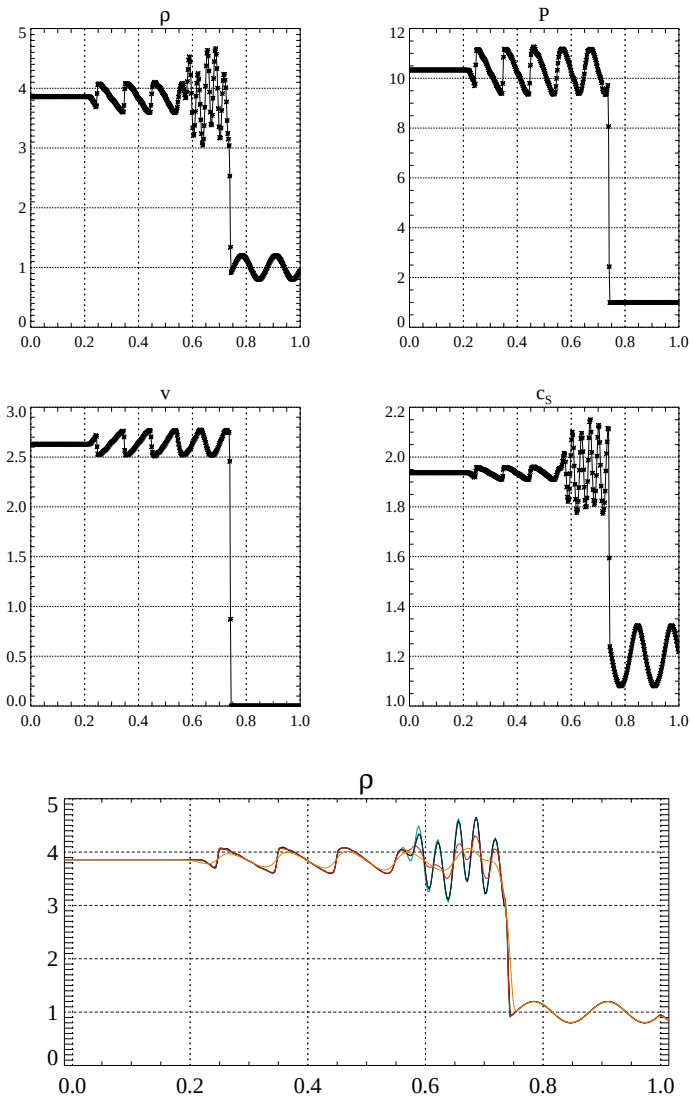

Figure 4.4: The interaction of a shock and a density wave at $t = 0.18$. The plots show the density (top left panel), the gas pressure (top right panel), the fluid velocity (middle left panel), and the sound speed (middle right panel). We used 3rd-oder Runge-Kutta time stepping, MP-5 reconstruction and the MUSTA(1)-HLL solver. The grid size was $m_x = 400$ zones, and the CFL factor was CFL $= 0.8$.
The bottom panel displays the density profile of the flow for $m_x = 400$ and different reconstruction algorithms: blue, green, red, and orange represent WENO-4, MP-5, MC, and PCM, respectively.

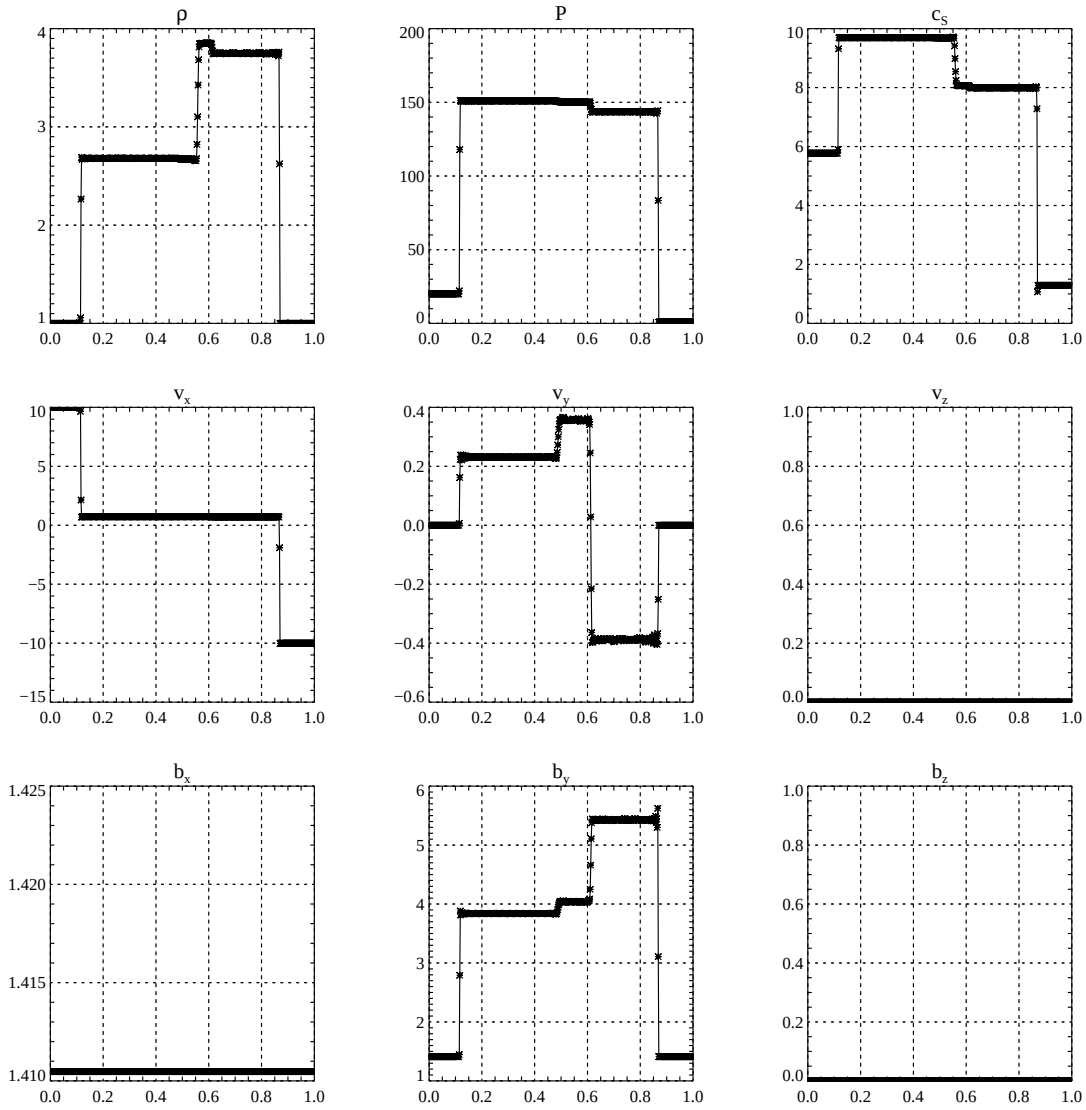

Figure 4.5: The MHD Riemann problem 1a at $t = 0.08$ simulated using 3$^{\text{rd}}$-order Runge-Kutta time integration, MP-5 reconstruction and the MUSTA(1)-HLL solver. The grid has 512 zones, and the CFL factor was 0.95. The panels show in the top row the gas density ρ, the gas pressure P and the sound speed c_S, in the middle row the velocity components, and in the bottom row the components of the magnetic field. The Riemann structure consists of (from left to right) a fast shock, a slow rarefaction, a contact discontinuity, a slow shock, and another fast shock.

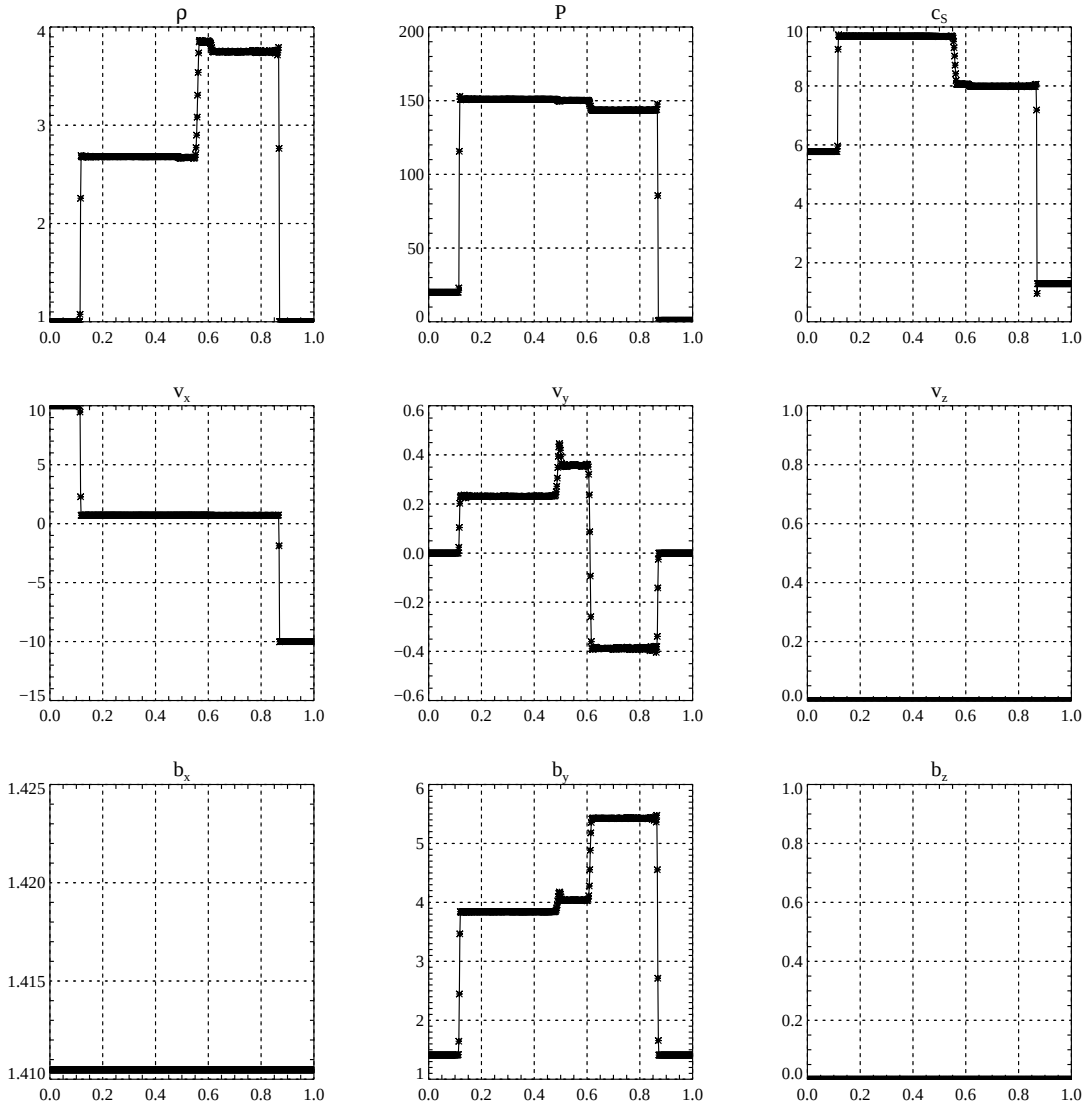

Figure 4.6: The same as Fig. 4.5, but computed using MC reconstruction.

The flow at $t = 0.03$ consists of a fast shock, a slow shock, a contact discontinuity, a slow rarefaction, and a fast rarefaction wave.

Using the same numerical setup as for the previous test, we can resolve the structure though with some overshoot in the velocities at the tip of the rarefaction waves, see Fig. 4.8. These numerical artefacts are on the same level as for MC reconstruction. We, nevertheless, regard this result as a *caveat* pointing at a situation where MP-5 reconstruction will meet its limitations. The same test, computed using WENO-4 reconstruction and a CFL factor of CFL $= 0.7$ (Fig. 4.8), reveals that this method is less prone to such oscillations near rarefaction waves.

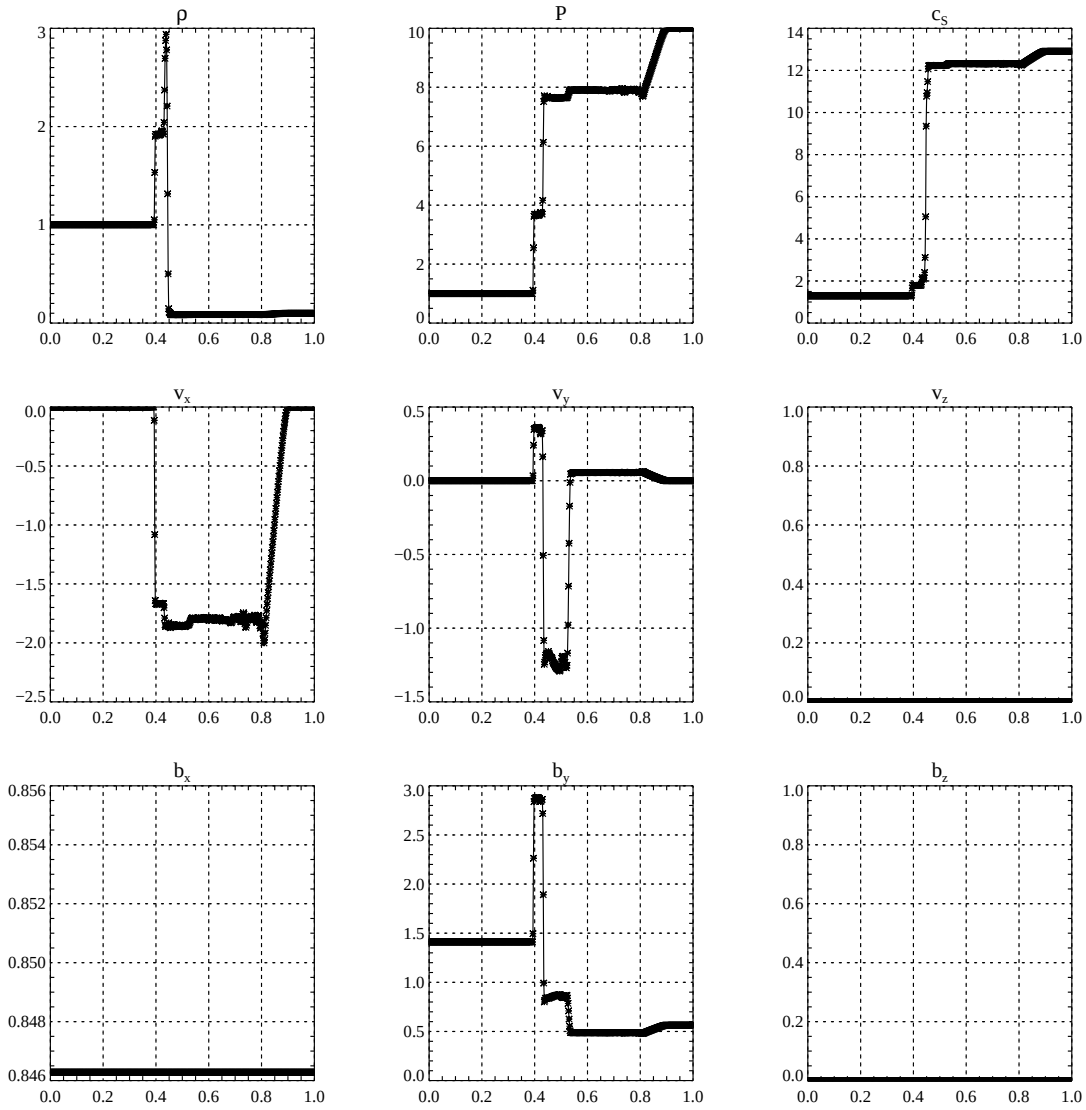

Figure 4.7: The same as Fig. 4.5, but for Riemann problem 1b at $t = 0.03$. The Riemann structure consists of (from left to right) a fast shock, a slow shock, a contact discontinuity, a slow and a fast rarefaction wave.

MHD Riemann problem 2a - rotational discontinuities and shocks By allowing all three field and velocity components to be non-zero, we can construct rotational discontinuities across which

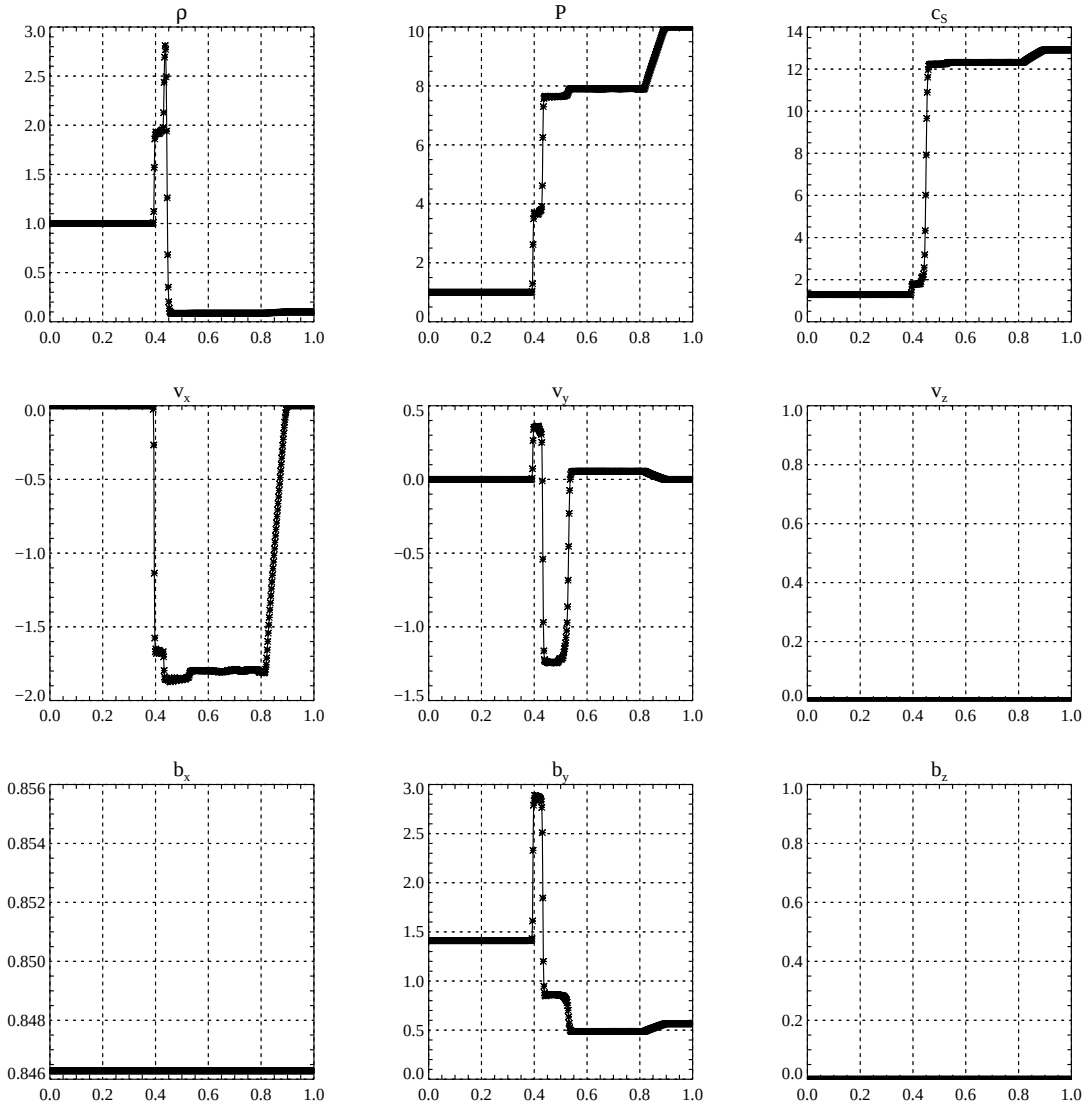

Figure 4.8: The same as Fig. 4.7, but using WENO-4 reconstruction, and a CFL factor CFL $= 0.7$.

the tangential magnetic field rotates by a certain angle. One such test has the initial state

$$(\rho, v_x, v_y, v_z, P, b_x, b_y, b_z)^{\mathrm{L}} = (1.08, 1.2, 0.01, 0.5, 0.95, 2/\sqrt{4\pi}, 3.6/\sqrt{4\pi}, 2/\sqrt{4\pi}), \tag{4.6a}$$

$$(\rho, v_x, v_y, v_z, P, b_x, b_y, b_z)^{\mathrm{R}} = (1, 0, 0, 0, 1, 2/\sqrt{4\pi}, 3.6/\sqrt{4\pi}, 2/\sqrt{4\pi}). \tag{4.6b}$$

At $t = 0.2$, the flow is characterised by a central contact discontinuity, and a pattern of a slow shock, a rotational discontinuity, and a fast shock on each side of the contact discontinuity.

We simulated this problem using MP-5 reconstruction, MUSTA(1)-HLL solver and 3$^{\mathrm{rd}}$-order Runge-Kutta time integration. The CFL factor is 0.8. In the result (Fig. 4.9), all waves are sharply resolved with little overshooting. We note that the fast shocks are resolved by 2 zones, whereas the slow ones need 3 zones.

MHD Riemann problem 2b – rotational discontinuities and rarefactions The initial data are

$$(\rho, v_x, v_y, v_z, P, b_x, b_y, b_z)^{\mathrm{L}} = (1, 0, 0, 0, 1, 3/\sqrt{4\pi}, 6/\sqrt{4\pi}, 0), \tag{4.7a}$$

$$(\rho, v_x, v_y, v_z, P, b_x, b_y, b_z)^{\mathrm{R}} = (0.1, 0, 2, 1, 10, 1/\sqrt{4\pi}, 1/\sqrt{4\pi}, 0). \tag{4.7b}$$

This problem is fairly similar to problem 1b, having the same Riemann structure as that one, only modified by rotational discontinuities inserted after the left- and right-moving fast shock waves. The rotational discontinuities have nearly the same velocity as the slow waves have. Thus, they lie nearly on top of these waves.

Simulating the model using the same numerical setup as above, we find that the discontinuities, in particular the shock waves, are resolved well, with some amount of overshooting present near the rarefaction waves. Despite the difficulty of very similar wave speeds, we can identify all waves, although the maximum value of b_z is too low in our results.

MHD Riemann problem 3a – magnetosonic shocks The third group of Riemann problems from Ryu & Jones (1995) involves magnetosonic shocks and rarefaction waves. The Riemann problem defined by

$$(\rho, v_x, v_y, v_z, P, b_x, b_y, b_z)^{\mathrm{L}} = (0.1, 0, 0, 0, 10, 0, -1/\sqrt{4\pi}, -2/\sqrt{4\pi}), \tag{4.8a}$$

$$(\rho, v_x, v_y, v_z, P, b_x, b_y, b_z)^{\mathrm{R}} = (0.1, 0, 0, 0, 0.2, 0, 1/\sqrt{4\pi}, 2/\sqrt{4\pi}) \tag{4.8b}$$

evolves into two magnetosonic shocks separated by a tangential discontinuity.

Our solution, obtained with the same numerical setup as used in the last test, see Fig.4.11, exhibits sharply resolved shocks and only minor smearing of the rotational discontinuity. We see a numerical artifact in the density and pressure at the location of the rotational discontinuity which is a typical feature of many numerical MHD schemes in this test. It is also present when solving the equations with different schemes, and seen by Ryu & Jones in their test, too.

MHD Riemann problem 3b – magnetosonic rarefaction waves We now test the ability of our code to handle magnetosonic rarefaction waves. The initial conditions are

$$(\rho, v_x, v_y, v_z, P, b_x, b_y, b_z)^{\mathrm{L}} = (1, 0, 0, 0, 1, 0, 1, 0), \tag{4.9a}$$

$$(\rho, v_x, v_y, v_z, P, b_x, b_y, b_z)^{\mathrm{R}} = (1, 0, 0, 0, 1, 0, 1, 0). \tag{4.9b}$$

In our solution, the rarefaction waves are resolved well. However, we see small overshooting at their end points, and a small glitch in the centre. Furthermore, the initial symmetry about the grid centre is preserved exactly.

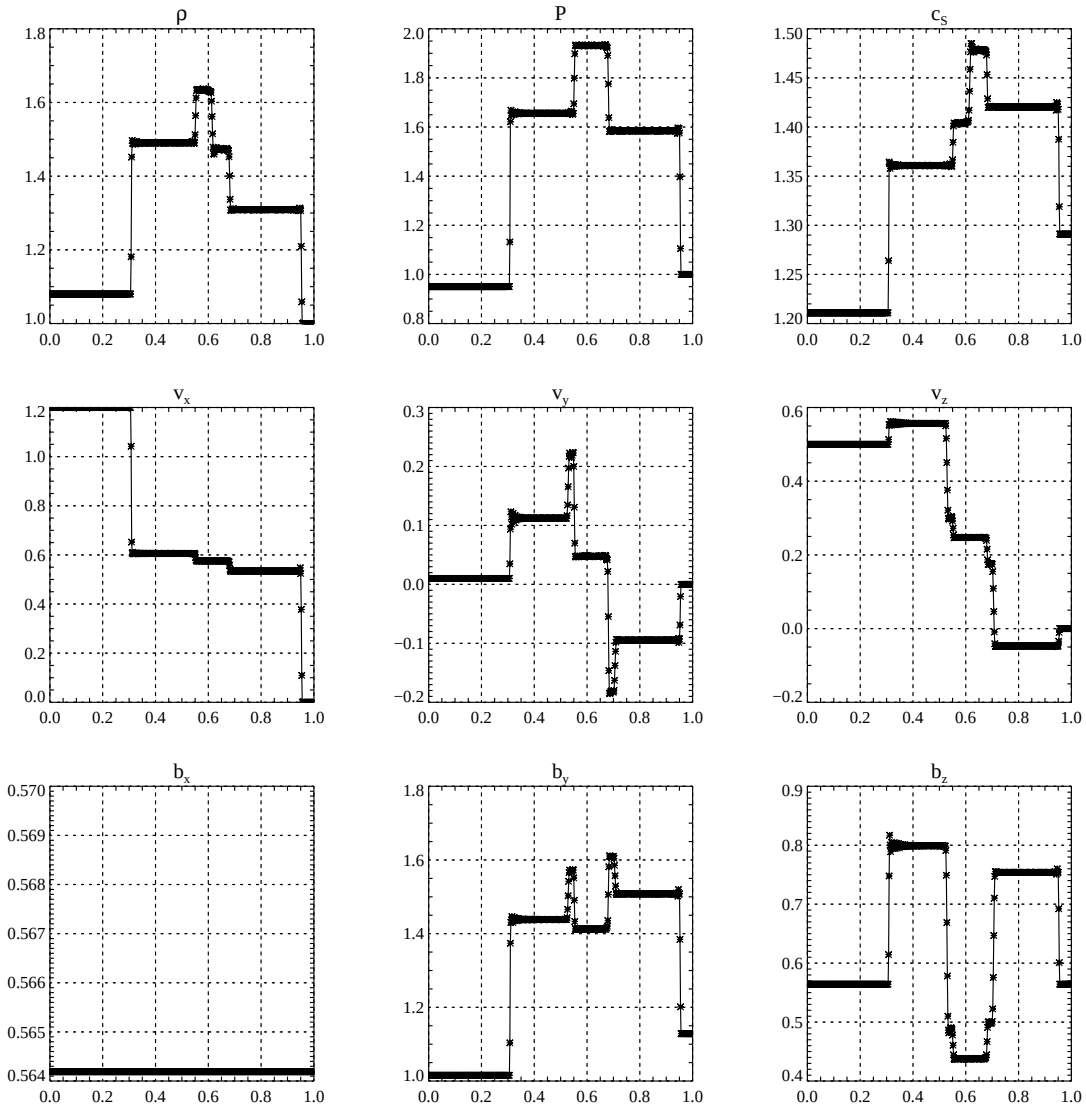

Figure 4.9: The same as Fig. 4.5, but for Riemann problem 2a at $t = 0.2$. The reconstruction is MP-5, the Riemann solver MUSTA(1)-HLL, and the time integrator Runge-Kutta of 3rd order. The flow exhibits (from left to right) a fast shock, a rotational discontinuity, a slow shock, a contact discontinuity, a slow shock, a rotational discontinuity, and a fast shock.

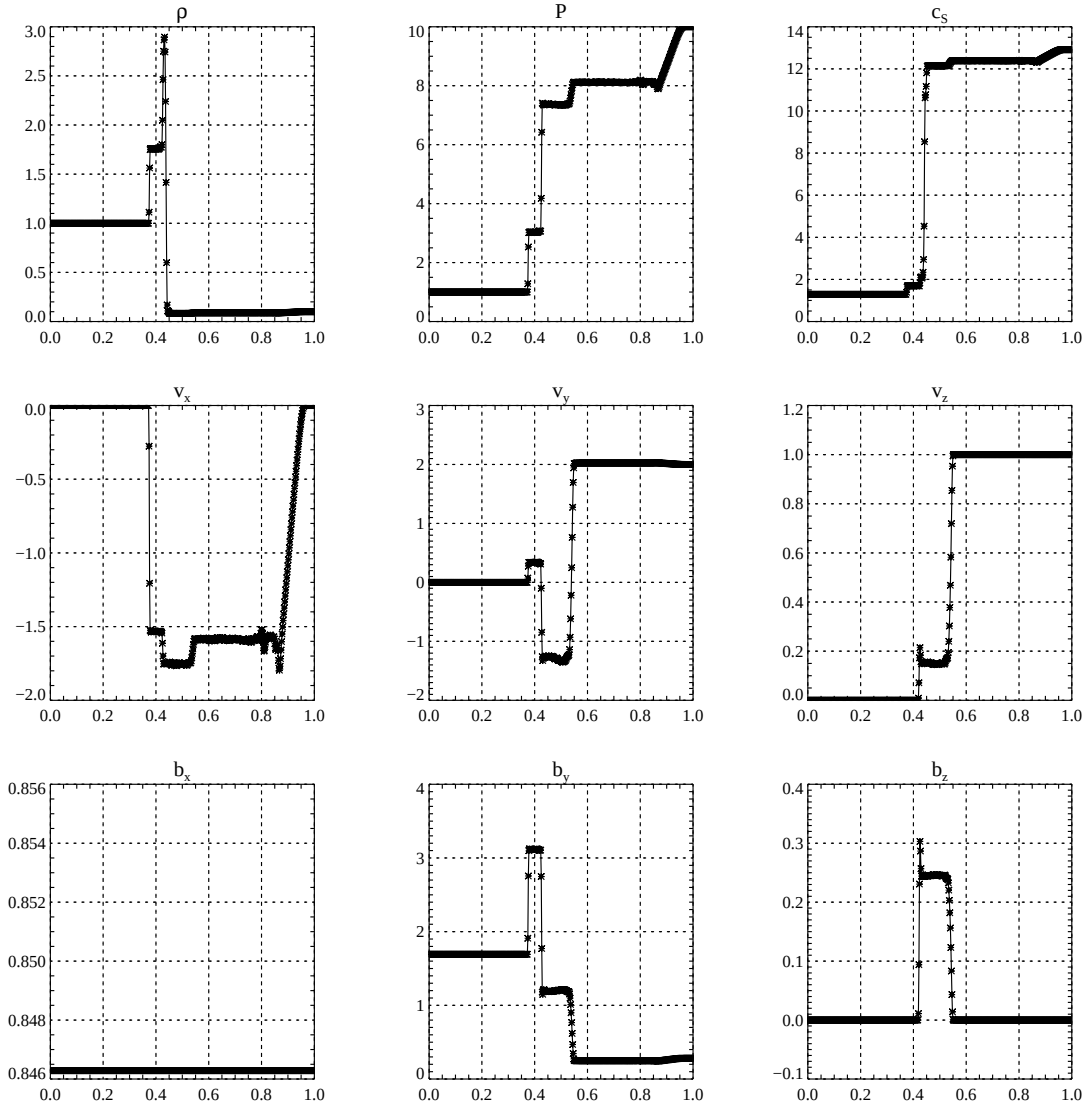

Figure 4.10: The same as Fig. 4.5, but for Riemann problem 2b at $t = 0.035$. The reconstruction is MP-5, the Riemann solver MUSTA(1)-HLL, and the time integrator Runge-Kutta of 3rd order. The flow exhibits (from left to right) a fast shock, a rotational discontinuity, a slow shock, a contact discontinuity, a slow rarefaction, a rotational discontinuity, and a fast rarefaction wave.

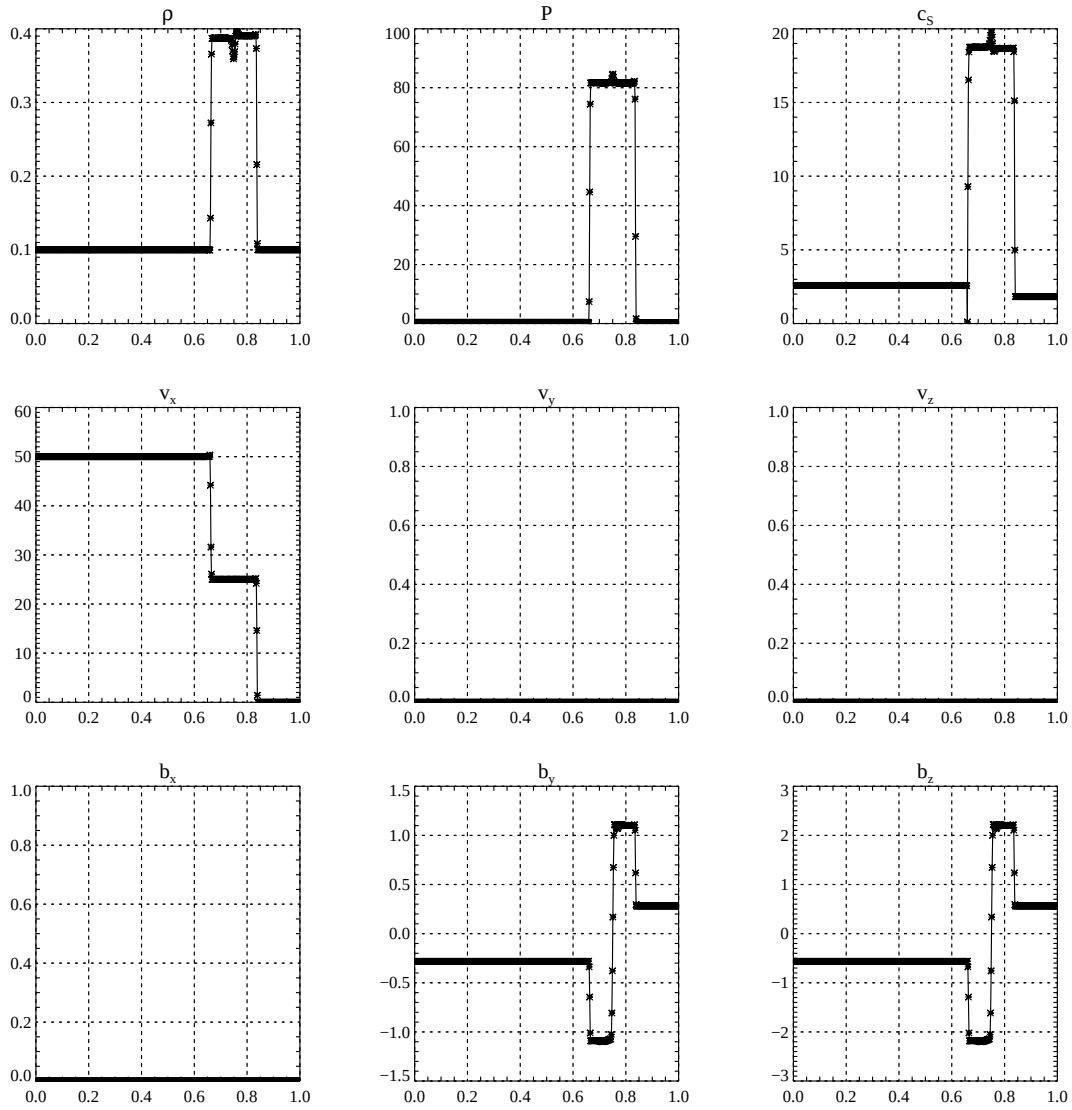

Figure 4.11: The same as Fig. 4.5, but for Riemann problem 3a at $t = 0.01$. The reconstruction is MP-5, the Riemann solver MUSTA(1)-HLL, and the time integrator Runge-Kutta of 3rd order. The flow exhibits (from left to right) a a magnetosonic shock, a tangential discontinuity, and magnetosonic shock.

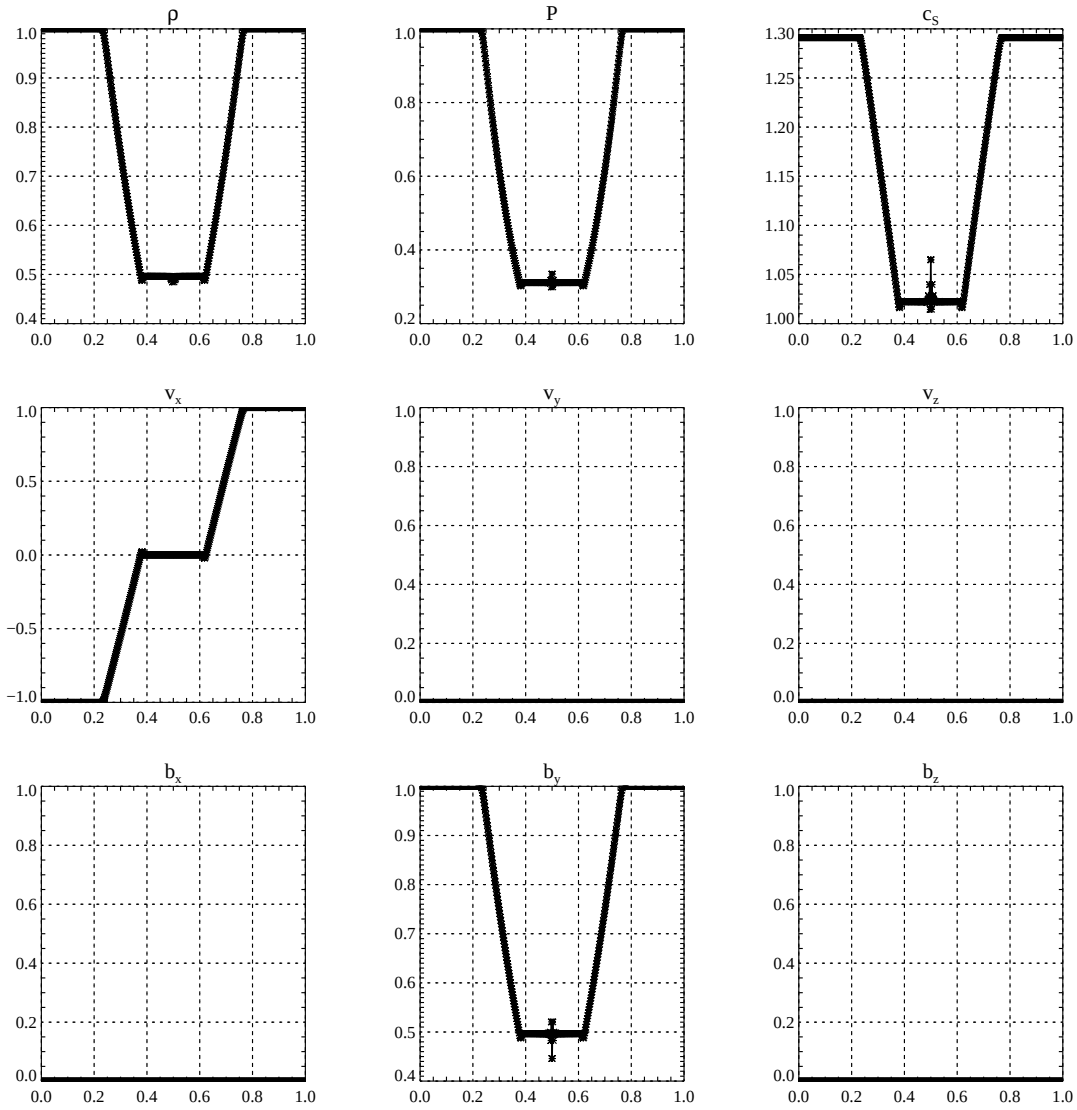

Figure 4.12: The same as Fig. 4.5, but for Riemann problem 3b at $t = 0.1$. The reconstruction is MP-5, the Riemann solver MUSTA(1)-HLL, and the time integrator Runge-Kutta of 3rd order. The flow exhibits (from left to right) two magnetosonic rarefaction waves.

MHD Riemann problem 4a – switch-on fast shock The next set of tests involves switch-on and switch-off waves in which the tangential magnetic field changes between zero and a non-vanishing value. The first of these tests,

$$(\rho, v_x, v_y, v_z, P, b_x, b_y, b_z)^{\mathrm{L}} = (1,0,0,0,1,1,1,0), \tag{4.10a}$$
$$(\rho, v_x, v_y, v_z, P, b_x, b_y, b_z)^{\mathrm{R}} = (0.2,0,0,0,0.1,1,0,0), \tag{4.10b}$$

develops a fast rarefaction, a slow rarefaction, a contact discontinuity, a slow shock, and a switch-on fast shock.

All waves are resolved well, and only minor overshooting is present near the slow rarefaction. The magnetic field is switched on within 3 zones at the rightmost shock.

MHD Riemann problem 4b – switch-off fast rarefaction We test the ability of the code to treat switch-off rarefaction waves using the initial data

$$(\rho, v_x, v_y, v_z, P, b_x, b_y, b_z)^{\mathrm{L}} = (0.4, -0.66991, 0.98263, 0, 0.52467, 1.3, 0.0025293, 0), \tag{4.11a}$$
$$(\rho, v_x, v_y, v_z, P, b_x, b_y, b_z)^{\mathrm{R}} = (1,0,0,0,1,1.3,1,0), \tag{4.11b}$$

from which a contact discontinuity and a switch-off fast rarefaction wave develop.

In the numerical solution, we see, as Ryu & Jones (1995) did in their study, small artefacts: a right-moving slow and a right-moving hydrodynamic wave. Apart from these structures, our code handles these waves well.

MHD Riemann problem 4c – switch-off slow shock The next test has the initial data

$$(\rho, v_x, v_y, v_z, P, b_x, b_y, b_z)^{\mathrm{L}} = (0.65, 0.667, -0.257, 0, 0.5, 0.75, 0.55, 0), \tag{4.12a}$$
$$(\rho, v_x, v_y, v_z, P, b_x, b_y, b_z)^{\mathrm{R}} = (1, 0.4, -0.94, 0, 0.75, 0.75, 0, 0). \tag{4.12b}$$

At $t = 0.15$, the flow exhibits a fast shock, a switch-off slow shock, a contact discontinuity, and a hydrodynamic shock.

In our result, the flow features are represented well, with sharp discontinuities. We find small spurious oscillations right of the contact discontinuity.

MHD Riemann problem 4d – switch-on slow rarefaction This test, evolving until $t = 0.16$ into a hydrodynamic rarefaction, a switch-on slow rarefaction, a contact discontinuity, a slow shock, a rotational discontinuity, and a fast rarefaction, starts with the initial data

$$(\rho, v_x, v_y, v_z, P, b_x, b_y, b_z)^{\mathrm{L}} = (1,0,0,0,1,0.7,0,0), \tag{4.13a}$$
$$(\rho, v_x, v_y, v_z, P, b_x, b_y, b_z)^{\mathrm{R}} = (0.3,0,0,1,1,0.7,0,0.2). \tag{4.13b}$$

Our code is able to track all waves accurately, with, however, the now well-known oscillations near the fast rarefaction.

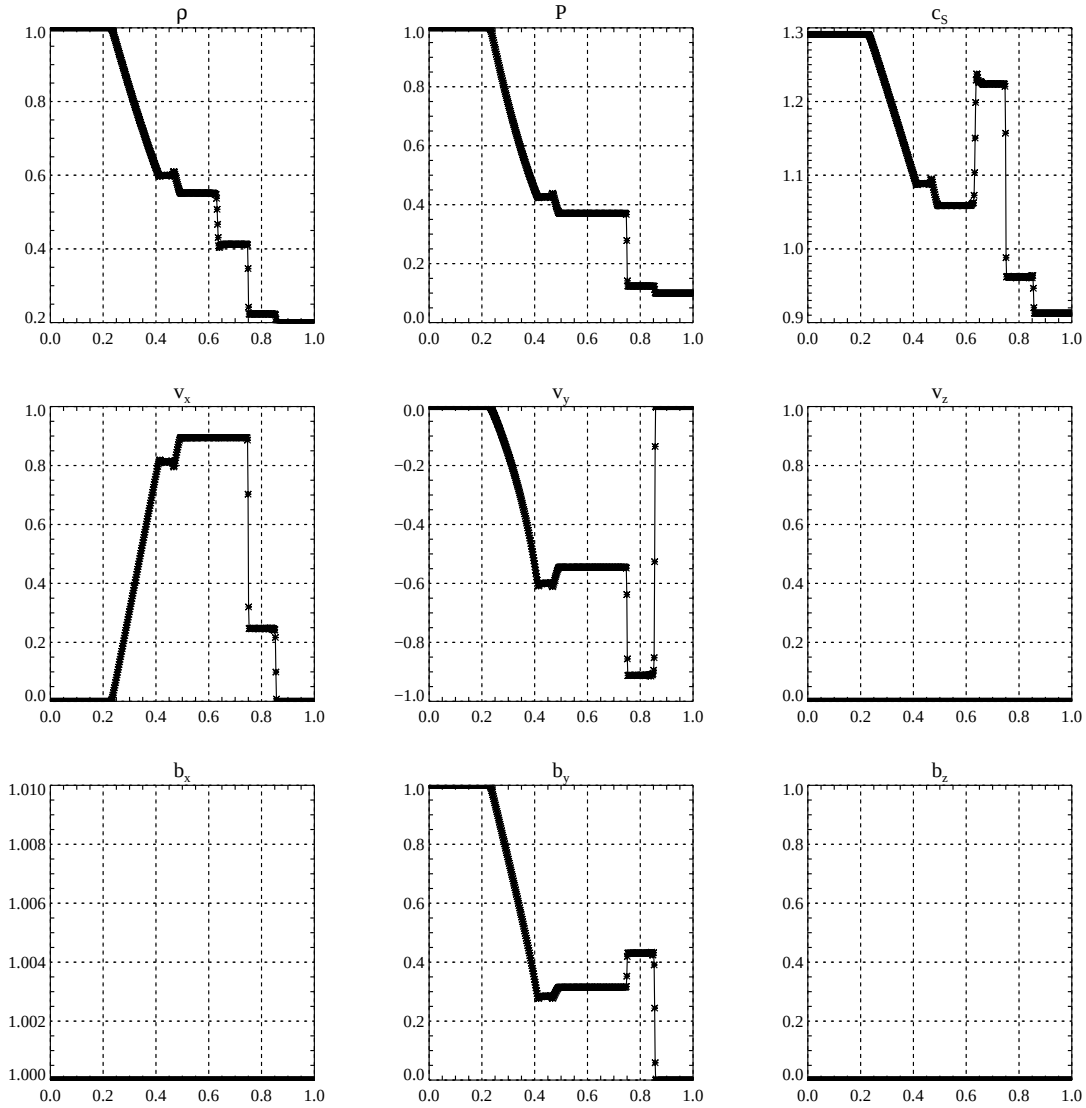

Figure 4.13: The same as Fig. 4.5, but for Riemann problem 4a at $t = 0.15$. The reconstruction is MP-5, the Riemann solver MUSTA(1)-HLL, and the time integrator Runge-Kutta of 3rd order. The flow consists of (from left to right) a fast rarefaction, a slow rarefaction, a contact discontinuity, a a slow shock, and a switch-on fast shock.

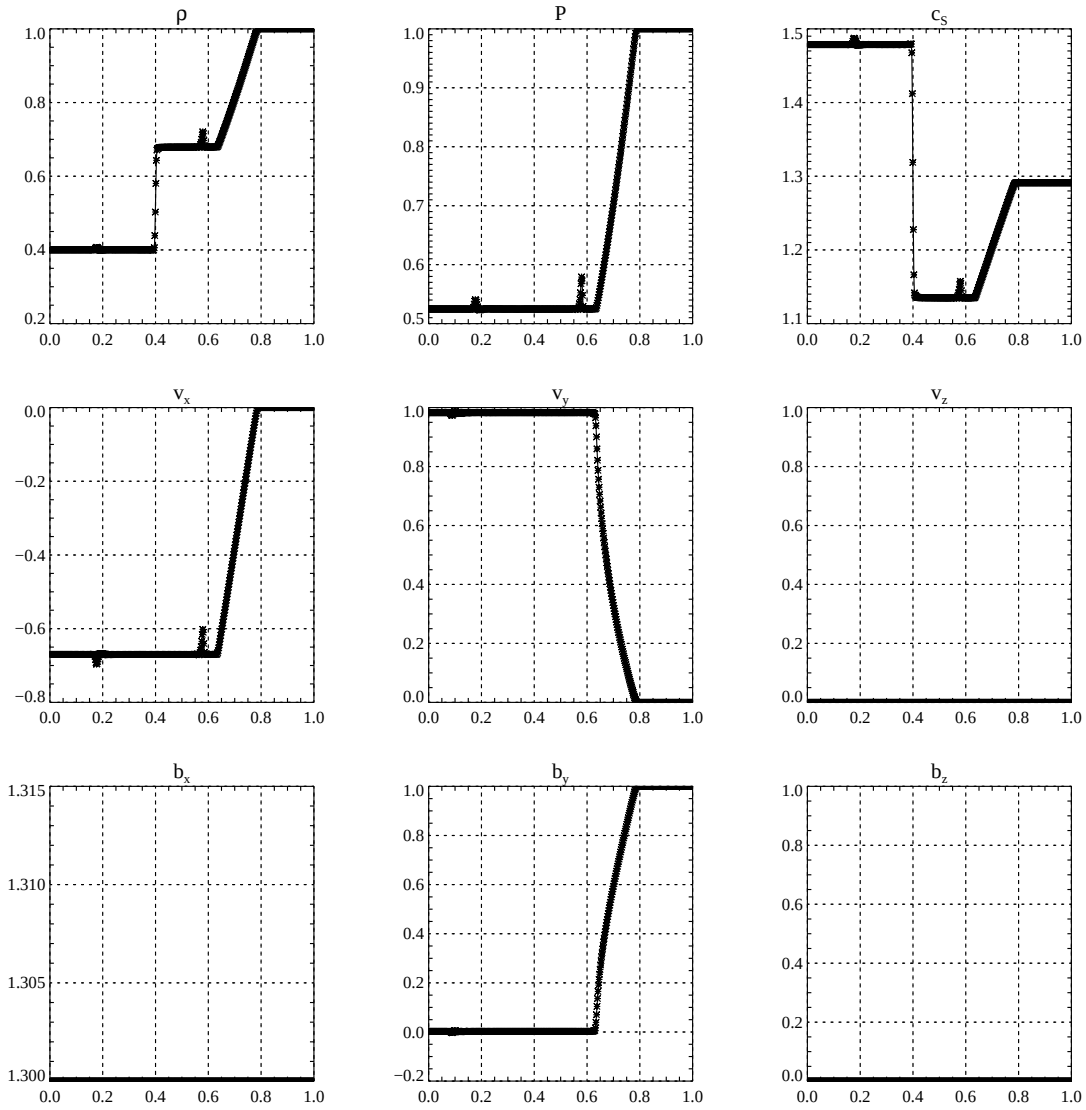

Figure 4.14: The same as Fig. 4.5, but for Riemann problem 4b at $t = 0.15$. The reconstruction is MP-5, the Riemann solver MUSTA(1)-HLL, and the time integrator Runge-Kutta of 3rd order. The flow consists of (from left to right) a contact discontinuity and a switch-off fast rarefaction.

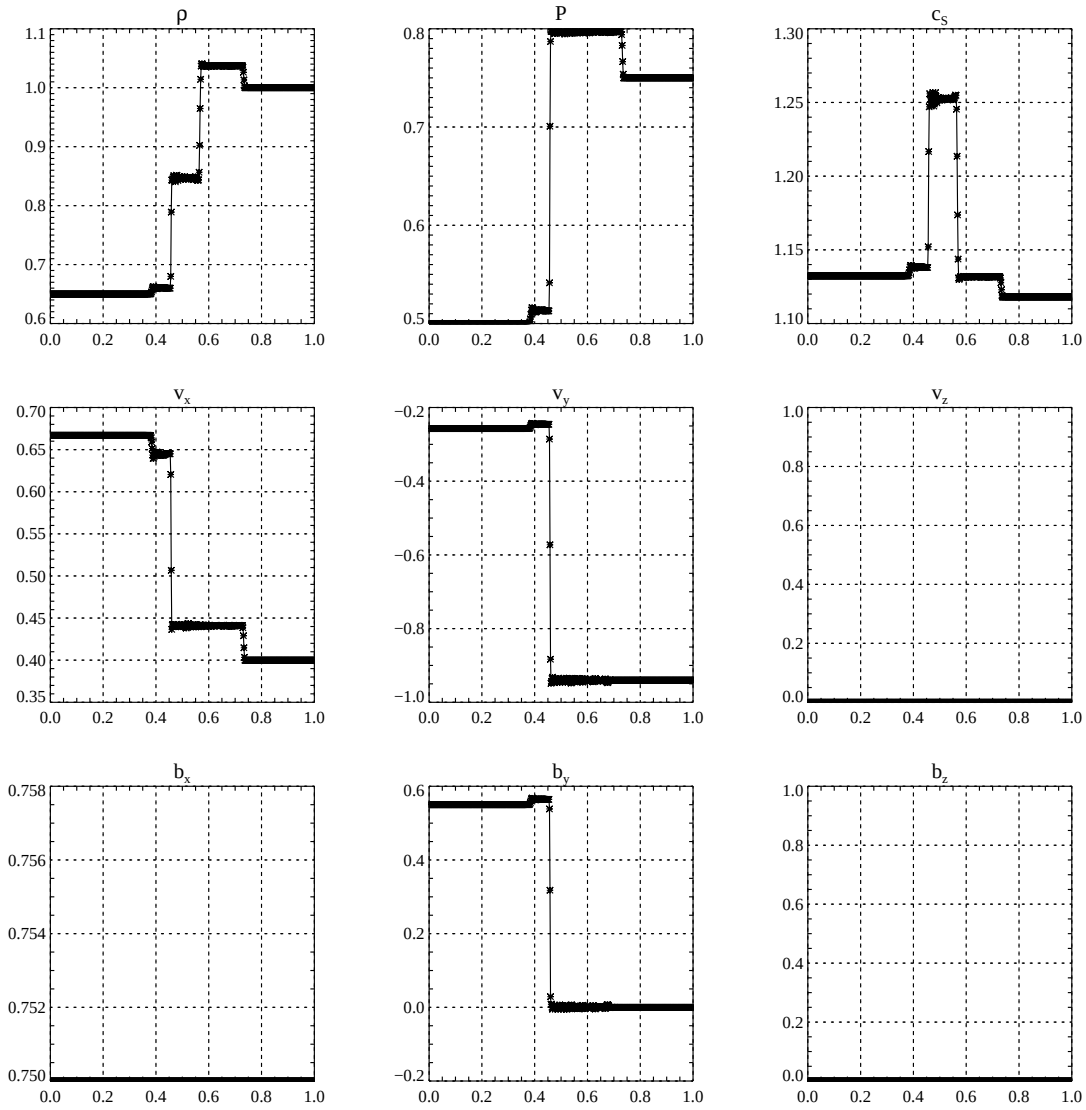

Figure 4.15: The same as Fig. 4.5, but for Riemann problem 4c at $t = 0.15$. The reconstruction is MP-5, the Riemann solver MUSTA(1)-HLL, and the time integrator Runge-Kutta of 3rd order. The flow consists of (from left to right) a fast shock, a switch-off slow shock, a contact discontinuity, and a hydrodynamic shock.

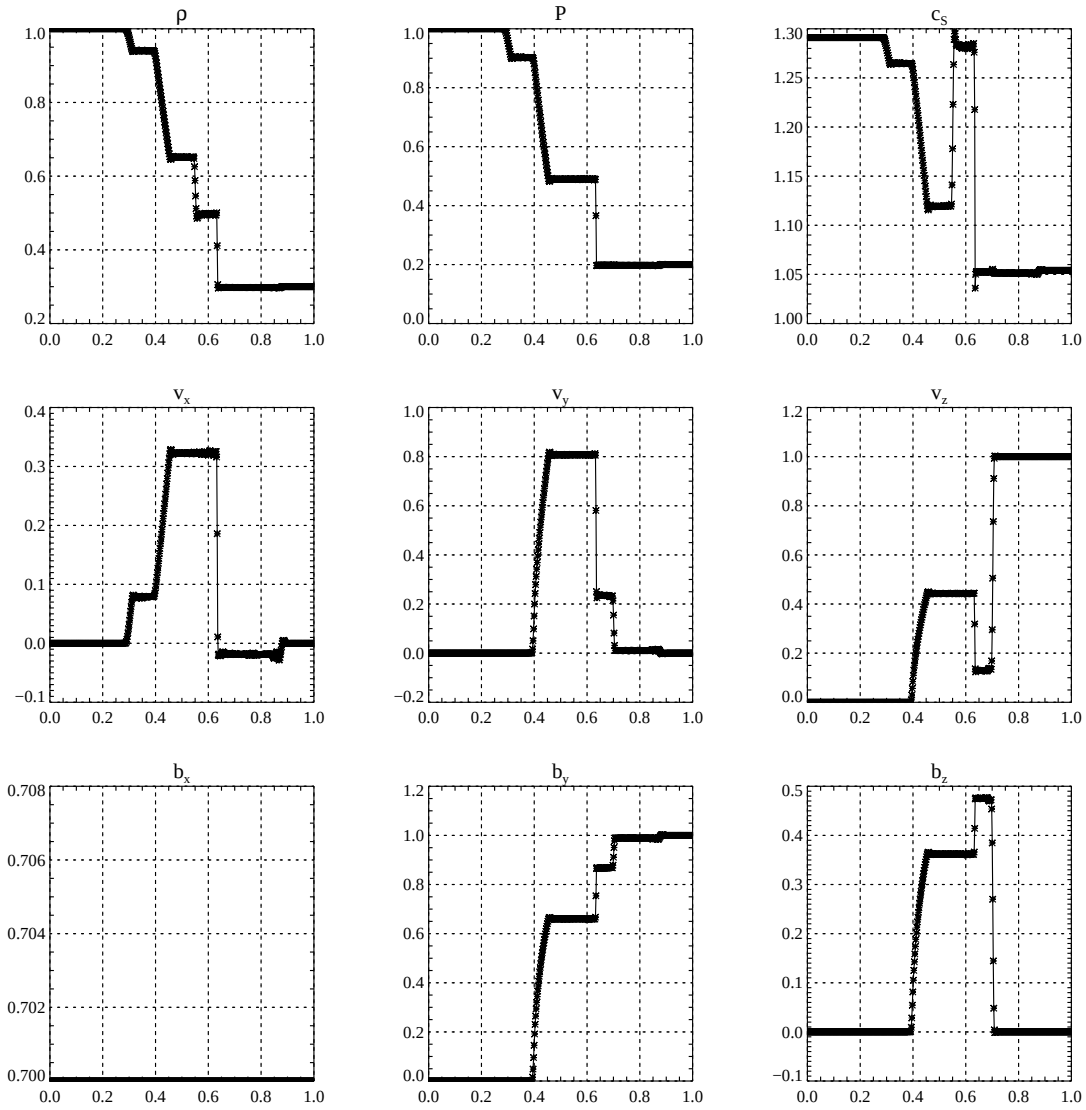

Figure 4.16: The same as Fig. 4.5, but for Riemann problem 4d at $t = 0.16$. The reconstruction is MP-5, the Riemann solver MUSTA(1)-HLL, and the time integrator Runge-Kutta of 3rd order. The flow consists of (from left to right) a hydrodynamic rarefaction, a switch-on slow rarefaction, a contact discontinuity, a slow shock, a rotational discontinuity, and a fast rarefaction.

MHD Riemann problem 5a – slow compound The final two tests evolve *compound waves*, which consist of a shock and a rarefaction of the same wave family (i.e., slow or fast). The first problem has the initial data

$$(\rho, v_x, v_y, v_z, P, b_x, b_y, b_z)^{\mathrm{L}} = (1, 0, 0, 0, 1, 0.75, 1, 0), \tag{4.14a}$$

$$(\rho, v_x, v_y, v_z, P, b_x, b_y, b_z)^{\mathrm{R}} = (0.125, 0, 0, 0, 1, 0.75, -1, 0). \tag{4.14b}$$

It evolves into a fast rarefaction, a slow compound, a contact discontinuity, a slow shock, and a fast rarefaction. The slow compound, located at $x \approx 0.47$ at $t = 0.1$, is composed of a slow shock and a slow rarefaction attached to the right-hand side of the shock, propagating at the same velocity.

These structures are finely resolved. The shock component of the compound is resolved by two cells in the pressure jump, and the linear profile of the rarefaction is reproduced with reasonable accuracy.

MHD Riemann problem 5b – fast compound The second problem involving compound waves evolves from

$$(\rho, v_x, v_y, v_z, P, b_x, b_y, b_z)^{\mathrm{L}} = (1, 0, 0, 0, 1, 1.3, 1, 0), \tag{4.15a}$$

$$(\rho, v_x, v_y, v_z, P, b_x, b_y, b_z)^{\mathrm{R}} = (0.4, 0, 0, 0, 0.4, 1.3, -1, 0). \tag{4.15b}$$

At later time, the solution consists of a fast compound, a slow shock, a contact discontinuity, a slow shock, and a fast rarefaction.

We note the same result as in the previous test: the compound wave is resolved well, with the shock resolved in two zones and a well reproduced linear profile of the rarefaction.

MHD Riemann problems: summary In all MHD Riemann tests presented above, our code has proven able to track the position and amplitude of the waves with good accuracy. The jumps associated with shock waves are resolved by a few, typically at most 2 zones. Depending on the reconstruction, however, some overshooting does occur. Using MP-5 reconstruction, this overshooting is modest, never spoiling the solution away from the discontinuity or leading to numerical instability. Overshooting is significantly reduced for the WENO-4 scheme, which, furthermore, has an accuracy similar to the MP-5 scheme. In general, rarefaction waves are reproduced well. The only restriction to this is that, for MP-5, we observe a certain level of overshooting near the high-velocity end of the wave. This phenomenon, again, is reduced considerably when using WENO-4. Contact discontinuities require more zones for resolution; we typically find up to 5 zones necessary. The same number of grid cells suffices to resolve tangential discontinuities and rotational discontinuities. We note that our code does not make use of steepening algorithms for any of these discontinuities.

Estimating the order of the method We finally present results from simulations of continuous initial data. Using these results, we will give an estimate of the numerical order of accuracy of some of our schemes. We followed the evolution of a magneto-sonic wave for which the initial data on the domain $x \in [0;1]$ are given by

$$\rho = 1, \qquad P = 0.3, \tag{4.16a}$$

$$v_x = 10^{-4}\sin(2\pi x), \qquad v_y = 0, \qquad v_z = 0, \tag{4.16b}$$

$$b_x = 0, \qquad b_y = (1 + v_x)/\sqrt{(2)}, \qquad b_z = 0. \tag{4.16c}$$

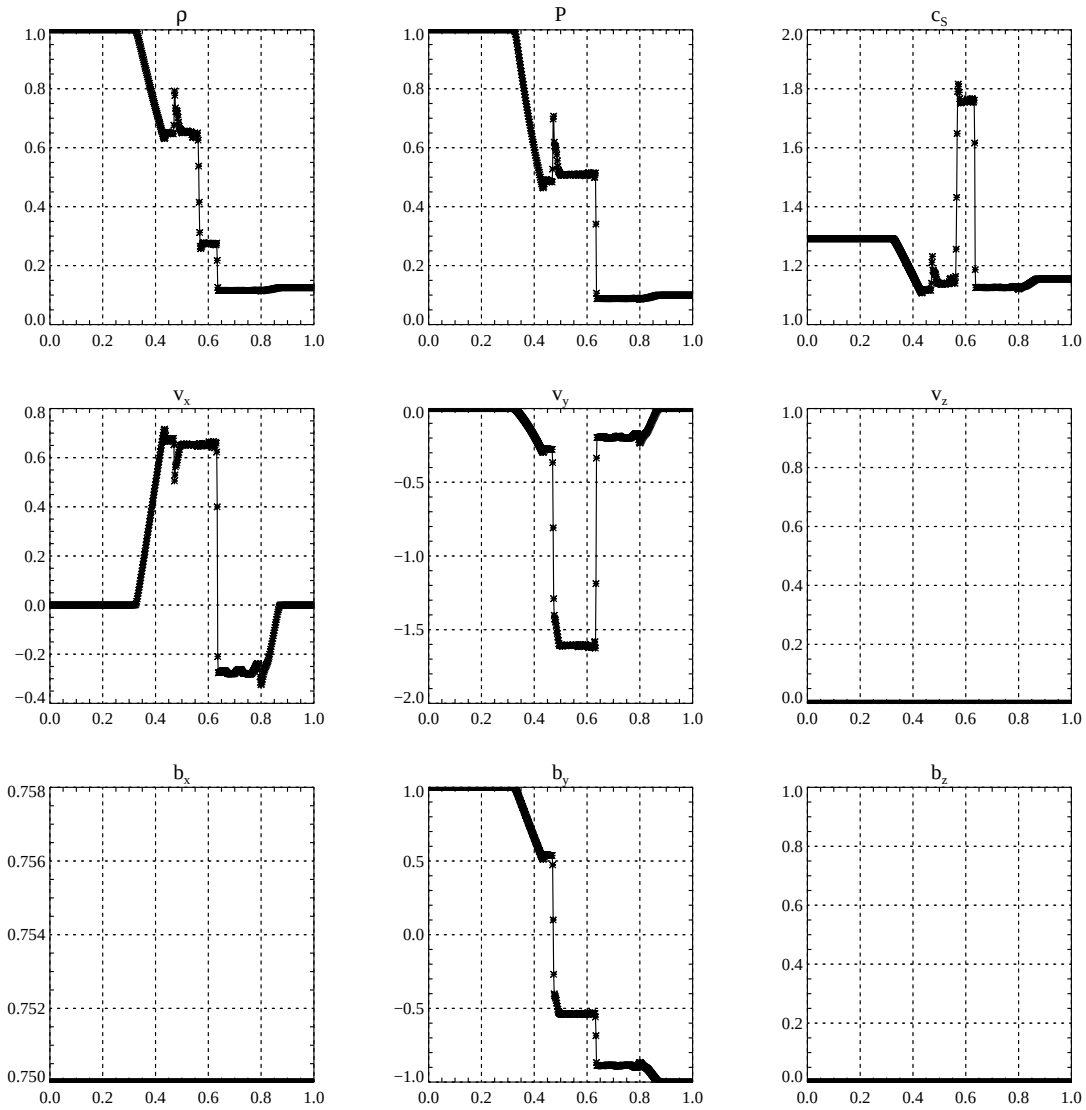

Figure 4.17: The same as Fig. 4.5, but for Riemann problem 5a at $t = 0.1$. The reconstruction is MP-5, the Riemann solver MUSTA(1)-HLL, and the time integrator Runge-Kutta of 3rd order. The flow consists of (from left to right) a fast rarefaction, a slow compound, a contact discontinuity, a slow shock, and a fast rarefaction.

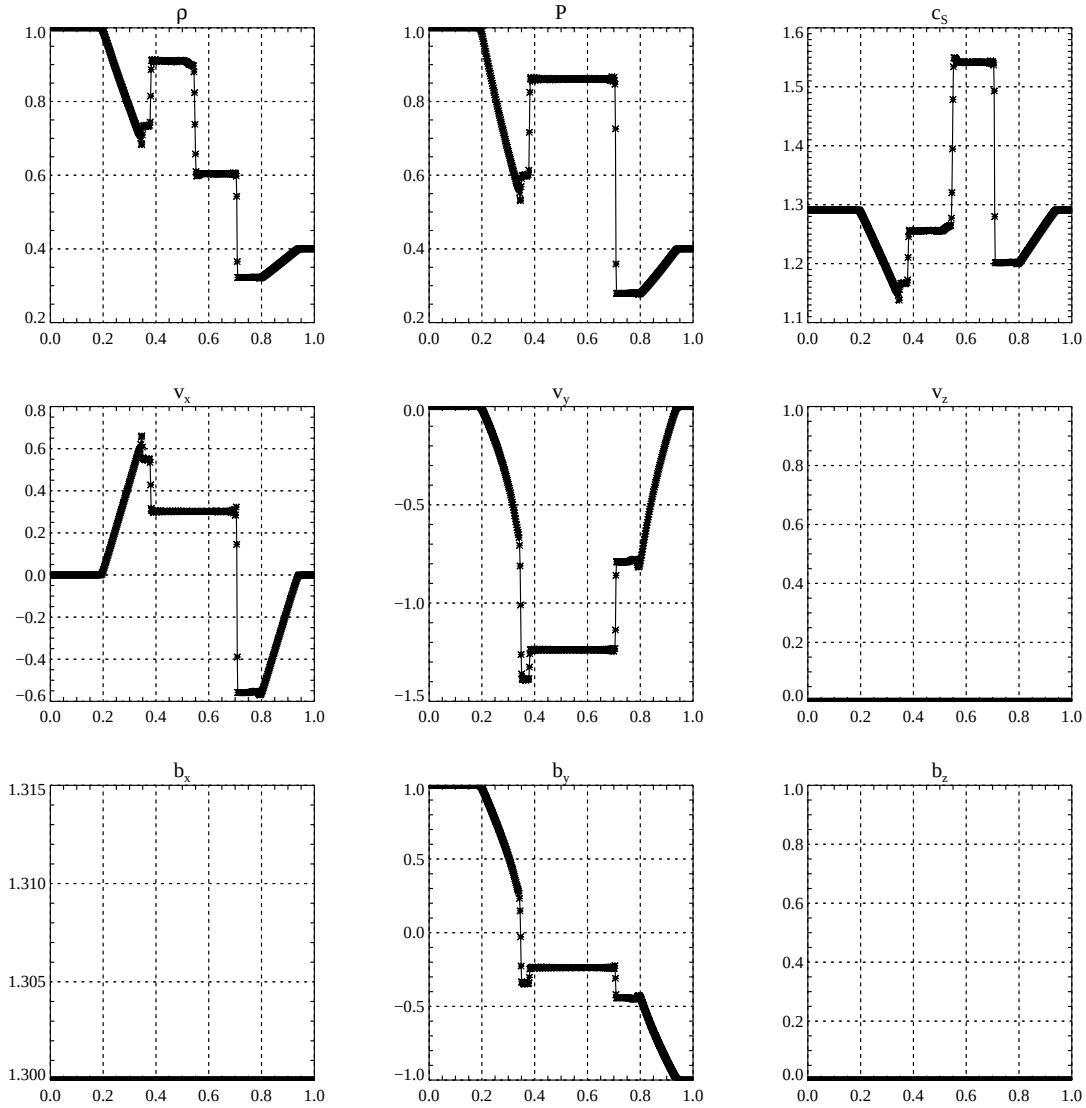

Figure 4.18: The same as Fig. 4.5, but for Riemann problem 5b at $t = 0.16$. The reconstruction is MP-5, the Riemann solver MUSTA(1)-HLL, and the time integrator Runge-Kutta of 3rd order. The flow consists of (from left to right) a fast compound, a slow shock, a contact discontinuity, a slow shock, and a fast rarefaction.

The analytic expression for v_x at $t = 4$ is identical to the initial data.

For simulations using different numerical schemes and grid resolution, we compute the L_1 norm of the error in v_x,

$$L_1 = \frac{\int \mathrm{d}x |v_x^m - v_x^{\mathrm{an}}|}{L}, \tag{4.17}$$

where superscripts ^{m} and $^{\mathrm{an}}$ refer to the numerical solution at m grid cells and the analytic one, respectively; L is the grid length. The method is of n^{th} order, if the L_1 error scales with grid resolution δx as $L_1 \propto \delta x^{-n}$.

The results, displayed in Fig. 4.19 and summarised in Tab. 4.1, show the superiority of the high-order reconstruction schemes over PCM and TVD-PLM schemes. In this figure, different reconstruction schemes are distinguished by colour: PCM, MM, MC, MP-5, MP-7, MP-9, and WENO-4 are displayed in yellow, bright orange, orange, red, green, blue, and black lines and symbols, respectively. Different Riemann solvers are distinguished by symbols: we use $+$, $\diamond$, and $\triangle$ to refer to MUSTA(1)-HLL, MUSTA(0)-LxF, and MUSTA(1)-LxF, respectively. In all computations, we used 3$^{\mathrm{rd}}$-order Runge-Kutta time integration and a CFL factor of 0.8.

We first note that, in this subsonic test, the choice of the Riemann solver makes only little difference. As expected, all schemes follow a power law until the error has dropped to a minimum value of $L_1 \approx 8 \times 10^{-8}$. We attribute this level to numerical noise, e.g., in the integration of the L_1 norm. From the slopes of the power laws, we obtain the numerical orders of accuracy given in Tab. 4.1. The resulting orders meet the expectations: PCM and PLM have orders of approximately 1 and 2, whereas the higher-order schemes are considerably more accurate. There is not much difference between the MP schemes, all having orders around 3, but WENO-4 turns out to be the most accurate with an order of 4. To reach the noise level with MC reconstruction, the grid has to be four times finer than the grid required with one of the higher-order schemes.

	PCM	MM	MC	MP-5	MP-7	MP-9	WENO-4
order	0.9	1.8	2.4	3.3	3.0	3.0	4.1

Table 4.1: Estimates of the numerical order of accuracy of different reconstruction schemes as obtained from the convergence test on the magneto-sonic wave initial data.

4.1.2 Two-dimensional problems

We finally will present a few two-dimensional test problems our code had to pass before put into service.

Orszag-Tang vortex The Orszag-Tang vortex, originally studied by Orszag & Tang to investigate the transition of MHD flows to turbulence, has become a popular test for MHD codes. The fluid initially has uniform density ρ_0 and pressure P_0; the velocity and magnetic fields are given by

$$\vec{v} = \begin{pmatrix} -\sin(y) \\ \sin(x) \end{pmatrix}, \tag{4.18a}$$

$$\vec{B} = \begin{pmatrix} -\sin(y) \\ \sin(2x) \end{pmatrix}. \tag{4.18b}$$

The vector fields are normalised, $|\vec{B}| = 1 = |\vec{v}|$. The initial density and pressure are parametrised by the Mach number $M^2 = \frac{\rho_0}{\gamma P_0}$ and the plasma beta $\beta = 8\pi P_0$, for which we set $M^2 = 1$ and

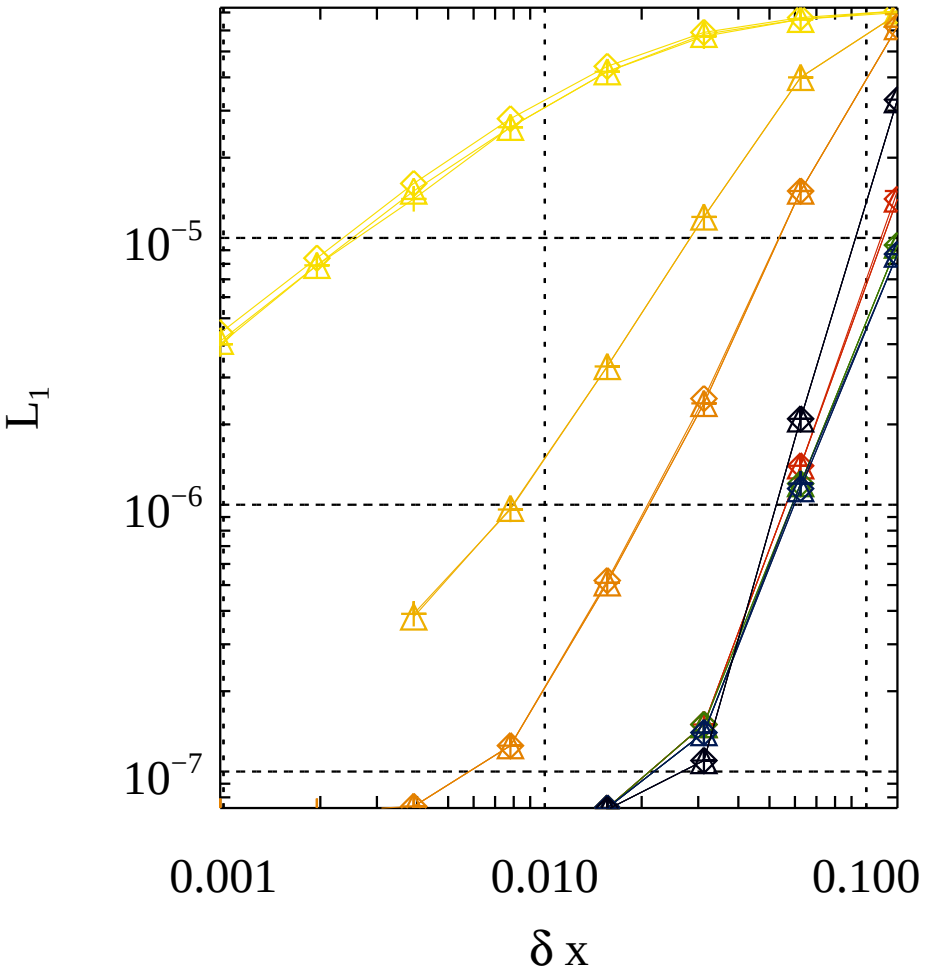

Figure 4.19: The L_1 norm of the errors of our numerical solutions of the propagation of a magneto-sonic wave to $t = 4$. We compare different schemes: colours distinguish between reconstruction schemes (yellow, bright orange, orange, red, green, blue, and black represent PCM, MM, MC, MP-5, MP-7, MP-9, and WENO-4 schemes, respectively), and symbols distinguish between Riemann solvers ($+$, $\diamond$, and $\triangle$ stand for MUSTA(1)-HLL, MUSTA(0)-LxF, and MUSTA(1)-LxF, respectively).

$\beta = 10/3$. We use 3rd-order Runge-Kutta time integration, the MUSTA(1)-HLL solver and MP-5 reconstruction. The grid is set to $m_x \times m_y = 128 \times 128$ zones and periodic BC are assumed; the CFL number is set to CFL $= 0.95$. There is no analytic solution to this test, but we can compare the results not only among our different schemes, but also to various simulations of other authors.

At $t = 0.5$, the flow has developed a quite complicated structure. Initially smooth waves have steepened into discontinuities. Both the magnetic and velocity field fill only – fairly disjoint – parts of the grid. Density and gas pressure show large variations on small length scales; they are smallest in regions of strong field or high velocity.

Our code is able to reproduce the results from Zachary et al. (1994); Dai & Woodward (1998) very well (Fig. 4.20). The discontinuities are resolved very sharply and do not show significant oscillations (cf. bottom panels of Fig. 4.20). We also want to point out that the initial rotational symmetry is preserved: if we rotate the numerical solution about the grid centre and subtract the resulting MHD variables from the original solution, we get exactly zero.

A wind tunnel We tested the code in a further two-dimensional problem involving the transition of laminar to turbulent motion. We set a circular blob (radius $r = 0.2$) of dense ($\rho = 100$) matter in equilibrium (constant pressure of $P = 1$) into a surrounding fluid of density $\rho = 1$. The fluid was permeated by a uniform magnetic field $\vec{b} = (0.1, 0, 0)^T$. At $t = 0$, we started to inject a wind of velocity $v_w \approx (0.3, 0, 0)^T$ from the left boundary ($x = -1$) into the grid. The grid extended from -1 to 7 and from 0 to 2 in x- and y-direction, respectively, and was covered by 640×160 zones. The wind streams past the dense blob, pushing it towards the right boundary. Because of its large inertia, the blob remains coherent throughout the test. It is affected by the wind, however, in two ways: it is deformed by the wind, and it looses a small amount of matter. In the wake behind the blob, a turbulent vortex strait forms, similar to the Karman vortex strait of flow past a grid of wires. Thin filaments form in the wake, and the magnetic field is concentrated in thin sheets (see Fig. 4.21). The turbulent fields with their wave-like and sheet-like structures are resolved well.

Komissarov problem We next consider a test well-known among practitioners of general relativistic MHD as *Komissarov's problem*. The non-relativistic version was used as a test by Kössl et al. (1990). In a gas of uniform density ρ_0, threaded by a uniform magnetic field b_y^0, an explosion is initiated by an overpressure P_1 in the central region of the grid; the pressure outside of this region is P_0. We may consider a 2d or a 3d version of the problem; then, the pressurised versions correspond to a central cylinder or sphere.

Sedov solution Without magnetic field, the well-known *Sedov solution* should be recovered. A cylindrically/spherically symmetric shock wave propagates outwards, and in the post-shock region, the HD variables follow analytic profiles. The functions governing the profiles, can be expressed in terms of the shock radius at time t, $\xi(t)$, e.g., $P(R,t) = P(R/\xi(t))$ (where $R = \varpi$ in cylindrical coordinates, and $R = r$ in spherical coordinates). The shock radius is given by

$$\xi(t) = \beta_\nu(\gamma) \left(\frac{E t^2}{\rho_0} \right)^{1/(\nu+3)} . \tag{4.19a}$$

The radius depends on the explosion energy, E, the density of the ambient medium, ρ_0, and a function β_ν of the adiabatic index γ. The parameter ν distinguishes between geometries: $\nu = 1$

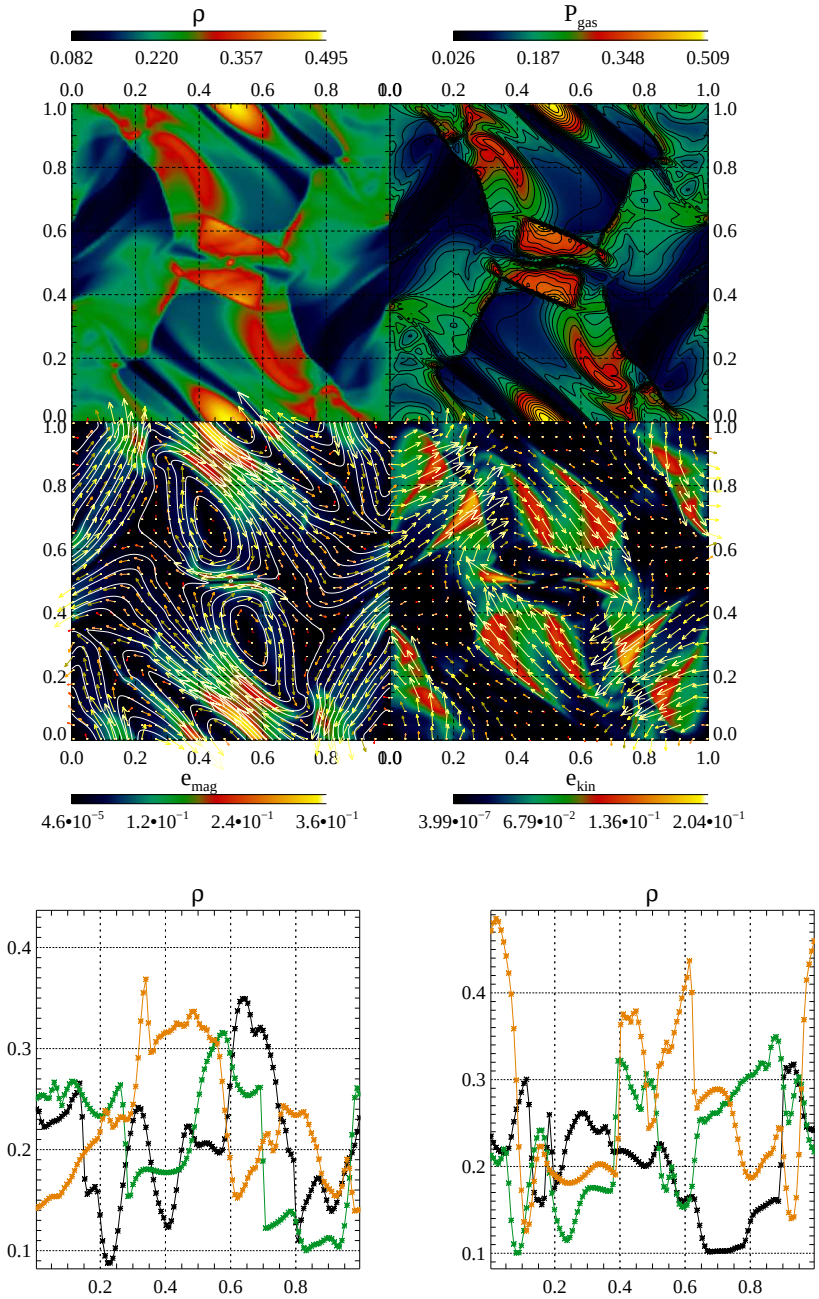

Figure 4.20: The Orszag-Tang vortex at $t = 0.5$. We computed the results using 3$^{\text{rd}}$-order Runge-Kutta time integration, the MUSTA(1)-HLL solver, and MP-5 reconstruction on a grid of $m_x \times m_y = 128 \times 128$ zones with a CFL factor of 0.95. The upper two rows show the gas density ρ (top left panel), gas pressure P_{gas} (top right panel), kinetic energy density e_{kin} (middle right panel), and magnetic energy density e_{mag} (middle left panel). Additionally, the top right panel shows contours of the gas pressure, the middle right panel shows velocity vectors and the middle left panel shows vectors and field lines of the magnetic field. The vectors are coloured according to their magnitude. The bottom panels show horizontal and vertical slices through the density distribution. The black, green, and orange lines represent $\rho(x,y)$ for $y = 0.160, 0.316, 0.473$ (left panel) and $\rho(x,y)$ for $x = 0.160, 0.316, 0.473$ (right panel), respectively.

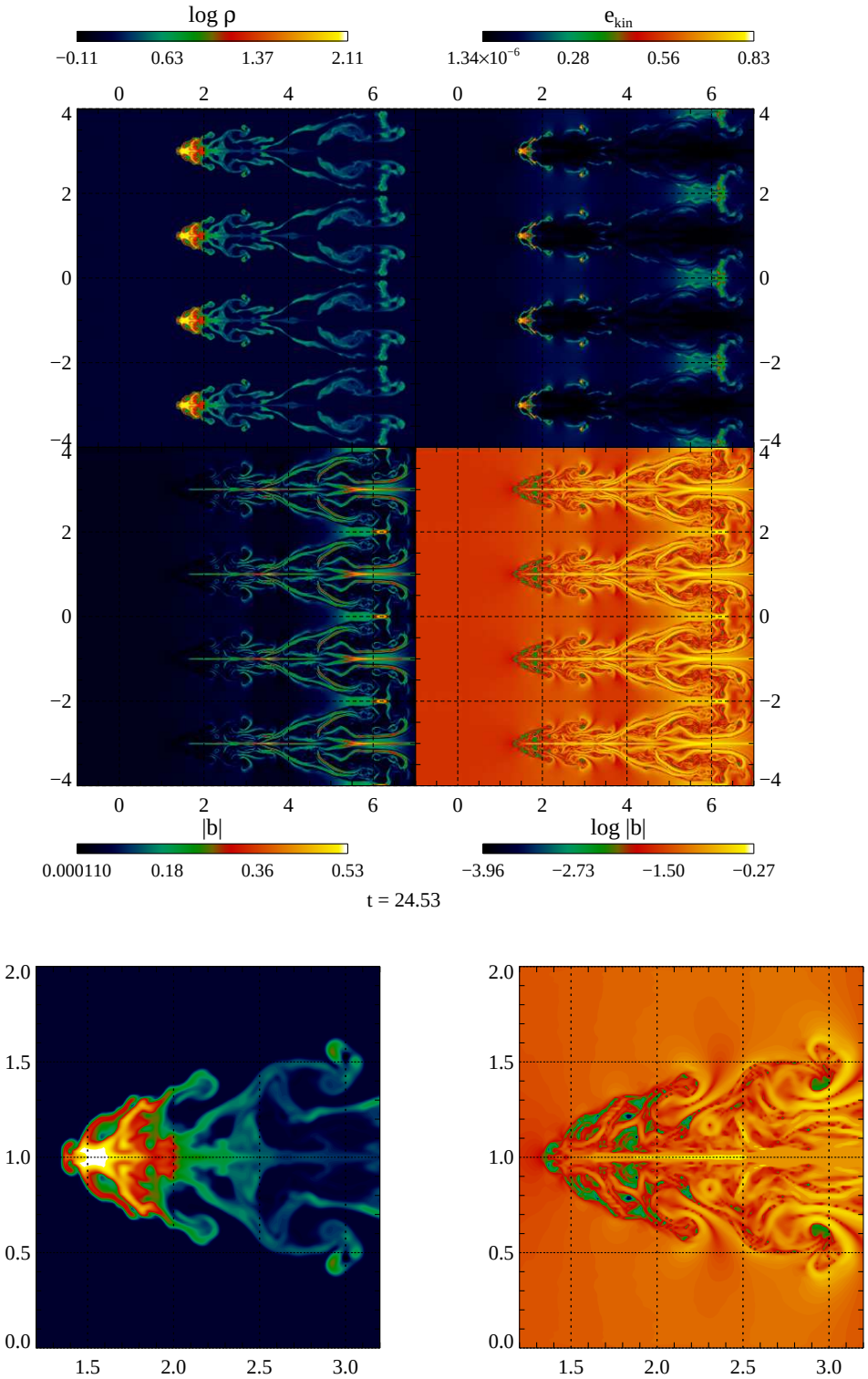

Figure 4.21: The wind tunnel test: flow at $t = 24.53$. The top panel shows (left to right, top to bottom) the gas density, the kinetic energy, the magnetic field strength, and the logarithm of the field strength. We plotted the flow pattern corresponding to a grid of blobs initially located at $(x;y) = (\ldots,-3,-1,1,3,\ldots;0)$. In the bottom panels, we show a close-up of the logarithm of the density (left) and the magnetic field (right) in the region $x \in [1.2,3.2]$, $y \in [0,2]$.

and $\nu = 2$ for cylindrical and spherical symmetry, respectively. The post-shock density, pressure, and velocity can be given in terms of the shock velocity $w = \partial_t \xi$,

$$\rho_1 = \frac{\gamma+1}{\gamma-1}\rho_0, \tag{4.19b}$$

$$P_1 = \frac{2}{\gamma+1}\rho_0 w^2, \tag{4.19c}$$

$$v_1 = \frac{2}{\gamma+1}w. \tag{4.19d}$$

We computed the Sedov solution both in axial and spherical symmetry. To compute the solutions, we used, however, our code in Cartesian geometry. To get the cylindrical solution, we set a circular region of pressure $P_1 = 10^5$ into the centre of a 2d grid, assuming symmetry along the third direction (z). For the spherical solution, we evolved the test on a 3d grid with the overpressure confined to a spherical region in the grid centre.

We used 3$^{\text{rd}}$-order Runge-Kutta time integration, the MUSTA(1)-HLL solver, and MP-5 reconstruction in the test. The grids had sizes of $m_x \times m_y = 400 \times 400$ (cylindrical explosion) and $m_x \times m_y \times m_z = 100 \times 100 \times 100$ (spherical explosion) covering the physical domains $(x,y) \in [-4,4]^2$ and $(x,y,z) \in [-1,1]^3$, respectively. The results of the 2d and 3d simulations are displayed in Fig. 4.22. They agree well with the analytic expressions. The shock wave is resolved sharply, and no oscillations are met. Despite the large jump in pressure, no instability occurs. The cylindrical/spherical symmetry of the problem is preserved well even though the problems are not evolved in coordinates adapted to the symmetry.

Weak magnetic fields We now perform the tests with the Kössl et al. (1990) settings, i.e., a 2d grid ranging from -1 to 1 in both directions, and an overpressure of $P_1 = 100$ in a region of radius 0.1. We used a grid of 150×150 zones and the same solvers as above.

When the magnetic field increases to a finite yet small (measured by the plasma β) value, the shock wave becomes slightly elongated in field direction since the field lines resist being bent by transverse fluid motion. For a stronger field, the fluid motion is essentially confined to the direction parallel to the field. In this direction, a multiple-shock structure emerges, whereas magneto-sonic waves are emitted in the perpendicular direction.

Our results show a good agreement with previous simulations, e.g., the ones by Kössl et al. (1990). The wave structures are resolved well and sharply, and the initial symmetry is preserved exactly (the asymmetries present in the figures are artefacts of the plotting rather than asymmetries of the data).

Extreme β – positivity of the internal energy We also try to evolve the system for very extreme values of β. For $P_0 = 1$ and $B_y = 10^5$, depicted in Fig. 4.24, the code is still able to ensure a physically sound evolution. Unphysical values of the internal energy appear only occasionally; apparently, the overriding of unphysical states within the MUSTA scheme suffices to prevent the evolution from becoming unstable.

We note that we can also handle more extreme magnetic fields (we tried $P_0 = 1$ and $B_y = 10^8$) in this way. The unmodified system fails when we set $P_0 = 10^{-5}$. Thus, $\beta \approx 2 \times 10^{13}$ in the outer regions. In this case, negative internal energies can only be avoided by corrections from the additional evolutionary equations for the partial energies. We choose to correct the total energy

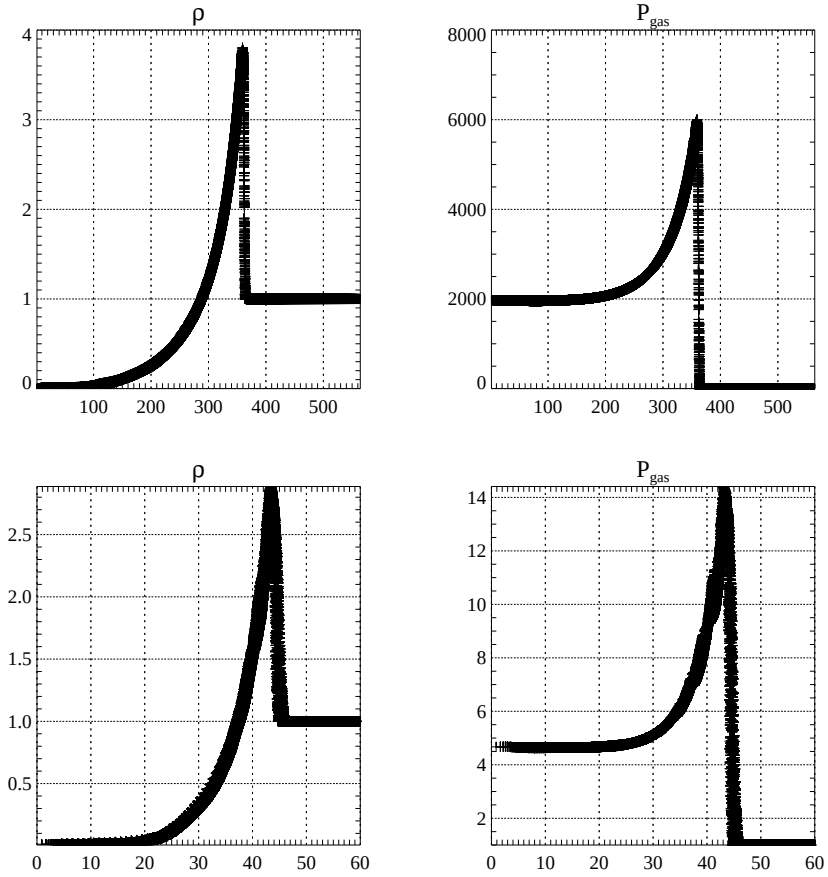

Figure 4.22: The results of the $2d$ at $t = 2$ (upper panels) and $3d$ at $t = 4$ (lower panels) Sedov test. The left and right panels show the density and the pressure as a function of distance from the centre of the explosion, respectively.

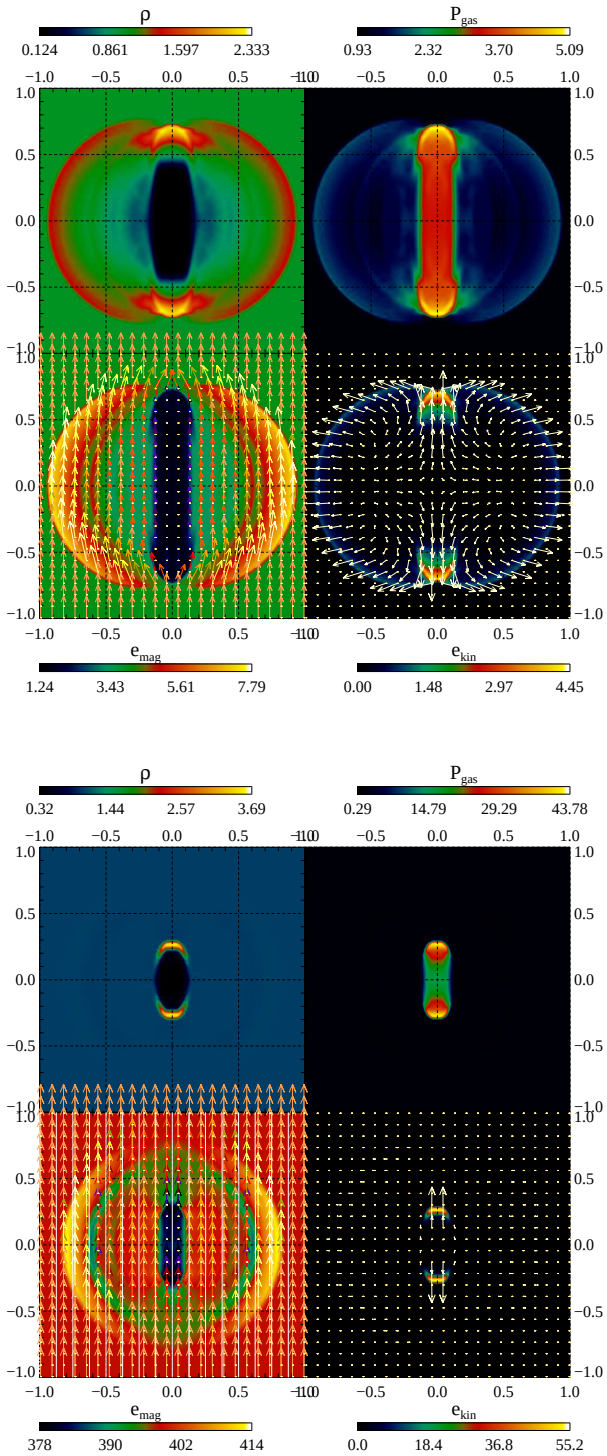

Figure 4.23: The Komissarov tests for $B_y = 10$ at $t = 0.16$ (top 4 panels) and $B_y = 100$ (bottom four panels) at $t = 0.025$. In each of the two groups of panels, the upper left and right ones, and the bottom left and right ones display colour-coded the gas density, gas pressure, magnetic energy density, and kinetic energy density. Additionally, in the bottom left panels, the magnetic field is represented by field vectors and field lines, and the bottom right panels show velocity field vectors. The colours of the vectors refer to their magnitude.

from the magnetic and kinetic energy, but only near zones where unphysical values of the internal energy occured (we applied the correction in a five-zone neighbourhood of a zone with unphysical MHD state). Using this scheme, we could evolve the system stably. Due to the corrections based on non-conserved partial energies, the total energy is only conserved up to a relative error of $\sim 10^{-10}$.

In these systems, the dynamics of the gas is fairly slow compared to the time scale set by Alfvén waves. We can setup a more dynamic situation by allowing for a large explosion energy, i.e., by increasing P_1. We set $P_{0,1} = 1, 10^5$ and $B_y = 10^5$. In this test, we corrected the total energy from the magnetic and kinetic partial energies in and near cells where the internal energy was negative. The relative error in total energy caused by this procedure is of the order of 10^{-8}.

4.2 Radiative transfer

We validated our implementation of the TMT system of RT on a number of standard tests proposed by Pons et al. (2000). These problems assess the performance of the scheme in the diffusion and free-streaming limits as well as in the intermediate regime. Note that we set $c = 1$ in all of these tests.

All of the Pons et al. (2000) tests are performed in spherical symmetry. They involve radiation propagating through a static background fluid at rest. No specific physical model is assumed for the radiation. The matter interacts with radiation only via isotropic scattering, and the opacities χ are pre-defined functions of radius, depending neither on any fluid nor on any radiation property. Hence, there is no need for a energy-dependent treatment of the radiation, and a single grey TMT system suffices to catch all physics.

Thus, the equations to be solved including geometric and interaction source terms read:

$$\partial_t \mathfrak{E} + \frac{\partial (r^2 \mathfrak{F})}{\partial r^3/3} = 0, \tag{4.20a}$$

$$\partial_t \mathfrak{F} + \frac{\partial (r^2 \mathfrak{P})}{\partial r^3/3} = -\chi \mathfrak{F} + \frac{\mathfrak{E} - \mathfrak{P}}{r}. \tag{4.20b}$$

To solve the Eqn. (4.20) numerically, we employ 2^{nd}-order Runge-Kutta time stepping, the MUSTA(1)-HLL solver, and high-order (WENO-4) reconstruction. We test different closure relations. To treat the diffusion limit correctly, we apply alternatively the Jin et al. (2000) or the Jin & Levermore (1996) schemes as described in Sect. 3.2.1. We found that both schemes suffice to enforce the correct diffusive limit stably and without affecting the hyperbolic limit. They should, however, not be used in combination in order to avoid incorrect diffusion in the transition regime between the hyperbolic and parabolic schemes around $\mathrm{Pe} = 1$.

Diffusion limit We assume a constant opacity such that the optical depth is large and the system is in the diffusion limit. We set up a uniform radial grid covering a radial domain $r \in [0, 1]$ and take two opacities, $\chi = 100, 10^5$, corresponding to $\tau = 100, 10^5$. We used the polynomial Monte-Carlo closure relation, but the results do not depend on this choice since all closures correctly fulfil the diffusion constraint $\mathfrak{P} = \frac{1}{3}\mathfrak{E}$ in the diffusion limit.

The test simulates the outward diffusion of radiation energy described by a Dirac δ peak in the grid centre at $t = 0$. The problem has an analytic solution for $t > 0$ which we use to construct the

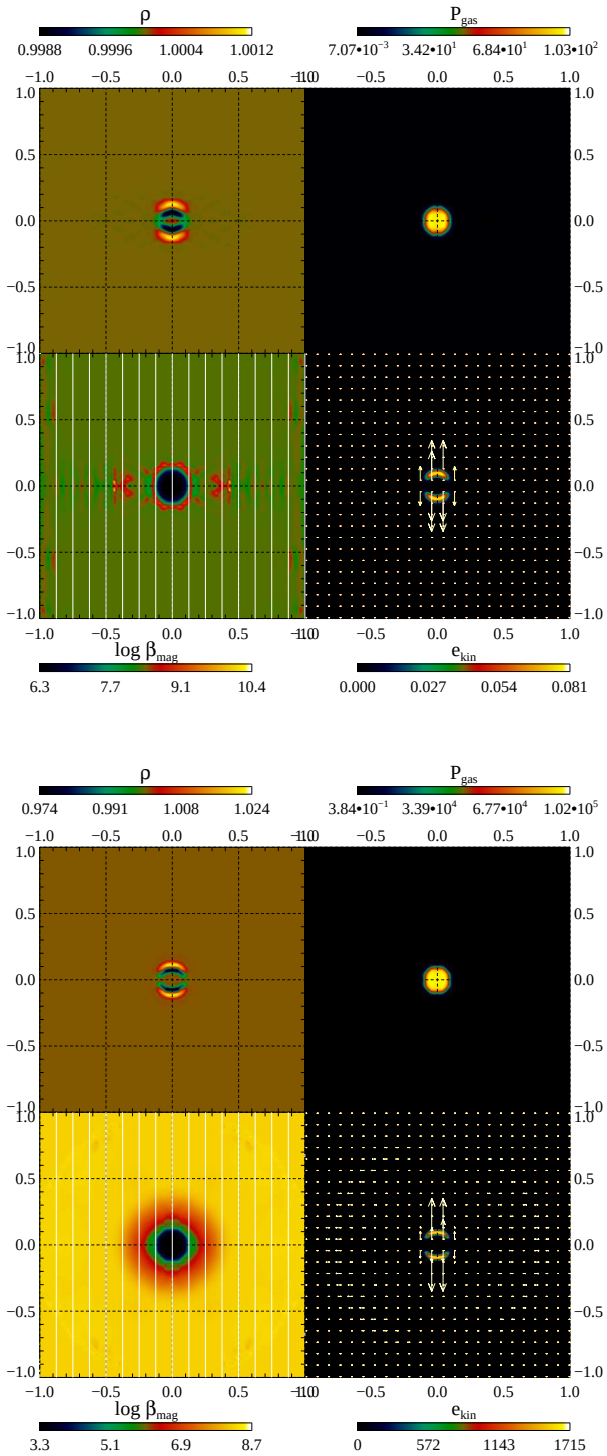

Figure 4.24: The Komissarov tests for $P_{0,1} = 1, 100$ and $B_y = 10^5$ at $t = 2.5 \times 10^{-4}$ (top 4 panels), and $P_{0,1} = 1, 10^5$ and $B_y = 1$ (bottom four panels) at $t = 2.5 \times 10^{-5}$. In each of the two groups of panels, the upper left and right ones, and the bottom left and right ones display colour-coded the gas density, gas pressure, β_{mag}, i.e., the ratio of magnetic pressure to gas pressure, kinetic energy density. Additionally, in the bottom left panels, the magnetic field is represented by field lines, and the bottom right panels show velocity field vectors. The colours of the vectors refer to their magnitude.

In first simulation, we did not resort to any non-conservative extensions of the MHD system, but the more extreme conditions in the second test required us to employ corrections to the total energy based on the equation for the (non-conserved) magnetic energy density.

initial data, and to verify our numerics:

$$\mathfrak{E}(r,t) = \left(\frac{\chi}{t}\right)^{3/2} \exp\left(-\frac{3\chi r^2}{4t}\right), \tag{4.21a}$$

$$\mathfrak{F}(r,t) = \frac{r}{2t}\mathfrak{E}(r,t). \tag{4.21b}$$

Moderate diffusion We discuss the case $\chi = 100$. The initial time is $t_0 = 1$. Depending on the grid size $m_r \sim 100$, the Peclet number is of order unity. Thus, we can run this test using the purely hyperbolic scheme (Pe $\lesssim 1$, i.e., $m_r \gtrsim 100$) or applying the parabolic modifications (for coarser grids).

By varying the radial resolution around the critical value, $\mathrm{Pe_c} = 1.2$, we can study the transition from the hyperbolic to the parabolic regime. The results are shown in Fig. 4.25.

For $m_r = 200$ and Pe $= 0.5$, the purely hyperbolic scheme is applied. We find a very good agreement between the numerical solutions and the analytic ones. For $m_r = 40$ (Pe $= 2.5$), the scheme fully relies on the parabolic terms. In this case, the analytic solution is reproduced evenly well.

Both results are not unexpected. A more intricate regime is the transition between the two schemes, at intermediate Pe. We have to ensure that no artefacts are produced by the gradual "switching" from one scheme to the other one. We consider values around $m_r = 80 \Leftrightarrow$ Pe $= 1.25$. The weight of the parabolic terms is $\Xi \approx 0.57$. The scheme also performs well in this intermediate regime, and the transition between the two methods of evolving the flux appears to be very smooth; the correct analytic solution is reproduced very well for all tested grids.

Extreme diffusion For $\chi = 10^5$, the Peclet number is larger than unity for any reasonably large grid. We used $m_r = 100$, i.e., Pe $= 10^3$, to simulate this test. Our results for initial data taken from the analytic solution at $t = 200$ are shown in Fig. 4.26. Using the modifications to accommodate to the parabolic limit, out code passes the test without any problems. We note that the standard hyperbolic scheme fails here due to the stiffness of the system.

Validity of the hyperbolic scheme Using the unmodified hyperbolic scheme, we simulated the same problem as above for different Peclet numbers to determine the maximum Pe the scheme can handle without the Jin et al. (2000) corrections. As expected, we cannot go significantly beyond Pe $= 1$ without encountering instability; Pe $= 1.2$ appears to be feasible.

Free streaming We now present tests of the opposite limit of vanishing opacity $\chi = 0$, i.e., optical depth $\tau = 0$. In this case, the free-streaming limit is valid, and the pressure tensor is given by $\mathfrak{P} = \mathfrak{E}$.

Following Pons et al. (2000), we simulate the propagation of a Gaussian wave from the grid centre outwards. The analytic solution is

$$\mathfrak{E}(r,t) = \frac{1}{r^2}\exp[-(r-t)^2], \tag{4.22a}$$

$$\mathfrak{F}(r,t) = \mathfrak{E}(r,t). \tag{4.22b}$$

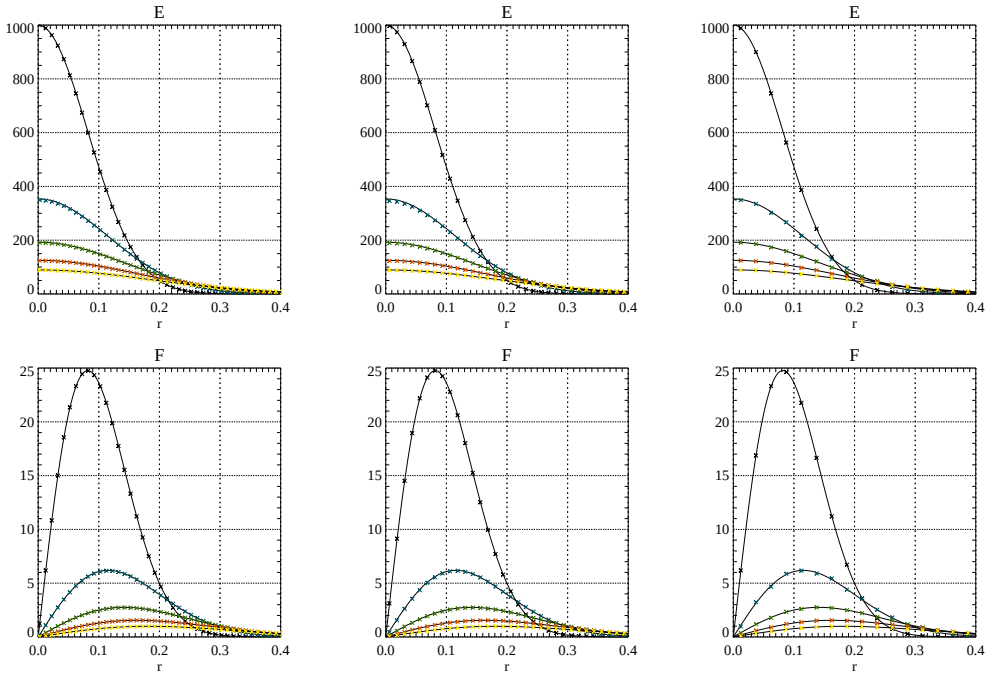

Figure 4.25: The results of the moderate diffusion ($\chi = 100$) test from Pons et al. (2000). The top and bottom panels show the energy density and the energy flux, respectively. In each panel, we compare the analytic solution (black solid lines) with the numerical result (symbols) at $t = 1$ (initial data; black), $t = 2$ (blue), $t = 3$ (green), $t = 4$ (red), and $t = 5$ (yellow). The left panels correspond to $m_r = 200$, i.e., a solution obtained by the purely hyperbolic scheme (for clarity, not all grid cells are represented by symbols). The middle row corresponds to $m_r = 80$, in the transition between hyperbolic and parabolic treatment of the TMT system, and the right panels show $m_r = 40$, i.e., a computation with the parabolic modifications.

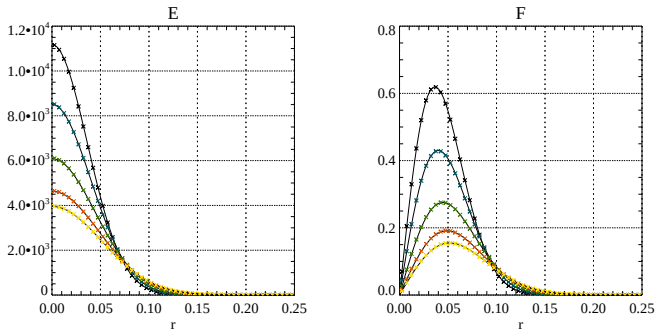

Figure 4.26: The extreme diffusion test, $\chi = 10^5$. We used a grid of $m_r = 100$ zones for the simulations. We compare our numerical results (symbols) to the analytic solution (solid black line). The different colours refer to different time steps: black, blue, green, red, and yellow symbols show the solution at $t = 200$ (initial data), $t = 240$, $t = 300$, $t = 360$, and $t = 400$, respectively.

The physical domain stretches from $r = 0.2$ out to $r = 10.2$ and is covered by $m_r = 200$ grid cells. We start the evolution at $t = 2.5$.

As in the previous test, the closure is constrained by the limit (now free streaming rather than diffusion) and hyperbolicity requirements. Thus, there is no major influence of the closure relation applied. We again selected the Monte-Carlo closure. The results are displayed in Fig. 4.27. The analytic solution is reproduced with high accuracy. Comparing different reconstruction techniques, we again note a superiority of the high-order methods w.r.t., e.g., PLM schemes.

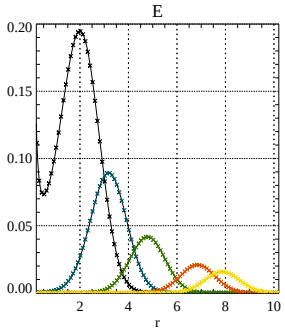

Figure 4.27: The free-streaming problem: energy as a function of radius for 5 different times: the numerical solution at $t = 2.5, 3.5, 5, 7, 8$ is shown by the black, blue, green, red, and yellow symbols, respectively, and the analytic results for the same times are shown by the solid black lines. For clarity, not all grid cells are represented by symbols.

Radiating sphere We turn to the problem of a sphere radiating isotropically into vacuum, i.e., into a surrounding region of vanishing opacity. The initial and boundary conditions are given by Pons et al. (2000), as well as an analytic solution of the problem.

We simulate the radiation propagation in the vacuum around the sphere (radius $R = 1$). Our numerical grid covers the inner part of the vacuum, extending from $r_{\min} = R$ to $r_{\max} = 20$, and consists of $m_r = 200$ zones. We set the energy density and flux through the interior boundary to $\mathfrak{E}(R;t) = 2t$, and $\mathfrak{F}(R;t) = 0.5\mathfrak{E}(R;t)$, respectively, i.e., the analytic solution given by Pons et al. (2000) applies with $C = 1$. We show results of our simulations for different times in Fig.4.28. We used the Monte-Carlo closure in the simulations depicted here, but confirmed that there is only little difference between the limiters as observed by Pons et al. (2000). We find a good agreement between the analytic and numeric solutions, but note – similar to the results of Pons et al. (2000) – a slight increase of the energy density and flux in the numerical simulation.

Radiative heating and cooling In the next set of tests, we follow the diffusion of radiation through an opaque medium ($\chi = 100$). We start with the solution describing the stationary diffusion of radiation of a constant luminosity $\mathfrak{L} = 4\pi r^2 \mathfrak{F}(r)$:

$$\mathfrak{E}(r) = \frac{\mathfrak{L}}{4\pi}\left[\frac{1}{R^2} + 3\chi\left(\frac{1}{r} - \frac{1}{R}\right)\right], \tag{4.23a}$$

$$\mathfrak{F}(r) = \frac{\mathfrak{L}}{4\pi r^2}, \tag{4.23b}$$

where R (here $R = 12$) is the outer radius of the sphere. Following Pons et al. (2000), we set $L = 4\pi$.

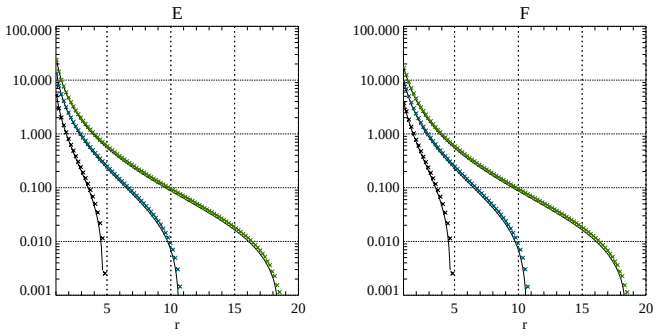

Figure 4.28: A comparison of numerical (symbols) and analytic (solid lines) results for the radiating-sphere test problem: the energy density (left panel) and flux (right panel). We show the solutions for $t = 4$ (black), $t = 10$ (blue), and $t = 18$ (green). Only every second of the grid zones is represented by a symbol.

We add a radiation source according to one of the following prescriptions:

1. No source at all. In this case, the radiation energy should diffuse outwards.
2. A central point source, represented by a finite luminosity $\mathfrak{L}_1$ through the inner boundary (at $R_{\rm min} = 1$. We set $\mathfrak{L}_1 = 10\mathfrak{L}$. As a consequence, additional energy is pumped into the medium, leading to an increasing E inside the sphere until the new radiative equilibrium, described by Eqn. (4.23) for $\mathfrak{L} = \mathfrak{L}_1$, is reached.
3. A shell source at a finite radius $R_{\rm s} = R_2$. The resulting equilibrium radiation field, attained for $t \to \infty$, is twofold: in the interior ($r < R_{\rm s}$), the luminosity is zero, and the energy density is constant, whereas outside of the shell, we recover the situation of outward diffusion at constant luminosity.

We show the numerical results for the three cases in Figs. 4.29 – 4.31. In the simulations, we used a grid of $m_r = 200$ zones uniformly distributed between $R_{\rm min} = 1$ and $R = 12$.

We reproduce the results from the first test (diffusion without source) as shown by Pons et al. (2000) very well: the radiation diffuses out in accordance with their results (Fig. 4.29). We only find a different behaviour of the luminosity at the outer grid boundary which we attribute to different formulations of the outer BCs. This only affects a few zones near the edge of the grid without influencing the rest of the domain significantly.

If we switch on a central point source of luminosity $\mathfrak{L}_1 = 10\mathfrak{L}_0$, the transformation of the diffusive profile to one corresponding to $\mathfrak{L}_1$ occurs in good agreement with the simulations of Pons et al. (2000) (Fig. 4.30). At the end of our simulations, the radiation field has reached a state of nearly constant luminosity $\mathfrak{L}_1$.

The final test problem of this set was simulated with a shell source at a radius of $R_2 = 6$. Our code correctly reproduces the transition to a stationary state of zero luminosity inside R_2 and constant luminosity outside R_2 (Fig. 4.31). The two states are separated by a well-resolved sharp discontinuity at R_2.

A more complex example Pons et al. (2000) considered a more complex structure as a toy

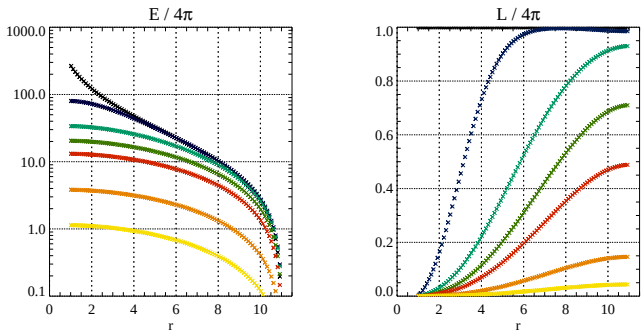

Figure 4.29: Radiative heating and cooling without any energy sources. The left and right panels show the energy and the luminosity (in units of 4π) at seven different times: $t = 0$ (black symbols), $t = 507$ (blue), $t = 2028$ (light green), $t = 3492$ (dark green), $t = 5014$ (red), $t = 9520$ (orange), and $t = 14000$ (yellow).

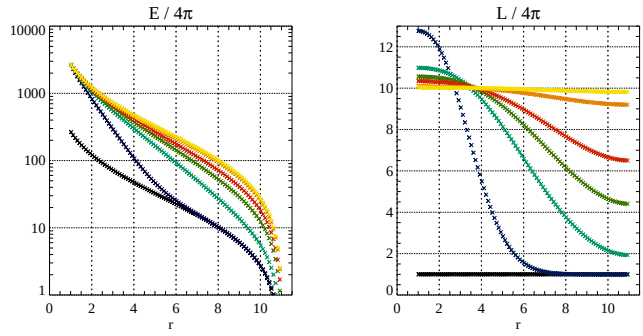

Figure 4.30: Radiative heating and cooling with a central energy source of luminosity $L = 40\pi$. The left and right panels show the energy and the luminosity at seven different times: $t = 0$ (black symbols), $t = 504$ (blue), $t = 2016$ (light green), $t = 3473$ (dark green), $t = 4985$ (red), $t = 9523$ (orange), and $t = 14000$ (yellow).

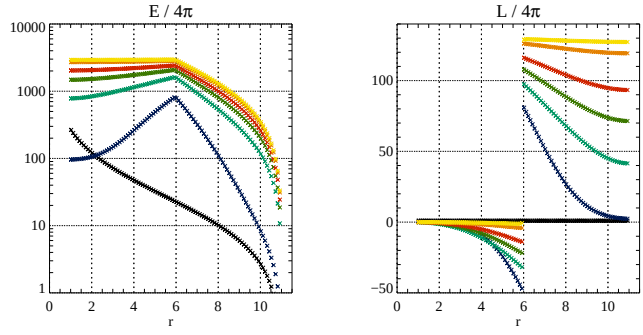

Figure 4.31: Radiative heating and cooling with a shell source at radius $r = 6$. The left and right panels show the energy and the luminosity at seven different times: $t = 0$ (black symbols), $t = 504$ (blue), $t = 2016$ (light green), $t = 3473$ (dark green), $t = 4985$ (red), $t = 9523$ (orange), and $t = 14000$ (yellow).

model for a star: an opacity profile of the form

$$\chi(r) = \begin{cases} \chi_0 & \text{if } r \leq 1, \\ \chi_0 / r^\alpha & \text{if } 1 < r \leq 10, \\ 0 & \text{if } 10 < r \leq 15, \\ \chi_0 & \text{if } 15 < r \leq 17, \\ 0 & \text{if } 17 < r \end{cases} \tag{4.24}$$

where $\chi_0 = 1000$ and $\alpha = 2$. For the initial data, we set $\mathfrak{E} = 1$ inside the star, i.e., for $r \leq 10$, $E = 10^{-6}$ outside, and $F = 0$ everywhere. The rationale for this opacity profile is to mimic an opaque stellar core surrounded by an envelope of decreasing opacity and a transparent circumstellar region. In this region, we set an optically thick "cloud". The combination of opaque, transparent and intermediate regions makes this test particularly useful to probe the validity of our RT scheme throughout these different regimes. As stated by Pons et al. (2000), the test illustrates the ability of the method to handle cases in which FLD methods may beset with problems.

The results of our simulations of this test are shown in Fig. 4.32. We compare three different closure relations: the Monte-Carlo, the Minerbo, and the M1 models. All three give similar results in good agreement with those presented by Pons et al. (2000) with Kershaw's closure.

We additionally simulated the test with a steeper opacity gradient in the envelope, $\alpha = 4$ (Fig. 4.33). The optical depth of the envelope is now $\tau = 333$ rather than $\tau = 900$ for $\alpha = 2$. In this case, the radiation leaks out faster through this region, with larger flux factors $\mathfrak{f} = \mathfrak{F}/c\mathfrak{E} \sim 0.6$ close throughout the entire evolution – using standard parameters, $\mathfrak{f}$ is large in the initial phase but drops to approximately zero later. In the free-streaming region ($10 < r \leq 15$), f approaches unity whereas it is small for $\alpha = 2$ except in the first stages of the evolution. The radiation, streaming out of the star much more rapidly eventually hits the cloud acting as a bottleneck. The highly opaque region ponds the radiation flow leading to a rapid increase of the energy density, and the flux factor drops to zero as the energy diffuses out. In this simulation, the Peclet number becomes unity for $r \approx 3.4$. At this point, our scheme gradually switches between hyperbolic and diffusive fluxes. We do not observe any impact of this transition on the radiation field: both $\mathfrak{E}$ and $\mathfrak{F}$ vary continuously across this region.

4.2.1 Radiation hydrodynamics

We now turn to a more complex situation: simulations of stellar core collapse and post-bounce evolution with both hydrodynamics and neutrino transport, i.e., the full RHD scheme. In these simulations, we, however, do not seek to answer the fascinating questions regarding the SN mechanism, but rather have in mind a technical and far less fundamental issue: how does our code behave in this case, with strong gravity, a complex EOS, collapse, a strong shock, and complicated neutrino-matter reactions?

Physics of our simulations Since the exact details of the evolution are not our prime interest, we reduced the complexity of the problem by only considering electron neutrinos and antineutrinos, and by restricting ourselves to the grey RT system.

We used the Minerbo closure and included the following neutrino-matter reactions:

1. nucleon absorption,

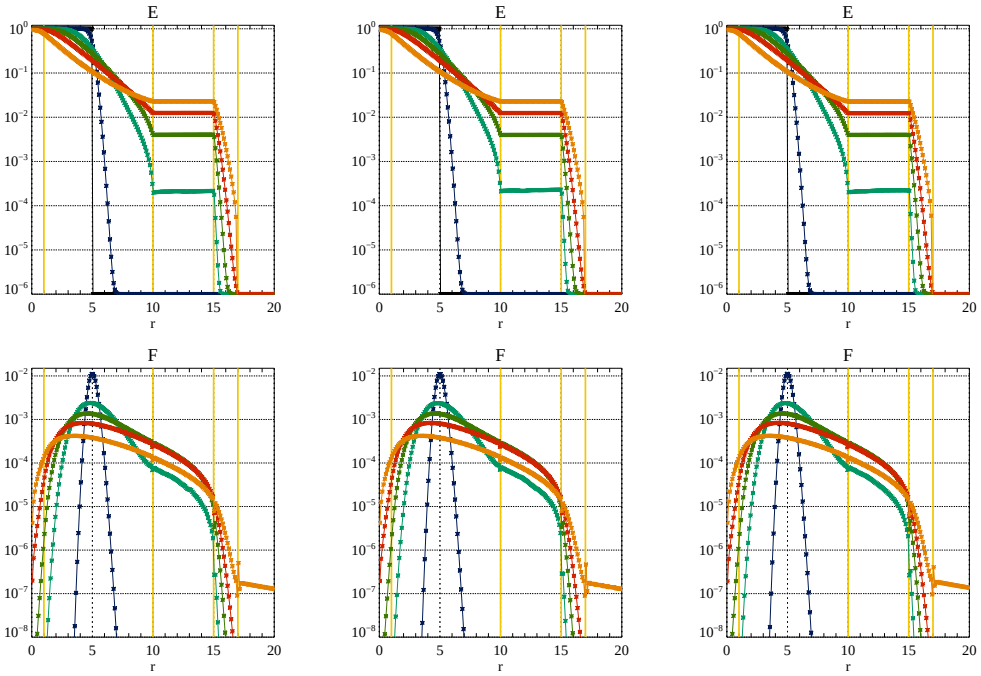

Figure 4.32: The stellar toy model of Pons et al. (2000). We show the energy density (top panels) and the flux (bottom panels) for different times: black, blue, light green, dark green, red, and orange correspond to $t \sim 0, 5, 100, 250, 500$, and 100, respectively. The regions of different opacity are marked by the yellow vertical lines at $r = 1, 10, 15, 17$. The left, middle, and right panels show the results using the Monte-Carlo, the Minerbo, and the M1 closure, respectively.

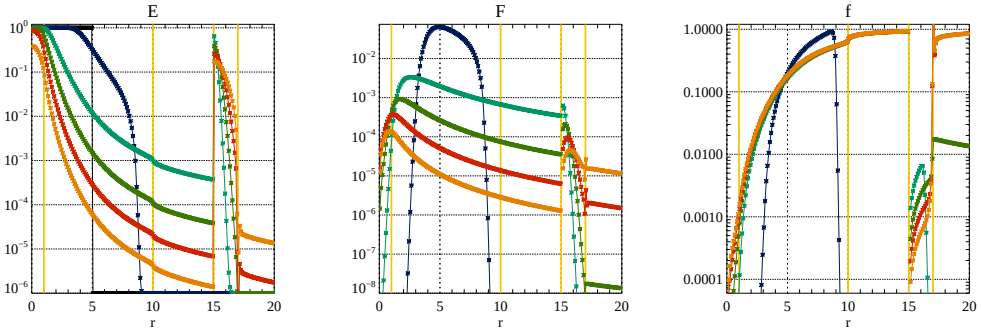

Figure 4.33: The stellar toy model with reduced opacity in the envelope: results from a simulation using the Monte-Carlo closure. We show the energy density (left panel), flux (middle panel), and the flux factor (right panel) for $t = 0$ (black), $t \approx 4$ (blue), $t \approx 100$ (light green), $t \approx 250$ (dark green), $t \approx 500$ (red), and $t = 1000$ (orange). The vertical yellow lines denote the boundaries of the stellar core ($r = 1$), envelope ($r = 10$), and the inner and outer boundaries of the cloud ($r = 15, 17$).

2. nucleon scattering,
3. nuclear scattering,

described by the reaction rates from Cernohorsky & van Weert (1992). To compute the grey source terms, we integrated the differential rates over an assumed Fermi-Dirac spectrum of the neutrinos.

We simulated a star of main-sequence mass $M = 40\,M_\odot$ and solar metalicity evolved up to the immediate pre-collapse state by Woosley et al. (2002). We used Newtonian gravity and the Shen EOS. We used a grid of $m_r = 500$ zones spaced logarithmically in radius from the centre of the star out to $R \approx 10^4\,\mathrm{km}$. The grid spacing was $(\delta r)_{\min} \approx 500\,\mathrm{m}$ in the centre and $(\delta r)_{\max} \approx 160\,\mathrm{km}$ in the outermost regions. The outer boundaries were set to outflow.

Results The main result is that we are able to simulate the collapse and post-bounce evolution of such a star. Even without detailed spectral transport and interactions, we can reproduce certain general features of more detailed simulations, in particular the lack of a prompt explosion.

We show the initial radial profile of various HD and neutrino variables in Fig. 4.34. The central density is $\rho_c \approx 3.8 \times 10^{10}\,\mathrm{g\,cm^{-3}}$, and the gas is already in infall since the adiabatic index in most of the gas is $\Gamma \lesssim 1.317$, i.e., below the critical value for stability, $\Gamma_{\mathrm{crit}} = \frac{4}{3}$. The gas is still fairly electron rich, with $Y_e > 0.44$ in the entire star. We compute the neutrino field at this point by assuming LTE between radiation and matter, and start with a very small initial flux. Thus, the neutrino variables at this time are only very artificial initial states; due to the reactions with matter, they soon evolve to a more meaningful state. We can see this at a later time, $t = 46.9\,\mathrm{ms}$ (Fig. 4.35). The HD profiles have changed only little. Neutrinos created in the centre by emission reactions leave the core nearly freely. Because the deleptonisation reactions produce ν_e rather than $\bar{\nu}_e$, the neutrino energy is predominantly in electron neutrinos with only very little contribution of antineutrinos.

We proceed to a later stage in collapse, $t = 211.1\,\mathrm{ms}$ (Fig. 4.36). The central density is now $\rho_c \approx 1.4 \times 10^{11}\,\mathrm{g\,cm^{-3}}$. The inner core falls now homologously, i.e., $v_r \propto r$; the maximum infall velocity is now supersonic. Still, the collapse is adiabatic, as can be seen by the entropy which is nearly unchanged from the initial state. The electron fraction in the centre has decreased to $Y_e \approx 0.4$ due to radiation of neutrinos.

During the following stages of collapse, Y_e continues to decrease. At the time of shock formation ($t \approx 228.8\,\mathrm{ms}$, Fig. 4.37), it is as small as 0.2 in the centre. In the post-shock region, the opacity is now very large, and the radiation has to diffuse out slowly: neutrino-trapping conditions are reached in the increasingly dense (ρ has reached nuclear-matter density) and hot (T exceeds 10 MeV behind the shock) environment. The Peclet number is now far beyond unity, and the total optical depth of the inner core is $\tau \sim 7 \times 10^4$. The shock wave propagates outwards, but is slowed down by energy losses until it stalls at $r \approx 150\,\mathrm{km}$ (Fig. 4.38 shows the state at $t = 254.6\,\mathrm{ms}$). The post-shock velocity is negative; no prompt explosion occurs. The central electron fraction has stabilised at a value of $Y_e \approx 0.2$, but we find a depletion of electrons in the immediate post-shock region. The inner core has a stable entropy profile and is heated up to $T \gtrsim 11\,\mathrm{MeV}$. We followed the further evolution of the model up to $t \approx 332.1\,\mathrm{ms}$, i.e., 100 ms post bounce (Fig. 4.39). Apart from the accretion of gas through the standing accretion shock, not much happens during this epoch.

Finally, we show the total neutrino luminosity at different times (Fig. 4.40) around bounce. The different curves show the increase of the luminosity during collapse and the breakout of an intense neutrino burst shortly after bounce as the shock reaches less dense and, hence, less opaque material. In the later stages, the luminosity outside the shock is roughly constant with radius.

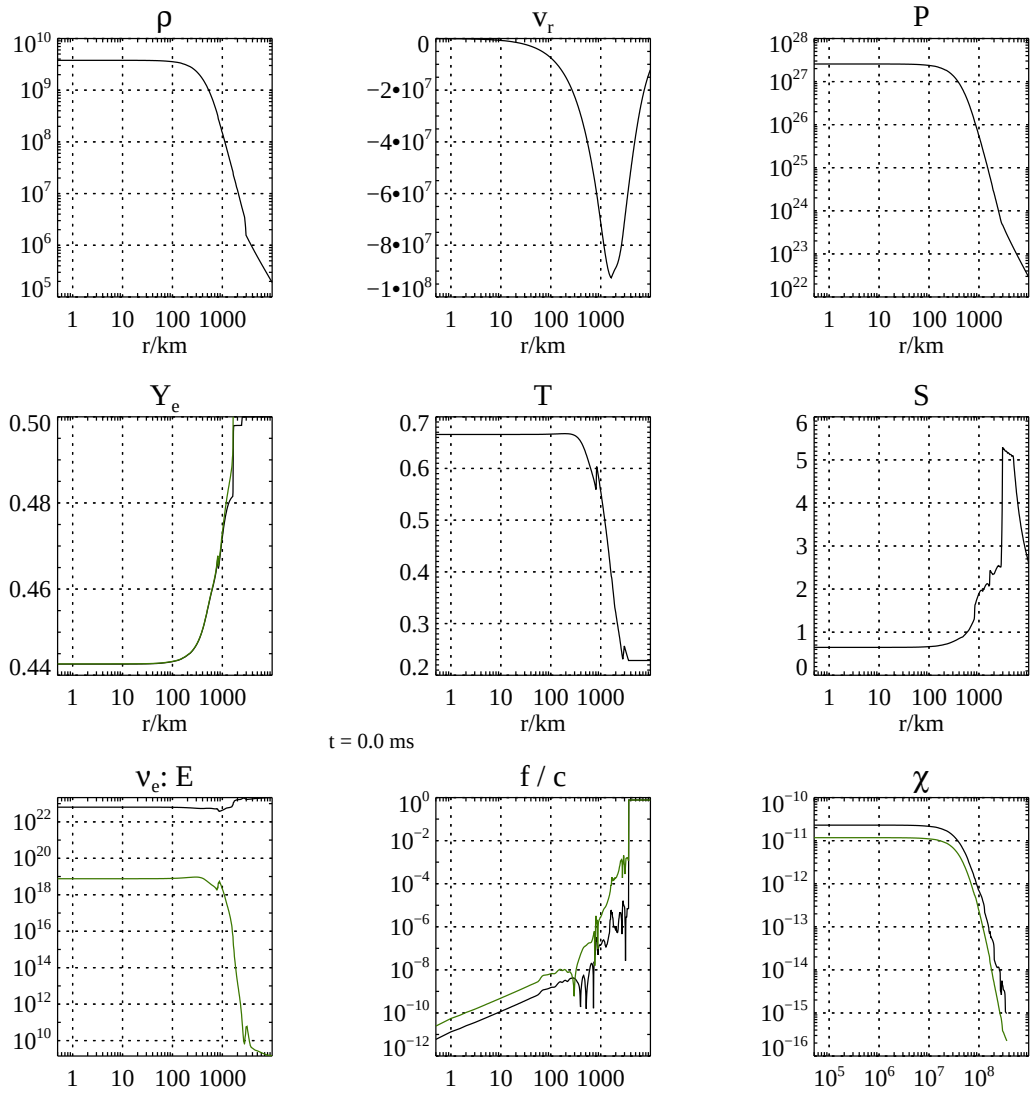

Figure 4.34: Radial profiles of the collapsing core of a star of $40M_\odot$: initial data at $t = 0$. The top panels display the density (left), radial velocity (middle), and pressure (right). In the v_r plot, additional lines may indicate the sound speed c_S and its negative (these lines are off the scales for $t = 0$, but may be visible in later plots). In the middle row, the left panel shows the electron fraction Y_e by a black line and the total lepton fraction Y_l (i.e., the net fraction of electrons and electron neutrinos) by a green line; in the middle and right panels, the temperature (in MeV) and entropy are plotted. The bottom panels display different neutrino variables: the energy density (left), flux factors (middle), and opacities (right) of electron neutrinos and antineutrinos. We distinguish between ν and $\bar{\nu}$ by colour: black and green lines represent ν and $\bar{\nu}$, respectively. In the plot of the flux factors, we show negative values of f by dashed lines.

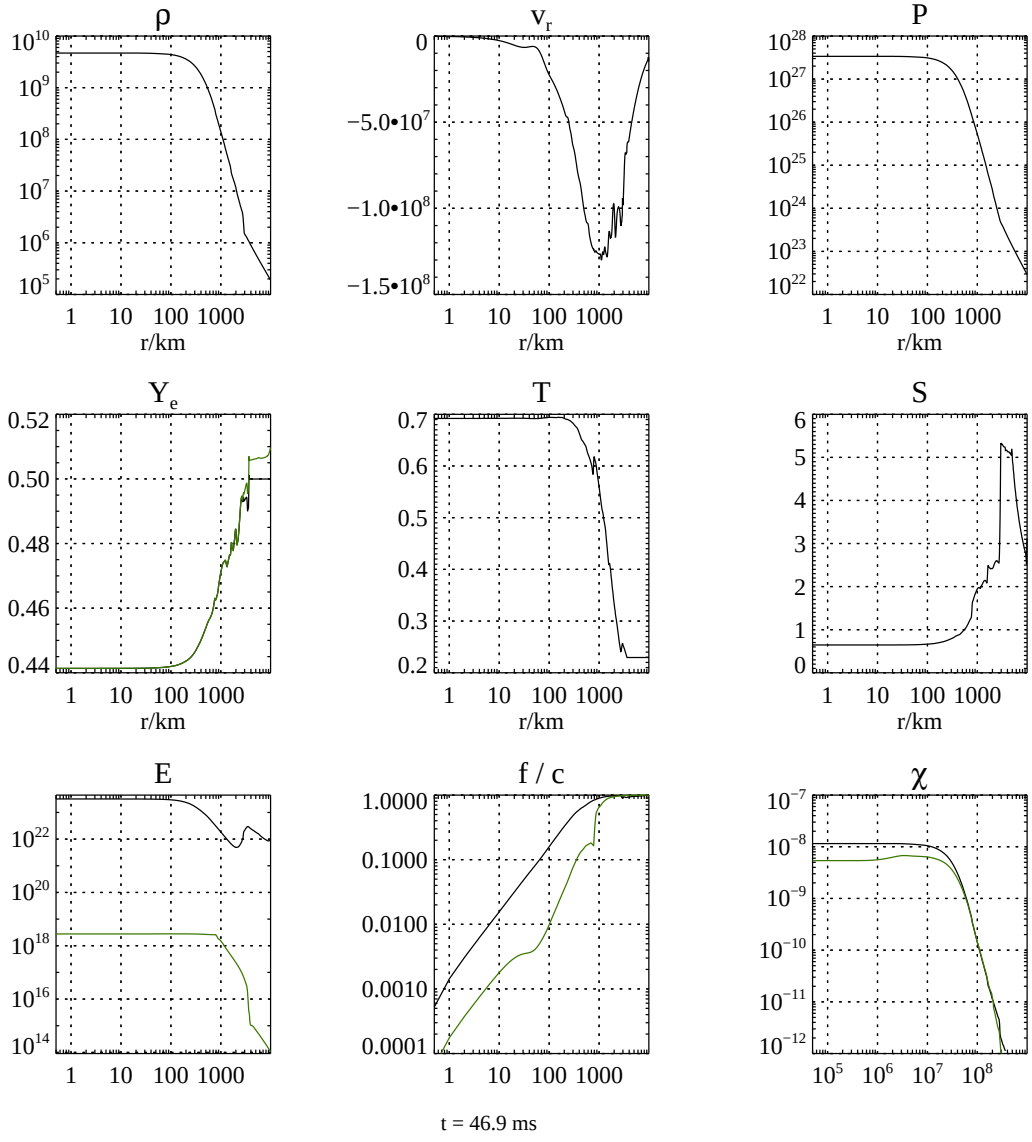

Figure 4.35: Same as Fig. 4.34, but for $t = 46.9\,\mathrm{ms}$. Time is sufficiently advanced for the neutrino field to depart from the artificial initial data towards a state consistent with the gas thermodynamics.

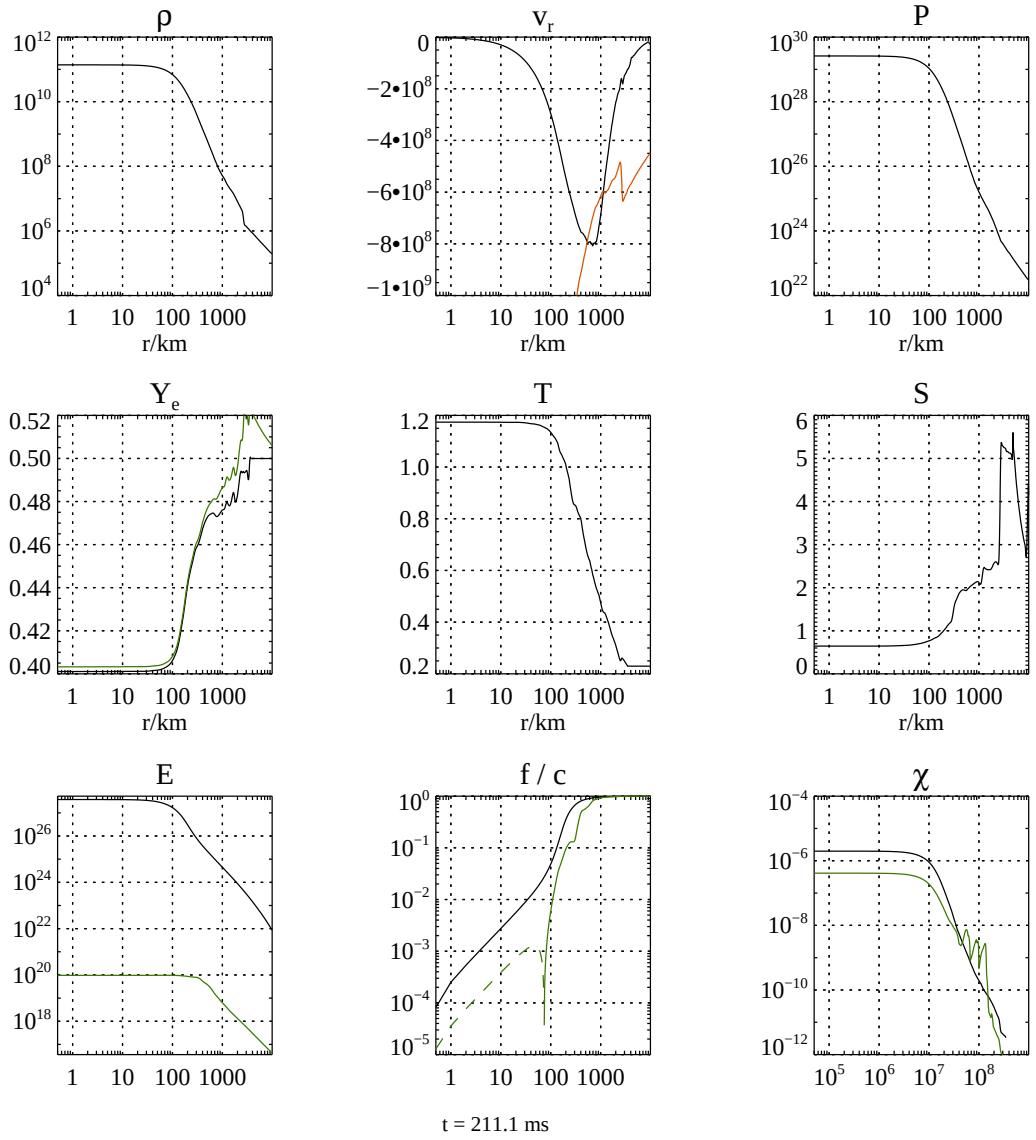

Figure 4.36: Same as Fig. 4.34, but for $t = 211.1\,\mathrm{ms}$. The infall profile is homologous, and the electron fraction decreases due to deleptonisation reactions; neutrinos still stream out freely.

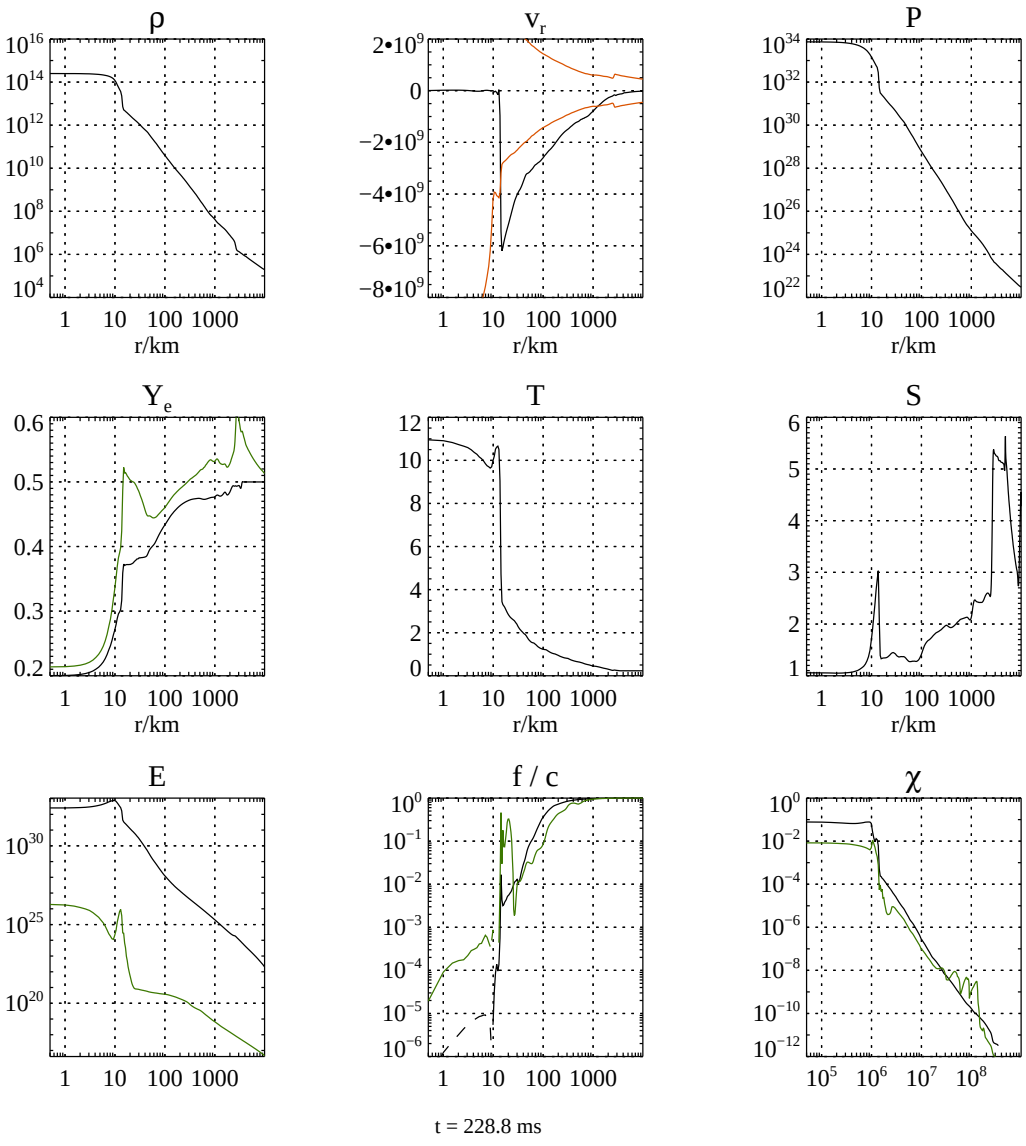

Figure 4.37: Same as Fig. 4.34, but for $t = 228.8\,\mathrm{ms}$. Neutrino trapping has already set in, and shock formation is about to occur. A hot, dense inner core has formed behind the shock, with an electron fraction of only 0.2 in the centre.

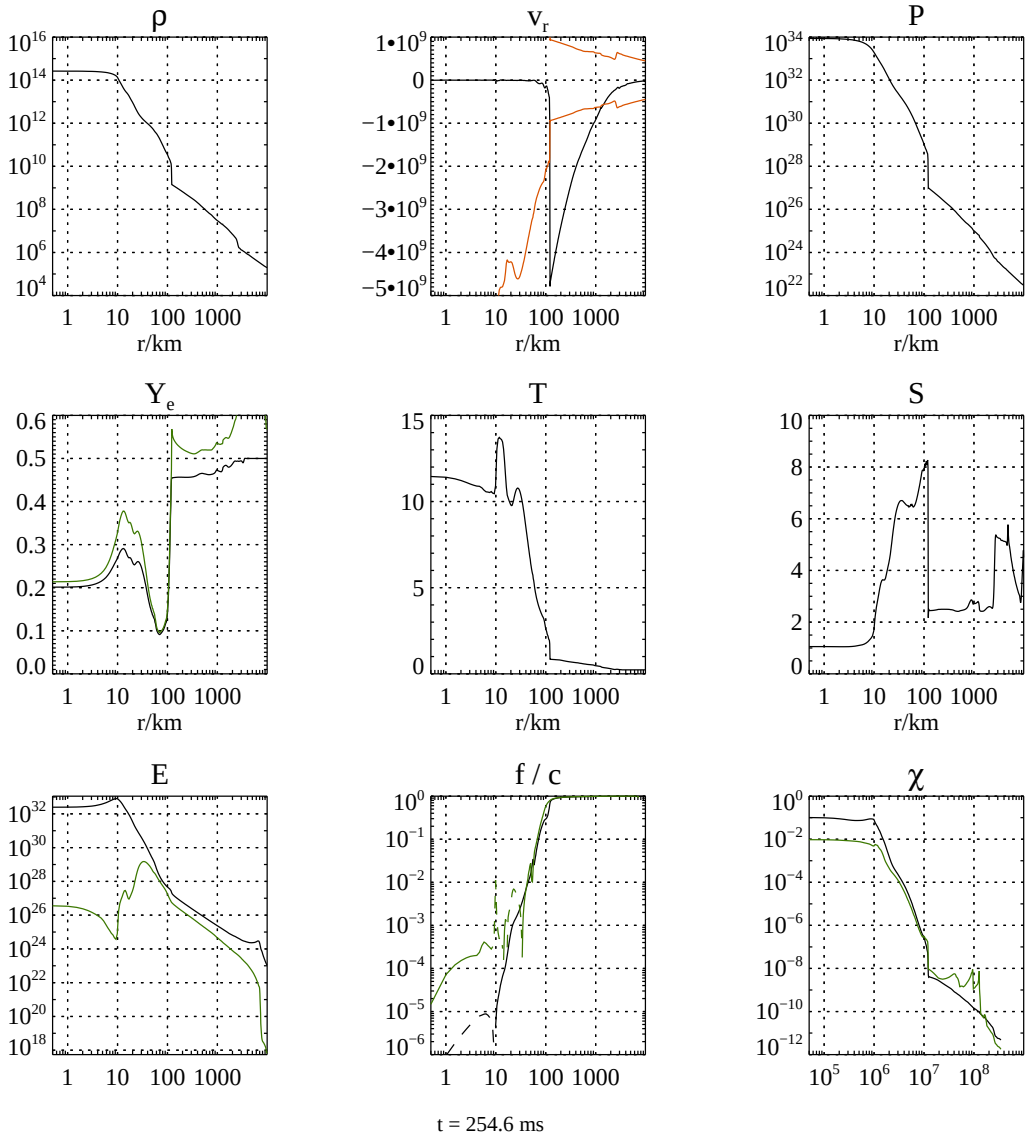

Figure 4.38: Same as Fig. 4.34, but for $t = 254.6\,\mathrm{ms}$. The shock stalls at $r \approx 150\,\mathrm{km}$, and the thermodynamic state of the inner core has stabilised.

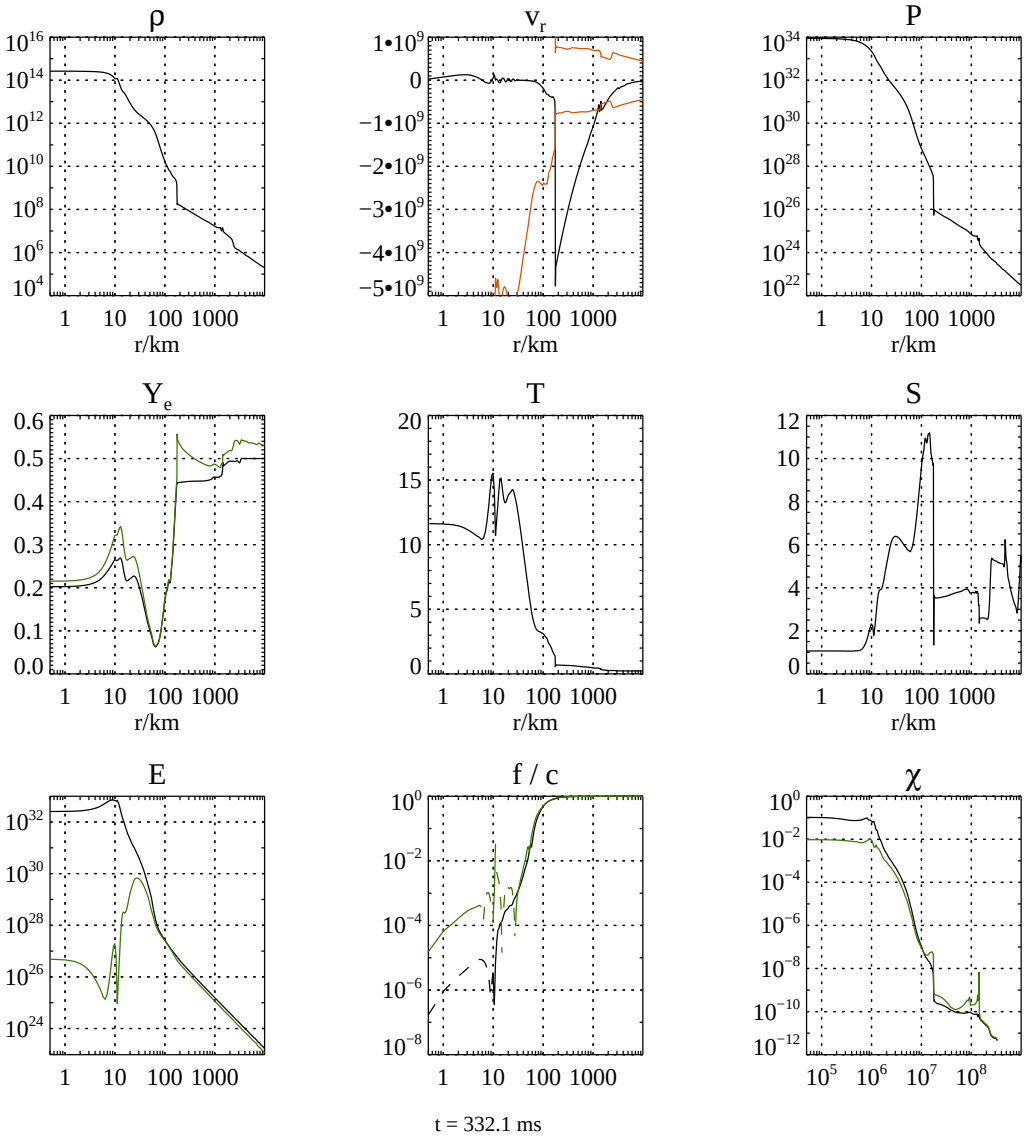

Figure 4.39: Same as Fig. 4.34, but for $t = 332.1\,\mathrm{ms}$, i.e., at the end of our test run.

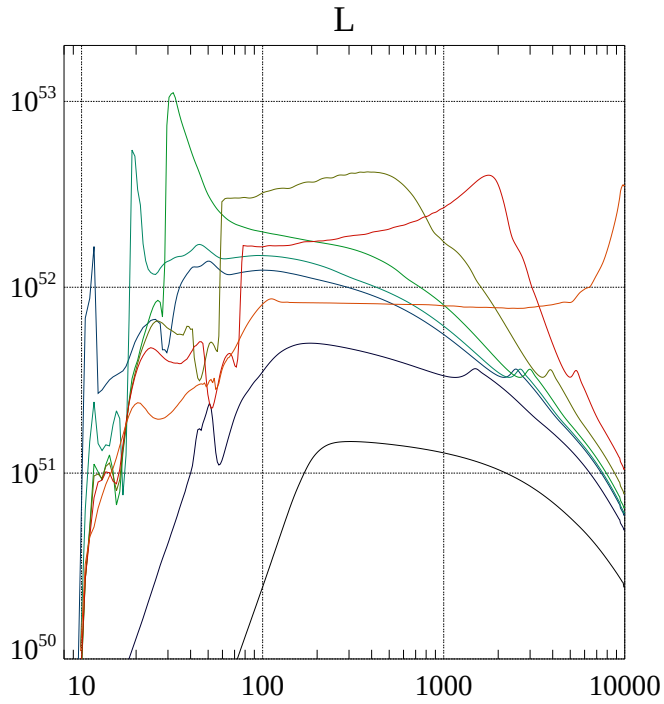

Figure 4.40: The total neutrino luminosity of the stellar core versus radius at different times around core bounce: $t = 211.1\,\mathrm{ms}$, $225.2\,\mathrm{ms}$, $228.6\,\mathrm{ms}$, $229.1\,\mathrm{ms}$, $230.2\,\mathrm{ms}$, $233.1\,\mathrm{ms}$, $238.1\,\mathrm{ms}$, and $265.6\,\mathrm{ms}$ are shown by the black, dark blue, medium blue, light blue, green, dark green, red, and orange lines, respectively.

A concluding remark As said before, it was not our goal to make detailed predictions concerning the explosion of massive stars. Instead, we can draw some conclusions on our RHD method from the simulations. We note that we can reproduce some of the basic features of detailed multi-group spherically symmetric SN simulations with our code. The core deleptonises during collapse, the prompt shock formed at bounce does not explode the star but turns into a standing accretion shock, and a strong burst of neutrino luminosity is emitted by the core after bounce.

Chapter 5

Applications

GET YOUR FACTS FIRST, AND THEN YOU CAN DISTORT THEM AS MUCH AS YOU PLEASE.

Mark Twain

Our code, employing high-resolution numerical methods, is suited particularly well for the study of hydromagnetic instabilities and turbulence. Many systems are subject to instabilities and consequently undergo a transition to turbulence. Of these, we selected two shear-flow instabilities: the hydromagnetic KH instability and the MRI. We will introduce both systems in this chapter and discuss our numerical setup and simulation results.

5.1 Hydromagnetic Kelvin-Helmholtz instability

5.1.1 The physical system

Shear flows are very common HD phenomena, both on earth and in astrophysical environments. As the simplest model for such a system, consider a velocity field with a sharp shearing interface,

$$\vec{v} = \begin{cases} (-v_0, 0, 0)^T & \text{if } y < 0 \\ (v_0, 0, 0)^T & \text{if } y > 0 \end{cases} \tag{5.1}$$

(v_0 is a constant (subsonic) velocity) in a fluid of homogenous density and pressure (see Fig. 5.1). We ignore gravity. Then, if ideal HD applies, the fluid is unstable against the KH instability on any length scale independent of the shearing velocity (e.g., Chandrasekhar 1961). Any perturbation of the shearing interface (of the form $A\exp[ikx - \sigma t]$, where k and σ are the wave number and growth rate of the mode, respectively) will grow exponentially with a growth rate inversely proportional to the wave length, $\sigma = kv_0$. If the shear layer has a finite thickness h_y, the growth rate has a maximum at $k \sim h_y^{-1}$ and approaches zero for modes of shorter wave length. In the non-linear phase, the well-known KH vortices form in a broad transition layer across which the x component of the velocity varies gradually from $-v_0$ to v_0.

Examples on the earth include different layers in the earth's atmosphere streaming along each other visible in magnificent KH clouds, the estuaries of rivers (a particularly beautiful example

is the confluence of the rivers Inn and Salzach near Simbach or the rivers Inn and Mangfall in Rosenheim), and, of course, various flows in technical devices. In astrophysics, the KH instability appears on all scales, from the magnetopause of the earth to stellar explosions and jets.

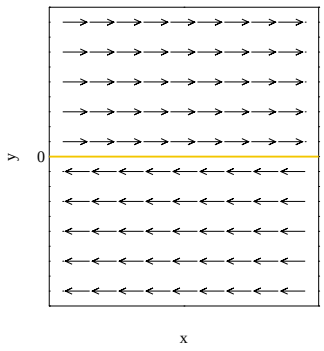

Figure 5.1: A KH unstable velocity field.

If the flow is magnetised, the properties of the instability are modified; for the linear stability analysis, see Chandrasekhar (1961), and for numerical simulations, see, e.g., Malagoli et al. (1996); Frank et al. (1996); Jones et al. (1997); Keppens & Tóth (1999); Keppens et al. (1999); Jeong et al. (2000); Ryu et al. (2000). The influence of the field depends both on the geometry and the field strength.

By virtue of the magnetic tension, field lines resist bending but can easily be dislocated as a whole in directions orthogonal to $\vec{b}$. If a magnetic field threads the 2d KH-unstable system of Eqn. (5.1) in z direction, the shear flow and the perturbation only lead to a displacement of the field lines without bending. The field, thus, only impacts the flow via the magnetic pressure $\frac{1}{2}b_z^2$, and the stability properties and growth rates of the instability do not change. If, on the other hand, the field is oriented along the shearing interface, $\vec{b} = (b_x, 0, 0)^T$ (or has at least a non-zero x component), any perturbation of the interface has to bend the field lines and, thus, requires the flow to work against magnetic tension. The energy density required is larger for perturbations of short wave length. Thus, the magnetic field stabilises the shortest modes, and, for sufficiently strong field, all modes will be stabilised. Weaker fields do not suppress the instability but lead to considerable modifications in the non-linear evolution (Malagoli et al. 1996; Frank et al. 1996; Jones et al. 1997; Ryu et al. 2000).

We shortly summarise results from previous simulations (see Ryu et al. 2000,and references therein). We assume a flow-aligned initial magnetic field, i.e., $\vec{b} = (b_x, 0, 0)^T$.

1. For sufficiently strong initial fields, i.e., for an initial Alfvén number $M_\mathrm{A} = v_0/c_\mathrm{A} \lesssim 1$, stabilisation occurs, and the initial perturbation is damped very quickly.
2. If the field is slightly weaker, with an Alfvén number $M_\mathrm{A} \gtrsim 1$, the instability is stabilised only in the non-linear regime. The field is amplified in the KH vortex and becomes strong enough to prevent non-linear turbulence.
3. Even weaker fields with $M_\mathrm{A} \gtrsim 2$ do not provide stabilisation neither in the linear nor in the early non-linear phases. In their simulations of weak initial fields, Jones et al. (1997) distinguish between the *disruptive* and *dissipative* regimes. If the field is strong enough to reach an Alfvén number of 0.5 within one vortex rotation, the KH vortex is disrupted by magnetic reconnection, leading to a broad, laminar transition layer between the oppositely streaming regions of the fluid. In the dissipative regime, the field does not disrupt the vortex,

but enhances dissipation due to reconnection via tearing-mode instabilities. Turbulence develops and, lacking further energy input, decays slowly. Note that the reconnection can be due to both physical and the inevitable numerical resistivity.

4. In 3d, the KH vortex can be destabilised even without magnetic field by HD perturbations along its axis. For non-vanishing magnetic field, additional field amplification is observed due to secondary vortices.

Our study of the MHD KH instability is motivated by our interest in the physics underlying the instability as well as by a particular astrophysical system, viz. the shear interface forming between two merging neutron stars. Considered to be the most promising model for short GRBs, this system was investigated by several authors (e.g., Oechslin et al. 2002; Oechslin & Janka 2006; Oechslin et al. 2007; Rosswog et al. 2000; Rosswog & Davies 2002; Rosswog & Liebendörfer 2003; Rosswog et al. 2003; Rosswog 2007), in most cases using the SPH method. After a phase of inspiral due to the loss of orbital angular momentum and energy by gravitational radiation, the two merging NS touch each other in a rather thin contact surface. Rotating about the barycentre of the system, the gas inside the two stars has opposite tangential velocities on either side of the contact surface. Thus, the surface is unstable to the KH instability. In numerical simulations, the growth of the instability has been observed, at first only in the HD limit, but recently also including magnetic fields (Price & Rosswog 2006; Rosswog 2007). In these simulations, an extremely fast amplification of the magnetic field in the KH vortices is observed, reaching field strengths exceeding 10^{15} G within one millisecond. We want to check these claims by simulations using a grid-based MHD code as opposed to the SPH simulations of Price & Rosswog (2006), seeking confirmation by an independent numerical method. Since we are only studying a particular aspect of the merger problem, we use local simulations, i.e., we simulate only a small part of the contact surface using initial data resembling the situation in a merger.

5.1.2 Overview of our simulations

We performed two different sets of simulations: we use non-dimensional domain sizes and initial data to study the fundamental physics of the KH instability as well as values motivated by the merger case. The first set of models closely connects our study to the previous KH simulations of Malagoli et al. (1996); Frank et al. (1996); Jones et al. (1997); Keppens & Tóth (1999); Keppens et al. (1999); Jeong et al. (2000); Ryu et al. (2000). We used an ideal-gas EOS in these simulations. The merger simulations, on the other hand, allow us to compare our results to the ones by Price & Rosswog (2006). To roughly approximate the physical conditions in mergers, we used the hybrid EOS (see Sect. 2.1.2). Our simulations were performed both in 2d and 3d.

In all simulations, the shearing interface was perpendicular to the y direction with perturbed shearing velocities in x direction. We smoothened the interface by a tanh profile of a certain width, i.e.,

$$v_x = v_0 \tanh \frac{y}{h_y}, \tag{5.2}$$

where we set the width of the interface, h_y, to a tenth of the grid size. The same profile was used by Frank et al. (1996); Jones et al. (1997); Jeong et al. (2000); Ryu et al. (2000). We added a small sinusoidal perturbation in y (and z for 3d runs) velocity near the interface. The initial state had a homogenous density ρ_0 and pressure P_0. We used periodic BCs in x and z, if 3d, direction, and reflecting BCs in y direction.

5.1.3 Results

Non-dimensional simulations

We first discuss the non-dimensional simulations which allow us to investigate several aspects of the evolution of the KH instability in detail. Most of the simulations are similar to the ones performed previously by, e.g., Frank et al. (1996); Jones et al. (1997); Jeong et al. (2000); Ryu et al. (2000). However, we will also present a few new models, in particular concerning the MHD KH instability for supersonic flows. Tab. 5.1 gives an overview of the models we simulated.

model name	spatial dimensions	ρ_0	P_0	v_0	b_0	comments
nKH2-s-HD	2	1	0.6	0.5	0	HD model
nKH2-s-HD-o	2	1	0.6	0.5	0	outflow BC
nKH2-S-HD	2	1	0.0375	0.5	0	HD model
nKH2-S-HD-o	2	1	0.0375	0.5	0	outflow BC
nKH2-s-S	2	1	0.6	0.5	1	linear stabilisation
nKH2-S-S	2	1	0.0375	0.5	1	linear stabilisation
nKH2-s-I	2	1	0.6	0.5	0.2	non-linear stabilisation
nKH2-s-I-o	2	1	0.6	0.5	0.2	outflow BC
nKH2-S-I	2	1	0.0375	0.5	0.2	non-linear stabilisation
nKH2-S-I-o	2	1	0.0375	0.5	0.2	outflow BC
nKH2-s-W1	2	1	0.6	0.5	0.02	disruption/dissipation
nKH2-s-W1-o	2	1	0.6	0.5	0.02	outflow BC
nKH2-s-W2	2	1	0.6	0.5	0.008	disruption/dissipation
nKH2-s-W3	2	1	0.6	0.5	0.002	disruption/dissipation
nKH2-S-W1	2	1	0.0375	0.5	0.02	disruption/dissipation
nKH2-S-W1-o	2	1	0.0375	0.5	0.02	outflow BC
nKH3-1	3	1	0.6	0.5	0.02	$\Gamma = 5/3$, disruption/dissipation
nKH3-2	3	1	0.0375	0.5	0.02	$\Gamma = 5/3$, disruption/dissipation

Table 5.1: Initial data of non-dimensional models. We list the model name, the initial density and pressure, the shear velocity, and the initial magnetic field.

Two-dimensional models We will first discuss two-dimensional simulations of the KH instability, confronting the results for subsonic and supersonic shear flows. The simulations were performed on a grid of $m_x \times m_y = 200 \times 200$ zones, unless stated else.

Purely hydrodynamic simulations We begin the discussion with the HD case. We show results from the simulations of a KH-unstable shear layer with initial density $\rho_0 = 1$ and pressure $P_0 = 0.6$ in Fig. 5.2 (model nKH2-s-HD). The adiabatic index of the EOS was $\frac{4}{3}$, and the initial velocity was $v_0 = 0.5$, corresponding to a Mach number of $M_s \approx 0.56$. We perturbed the equilibrium with a sinusoidal y component of the velocity profile of a wavelength $\lambda = 2$ equal to the grid size. The results agree well with our expectations: the instability grows at a rate close to the analytic value $\sigma = kv_0 = \pi/2$, and shortly after the start of the evolution, a KH vortex forms at the shearing interface. The formation of the vortex goes along with a decrease of the total kinetic energy as some of the energy of the shear flow transfered into internal energy. Once the *cat's eye* is established, the further evolution is governed by its dissipation due to numerical viscosity. Owing

to the small numerical viscosity of our scheme, this process is very slow. Indeed, the kinetic and internal energies remain constant – except for oscillations – until the end of our simulation.

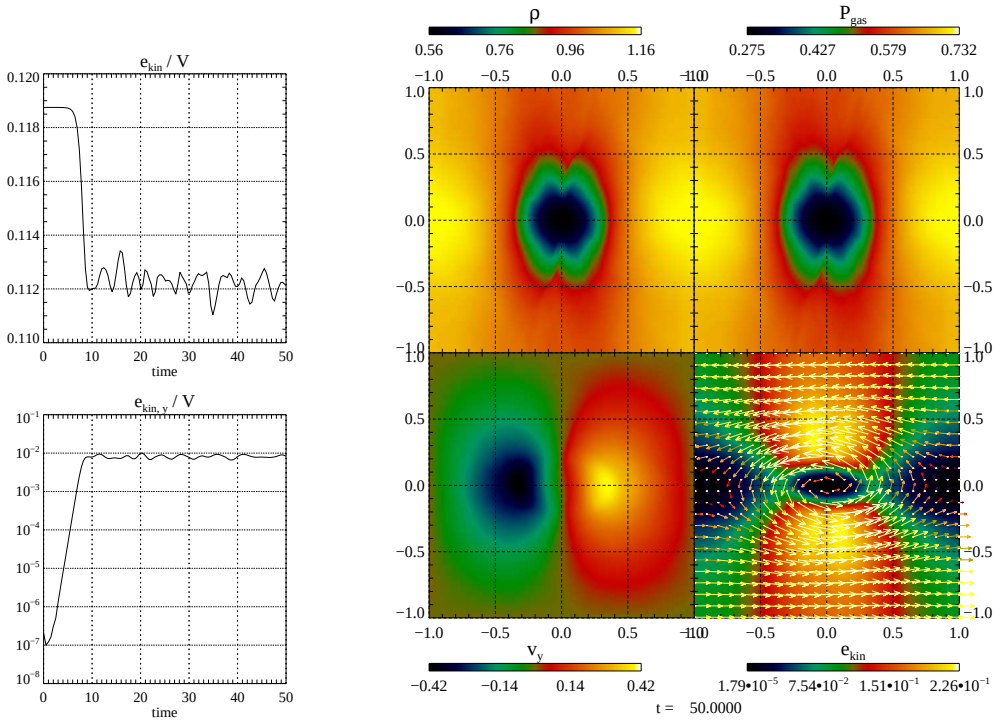

Figure 5.2: KH instability: non-magnetic case with subsonic shear, model nKH2-s-HD. The left panels show the temporal evolution of the volume-averaged total kinetic energy (top) and the volume-averaged kinetic energy in v_y (bottom). The panel on the right shows the fluid flow at $t = 50$. The individual panels show (left to right, top to bottom) density, pressure, v_y, and v_x. In the bottom right panel we show the velocity vector field, too.

We next discuss a model without magnetic fields in which we reduced the initial pressure to $P_0 = 0.0375$ keeping all the other initial data fixed (model nKH2-S-HD). Consequently, the flow is supersonic at a Mach number $M_s \approx 2.23$. In this case, the evolution is considerably different (see Fig. 5.3). In both cases, pressure waves are emitted initially near the interface that travel towards the top and bottom boundaries where they are reflected back towards the interface. There, reflection occurs again as waves returning from either boundary meet again. Thus, in both models, the evolution of the instability occurs in a background of pressure waves travelling resonantly back and forth in y direction and advected with the shear flow. These waves, reminiscent of the resonant modes identified by Perucho et al. (2007), are of little relevance to the subsonic model, but dominate the dynamics of the supersonic flow in which they steepen into shock waves. The formation of a KH vortex is delayed: the build-up of transverse kinetic energy (i.e., energy in the y component) and the conversion of energy from the shearing motion to internal energy is extremely slow compared to the subsonic case, with a growth rate that is reduced by a factor of ~ 10. Near the grid centre, several shock waves of different orientation interact after $t \approx 145$, leaving behind a complex flow pattern. The KH vortex is created in this flow, and, shortly afterwards, it possesses a distinctly elongated (in x direction) shape, and does not assume its characteristic shape before $t \gtrsim 160$ (as opposed to $t \sim 15$ in the previous model). Even at this stage and beyond, the presence of shock waves imprints substantial modifications onto the flow, most notable in the surroundings

of the vortex. The final values of the partial (i.e., kinetic, magnetic, and internal) energies show a strong decrease of the kinetic energy and a consequent increase of the internal one. Since the KH instability grows only very slowly and, if we take the final v_y as a measure, saturates at a lower level, we conclude that the main agent for kinetic dissipation in this model is shock heating rather than the KH instability.

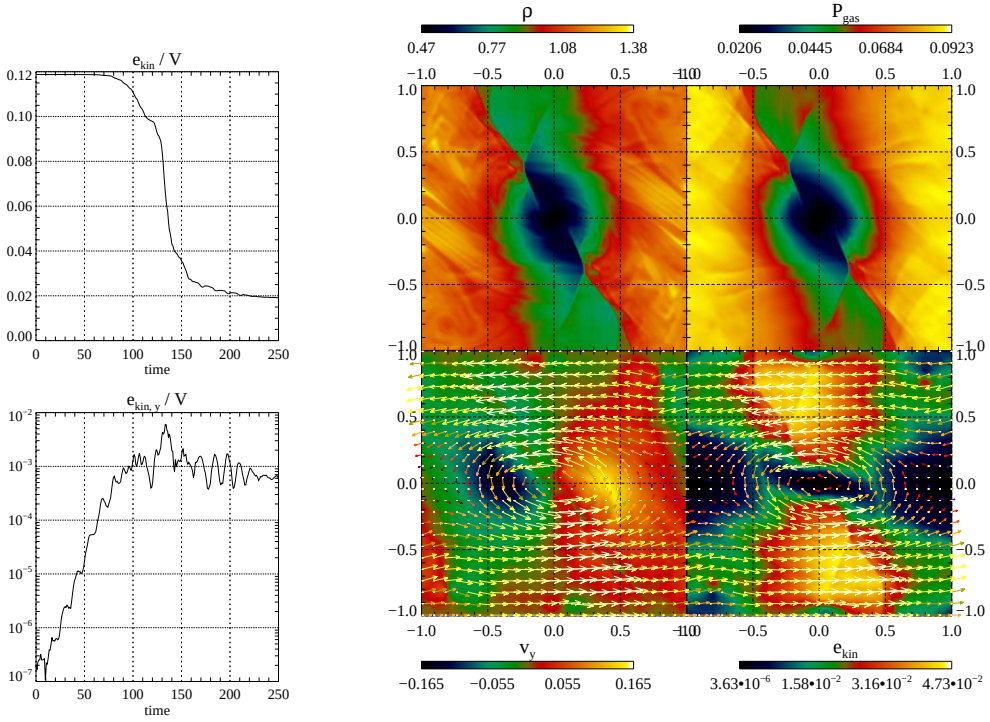

Figure 5.3: Same as Fig. 5.2, but for the supersonic non-magnetic case, nKH2-S-HD. The time at which the flow and magnetic fields are displayed is $t = 200$.

Strong field We now discuss models with a strong initial field, $b_0 = 1$ (models nKH2-s-S and nKH2-S-S). If the Alfvén number of the shear flow is less than unity, the magnetic tension suppresses the instability. The initial shear persists until the end of the simulation (see Fig. 5.4).

Intermediate field – nonlinear stabilisation If the magnetic field is reduced below the limit for linear stabilisation, the KH instability grows in the linear phase, and a KH vortex forms. With the field amplified in the overturning vortex, it eventually becomes large enough to resist further bending, thus stabilising the instability in the non-linear phase.

We demonstrate this for a model with $\rho_0 = 1$, $P_0 = 0.6$, $v_0 = 0.5$, and $b_0 = 0.2$, and an adiabatic index of $\Gamma = \frac{4}{3}$ (model nKH2-s-I, see Fig. 5.5). The instability develops and grows exponentially, but after the magnetic energy reaches a maximum, it gradually decreases again close to its initial value.

It is important to note that, although we are evolving the equations of ideal, i.e., non-resistive, MHD, numerical resistivity is present and enables effects similar to the ones due to a physical resistivity, viz. the reconnection of field lines and the dissipation of magnetic into internal energy.

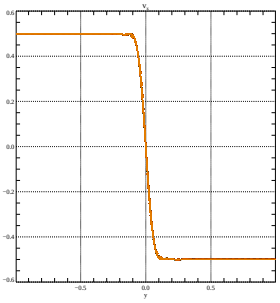

Figure 5.4: The KH instability with a strong initial field, model nKH2-s-S. We compare the initial shear profile $v_x(y;t=0)$ (dashed line) with the profiles at a later time, $v_x(y;t=50)$ (solid lines). Each solid line represents a profile at a given x coordinate. Because the profile is essentially unchanged during the evolution, the lines nearly lie on top of each other.

Though a purely numerical effect, this dissipation has a physical equivalent which it mimics: in ideal MHD (or for exceedingly large $\mathrm{Re_m}$), energy is transferred to ever smaller length scales in the turbulent cascades. Eventually, the magnetic energy injected at a large length scale reaches the scale set by the grid resolution. As a consequence, it can no longer be represented by the discretised magnetic fields. Instead, the sub-grid energy is assigned to the internal energy. Hence, numerical resistivity (and, analogously, numerical viscosity) acts as a sub-grid model for unresolved dynamics.

As a result of numerical resistivity, we observe the dynamics noted by Jones et al. (1997): the emergence of coherent flow and field structures and their subsequent disruption in intense reconnection events. These processes mediate the efficient conversion of kinetic energy to internal one. As a consequence, the kinetic energy decreases much stronger than in the non-magnetic case. The flow field at the end of the simulation shows little resemblance of a KH vortex. Instead, we find a broad transition region between oppositely streaming fluid layers, populated by thin magnetic flux sheets. The flow is rather laminar than turbulent, with elongated streaks of gas and field stretching across the domain.

We find significant differences to the behaviour described above when the shear flow is supersonic (model nKH2-S-I, Fig. 5.6). Considering the evolution of the internal energy, we find a final value relatively close to the subsonic model, very much unlike the non-magnetic version of the supersonic model. This is somewhat unexpected since we do not observe the formation of a KH vortex in this case but rather a shock-dominated dynamics similar to the non-magnetic model. Consequently, the shear profile in the final state of the simulation is much closer to the initial one than that of the subsonic model. The y component of the velocity which is generated almost entirely by the instability, grows significantly faster than without field, but saturates at a similar level. We attribute these effects to a minor importance of the shocks generated from pressure waves in this model. The magnetic field remains weak w.r.t. the internal or kinetic energy, but in the early phases of the evolution, on each side of the shear interface, a stable thin magnetically dominated layer develops isolating the interface from the outer region and preventing the formation of a vortex. The separation of an interior and an exterior region also reduces the intensity of the travelling pressure waves and, consequently, the dissipation of kinetic energy in shocks. The generation of a vortex in a way similar to the non-magnetic model, i.e., mediated by shocks interacting at the shearing interface, appears to be inhibited by the separation of the interface from its surroundings by the highly magnetised layer.

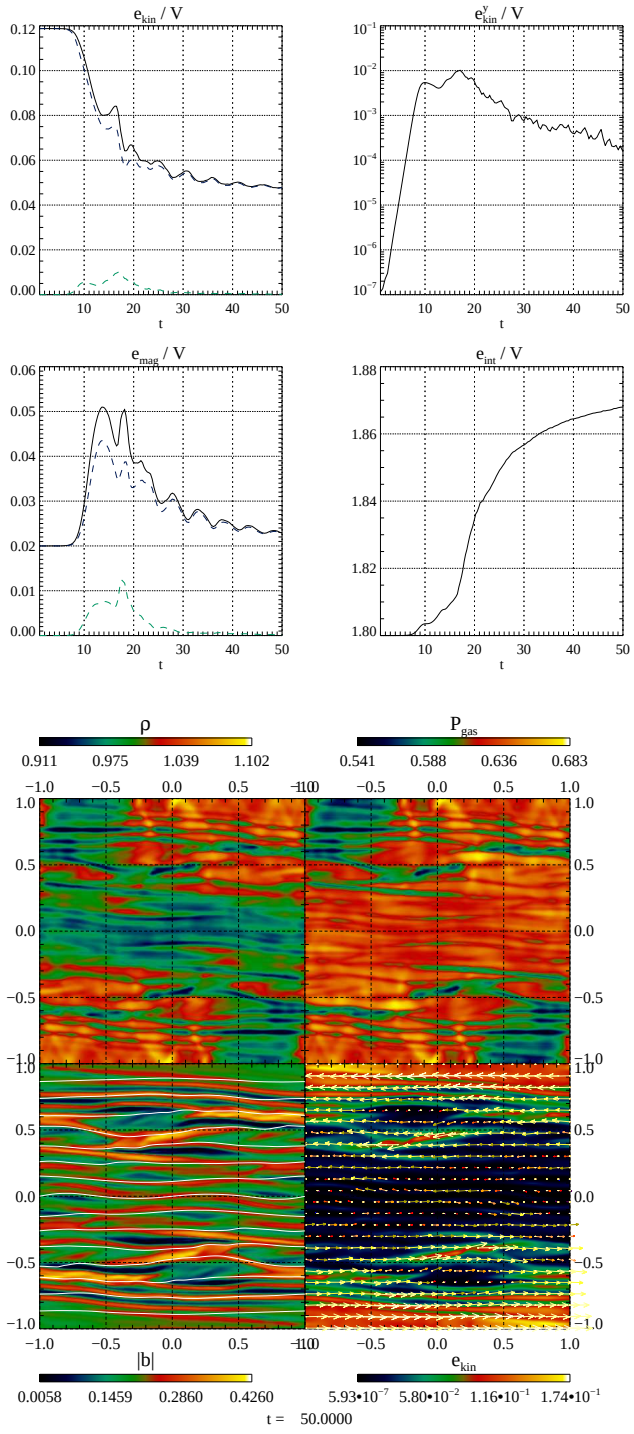

Figure 5.5: The KH instability with an intermediate magnetic field and subsonic flow, model nKH2-s-I. The four panels on top show the temporal evolution of (left to right, top to bottom) the volume-averaged kinetic energy (the solid black, dashed blue, and dashed green lines correspond to the total, the x, and the y component, respectively), the logarithm of the volume-averaged energy in y motion, the volume-averaged magnetic energy (the solid black, dashed blue, and dashed green lines correspond to the total, the x, and the y component, respectively), and the volume-averaged internal energy. The bottom group of four panels shows the model at $t = 50$. Here, the top left and right panels display the density and the pressure, respectively. The bottom left and right plots show the magnetic field strength and the kinetic energy density, respectively. In the bottom left and right panels, we plot the magnetic field lines and the velocity vectors, respectively.

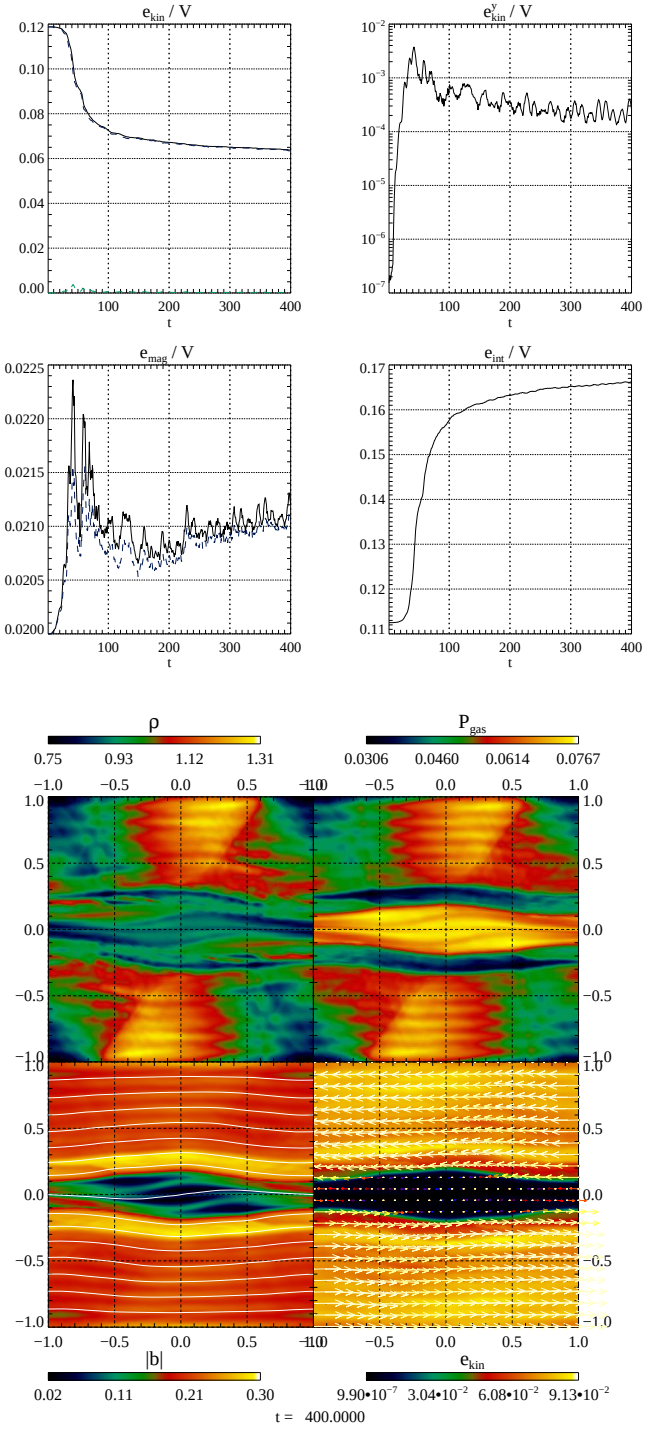

Figure 5.6: Same as Fig. 5.5, but for the supersonic model with intermediate field, nKH2-S-I. The time step displayed in the bottom set of panels is $t = 400$.

Weak fields – disruption and dissipation Models with an even weaker initial magnetic field were characterised as *disruption* or *dissipation models* by Jones et al. (1997). In both regimes, a KH vortex develops. The magnetic field forms thin flux sheets as it is wound up by the vortex overturns. If two flux sheets of opposite polarity come to lie close to each other, they become unstable against the resistive *tearing-mode instability* leading to the reconnection of field lines of different orientation and the conversion of magnetic energy into kinetic. Since the magnetic energy was previously amplified at the cost of the kinetic energy, the tearing modes essentially act as a catalyst facilitating the dissipation of kinetic energy into internal energy. These effects characterise the dissipation regime. In the disruption regime, another effect adds: the magnetic field eventually becomes strong enough for the flows generated in tearing modes to disrupt the vortex, leaving behind only a broad transition layer in which turbulent flow and magnetic fields decay slowly. The dynamics of the flow and the magnetic field is highly coupled since the fields are dominated by flux sheets in which the velocity and magnetic fields are aligned to a large degree, reminiscent of the *Alfvén effect* in MHD turbulence. Consistent with this observation is the near equipartition between the turbulent magnetic and kinetic fields, measured by the kinetic energy of the flow in y-direction and the magnetic energy of the y component of the field, that can be found in disruption models (see below).

Simulating a subsonic model with the same HD initial conditions (and the same resolution) as before, but $b_0 = 0.02$ (model nKH2-s-W1), we observe the typical dynamical evolution of the disruptive regime (Fig. 5.7). The instability grows in the linear phase exponentially, and KH vortex forms. The magnetic field develops a complex, tangled geometry around the vortex, and reconnection mediates the dissipation of kinetic energy; this decrease is more gradual than for stronger fields. The flow geometry is severely affected as the KH vortex disintegrates, leading to a final flow field much less laminar than for intermediate fields. The initially thin shear interface extends over the entire y range of the domain.

The magnetic field preserves a large number of thin coherent flux sheets of different lengths. This geometry is the key to the understanding of the problem how the field, although energetically the least important component of the system, can have such a pronounced effect on the flow. The field is *on (volume-)average* at any stage of the evolution significantly below the energy required for equipartition both with the velocity field and the internal energy (we will refer to these variables as the *kinetic* and *thermal equipartition fields*). Thus, a purely kinematic analysis based upon the comparison of the total energies would suggest that the field can be neglected. Nevertheless, as the field is amplified in the KH vortex, it becomes dominant in localised regions, viz. the thin flux sheets. The maximum field strength is of the order of the kinetic equipartition field. This local dominance suffices to impact the flow globally and change its geometry and evolution. As reconnection sets in, and leads to a decreasing flow velocity, and the disruption of the KH vortex, the maximum magnetic field strength decreases again. The field is still strongest in thin flux sheets and the field strength locally in or above equipartition with the kinetic energy. The total magnetic energy in the saturation state is roughly constant in time, but fluctuates strongly.

In the late-time state, all components of the magnetic field remain strong and fluctuate strongly. We find that, on average, the total energies of the y components of the kinetic and the magnetic field are in equipartition. The rather turbulent flow will decay on much longer time scales due to numerical viscosity.

We add a few comments on the dependence of the results on the grid resolution. As already noted by Jones et al. (1997), higher resolution leads to stronger rather than weaker dissipation, despite the reduced numerical diffusion. We confirm this by comparing simulations of the subsonic weak-field model for different resolutions (100^2, 200^2, 400^2, and 800^2 grid points, see Figs. 5.7 –

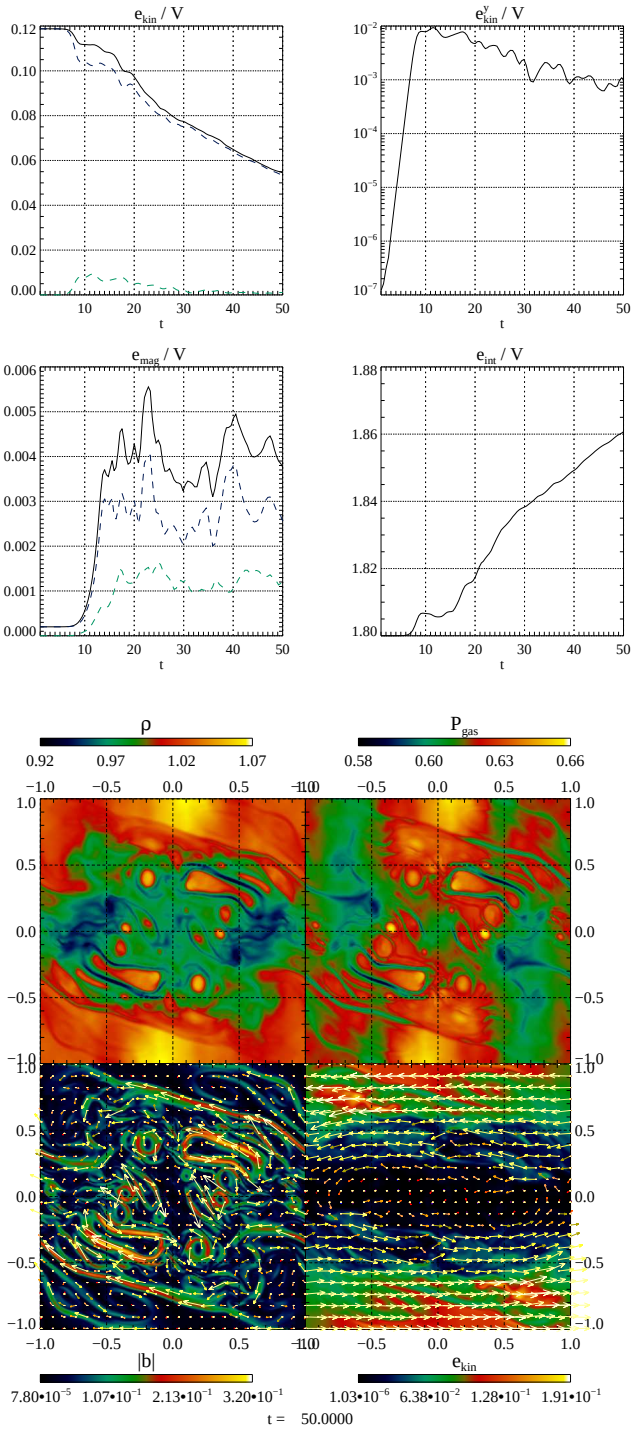

Figure 5.7: Same as Fig. 5.5, but for the subsonic model with a weak initial field, model nKH2-s-W1. The 2d plots of the bottom panels show the flow at $t = 50$. Differing from Fig. 5.5, we show the magnetic field topology (bottom left panel) not using field lines but rather by field vectors.

5.10). In all simulations, the linear phase of the instability is very similar, as can be seen, e.g., in the growth of the kinetic energy of y motion. The non-linear phase, on the other hand, depends on the resolution: the saturation level of the magnetic field is larger for better resolved simulations, and the conversion of kinetic to internal energy proceeds faster.

This behaviour can be understood by the dynamics of the flux sheets created around the vortex (Jones et al. 1997).

In all simulations, the magnetic energy resides in thin flux tubes that eventually reconnect when coming to lie close to each other. Only if the sheets have fields of the order of kinetic equipartition, their reconnection will dissipate sufficient energy to lead to a fast disruption of the vortex. If the energy is too small, only slow dissipation of the energy will occur instead of a fast global change of the dynamics.

On the other hand, the length scale of annihilation is set to a few grid cells by numerical resistivity. On finer grids, we can follow the stretching of the flux sheets by the vortical motion down to thinner sheets. Since it is the stretching of the flux sheets that amplifies the field, the magnetic energy that can be reached is larger in better resolved simulations. Thus, the development of the kinetic equipartition fields required for reconnection to affect the flow strongly in the disruptive regime can be resolved only on sufficiently fine grids. The enhanced numerical resistivity corresponding to a coarse grid can enable reconnection of flux sheets before the field reaches kinetic equipartition, thus preventing disruptive dynamics.

We confirm this by comparing the results of our simulations at different resolution. In the worst resolved of the simulations, i.e., at 100^2 grid cells, the vortex still persists as a coherent structure at $t > 100$, whereas all of the simulations employing finer grids clearly belong to the disruptive regime. Our simulation show approximately convergence in the evolution of the kinetic and internal energy for grids of at least 400^2 zones. At this point, the amplification of flux sheets can be resolved well enough to locally lead to kinetic equipartition fields (e.g., in the flux sheets in the bottom left panel of Fig. 5.9). The total magnetic energy, in contrast, still shows significant differences (compare the evolution of the magnetic energy in Figs. 5.9 and 5.10). We attribute these to the large temporal fluctuations in the turbulent flow which, possessing a random element, differ strongly between different resolutions, and to the importance of very fine structures of the magnetic field that can be resolved only on finer grids. We add one further observation where dissipation and disruption models differ: whereas, in the saturated state, the y components of velocity and magnetic field are in equipartition in the latter class of models, the kinetic energy in the y-direction is much larger than the magnetic energy in the same direction for dissipation models.

Guided by these simulations, we formulate the hypothesis that the generic behaviour of weak-field models is the disruption regime, and that the dissipative evolution of a simulation is a mere artefact of insufficient grid resolution. We speculate that a converged simulation is characterised by disruptive dynamics, i.e., by amplification of magnetic fields to kinetic equipartition in thin flux sheets, a global change of the dynamics, and equipartition of the transverse kinetic and magnetic energies in the saturated state. The main effect of the initial field strength should be to set the time scale of disruption by the time it takes to stretch the flux sheets sufficiently for the field to reach local kinetic equipartition strength.

We must add a remark on a technical difficulty implied by our hypothesis: a consequence of the dependence of the maximum field amplification by flux-sheet stretching on the numerical resolution is that the grid resolution required for convergence is a function of the initial field strength. For weaker fields, a larger amplification, corresponding to larger amount of stretching of

the flux sheets, is required to reach kinetic equipartition. Hence, we must be able to resolve finer flux sheets before dissipation by numerical resistivity sets in. As a consequence, a smaller cell width is necessary for weaker fields, and we may be unable to resolve the disruption dynamics for very weak fields on grids of computationally affordable size.

To test our hypothesis, we evolved subsonic models with very weak fields (we set $b_0 = 0.008$ and $b_0 = 0.002$ for models nKH2-s-W2 and nKH2-s-W3, respectively). When using a resolution of 200^2 grid points in both simulations, they are either dissipative ($b_0 = 0.008$) or essentially non-magnetic ($b_0 = 0.002$). A stable vortex forms, and thin magnetic flux sheets are wrapped up around the vortex. Once the vortex is formed, little or hardly any dissipation of kinetic energy occurs due to the weakness of the magnetic field. For the weaker of the two initial fields, $b_0 = 0.002$, even a resolution of 800^2 does not suffice to enter the disruptive regime, and only slow dissipation of kinetic into internal energy occurs. In the model with $b_0 = 0.008$, on the other hand, the vortex in the model with a resolution of 400^2 cells persists until the end of the simulation at $t = 50$ whereas it is disrupted by the magnetic field at a resolution of 800^2 cells. Comparing the latter simulation with one of a resolution of 1200^2 cells, we find that a resolution of 800^2 is sufficient for convergence. These simulations foster our hypothesis that, when resolved sufficiently well, the models show disruptive dynamics, and that the resolution required for convergence depends on the initial field strength. The results, furthermore, indicate that, as we argued above, for weaker initial fields, the disruption of the vortex occurs on longer time scales.

We finally compare models of different initial field strength and different resolution, but with the same HD background, i.e., density, pressure and shear velocity. We find that for disruption models (i.e., models that – according to our hypothesis – are converged), the *maximum field strength* is independent of the initial field and the grid resolution. This is consistent with our expectation that even very weak initial fields are amplified to local kinetic equipartition strength. The *mean magnetic fields*, on the other, depend on the initial field strength as does the vortex disruption time scale: the stronger the field initially, the stronger the mean field, and the shorter the disruption time.

Our results also allow us to draw a few conclusions on the dissipation properties of our code. The analogous models from Jones et al. (1997) (their models 6 and 7) were simulated with grids of 256^2 and 512^2 zones. For both grids they found dissipative dynamics. The results of our resolution study in mind, we suspect that the different behaviour of our models w.r.t. theirs comes from a significantly reduced numerical diffusion of our code using high-resolution methods. To further support this hypothesis, we simulated the same model using lower-order methods, viz. PLM reconstruction (minmod slope limiter) and a non-MUSTA solver. We observed a much more stable vortex, and less dissipation of kinetic into internal energy.

We briefly discuss a supersonic weak-field model with $P_0 = 0.0375$ (model nKH2-S-W1, see Fig. 5.11). The evolution differs both from the non-magnetic and the intermediate-field versions of the model. The early evolution is similar to the non-magnetic model as shocks form and interact, no layers of strong magnetisation shielding the shear interface. However, several flux sheets develop, the most magnetised of which (with a magnetic pressure amounting to $\beta > 1$) forms along the warped shear interface, preventing the formation of a stable vortex after the interaction of shocks as in the non-magnetic case. Instead, the resistive dissipation of the flux sheets leads to a flow pattern resembling that of the subsonic model: a broad transition region between oppositely flowing gas in which thin flux sheets are embedded. At this stage, shocks no longer play an essential role. The evolution of integral quantities such as the kinetic and internal energies is very similar to the non-magnetic case.

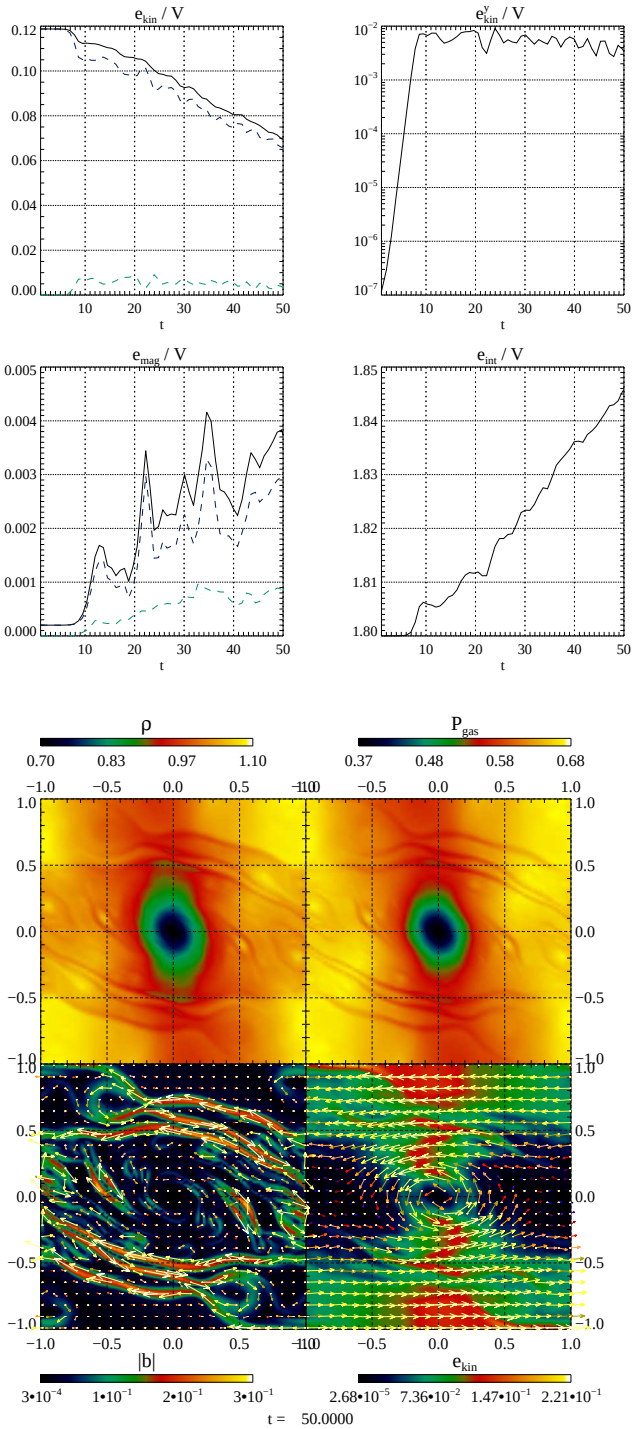

Figure 5.8: Same as Fig. 5.7, but for a grid size of 100 zones.

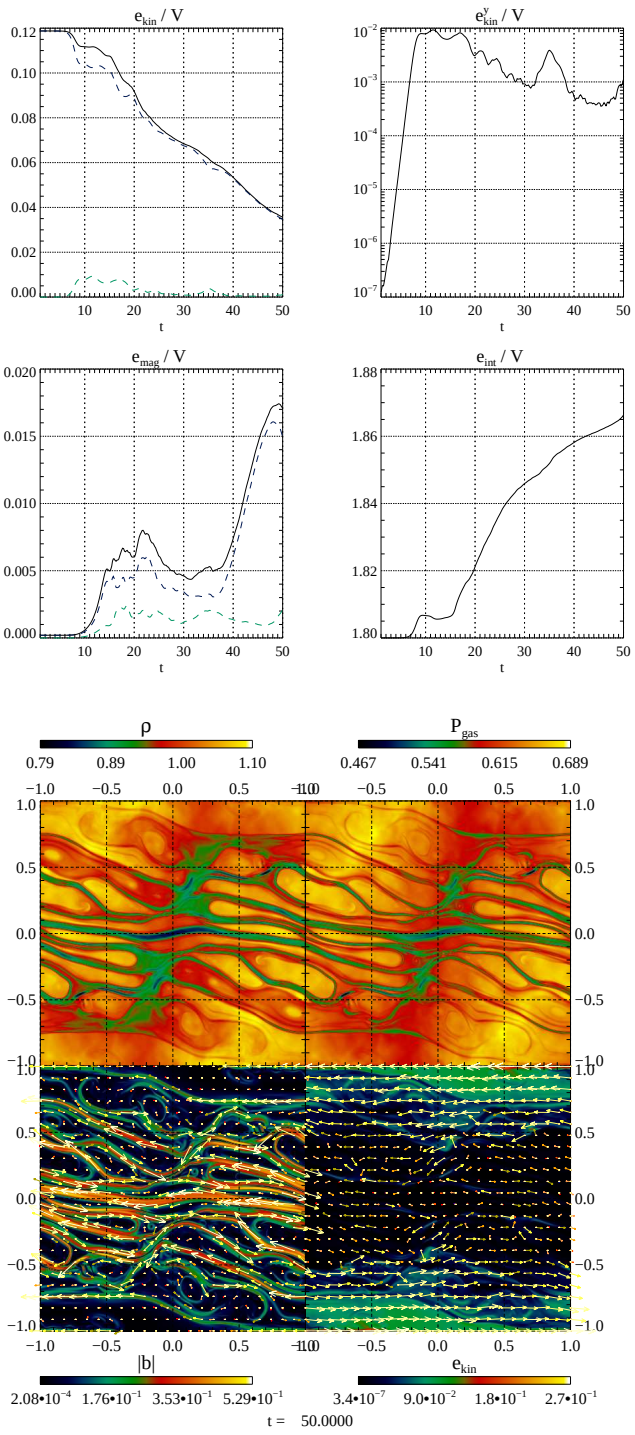

Figure 5.9: Same as Fig. 5.7, but for a grid size of 400 zones.

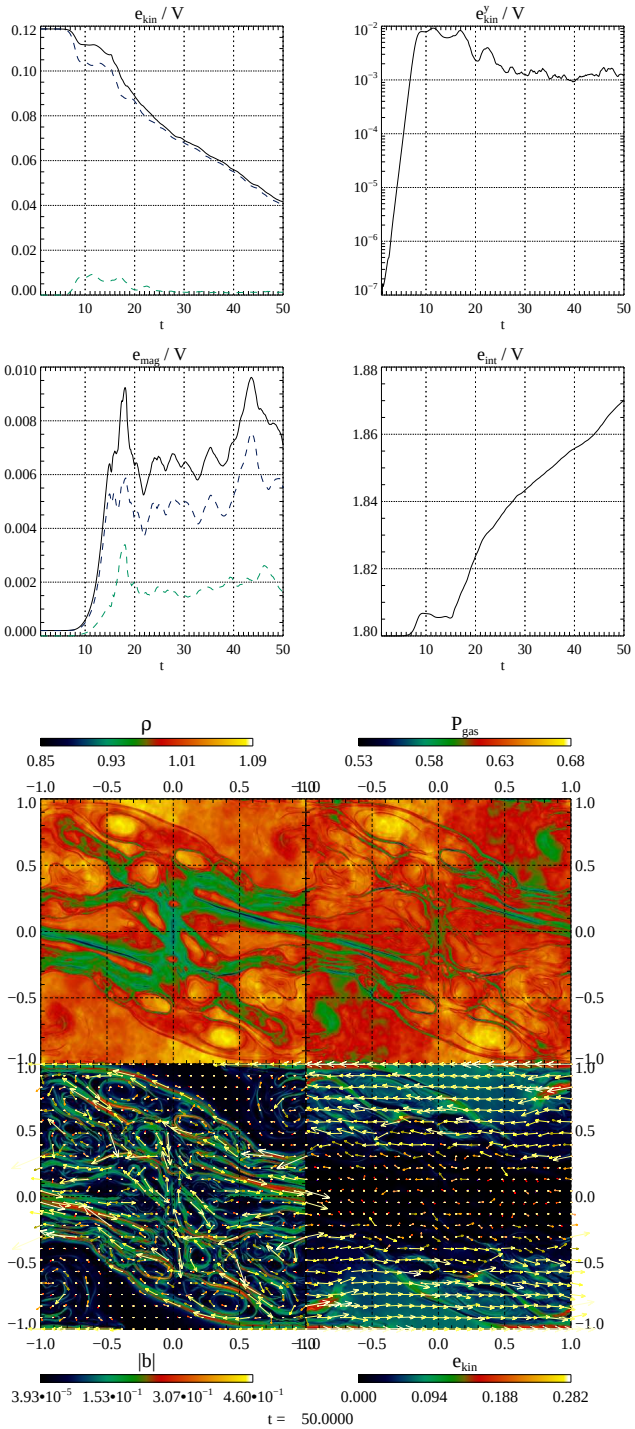

Figure 5.10: Same as Fig. 5.7, but for a grid size of 800 zones.

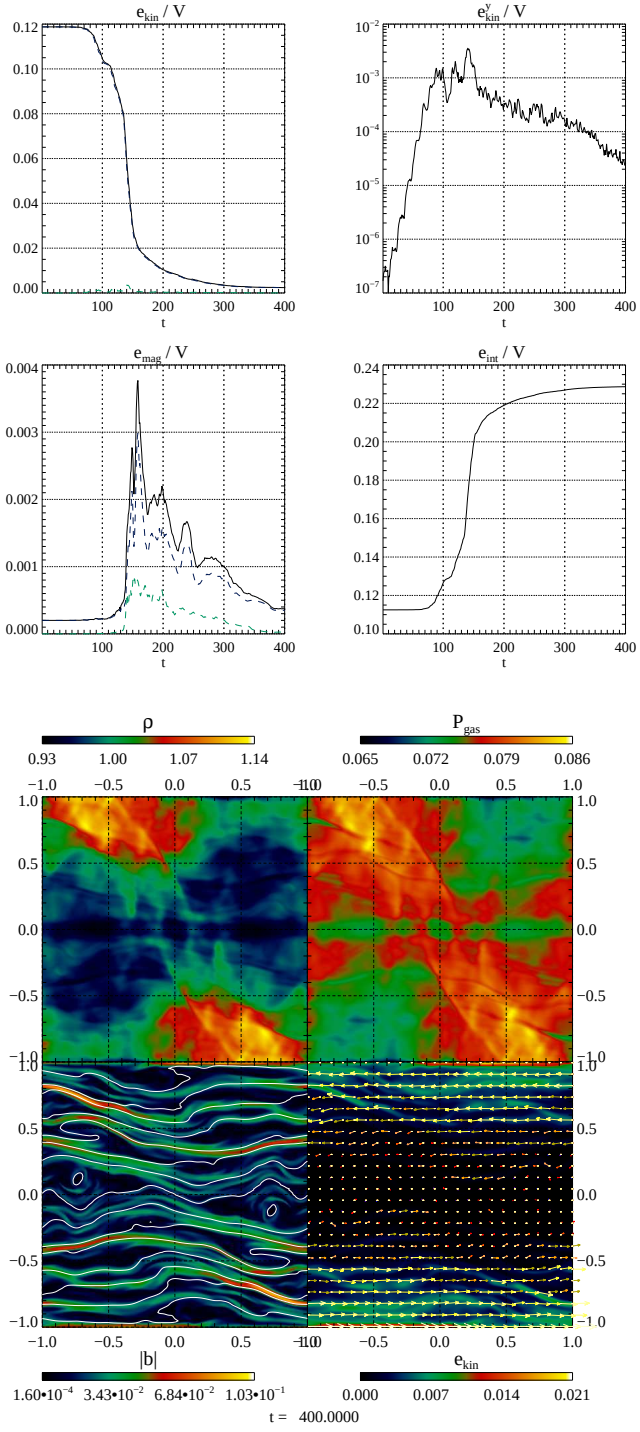

Figure 5.11: Same as Fig. 5.5, but for the supersonic model with weak initial field, model nKH2-S-W1. The bottom 2d plots show the state of the model at $t = 400$.

Influence of BCs In all models described up to now, we used reflective BCs in y direction, which will not apply to all KH-unstable systems. Thus, we simulated some of the models using outflow BCs in y, viz. the intermediate-field and weak-field versions of both the subsonic and the supersonic models.

For subsonic models, there is only a modest dependence on the BCs. Model nKH2-s-I-o evolves similarly to model nKH2-s-I during the linear and most of the saturation phase. Since the stabilised transition region that develops after the destruction of the KH vortex is not confined to the numerical domain by the BCs, it can grow in y extent to more than the grid size. During this growth, material and energy is removed from the grid by motions in y direction. We can draw similar conclusions for the weak-field version of the model, nKH2-s-W1-o, and the purely HD model nKH2-s-HD-o. In none of them does the dynamics depend crucially on the BCs.

In contrast, a large impact is observed in supersonic models because there, the reflection of pressure waves at the y boundaries is important to shape the shock waves that form from the pressure waves. With reflecting BCs, the system acts as a cavity for the waves, but, if we allow for outflow, the waves simply leave the grid and cannot affect the shear interface. As a consequence, the purely HD model nKH2-S-HD-o is stable. The initial perturbation is damped away rapidly, and the shear profile remains unchanged. With weak magnetic fields, on the other hand, the instability is present, but much weaker than with reflective BCs. We do not observe the shocks that were dominant for models with reflective BCs. This emphasises their importance for the development of the supersonic KH instability. If a vortex forms at all, it is much less prominent than in previous models.

The influence of the results on further physical parameters such as the grid size is left for further investigation.

Three-dimensional models In three-dimensional simulations, Ryu et al. (2000) noted that the KH vortex is unstable against (purely) HD instabilities: coherent vortex tubes near the vortex exert non-axial stresses on the vortex, and fluid elements are prone to the so-called *elliptic instability*, an instability caused by time-dependent shear forces fluid elements feel as they orbit the vortex on elliptic trajectories. The result is isotropic decaying turbulence. If a (weak) magnetic field is present and disrupts the vortex, the post-disruption flow shows a larger degree of organisation than without magnetic fields due to the prevalence of flux tubes and sheets in which the magnetic and kinetic fields are aligned.

We studied the disruption regime in three-dimensional models, too. The evolution of model nKH3-1 shows the typical characteristics of a weak-field disruption model. The temporal evolution of the model, computed on a grid of 320^3 zones is displayed in Fig. 5.12, and the topology of the magnetic field is shown in Fig. 5.13. The kinetic energy decreases, being transformed into internal energy by the magnetic field, which is amplified up to kinetic equipartition locally. Different from the two-dimensional models, the energy of the y and z components of the magnetic field are significantly larger than the kinetic energies of the corresponding velocity components. The structure of the magnetic field is dominated by thin flux tubes. During the disruption of the vortex, the flux tubes first possess a very tangled, locally approximately isotropic shape, but become more and more elongated in x direction later, until they finally are roughly constant in x-direction. The large-scale magnetic field shapes the resulting turbulent velocity field by reducing the extension of features in the cross-field direction and expanding them in the parallel direction to the field. This reduction of dimensionality is typical for MHD turbulence.

We note some interesting observations regarding the final state (Fig. 5.14): the flow can be divided into regions of intense magnetisation (high β) and low-density, but low velocity, both in the x component (i.e., the original shear) and in the orthogonal components. We find local overturn motions (these can be identified in the bottom right panel of the figure by the bright orange regions). In these regions, the field is weak, and the fluid motion is inhibited in directions perpendicular to the field lines. These phenomena are reminiscent of effects well-known from MHD turbulence: the Alfvén effect leads to a quasi-2d structure of the field and the flow, and the magnetic field and the flow are separated due to the expulsion of magnetic flux from overturning cells and the suppression of cross-field motion. As a result, magnetic flux accumulates in calm flow regions.

We finally show the results of a three-dimensional simulation of a supersonic model, model nKH3-2 (Fig. 5.15). We observe the emergence of shock waves from resonantly travelling pressure waves. After the transient formation of vortex-like patterns, these features are rapidly disrupted. Dissipation of kinetic to internal energy occurs very efficiently. The final state of the model is similar to that of the subsonic model nKH3-1: we find quasi-2d MHD turbulence, dominated by flux tubes, in the familiar broadened shear layer.

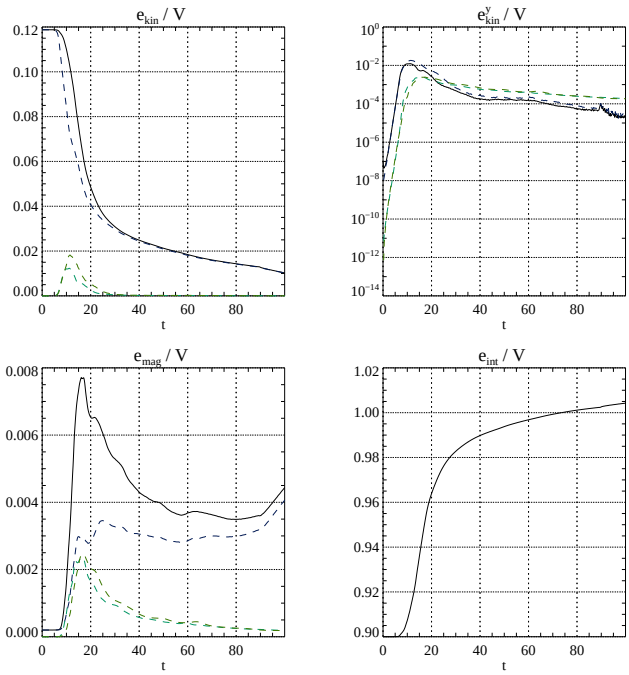

Figure 5.12: Temporal evolution of the three-dimensional model nKH3-1. The top left panel shows the kinetic energy versus time: the total energy and the partial kinetic energies of the x, y, and z components are shown by the solid black, the dashed blue, dark green, and light green lines, respectively. The top right panel shows the logarithm of the y and z partial kinetic and magnetic energies, with solid black and dashed blue corresponding to the y and z partial kinetic energies and dashed dark green and light green corresponding to the y and z partial magnetic energies, respectively. The bottom left panel shows the temporal evolution of the magnetic energy: solid black, dashed blue, dark green, and light green lines correspond to the total, and the x, y, and z partial energies, respectively. The bottom right panel shows the evolution of the volume-averaged internal energy.

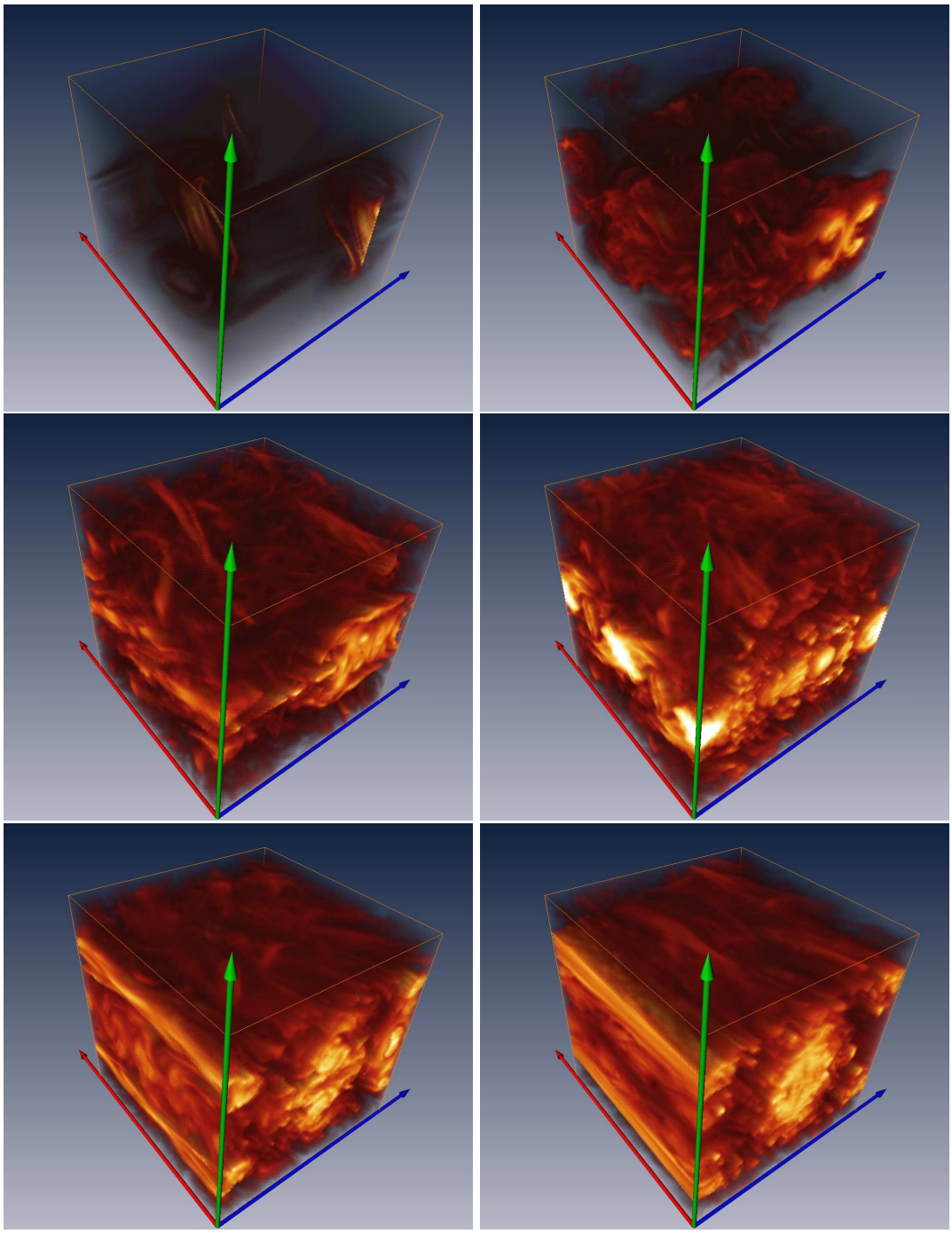

Figure 5.13: The structure of the magnetic field of model nKH3-1. The panels show a volume rendering of the magnetic field strength, $|\vec{b}|$, at different times, $t = 9.1$, $t = 15.7$, $t = 24.4$, $t = 34.0$, $t = 66.7$, and $t = 87.5$ (left to right, top to bottom). The x, y, and z axes are represented by the red, green, and blue arrows, respectively.

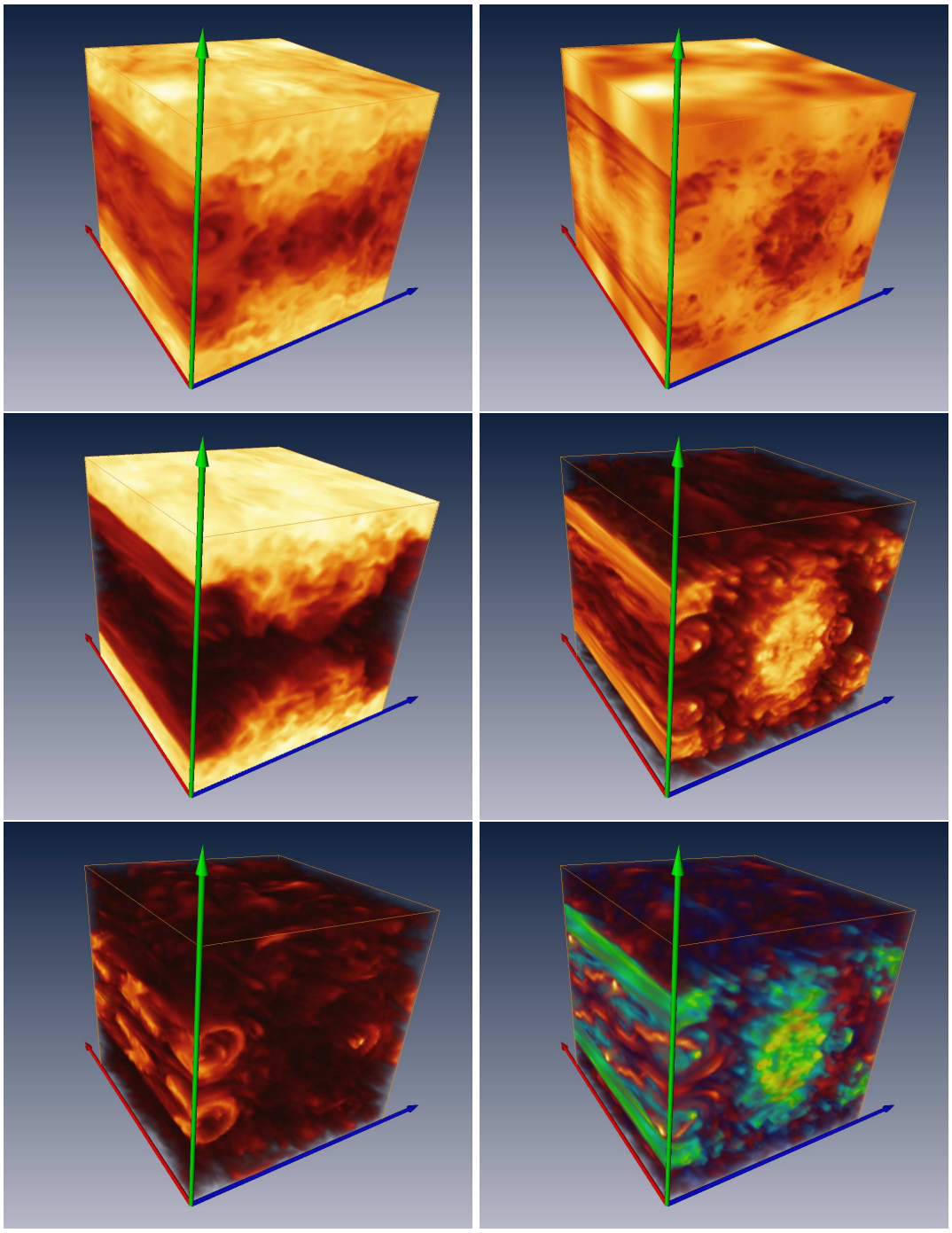

Figure 5.14: The flow and field structure of model nKH3-1 at $t = 87.5$. The axes are coded by the same colours as in Fig. 5.13. The panels show volume renderings of different variables. The top left and right panels show the density and the gas pressure, respectively. The middle left and right panels show the modulus of the velocity $|\vec{v}|$, and the x component of the magnetic field, respectively. The bottom left panel shows the strength of the orthogonal magnetic field, $\sqrt{b_y^2 + b_z^2}$. The bottom right panel shows a combined rendering of the magnetic field strength $|\vec{b}|$ (blue–green–yellow colours) and of the orthogonal velocity field, $\sqrt{v_y^2 + v_z^2}$ (reddish colours).

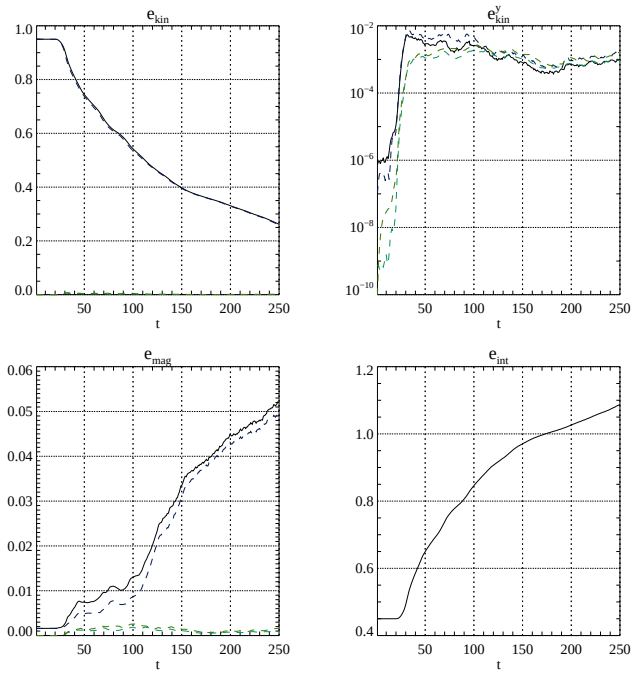

Figure 5.15: Same as Fig. 5.12, but for model nKH3-2.

Merger-motivated simulations

We now discuss models that explore the growth of the KH instability at the contact interface of two merging NS. We used the hybrid EOS to describe the NS matter. The initial data were set to values mimicking the conditions at the contact interface, and the geometry was the same as in the models discussed above. We used a grid of size $(2\,\mathrm{km})^2$ in 2d and $(2\,\mathrm{km})^3$ in 3d simulations, and triggered the instability by applying perturbations of the same type as before. The models are listed in Tab. 5.2. We used a resolution of 800^2 cells in 2, and 100^3 cells in 3d, and reflecting BCs in y-direction. This choice is more appropriate than outflow BCs, since we expect the matter near the contact surface to consist of relatively tenuous gas bounded by the very steep density gradients of the colliding NS acting as a hard wall. We note, however, that these are artificial conditions, i.e., our results do not unambiguously carry over to an actual merger system.

Two-dimensional models We first consider a cold model (i.e., vanishing entropy, $S = 0$) matter of an initial density $\rho_0 = 10^{13}\,\mathrm{g\,cm^{-3}}$. For a shear velocity of $1.8 \times 10^9\,\mathrm{cm\,s^{-1}} \approx 0.5 c_\mathrm{s}$, and an initial magnetic field of $b_0 = 10^{13}\,\mathrm{G}$ (model mKH2-1, see Fig. 5.16), we find the well-known dissipative behaviour. The instability grows within ~ 0.5 milliseconds and saturates with a stable KH vortex. The magnetic field is amplified by a factor of ~ 100, leading to maximum field strengths around $10^{15}\,\mathrm{G}$. Similar to all models discussed above, the flow geometry is reflected in the field geometry: the field is highly intermittent and consists of many thin flux sheets. Thus, the total magnetic energy as well as the Maxwell stress components correspond to a mean field strength of much less than the maximum value, viz. $\sim 10^{14}\,\mathrm{G}$. Having in mind our previous results, we suspect that the dissipative dynamics is only an artefact of our resolution (800×800 cells) which does not allow to resolve the development of extremely thin flux sheets where dissipation occurs.

We consider next models which, due to sufficient resolution, exhibit disruptive dynamics. We

model name	dimensions	ρ_0 $[10^{13}\mathrm{g\,cm^{-3}}]$	S_0	v_0 $[10^{9}\mathrm{cm\,s^{-1}}]$	b_0 $[10^{13}\mathrm{G}]$
mKH2-1	2	1	0	1.8	1
mKH2-2	2	1	0	1.8	10
mKH2-3	2	1	0	2.9	10
mKH2-4	2	1	4	1.8	10
mKH2-5	2	1	4	4.2	20
mKH2-6	2	1	4	6.3	40
mKH2-7	2	1	4	6.3	10
mKH3-2	3	1	0	1.8	10
mKH3-5	3	1	4	4.2	10

Table 5.2: The initial data of the merger-KH models. Given are the model name, the initial density, entropy, shear velocity and magnetic field, respectively.

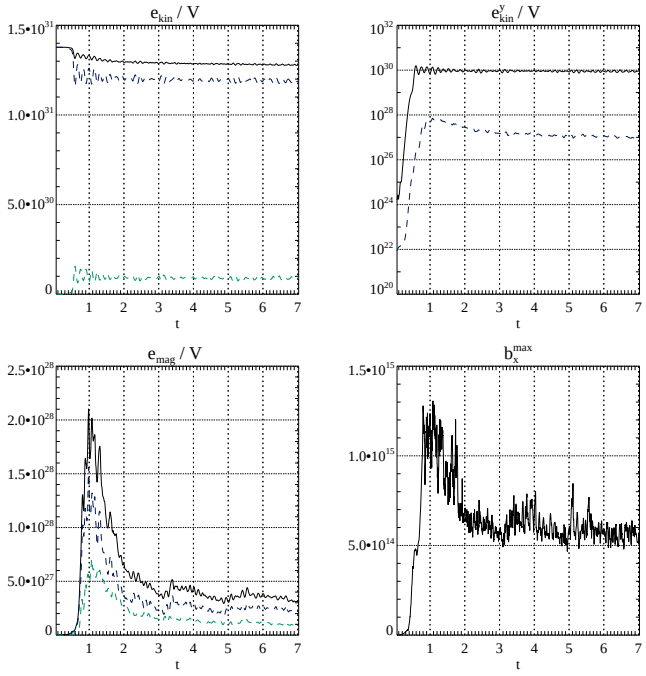

Figure 5.16: Temporal evolution of model mKH2-1. The top panels show the evolution of the volume-averaged kinetic energy (total, x, and y components are shown by solid black, dashed blue, and dashed green lines, respectively), and the logarithm of the y kinetic (solid line) and magnetic (dashed line) energies. The second row displays the volume-averaged magnetic energy (total, x, and y components are shown by solid black, dashed blue, and dashed green lines, respectively), and the maximum magnetic field versus time in milliseconds.

a model similar to the one discussed above, but with an initial magnetic field of 10^{14} G, model mKH2-2 (Fig. 5.17). In this case, we find disruption dynamics. Within less than 0.5 milliseconds the instability saturates, and about 0.3 milliseconds later the field is amplified to local kinetic equipartition. The maximum field strength rises to approximately 8×10^{15} G. As reconnection sets in, the vortex is disrupted within less than 0.5 milliseconds, and the maximum field strength decreases oscillating around approximately 3×10^{15} G at later epochs. The snapshot of the flow field in Fig. 5.17 shows the model at $t = 0.9$ ms. At this point, the magnetic field is wound up around the vortex, reaching a maximum field strength of 6.1×10^{15} G. The field topology consists of a number of thin flux sheets. Because of the increased magnetic pressure inside the sheets balancing the exterior gas pressure, the gas pressure (and density) is reduced within the sheets. Where flux sheets lie close to each other, reconnection sets in leading to a very complex pattern of flux sheets. At some points isolated circular flux sheets are created by reconnection. Sites of intense reconnection correspond to local maxima of the kinetic energy due to the acceleration of gas in tearing modes. The overall shape of the vortex is still affected only little, since it is not penetrated by flux sheets. But as the perturbations of the flux sheets caused by reconnection travel along the field lines, which themselves are advected by the shear flow and the vortical motion, the field-free region in the centre of the vortex shrinks. Consequently, the vortex is disrupted later on.

The evolution is very similar for model mKH2-3 (Fig. 5.18), which differs from model mKH2-2 only by a large shear velocity, $v_0 \approx 0.8 c_S \approx 2.9 \times 10^9 \,\mathrm{cm\,s^{-1}}$. The model belongs to the dissipation class. Since the shear velocity is close to the sound speed, and v_x increases locally to Mach numbers slightly above unity as the vortex forms, the model shares some of the characteristics of supersonic models. In the early phases, shock waves form, but the dynamics is close to that of a subsonic model. After ~ 1.2 millisecond, a KH vortex has formed, which is disrupted later by the same mechanism as in model mKH2-2, albeit somewhat slower, probably due both to the larger Alfvén number of the shear flow and the locally supersonic motion.

We now turn towards models with a larger entropy, $S = 4$. The sound speed of these models is correspondingly larger, $c_S \approx 8.4 \times 10^9 \,\mathrm{cm\,s^{-1}}$. We start with the same shear velocity as in model mKH2-1, $v_0 \approx 0.2 c_S \approx 1.8 \times 10^{14} \,\mathrm{cm\,s^{-1}}$ (model mKH2-4, Fig. 5.19). From the large similarity of this model and model mKH2-2 (Fig. 5.17), we conclude that, for fixed shear velocity, the increase of the entropy influences the evolution of the KH instability only minor weakly. This is not surprising, since – for subsonic velocities – the evolution of the instability is roughly adiabatic.

The next model, mKH2-5 (Fig. 5.20) has the same entropy as mKH2-4, but a larger shear velocity. We set $v_0 = 4.2 \times 10^9 \,\mathrm{cm\,s^{-1}} \approx 0.5 c_S$. Along with the shear velocity, we increase the initial magnetic field to $b_0 = 2 \times 10^{14}$ G. The model is disruptive – note that the energies of the transverse (y) components of the magnetic field and the velocity are in equipartition. The field is amplified to values of $\sim 2 \times 10^{16}$ G.

If we increase the shear velocity further to $v_0 = 6.3 \times 10^9 \,\mathrm{cm\,s^{-1}} \approx 0.75 c_S$ (model mKH2-6, Fig. 5.21), the Mach number of the flow exceeds unity during the formation of the vortex, and shocks are formed. The larger velocity requires a stronger magnetic field in order to reach kinetic equipartition. Thus, starting from a rather weak initial, we have to follow the amplification of the field by a larger factor than for slower shear flows. Consequently, we need a very fine grid – otherwise, the model will not dissipative rather than disruptive dynamics. This is the case for model mKH2-7 with a initial field strength $b_0 = 10^{14}$ G. To avoid the need for finer grids, we used an initial field strength $b_0 = 4 \times 10^{14}$ G model for model mKH2-6. After the linear phase, the energies of the y component of the velocity and the magnetic field are in equipartition, indicating the turbulent disruption regime. The dissipation of kinetic energy into internal one occurs very rapidly, and, already at $t \approx 0.6$ ms, the KH vortex has lost its coherence. Temporarily,

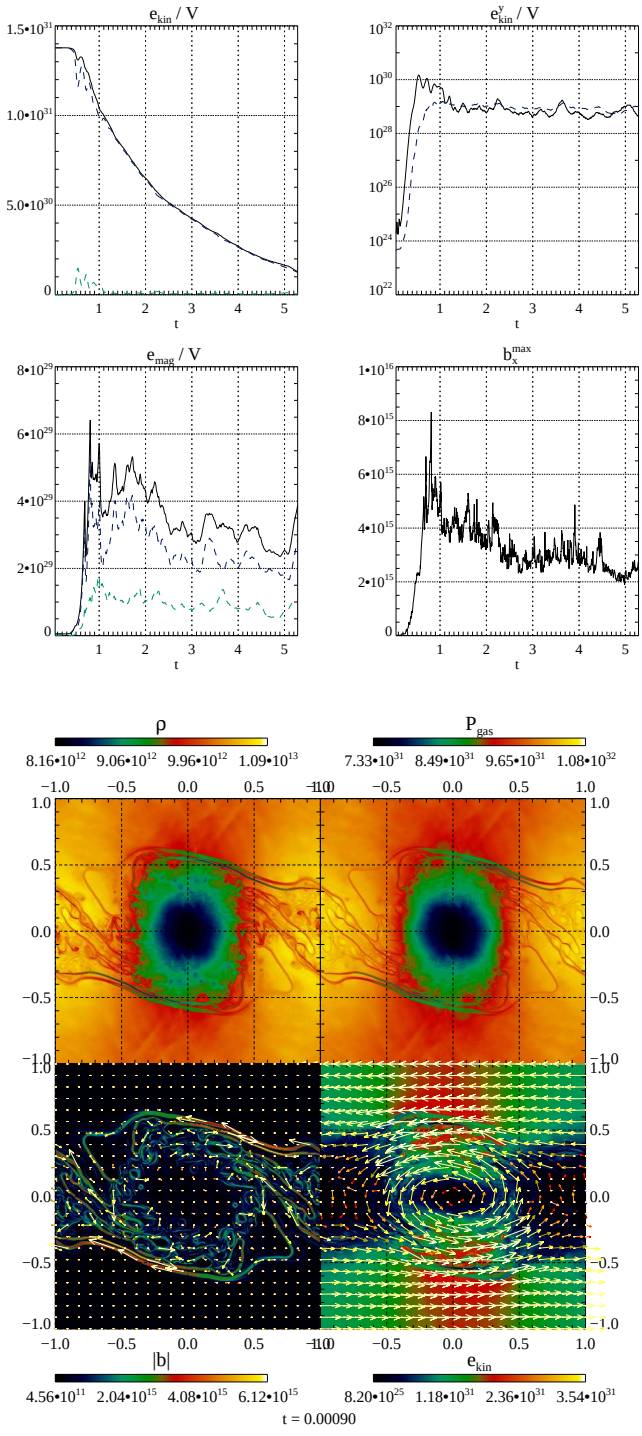

Figure 5.17: Model mKH2-2: temporal evolution and a snapshot at $t = 0.9\,\mathrm{ms}$. The top panels show the same variables as in Fig. 5.16. The contour plots show gas density (top left), gas pressure (top right), magnetic field (bottom left), and kinetic energy (bottom right). Additionally, vectors of the magnetic and velocity field are drawn in the bottom left and right panels, respectively. The x and y coordinates of the contour plots are given in units of kilometres.

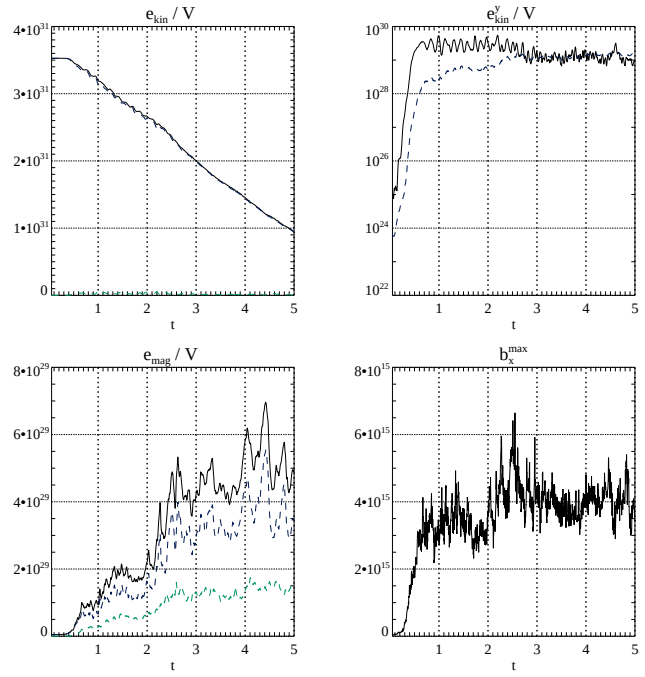

Figure 5.18: Same as Fig. 5.16, but for model mKH2-3.

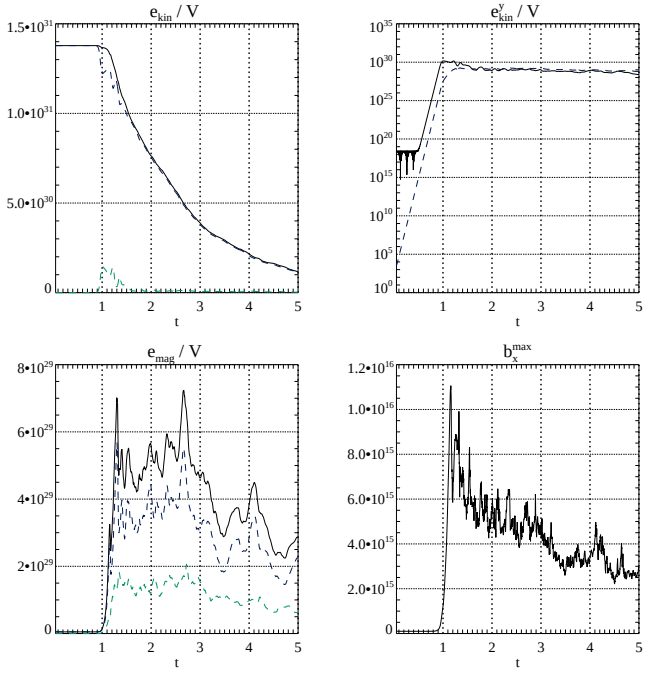

Figure 5.19: Same as Fig. 5.16, but for model mKH2-4.

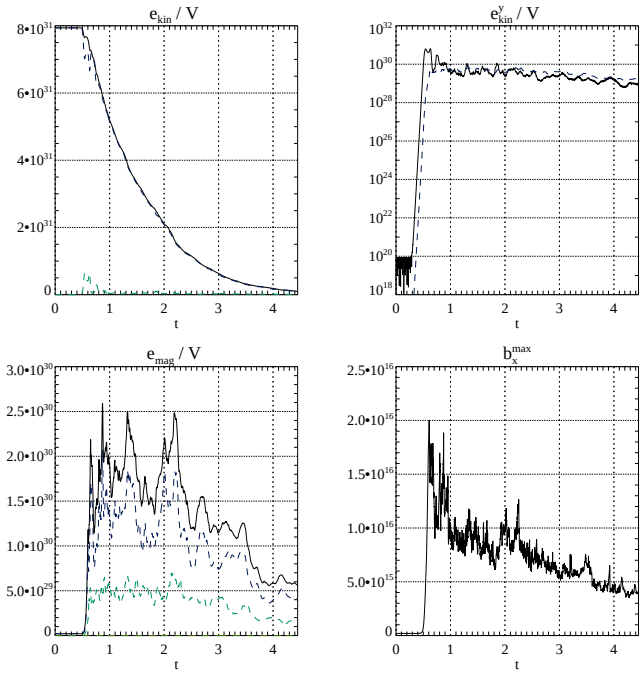

Figure 5.20: Same as Fig. 5.16, but for model mKH2-5.

the field reaches maximum values in excess of 2×10^{16} G. The vortex is disrupted completely and is replaced by a broad transition region interspersed with magnetic flux sheets and small regions of high density confined by field lines. Because the large width of the transition region implies a smaller shear, and as an instability is not present anymore, the field does not grow but rather decreases, both in maximum and in mean strength. Nevertheless, the fields are still strong, $|\vec{b}| > 10^{15}$ G, at the end of the simulation.

Three-dimensional simulations We conclude the discussion with the three-dimensional version of models mKH-2 and mKH2-5: models mKH3-2 and mKH3-5, respectively. The temporal evolution of these models is shown in Figs. 5.22 and 5.23. We used a resolution of 100^3 zones for both models. In both models, disruption of the initial KH vortex occurs within the first 1.5 milliseconds (mKH3-2) and 0.7 milliseconds (mKH3-5), i.e., faster than in the two-dimensional models. The disruption is due to both the appearance of three-dimensional HD instabilities and the magnetic field. The maximum field strength the models reach are of the same order as in the corresponding two-dimensional models: at maximum and near the end of the simulation, we find $\sim 10^{16}$ G and several 10^{15} G, respectively. There is, however, a marked difference in the mean magnetic energies: unlike in the two-dimensional models, we find a phase of growth towards the end of the simulation. In this stage, mainly the x-component of the field grows. Based on our simulations, we cannot rule out the possibility that this is an artefact of the comparably low resolution of the model. To check this hypothesis requires more and better resolved simulations. We defer this interesting question to a future investigation.

Comparison with merger simulations We will now compare our results with the simulations by Price & Rosswog (2006). In the discussion, we have to carefully distinguish between true physical effects and artefacts of the finite grid resolution. In the earlier discussion, we pointed out

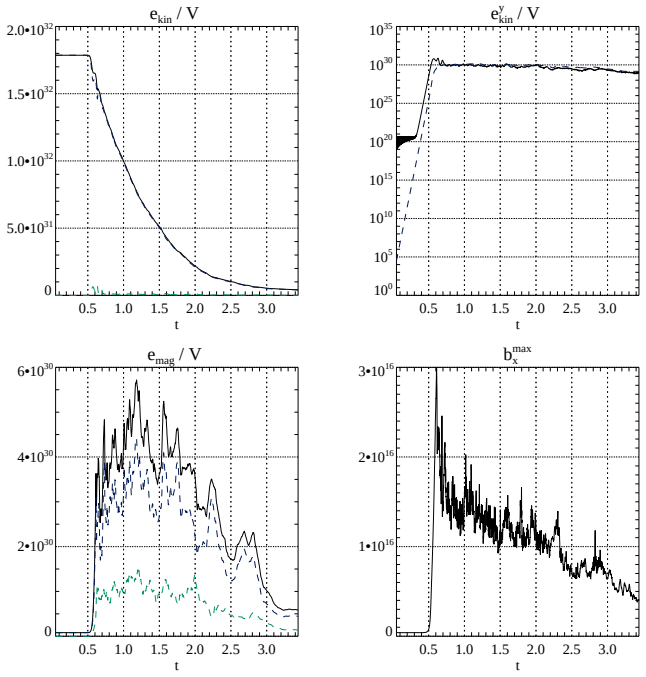

Figure 5.21: Same as Fig. 5.16, but for model mKH2-6.

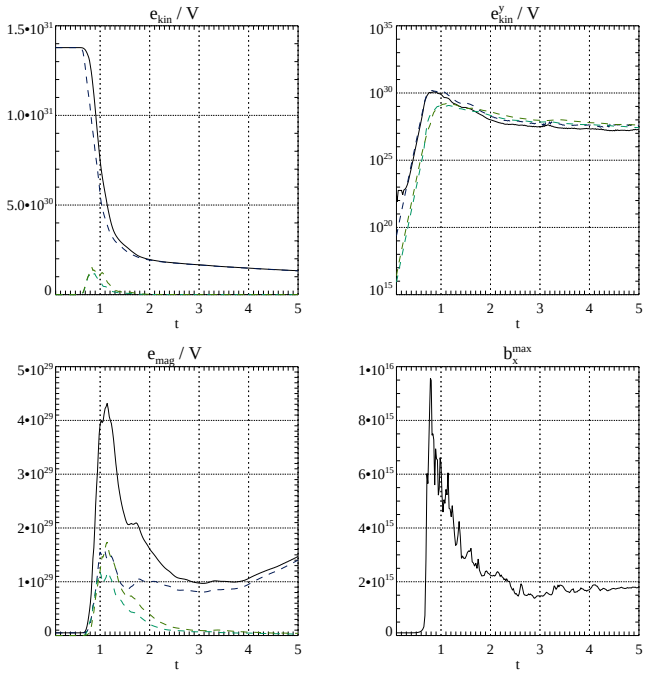

Figure 5.22: Same as Fig. 5.16, but for model mKH3-2.

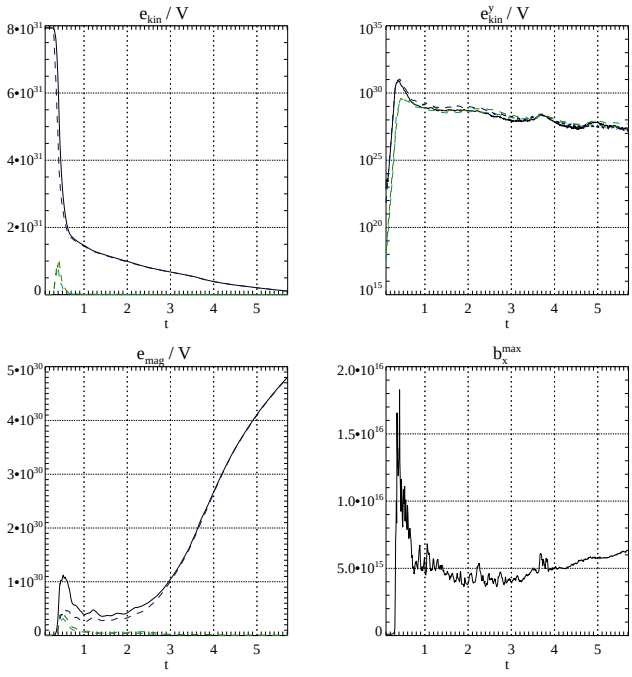

Figure 5.23: Same as Fig. 5.16, but for model mKH3-5.

the need for very fine grids to properly resolve the dynamics in case of small initial fields. Since we cannot afford infinite resolution, our models fall into two categories, viz. the ones which are converged (initially strong fields) and the ones far from convergence (initially weak fields).

We start the discussion with the converged models, i.e., the ones belonging to the disruption regime. In these cases, the maximum field strength and the dynamics are dictated by true physical effects rather than by the numerics, and, thus, the values we find are close to the physical ones. The maximum field strength is confined to thin flux ropes interacting with each other by tearing-mode reconnection. By virtue of these reconnection events, the field reacts back on the dynamics despite its significantly sub-equipartition strength. This backreaction prevents further growth, and hence limits the field strength.

In all of these models, we find maximum field strengths that are similar to the values found by Price & Rosswog (2006), i.e., of the order of several 10^{15} G, and transiently even stronger. On grounds of a kinematic analysis, i.e., neglecting the backreaction of the field onto the dynamics, Price & Rosswog (2006) estimated saturation fields of the order of $10^{16...18}$ G. The maximum field strengths of our models are at the lower end of this range, near the kinetic equipartition field. As the field lines are reconnected by tearing modes, the velocity decreases and the flow geometry is changed globally. The maximum magnetic field still remains near kinetic equipartition, thus decreasing with the kinetic energy. Consequently, in none of our models do we find sustained amplification to the enormous field strengths estimated by Price & Rosswog (2006) as upper bounds of amplification. Due to the intermittency of the fields, the mean magnetic fields are even considerably weaker. The reason for the discrepancy between our simulations and the kinematic estimate is that, by local backreaction of the field onto the flow, a very short and localised development of equipartition fields changes the flow globally such that the kinematic equipartition values based on the unmodified shear flow no longer apply.

If the field is too weak to impact the dynamics, i.e., if we are in an essentially HD or in the weak

dissipation limit, the field is amplified linearly. We observe amplification by approximately two orders of magnitude. Maximum field strengths are at most of the order of 10^{15} G, again confined to thin flux ropes. In these cases, the field amplification is limited not by physical effects but rather by the numerical resolution. Having in mind our resolution studies for non-dimensional models, we argue that, for sufficient (but unaffordable) resolution, the models enter the disruptive regime, and the field strength is again limited to near-equipartition values by reconnection in tearing modes and the resulting backreaction on the flow.

We note that the initial field strengths we require for the disruption regime given our typical grid resolution are already extremely large and most probably not representative for merging NS. On the other hand, based on our resolution studies, we argue that weaker initial fields will be amplified locally in thin flux sheets to a similar strength than these fields, although the amplification may require more time.

This result may seem disappointing, if one expects the creation of extreme magnetic fields at the contact surfaces of merging NS and a subsequent large impact of the magnetic fields on the dynamics of the merger. However, they can also be interpreted in a more optimistic way: the results highlight the possible dynamic importance of magnetic fields globally far below equipartition and point out the necessity of a self-consistent dynamic MHD modelling of merger events with high-order numerical methods and very good spatial resolution.

5.2 Magneto-rotational instability

THE MAGNETIC FIELD STRENGTH IS PROPORTIONAL TO OUR IGNORANCE.

John Hawley

5.2.1 Physical motivation

Our goal is to investigate the non-linear evolution of the MRI in the context of post-collapse SN cores. Using semi-global *shearing disc* simulations, we want to focus on the field amplification and the turbulence due to the instability, and to study the transport properties of the turbulent magnetic and flow fields. The most important question we will address is whether or not the MRI can develop, leading to field amplification, turbulence and enhanced transport, under the conditions of a SN core.

The study of MRI-unstable systems relies on *global* (or large-scale) as well as *local* simulations. Global simulations model the entire system (e.g., an accreting BH and the surrouding disc). They can address questions such as the influence of the overall disc geometry and the interaction with the surrounding medium. On the other hand, limited computational resources restrict the resolution of global simulations. Thus, they may not be able to accurately follow the evolution of the instability on small spatial scales. Local simulations, in contrast, focus on a small part of the system. Assuming generic conditions and replacing the surrounding matter by BCs, they allow one to use much finer grids and, thus, to explore the onset of the instability and the transition to turbulence in great detail.

A particularly useful tool of the local analytic and numerical analysis of shear instabilities in discs and stars is the *shearing sheet* technique. This technique applies a transformation to a frame of reference co-rotating with a representative region of the disc or star. We cover the region by

a Cartesian grid. Due to the co-rotation, the gravitational and the centrifugal forces cancel. The Coriolis force is retained but further effects of the rotation are ignored. This method is limited to systems without global gradients of, e.g., density or entropy. Thus, we use a modification accounting for such gradients, viz. the shearing disc technique (Klahr & Bodenheimer 2003), which will be explained later.

Linear theory Investigations of the stability of a (weakly) magnetised differentially rotating fluid by Velikhov (1959); Chandrasekhar (1960) and later by Balbus & Hawley (1991); Hawley & Balbus (1991, 1992); Balbus & Hawley (1992a,b) revealed the existence of the MRI as a powerful local linear[1] shear instability. Further insights into the stability properties of such a system were gained by Acheson (1978); Balbus (1995, 2001), extending the analysis also to situations involving density or entropy stratifications. The analysis carried out by these authors is fairly general. It covers both the parameter regimes most applicable to accretion discs (supported by Keplerian rotation, little influence of pressure stratification) and to stars (predominantly supported by pressure, entropy gradients important). For a comprehensive review of the MRI, we refer the reader to Balbus & Hawley (1998).

Since the instability is a local one, its linear evolution is typically studied by means of *WKB analysis*. This technique consists of determining the dispersion relation of wave-like perturbations of the form

$$Ae^{i(\vec{k}\cdot\vec{x}-\omega t)} \tag{5.3}$$

to the linearised equations, where A is the amplitude of the perturbations. From the dispersion relation, one can then read off the conditions for exponential growth of the perturbations and the growth rates as a function of wave number.

Non-magnetic instabilities Without magnetic fields and ignoring the effects of stratification, the linear stability is determined by the *Rayleigh criterion* (e.g., Tassoul 1978), demanding that, for stability, the specific angular momentum of the flow, $j = \varpi^2\Omega$, has to increase with distance from the rotational axis ϖ,

$$\partial_\varpi j > 0 \Rightarrow \text{stability}. \tag{5.4}$$

In the absence of, e.g., magnetic, forces able to redistribute angular momentum, a fluid element will retain its specific angular momentum j_0 as a perturbation drives it away from its original orbit ϖ_0 to a new radius $\varpi_1 > \varpi_0$. In a flow not satisfying (5.4), the fluid element will experience an additional uplift due to its excess angular momentum w.r.t. the value $j_1 < j_0$ of its new surroundings. This leads to an exponential run-away from the initial orbit, thus triggering an instability. In the opposite case, the restoring force will enable the fluid element to perform stable *epicyclic oscillations* with the epicyclic frequency κ, $\kappa^2 = \frac{1}{r^3}\partial_r\left[(r^2\Omega)^2\right]$, around its orbit.

On the other hand, the stability of a non-rotating, non-magnetised stratification is determined by the *Schwarzschild criterion* (e.g., Tassoul 1978)

$$\partial_r s > 0 \Rightarrow \text{stability}, \tag{5.5}$$

for the entropy s. If the stratification is unstable according to (5.5), the ensuing *buoyancy instability* (the analogous instability for incompressible fluids is the *Rayleigh-Taylor instability*) will quickly lead to convection. Please note that in the presence of composition gradients, the criterion has

[1] i.e., an instability of the linearised MHD system

to be modified; we will not consider this issue here, though important in global SN simulations, because of the simplified microphysics we employ in this study.

Considering a more general system involving both differential rotation and stratification, we can combine both criteria in the *Solberg-Høiland criterion* (e.g., Tassoul 1978), which for an EOS of the form $P \propto \rho^{\Gamma}$ reads

$$\left\{\begin{array}{ll} N^2 + \frac{1}{\varpi^3}\partial_\varpi j^2 & > 0 \\ (-\partial_z P)\left(\partial_\varpi j^2 \partial_z \ln(P\rho^{-\Gamma}) - \partial_z j^2 \partial_\varpi \ln(P\rho^{-\Gamma})\right) & > 0 \end{array}\right\} \Rightarrow \text{stability}, \tag{5.6}$$

where we introduced the *Brunt-Väisälä* or *buoyancy frequency*,

$$N^2 = N_\varpi^2 + N_z^2 = -\frac{1}{\Gamma\rho}\vec{\nabla}P \cdot \vec{\nabla}\ln(P\rho^{-\Gamma}). \tag{5.7a}$$

The Brunt-Väisälä frequency can be written in terms of the component-wise partial frequencies:

$$N_i^2 = -\frac{1}{\Gamma\rho}\partial_i P \cdot \partial_i \ln(P\rho^{-\Gamma}), \;\; i \in \{\varpi, z\}\,. \tag{5.7b}$$

In a convectively stable system, perturbed fluid elements will undergo stable oscillations at the Brunt-Väisälä frequency $N^2 > 0$, whereas in an unstable system, N^2 is negative.

If any of these HD instabilities is encountered, the evolution will tend towards a marginally stable state. The convection in a Schwarzschild-unstable system and the Rayleigh instability, e.g., will lead to a distribution of constant entropy and constant specific angular momentum, respectively.

MHD instability criteria An important concept in understanding the fundamental difference between magnetic and non-magnetic instabilities is the *free energy* of the rotating (or stratified) system (Balbus & Hawley 1998). This is the difference between the total energy of the (equilibrium) system and the minimum energy of all configurations with the same values of conserved quantities such as mass and angular momentum. If the free energy is positive, and the system has a path to relax to the configuration of least total energy, it will generally do so, and in many cases, the relaxation will be mediated by an instability feeding off the free energy reservoir.

The relaxed state consistent with a rotating disc is a concentration of all of the mass at the accretor and a dispersion of all of the angular momentum to infinity. The free energy reservoir is the gradient in angular velocity. Thus, even if a differentially rotating configuration is stable according to the Rayleigh criterion, (5.4), it will not have the minimum energy of all attainable configurations. The reason why it is nevertheless stable is that purely ideal hydrodynamical forces cannot tap the rotational free energy because they do not provide any means of redistributing angular momentum, which would be necessary for reaching the ground state. Instead, these forces only drive the system towards the minimum energy of a more restricted set of possible states, viz. all configurations with the same mass, total angular momentum and conserved specific angular momentum of all fluid elements.

Similarly, the relaxed state of a thermally stratified fluid is a medium of constant temperature, and the free energy source is the temperature gradient. This state is not in general attainable under the conditions of ideal hydrodynamics due to the lack of entropy redistribution mechanisms. Thus, the system will not evolve to the ground state, but rather to the marginally Schwarzschild-stable state.

We want to point out that neither viscous forces nor thermal conduction change this situation qualitatively as they act isotropically. They do not provide any spatial coupling, which, as we shall see, is required for allowing the fluid to overcome the limitations enforced by the conservation of specific angular momentum or temperature of the perturbed fluid element. Instead, by providing an exchange of angular momentum or entropy with the surroundings at the perturbed location, they tend to damp the instability.

By virtue of the Maxwell stresses, a magnetised fluid has additional paths of tapping free energy that are not available to a non-magnetised fluid. Hence, the presence of magnetic fields, however weak, brings about important modifications of the above criteria, e.g., differentially rotating Keplerian discs may suffer a rotational instability in the presence of a magnetic field while being stable if non-magnetised. In the following paragraphs, we will explain these modifications. We note that the modifications of the thermal (Schwarzschild) instability criterium are mainly relevant when thermal conduction plays an important role in a dilute plasma. Since we are not primarily interested in such a situation, we will focus mainly on rotational instabilities, and only briefly touch the convective ones.

If a fluid element in a differentially rotating magnetised system is perturbed, e.g., uplifted to a radius ϖ_1, it will remain connected to the neighbouring elements in its original orbit (radius $\varpi_0 < \varpi_1$) by magnetic field lines. The magnetic stresses will enable angular-momentum transport along these field lines and enforce co-rotation between the fluid element and its original orbit rotating at an angular velocity Ω_0. Hence, the uplifted fluid element will retain its angular velocity rather than its angular momentum. As a result, the fluid element will experience an additional uplift, if its angular velocity Ω_0 is larger than the one required for an equilibrium at the new location, Ω_1. Since this is the angular velocity of the background equilibrium flow, the magneto-rotational (*Balbus-Hawley)* instability condition is

$$\partial_\varpi \Omega > 0 \Rightarrow \text{stability}. \tag{5.8}$$

If a magnetic field is "switched on" in a Rayleigh-stable but Balbus-Hawley-unstable flow, the stable epicyclic oscillations will be destroyed by the field. An unstable perturbation will grow exponentially; in particular, the magnetic field will be amplified, leading to an exponentially increasing transport of angular momentum. In a disc, this does not necessarily lead to a state of uniform rotation. Instead, it enables efficient accretion, concentrating the mass in the centre while transporting the angular momentum to infinity.

A particularly interesting property of (5.8) is that it does not depend on the magnetic field. However weak, any field will destabilise a differentially rotating system violating (5.8). There is no possibility to recover the hydrodynamic Rayleigh criterion from the magnetic one by taking the limit $b \to 0$.

To derive the modifications of the thermal instability due to MHD effects, Balbus (2001) assumed a Coulomb thermal conductivity, which is entirely suppressed across field lines. Using similar arguments he showed that, in this case, it is not the entropy gradients, but the temperature gradients that determine the stability of a stratified fluid. The Schwarzschild criterion must be modified yielding

$$\partial_r T > 0 \Rightarrow \text{stability}. \tag{5.9}$$

The physical agent behind this modification is the channelling of the thermal conduction along the field lines connecting a perturbed fluid element to its original surroundings. The applicability to the dense gases we are interested in is quite limited. Thus, we will not consider this aspect any longer, but rather apply the standard criteria for thermal instability.

Rotational and thermal instability are only special cases of the same MHD instability rather than two independent instabilities. Balbus (1995, 2001); Menou et al. (2004) derived the general dispersion relations treating the cases on a common ground. Balbus (1995) included a thermal stratification into the original magneto-rotational instability, but still restricted his analysis to adiabatic processes, in which the entropy of a displaced fluid element is conserved. This restriction was lifted by Balbus (2001), who included thermal conductivity as described above. Finally, Menou et al. (2004) added viscosity and resistivity to the analysis, arriving at a fairly complex dispersion relation. Because we are not primarily interested in diffusive processes, we will limit our scope to the Balbus (1995) results. The corresponding instability criterion replacing the non-magnetic Solberg-Høiland criteria, (67), is given by

$$\left\{\begin{array}{ll} N^2+\frac{1}{\varpi^3}\partial_\varpi\Omega^2 & >0 \\ (-\partial_z P)\left(\partial_\varpi\Omega^2\partial_z\ln(P\rho^{-\Gamma})-\partial_z\Omega^2\partial_\varpi\ln(P\rho^{-\Gamma})\right) & >0 \end{array}\right\} \Rightarrow \text{stability}, \tag{5.10}$$

i.e., exactly the same expressions, but with the specific angular momentum replaced by the rotational velocity. In the limit of a constant-entropy fluid, (5.10) is the classical Balbus-Hawley criterion. A convectively stable entropy gradient may, however, stabilise the MRI, whereas in a convectively unstable stratification, a combined magneto-rotational and magneto-convective instability will occur.

MHD instability growth rates We will now discuss perturbations of the form of Eqn. (5.3) to an equilibrium initial state. From the analysis of the linear dispersion relation, we can determine the growth rates as a function of wavenumber. A common dispersion relation for both limits, the magneto-rotational one and the magneto-convective one, can be given (Balbus 1995; Balbus & Hawley 1998):

$$\omega^2=\frac{k^2}{k_z^2}\tilde{\omega}+\tilde{\omega}^2\left(\frac{1}{\Gamma\rho}\mathscr{D}P\mathscr{D}\ln(P\rho^{-\Gamma})+\frac{1}{\varpi^3}\mathscr{D}(R^4\Omega^2)\right)-4\Omega^2\left(\vec{k}\cdot\vec{c}_{\rm A}\right)^2, \tag{5.11a}$$

where ω and $k=2\pi/\lambda$ are the complex frequency and the wave number of a mode of wave length λ, respectively. In Eqn. (5.11a), we used the following function of the mode frequency and the wave number

$$\tilde{\omega}^2=\omega^2-\left(\vec{k}\cdot\vec{c}_{\rm A}\right)^2, \tag{5.11b}$$

and the $\mathscr{D}$ operator

$$\mathscr{D}=\frac{k_\varpi}{k_z}\partial_z-\partial_\varpi. \tag{5.11c}$$

We will discuss some important properties of the dispersion relation in the following.

1. An important observation is that in (5.11a) the wave number k only appears multiplied with the Alfvén speed $c_{\rm A}$. Thus, typical length scales of the instability will depend linearly on the field strength. The product $kc_{\rm A}$ has the dimension of a frequency; it is the inverse Alfvén crossing time across one wave length of the mode.
2. We can derive the instability criterion, Eqn. (5.10), from the dispersion relation by searching for solutions of (5.11a) under the condition of marginal stability, $\omega=0$. If there is no such solution, then the system will be completely stable; otherwise, we will be able to identify regions of $kc_{\rm A}$ in which perturbations grow exponentially.

3. The instability criterion does not involve the magnetic field, and there is not continuous transition from the MHD to the HD criteria as $|\vec{b}| \to 0$. Thus, any magnetic field, no matter how weak, will require us to use the MHD rather than the HD stability criterion.
4. In an unstable system, not all wave numbers will be affected by the instability; instead, only long modes with
$$\left(\vec{k}\cdot\vec{c}_{\mathrm{A}}\right)^2 > \left(\vec{k}\cdot\vec{c}_{\mathrm{A}}\right)^2_{\mathrm{crit}} = N^2 - \frac{\partial\Omega^2}{\partial\ln\varpi} \tag{5.12}$$
will grow exponentially. In the last equality, we assumed that the perturbation is oriented in z direction, $k_\varpi = 0$. If the Alfvén crossing time for a given mode is smaller than a timescale set by the angular-velocity or entropy gradients of the system than the field can react quickly enough to the perturbations to resists being bent. Thus, short wave lengths are stabilised by magnetic tension. This is in contrast to the non-magnetic analogue of the dispersion relation (Goldreich & Schubert 1967) which does not depend on the modulus of the wave vector but only on its direction. In this case, instability prevails even for the shortest modes.
5. For the two limiting cases of instability solely due to angular-velocity gradients (*magneto-rotational modes*) and entropy gradients (*magneto-convective modes*), the dispersion relation is quite different:
   (a) In the magneto-rotational limit, the growth rate approaches zero for very long modes, i.e., $\lim_{\lambda\to\infty}\omega = 0$, and assumes a rather sharp maximum at
   $$(kc_{\mathrm{A}})^2_{\mathrm{max}} = -\left(\frac{1}{4} + \frac{\kappa^2}{16\Omega^2}\right)\frac{\partial\Omega^2}{\partial\ln\varpi} \tag{5.13a}$$
   Wave lengths larger than then the one given by (5.13a) are unstable, but their growth rate is rather small. The maximum growth rate is
   $$\omega_{\mathrm{max}} = \frac{1}{2}\left|\frac{\partial\Omega}{\partial\ln\varpi}\right|. \tag{5.13b}$$
   As a consequence, the wavelength of maximum growth, λ_{max} is proportional to the square root of the magnetic field strength, $\lambda_{\mathrm{max}} \propto B$. This growth rate is independent on the field strength; only the wave number for which it is assumed is a function of B. For small magnetic fields, the wave number of maximum growth corresponds to quite small spatial scales. Attempting to simulate the growth of such a mode, we have to resolve it by a few (~ 5) grid points. This puts a very severe restriction on global simulations because they require to cover a large range of length scales from the ones of the global system down to the fastest growing modes. As a consequence, we study the MRI using local simulations that focus on the small scales and disregard the large scales.
   (b) In the magneto-convective limit, the growth rate remains finite even in the limit $k \to 0$. Thus, large-scale simulations do not have any problems in resolving the instability.
6. Why is there no continuous transition from the MRI criterion to the non-magnetic Rayleigh criterion, if the field is negligible w.r.t. the angular velocity or the pressure?
   (a) From the scaling of spatial scales with the magnetic field, this can be understood in the following way: the maximum growth rate does not depend on the field strength; instead, for weaker fields, fast growth occurs for smaller length scales ($\lambda_{\mathrm{max}} \propto B$) because the weaker field can only provide an efficient connection of a perturbed fluid element to its original location over smaller scales. Nevertheless, this connection is present and able to mediate the instability.

(b) Thus, in the limit of vanishing field, $B \to 0$, all wavelengths are unstable and the fastest growth occurs at the same rate as for a finite field strength. This is true for ideal MHD. Viscosity and resistivity, however, stabilise the MRI in this limit (Balbus & Hawley 1998).

(c) As noted by Balbus & Hawley (1998), if we neglect viscosity and resistivity, the MRI is an instability of the Alfvén wave. The Alfvén wave is a pure MHD wave with no HD equivalent. As it is not compressional, the gas pressure does not play any role in Alfvén waves. Therefore, the exact ratio of the magnetic to the thermal pressure is of no importance to the evolution of an Alfvén wave, or its unstable version, an MRI mode. Hence, there is no weak-field limit of the MRI criterion that continuously approaches the Rayleigh criterion.

In Fig. 5.24, we summarise the behaviour of modes of different wavelength as a function of the magnetic field strength for a given Keplerian rotational profile. All modes with a wavelength longer than the one corresponding to $(kc_\mathrm{A})_\mathrm{crit}$ are unstable (coloured region). The fastest growth occurs at the wavelength corresponding to $(kc_\mathrm{A})_\mathrm{max}$ (marked by the black line). The maximum growth rate is independent of the field strength. The growth rate at a given λ, on the contrary, depends on the field strength. For very weak fields, only short wavelengths grow at a large rate.

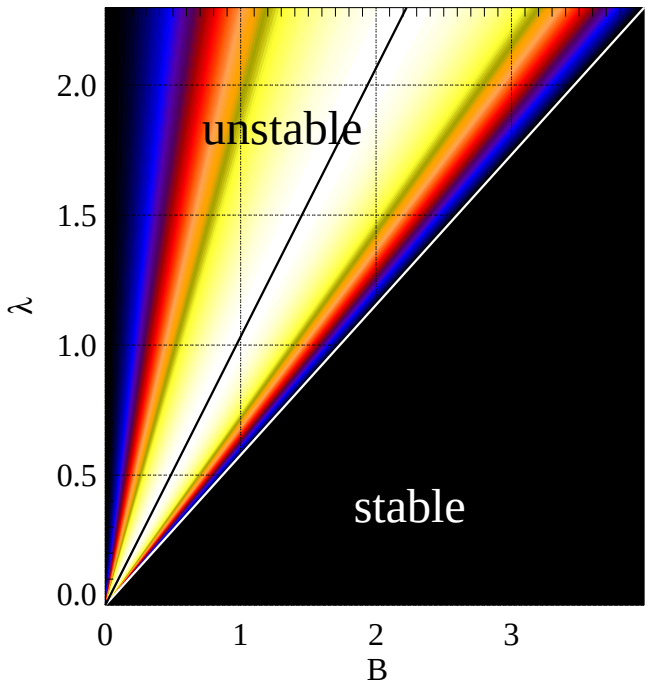

Figure 5.24: The region of instability of the MRI for a Keplerian rotational profile. We assume a density of 1 and a radius of $\varpi = 1$. The magnetic field strength B and the wavelength λ are given in units of the equipartition field with rotation and the radius, respectively. For given magnetic field strength B, all modes with a wavelength λ in the coloured region are unstable. The growth rate of the instability is colour-coded, with black and white colours corresponding to slow and fast growth, respectively. The region below the white diagonal line is stable. The line of maximum growth is indicated by a black line.

Non-linear evolution As the perturbation amplitudes become large compared to the background, the exponential growth of the instability passes into the non-linear saturation phase. This stage is characterised by turbulent velocity and magnetic fields giving rise to enhanced transport of angular momentum. Unlike the linear phase, the saturation phase cannot be treated reliably using analytic methods; instead, numerical simulations have to used. The main focus of such studies lies on the saturation field strengths and velocities, the resulting turbulent stresses, and their dependence on the conditions of the background flow.

Notable differences exist between two- and three-dimensional systems, and a dependence on the initial field geometry can be established. In 2d simulations, Hawley & Balbus (1991) observed the emergence of *channel flows*, a pattern of alternating inflows and outflows from the instability of a uniform field, $\vec{b} = (0,0,b_z)^T$. This particular flow field, typical for the linear phase, does not evolve into a state of turbulence; instead, the channel flows persist into the saturation state. They are accompanied by a strong growth of the field. If the initial field is not uniform in z direction but has a vanishing z flux (e.g., a sinusoidal profile $b_z(\varpi)$), then turbulence will set in and the field, after an intermediate phase of growth, will decay. Cowling's anti-dynamo theorem lies at the heart of the difference between these two cases. The theorem forbids any axisymmetric dynamo in an isolated system, thereby precluding sustained field growth in the second case. A uniform background field, on the other hand, connects the system with its surroundings and thus breaks the isolation of the system.

Goodman & Xu (1994) proved that the axisymmetric channel-flow MRI modes are exact solutions of the *non-linear* local (i.e., shearing sheet) incompressible MHD equations explaining the presence of the channel flows even in the non-linear regime of the instability. They showed, however, that the channel flows represent an unstable solution subject to secondary "parasitic" instabilities such as the KHs instability which cause the flow to quickly becomes into turbulent. This is observed in three-dimensional simulations (e.g., Hawley et al. 1995, 1996; Stone et al. 1996; Brandenburg et al. 1995), which enter a turbulent stage after the linear growth phase. The evolution of the channel solutions was later investigated in detail using numerical simulations by Sano & Inutsuka (2001); Sano (2007). These authors found that, though unstable in three-dimensional simulations, coherent channel flows can recurrently develop from the turbulent state of a three-dimensional model. In such cases, they lead to a transient enhancement of the field strength and the angular-momentum transport before they again decay due to magnetic reconnection.

The turbulent saturation phase is characterised by enhanced angular-momentum transport coefficients resulting from the Reynolds stress $v_i v_j$ as well as the Maxwell stress $b_i b_j$. Local simulations showed that the Reynolds stress transporting angular momentum inwards is compensated for by the outward transport due to the Maxwell stress by a factor of ~ 4 enabling efficient accretion. These results were confirmed by various local simulations (e.g., Sano et al. 2004) of accretion discs. Based on the simulations by Sano et al. (2004), Pessah et al. (2007) established scaling laws for the dependence of the Maxwell stress on physical (gas pressure and scale height) as well as numerical (grid resolution and domain size) parameters of the system.

Applications and open questions: accretions discs vs. stars The most important application of the MRI thus is the explanation of the enhanced angular-momentum transport in accretion discs. Though in special cases, there might be alternative explanations, the MRI is assumed to be the most universal mechanism responsible for creating the turbulent stresses in accretion discs.

Since differential rotation and magnetic fields are present in many stars as well, the MRI might play a role there, too. On the other hand, stellar structure and evolution is much less dominated

by rotation than discs are. Additionally, large entropy gradients in stars may provide either stabilisation or destabilisation which is not the case for a Keplerian disc. Thus, the results obtained for discs are not necessarily applicable to stars.

Estimates of the saturation amplitude of the magnetic field for the MRI in supernova cores were given by Akiyama et al. (2003). They assume that the field is amplified up to a significant percentage of the equipartition field, for which the magnetic energy density would be the same as the rotational energy density. This hypothesis, though appealing, still lacks confirmation by detailed numerical simulation. Our goal, thus, is to investigate the MRI in the system of a post-collapse stellar core. We seek to address the following questions:

1. Given typical conditions in such a core, does the MRI grow on timescales reasonably short w.r.t. the evolution of the core, i.e., a few 10 ms?
2. What are the saturation fields? In particular: do we observe dynamo action?
3. Do we find enhanced transport of angular momentum? Does the transport occur on timescales relevant to the dynamics?

5.2.2 Initial and boundary conditions

General setup We perform local simulations in 2d or 3d using a given rotational profile, and varying the entropy gradient, the initial field strength and geometry, and the grid size and resolution. We use the full MHD equations instead of the shearing sheet technique, because the shearing sheet equations do not allow for global radial gradients other than differential rotation. Our simulations start from an approximate equilibrium state similar to a post-collapse stellar core and follow the evolution into the non-linear phase. We assume a simplified hybrid EOS and neglect neutrino physics.

Initial conditions We construct the initial state of our simulations as equilibrium models with a given gravitational potential $\varphi(\varpi)$ taken from post-bounce states of our models for magneto-rotational collapse (Obergaulinger et al. 2006b) (the "background model"). We selected model A1B3G3 for the construction. The corresponding pre-collapse model is a rigid rotator with a rotational energy of 0.9% of the gravitational energy. The post-collapse rotational period of this models is $\sim 2.\,\mathrm{ms}$. Since we only simulate a small patch of the core (the grid size is a few kilometres in each direction), we hold the gravitational potential ϕ constant during the simulation.

Our computational grid is centred at $\varpi_\mathrm{c} = 15.5\mathrm{km}$ in the equatorial plane of the model and extends over $\Delta\varpi \in \{1\mathrm{km}, 2\mathrm{km}\}$. The vertical and azimuthal extents of the grid are $\Delta z = \Delta\varpi$ and $\varpi_\mathrm{c}\Delta\phi \in \{1\mathrm{km}, 2\mathrm{km}, 4\mathrm{km}\}$. To compute the initial model, we map the gravitational potential at the equator of the basic model to our grid, disregarding any dependence on z. We specify the rotational profile and the maximum density $\rho_\mathrm{max} \sim 2...3 \times 10^{13}\,\mathrm{g\,cm^{-3}}$. We then compute the density profile from the equilibrium condition

$$-\rho\,\partial_\varpi\varphi = \rho\Omega^2\varpi - \partial_\varpi P, \tag{5.14a}$$

assuming that the pressure depends upon the density according to the hybrid EOS (see sect. 2.1.2) and that the entropy profile $s(\varpi)$ is characterised by a constant part s_0 and a radial derivative $\partial_\varpi s$. The rotational profile is given by

$$\Omega = \Omega_0(\varpi/\varpi_0)^{\alpha_\omega}. \tag{5.14b}$$

In both profiles, we set $\varpi_0 = 15\mathrm{km}$. We set the angular velocity to $1900\,\mathrm{s^{-1}}$ at $15.0\,\mathrm{km}$, and the exponent of the Ω profile to -1.25. The rotational of our initial model is similar, but somewhat

slower, than in model A1B3G3 at a radius of 15 km. The resulting density profile has a mean value of $\approx 2.5 \times 10^{13}\,\mathrm{g\,cm^{-3}}$ and a scale height $H_\rho \approx 3.8\,\mathrm{km}$. We show the resulting profiles for a typical equilibrium background model in Fig. 5.25. This model lives in a radial domain of $\varpi \in [14.5\,\mathrm{km}, 16.5\,\mathrm{km}]$ and has vanishing entropy.

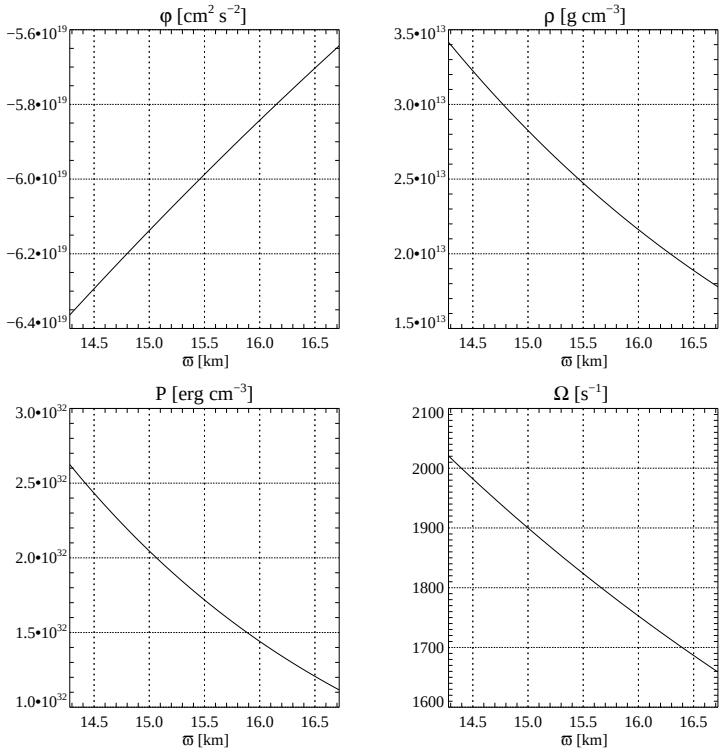

Figure 5.25: Radial profiles of one of our MRI background models. The panels show (left to right, top to bottom) the gravitational potential, the density, the gas pressure, and the angular velocity as a function of radius, respectively.

We add a magnetic field of on of the following simple geometries:

1. a uniform field in z direction,
2. a field in z direction with vanishing flux,
3. a uniform toroidal field.

To trigger the instability, we add ϖ and z velocity components varying randomly or sinusoidally with an amplitude of $\approx 2.5\%$ of the ϕ component. Except for this perturbation, our initial data do not depend on the z coordinate. In the equatorial plane, this is a valid approximation.

Boundary conditions The BC, in particular the radial ones, deserve special mention. We apply periodic BC in ϕ and z directions; for testing the influence of these boundaries, we performed also test runs with reflecting z boundaries, but we did not find a major influence of these settings on the solution.

We treated the radial boundaries using the shearing disc method (Klahr & Bodenheimer 2003), a variant of the shearing sheet method (Hawley et al. 1995). shearing sheet boundaries are essentially periodic BC that take into account the shearing of the inner and outer surface of the grid due to differential rotation. Instead of copying an inner zone along its radial ray to the outer grid ghost

zones, we transport the zone to a location in the outer ghost zones that is shifted in the azimuthal direction by a certain offset $\delta\phi$. The offset is given by the difference of the unperturbed inner and outer angular velocities (Ω_i and Ω_o) and the time t,

$$\delta\phi = (\Omega_\mathrm{o} - \Omega_\mathrm{i})t; \tag{5.15}$$

which is zero at the start of the simulation and grows in time, consistently with the differential rotation.

The shearing disc boundaries additionally account for global gradients of the MHD variables which violate the periodicity of the shearing sheet. Please note that a global angular-velocity gradient is consistent with the shearing sheet simulations. It does not demand a treatment according to shearing disc boundaries, because the gradient of the angular velocity does not appear in the co-rotating shearing sheet equations. However, because we do not use the shearing sheet equations, we have to include the Ω-gradient in our simulations explicitely; thus, we must apply shearing disc boundaries even when there are gradients in ρ, s, or other variables. We have to perform two subsequent steps to apply the boundary conditions:

1. First, we apply the standard shearing sheet boundaries to obtain preliminary values of the MHD variables in the ghost zones.
2. We then apply scaling laws to these variables, e.g.,

$$u_{r+i} = u_{l+i}\alpha^u, \tag{5.16}$$

where r, l and i are the indices of the right and left grid boundary and a cell index, respectively, and α^u is a scaling parameter. We obtain this parameter from the scaling law of the unperturbed background state u. As an example, for the angular velocity of a Keplerian disc ($\Omega \propto \varpi^{-3/2}$), $\alpha^\Omega = (\varpi_{r+i}/\varpi_{l+i})^{-3/2}$. The only exception from this law is the radial velocity, v_ϖ, where we do not take the scaling law from the unperturbed state, yielding $\alpha^{v_\varpi} = 1$, but rather impose the constraint of mass conservation: the mass fluxes ρv_ϖ at the inner and at the outer boundary must be equal. Thus, we have to scale the velocity by the ratio of the surfaces of the outermost and innermost grid cells, respectively.

We observe that the pseudo-periodic BC can lead to resonant oscillations in radial direction. To suppress these oscillations, we follow the method of Klahr & Bodenheimer (2003) who damp the radial velocity in the innermost and outermost n zones of the grid by a small factor f in each time step, $v_\varpi \rightarrow v_\varpi(1-f)$. Taking $n = 2$ and $f = 0.0125$, we do not see any indications of such oscillations.

Finally, we want to note an important difference between shearing sheet and shearing disc simulations: performed in a co-rotating Cartesian box without any global radial gradients (the differential rotation is represented by the BC and cannot be altered significantly), a shearing sheet simulation is essentially local, whereas a shearing disc simulation, retaining all global gradients, may allow for a modification of these gradients. In particular, angular-momentum is conserved only approximately, and, thus, the differential rotation profile can be distorted by the angular-momentum transport due to MRI. In case of very vigorous transport, such modifications can lead to significant differences between shearing sheet and shearing disc simulations as the MRI can react back onto the rotational profile more efficiently in shearing disc simulations. Thus, we may classify shearing disc simulations as *semi-global*.

5.2.3 Results

In this section, we will summarise the most important results from our simulations. We will focus on the field amplification and the Maxwell stresses. In all cases, we observe these quantities to be rather variable in time and space. Thus, we will present averages of these quantities over the entire computational domain and over several rotational periods. One of the main objectives will be to obtain the scaling behaviour of the Maxwell stress with the hydrodynamic profile of the model.

Two-dimensional simulations

Overview of models As a first step, we simulated axisymmetric versions of several models. Comparing in particular the linear phase of these models with results from previous studies, we could confirm that our code is able to follow the growth of the MRI in an unstable system and that the MRI indeed can develop in supernova cores.

The 2d models are summarised in Tab. 5.3 (uniform initial field) and Tab. 5.4 (zero-flux initial field). Since the instability of a toroidal field is generically non-axisymmetric, we only simulate models with either uniform or zero-net-flux b_z field in 2d. In all models, we used a radial domain of $\varpi \in [15\,\mathrm{km}, 16\,\mathrm{km}]$

model name	Ω_0 $\left[\mathrm{s}^{-1}\right]$	α_Ω	s_0	$\partial_\varpi s$	b_0 $\left[10^{12}\,\mathrm{G}\right]$
U2-1	1900	-1.25	0	0	2
U2-2	1900	-1.25	0	0	4
U2-3	1900	-1.25	0	0	6.4
U2-4	1900	-1.25	0	0	10
U2-5	1900	-1.25	0	0	20
U2-6	1900	-1.25	0	0	40
U2-7	1900	-1.25	0.2	0.02	10
U2-8	1900	-1.25	0.2	0.04	10
U2-9	1900	-1.25	0.2	0.08	10
U2-10	1900	-1.25	0.2	-0.1	10^{-8}
U2-11	1900	-1.25	0.2	-0.02	10
U2-12	1900	-1.25	0.2	-0.1	10

Table 5.3: A list of the two-dimensional MRI models with uniform b_z field. The 1st column gives the name of the model, the 2nd and 3rd columns specify the rotational profile, the 4th gives the entropy profile, and the 5th column gives the initial magnetic field, respectively.

Before discussing the results, we introduce the *MRI wavelength*

$$\lambda_{\mathrm{MRI}} = \frac{2\pi c_{\mathrm{A}}}{\Omega} \approx 6.6\,\mathrm{km}\left(\frac{b}{10^{15}\,\mathrm{G}}\right)\left(\frac{\rho}{2.5\times 10^{13}\,\mathrm{g\,cm^{-3}}}\right)^{-\frac{1}{2}}\left(\frac{\Omega}{1900\,\mathrm{s^{-1}}}\right)^{-1}, \tag{5.17}$$

representing the basic scaling length of MRI theory. In Eqn. (77), we expressed λ_{MRI} in terms of typical values of our models. Given by the distance an Alfvén wave travels within one rotational period, λ_{MRI} sets (apart from $\mathcal{O}(1)$ numerical factors) the scale below which perturbations are stabilised by magnetic tension, and determines the fastest growing modes. This has two important consequences:

model name	Ω_0 $[\mathrm{s}^{-1}]$	α_Ω	entropy profile	b_0 $[10^{12}\,\mathrm{G}]$
Z2-1	1900	−1.25	vanishing	2
Z2-2	1900	−1.25	vanishing	4
Z2-3	1900	−1.25	vanishing	10
Z2-4	1900	−1.25	vanishing	20
Z2-5	1900	−1.25	vanishing	40

Table 5.4: A list of the two-dimensional MRI models with zero-flux b_z field. The 1st column gives the name of the model, the 2nd and 3rd columns specify the rotational profile, the 4th gives the entropy profile, and the 5th column gives the initial magnetic field, respectively.

1. Given typical values of the 2d models, we expect a stabilisation for fields of the order of a few $10^{14}\,\mathrm{G}$. This value should set an upper bound to the saturation field strength.
2. We need to resolve an unstable wave length by a few grid cells. Since our grid width is 10...20 m, we expect fast growth only for fields of the order $10^{13}\,\mathrm{G}$ and stronger. For weaker initial fields, the growth rates should be reduced strongly because of the smaller MRI wave length.

Exponential growth, channel solutions and turbulence We, indeed, observe the exponential growth of the MRI in our models. The dependence of the growth rate on the initial field for the uniform-field models U2-1 through U2-6 and a grid spacing of 10 m is depicted in Fig. 5.26. We estimate the grow rate from the growth of the Maxwell stress components $M_{\varpi\varpi}$ and $M_{\varpi\phi}$ near the onset of exponential growth. We notice that the growth rate approaches a value of $\sim 800\,\mathrm{s}^{-1}$ when the field exceeds $\approx 6\times10^{12}\,\mathrm{G}$ ($\lambda_{\mathrm{MRI}}\approx 40\,\mathrm{m}$), and when the most unstable wave length is covered by a few grid cells.

The saturation phase starts when the field perturbation becomes comparable to the background field. Initially, the field is purely vertical; the ϖ component is created solely by the instability and hence is a measure of the strength of the perturbation. Therefore, the begin of the saturation phase can be approximately defined when the energy in b_ϖ becomes as large as the energy in b_z. At this epoch, the growth rate of the instability reduces (see Fig. 5.27), and the growth of the field energy becomes also noticeable in the energy contained in the b_z component.

The growth of the instability eventually saturates. We find, depending on the initial field geometry, the two main ways to saturation identified in previous investigations, albeit with slight modifications owing to our setup: channel flows and break-down into turbulence.

Channel flows The magnetic field provides a means for redistributing angular momentum along field lines connecting different fluid elements. Those fluid elements which loose rotational support by this process will sink down whereas the ones gaining angular momentum will start to rise. Thus, the typical pattern of alternating up- and down-flows comprising a channel flow can be identified in the linear growth phase of models with a non-vanishing b_z flux. As expected from the Goodman & Xu (1994) analysis, these coherent flows are rather stable and persist in the saturation phase. Their vertical wave length and hence their number is defined by b_z and the associated length scale $\lambda^z = \frac{2\pi c_{\mathrm{A}}^z}{\Omega}$. Here, $c_{\mathrm{A}}^z = \sqrt{b_z^2/\rho}$ is the Alfvén velocity corresponding to the b_z component. As the field strength and hence λ^z grows, we observe that the channels merge, only a small number of them surviving.

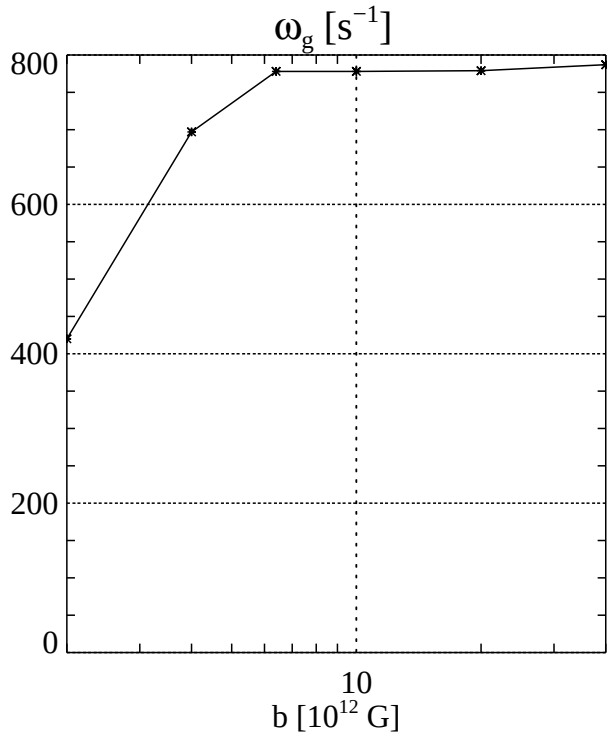

Figure 5.26: The MRI growth rate of models U2-1 through U2-6 as a function of initial field strength. We simulated the models using a grid spacing of 10 m.

We observe this evolution in models of series U2, if the initial field is sufficiently strong for the MRI wavelength to be resolved (see Fig. 5.28 for model U2-6). In these cases, the exponential growth of the instability persists into the saturation phase, although typically with reduced growth rates after the mean field strength of the b_ϖ component has reached that of the b_z component. At $t \approx 5\,\mathrm{ms}$, the growth accelerates again, and after a few ms, the mean Maxwell stress exceeds $10^{30}\,\mathrm{erg\,cm^{-3}}$. Then, the stresses rapidly decrease. Significant amount of angular momentum has been lost from the system during the last growth phase, and this loss persists even further in time.

Initially, the flow pattern consists of a number of densely packed channels of radial motion and field (Fig. 5.29, top right panel). As the field strength and, consequently the MRI wave length setting the vertical extent of the channels grow, the channels merge into less but more extended flows (see Fig. 5.30).

After the final growth phase, we find a large-scale flow consisting of one up-flow and one down-draft (Fig. 5.31). Thus, we recover the two-channel solution of Goodman & Xu (1994). The magnetic stresses, having a notable influence on the rotational profile already during the early evolution (note the perturbations in Ω at $t = 2.4\,\mathrm{ms}$ (Fig. 5.29), completely change $\Omega(\varpi, z)$ by enforcing co-rotation along field lines. The poloidal magnetic field in the channels is mostly radial, and hence since the field enforces the gas to co-rotate on field lines, the rotational profile is changed completely. Instead of a predominantly radial Ω gradient, the angular velocity does depend on z mainly. This disruption is facilitated by the fact that, in our models, the shearing disc boundaries allow for more pronounced accretion and angular-momentum transport than in shearing sheet simulations.

In these late stages, the field has grown to a maximum strength of up to a few $10^{15}\,\mathrm{G}$. Despite

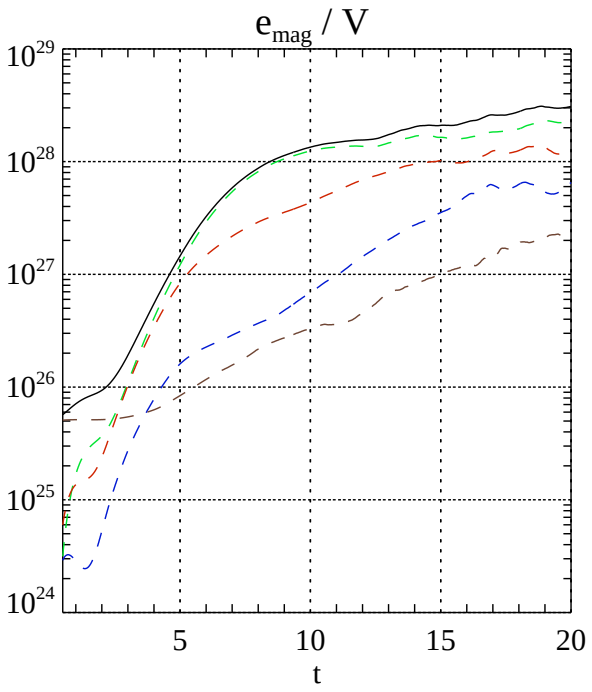

Figure 5.27: The first twenty milliseconds in the evolution of model U2-4. The solid black line displays the mean magnetic energy of the model, $\langle e^{\mathrm{mag}} \rangle = \frac{1}{\mathcal{V}} \int \mathrm{d}\mathcal{V} \vec{b}^2/2$. The dashed blue, green, and brown lines show the mean energy of the ϖ, ϕ, and z components of the magnetic field, respectively. The dashed red line corresponds to the absolute value of the mean Maxwell stress component $M_{\varpi,\phi}$.

the strong and highly ordered fields, the Maxwell stress has a chaotic temporal evolution and a relatively small net value. Hence, no further net angular-momentum transport occurs, as the fields acquire a certain degree of symmetry where positive and negative $M_{\varpi\phi}$ nearly balance each other. As a consequence, the total Maxwell stress $M_{\varpi\phi}$ decreases and oscillates around zero (cf. the red line in the last few milliseconds in Fig. 5.28). Most of the energy in differential rotation has been converted to magnetic energy. Nevertheless, typical values of the ratio of magnetic pressure to gas pressure, β, are much less than unity, at most reaching a few percent.

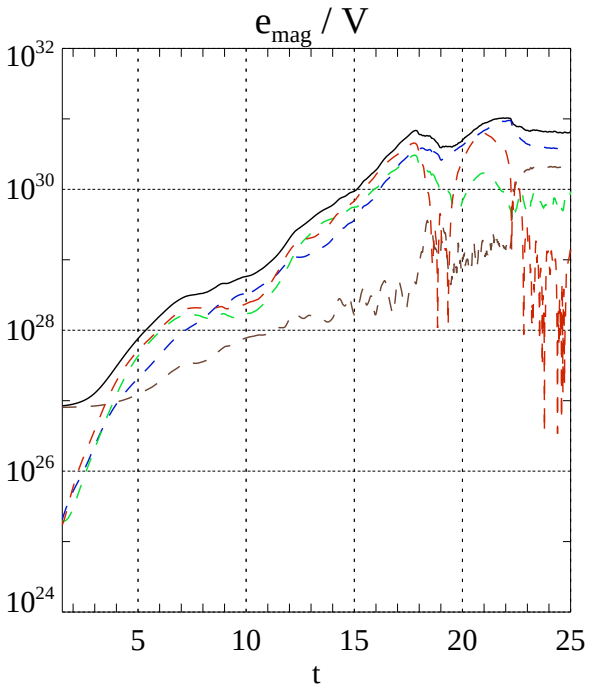

Figure 5.28: Same as Fig. 5.27, but showing the first 25 milliseconds of model U2-6. At late stages ($t \gtrsim 22\,\mathrm{ms}$, $\langle M_{\varpi\phi} \rangle$ oscillates about zero. Since we plot the logarithm of $|\langle M_{\varpi\phi} \rangle|$, changes of the sign of $\langle M_{\varpi\phi} \rangle$ correspond to minima of the red curve.

Turbulence The instability can saturate at a lower level without destroying the rotational profile. This happens if the channel flows are dissolved before reaching the stable state described above. Instead, a state of freely decaying turbulence develops. In model series U2, we observe this phenomenon mainly for weak initial fields for which the instability is under-resolved. To examine such a case, we compare simulations of model U2-3 on grids of 10 m and 20 m resolution. Large-scale channel flows develop in the better resolved model, but not in the one using the coarser grid. Using somewhat stronger or weaker initial fields ($b_z \approx 1 \times 10^{13}\,\mathrm{G}$ and $4 \times 10^{12}\,\mathrm{G}$, respectively), we do not observe such a dependence on the resolution: either both resolutions or none at all yield the two-channel solution.

In model series Z2 which – even for the strongest fields – do not develop stable channel flows, turbulence is the dominant evolutionary path. See Fig. 5.32 for the temporal evolution of model Z2-3.

In these cases, we observe the development of a multitude of flat channel-like flows in the linear

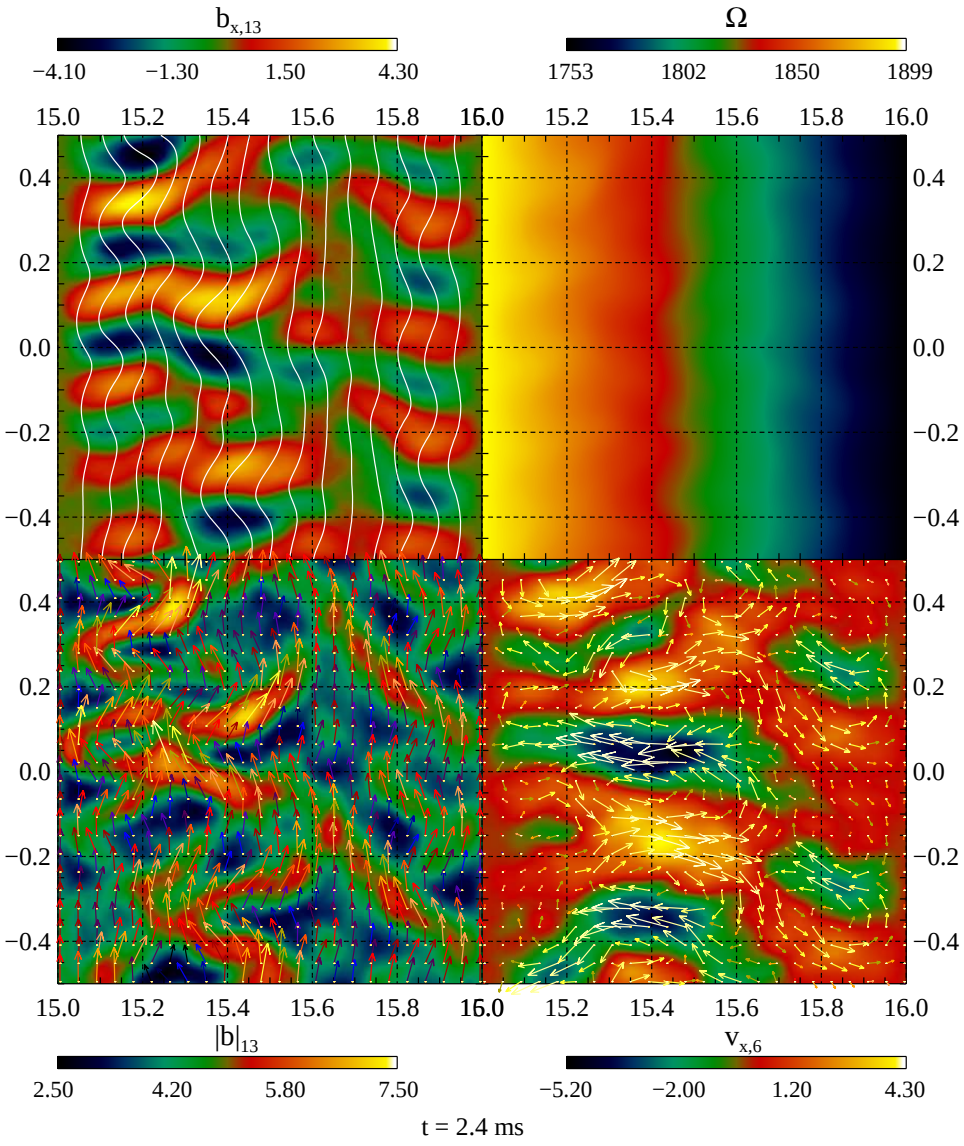

Figure 5.29: Snapshot of model U2-6 at $t = 2.4\,\mathrm{ms}$. The abscissa and ordinate correspond to the ϖ and z axes, respectively, and the coordinates are given in units of kilometres. The top left panel shows the ϖ component of the magnetic field together with magnetic field lines. The top right panel shows the angular velocity. The bottom left panel shows the modulus of the magnetic field strength together with field vectors, and the bottom right panel shows the ϖ component of the velocity and the flow field. The vectors are scaled such that an arrow of length 0.1 km corresponds to the maximum field strength / velocity in the domain. A subscript n to the name of a variable indicates a scaling of the variable by a factor 10^n.

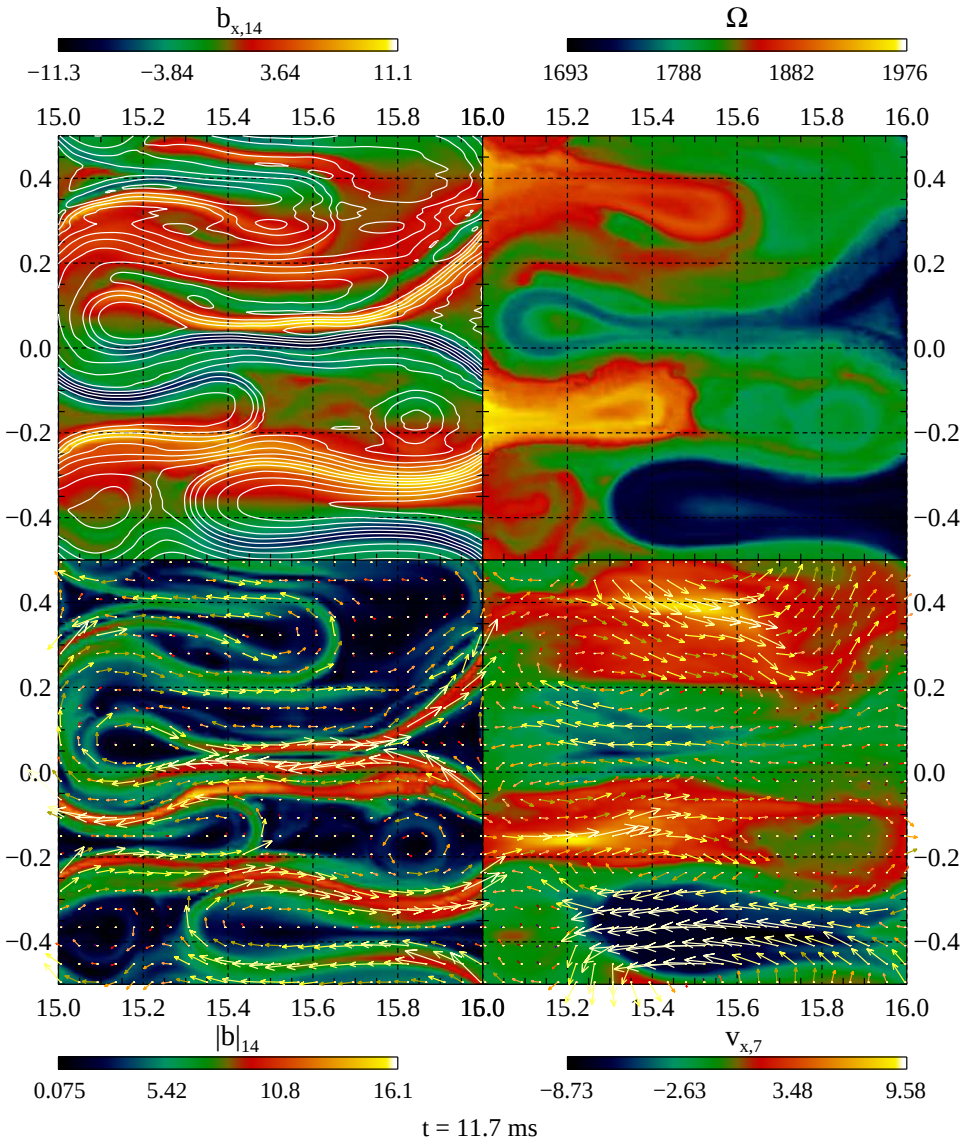

Figure 5.30: Same as Fig. 5.29, but at $t = 11.7\,\mathrm{ms}$.

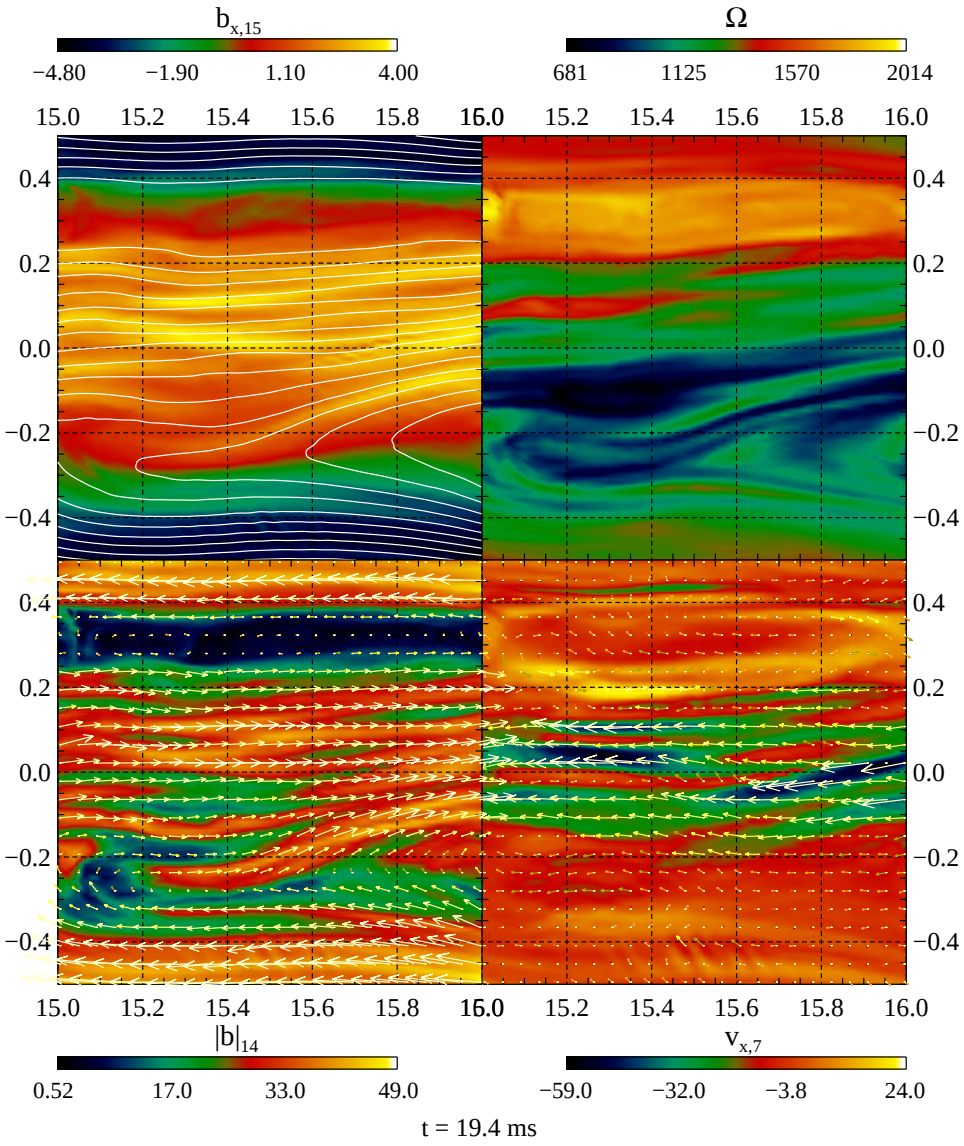

Figure 5.31: Same as Fig. 5.29, but at $t = 19.4\,\mathrm{ms}$.

phase (Fig. 5.33). The height of the channels is approximately given by the MRI wavelength. In the models of series Z2, separate channels develop in the two regions of positive and negative b_z, whereas in uniform-field models, they may span the whole radial range of the box. These flows do not merge to form a few large-scale channels, but, rather, they are prone to instability leading to a complex turbulent flow pattern (Fig. 5.34). On timescales much longer than the time we simulated, the turbulent velocity and magnetic fields will be damped by numerical viscosity. This is a consequence of the *anti-dynamo theorems* forbidding the existence of axisymmetric isolated dynamos (in the case described above, the large-scale z field connecting the box to infinity breaks the isolation).

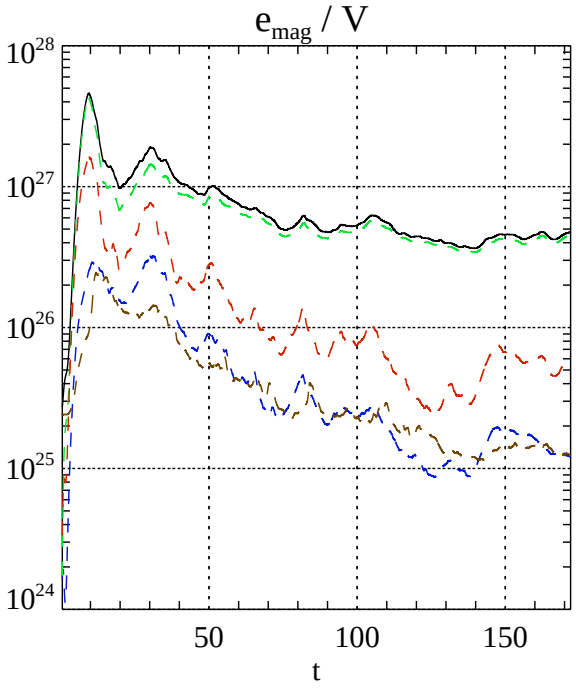

Figure 5.32: Same as Fig. 5.27, but showing the entire time evolution of model Z2-3.

Angular-momentum transport Whereas the appearance of channel flows affects the evolution of the flow drastically, the stresses that result in the turbulent non-channel runs are rather modest. To make an order-of-magnitude estimate of their effects on the rotational profile of the flow, we compute the timescale of angular-momentum transport by the Maxwell stress from the ϕ component of the momentum equation,

$$(\tau_j)^{-1} = \frac{1}{J}\partial_t J = \frac{1}{J}\partial_\varpi \varpi M_{\varpi\phi}. \tag{5.18a}$$

Inserting typical values of our models, we get

$$\tau_j \sim 740\,\mathrm{s}\left(\frac{R}{15.5\,\mathrm{km}}\right)\left(\frac{\Delta R}{1\,\mathrm{km}}\right)\left(\frac{\Omega}{1900\,\mathrm{s}^{-1}}\right)\left(\frac{\rho}{2.5\times10^{13}\,\mathrm{g\,cm}^{-3}}\right)\left(\frac{M_{\varpi\phi}}{10^{25}\,\mathrm{erg\,cm}^{-3}}\right)^{-1}. \tag{5.18b}$$

Here, R and ΔR are the radial position of our box, and a typical length scale on which $M_{\varpi\phi}$ varies, respectively. Thus, for the redistribution of angular momentum to be efficient on the timescales of

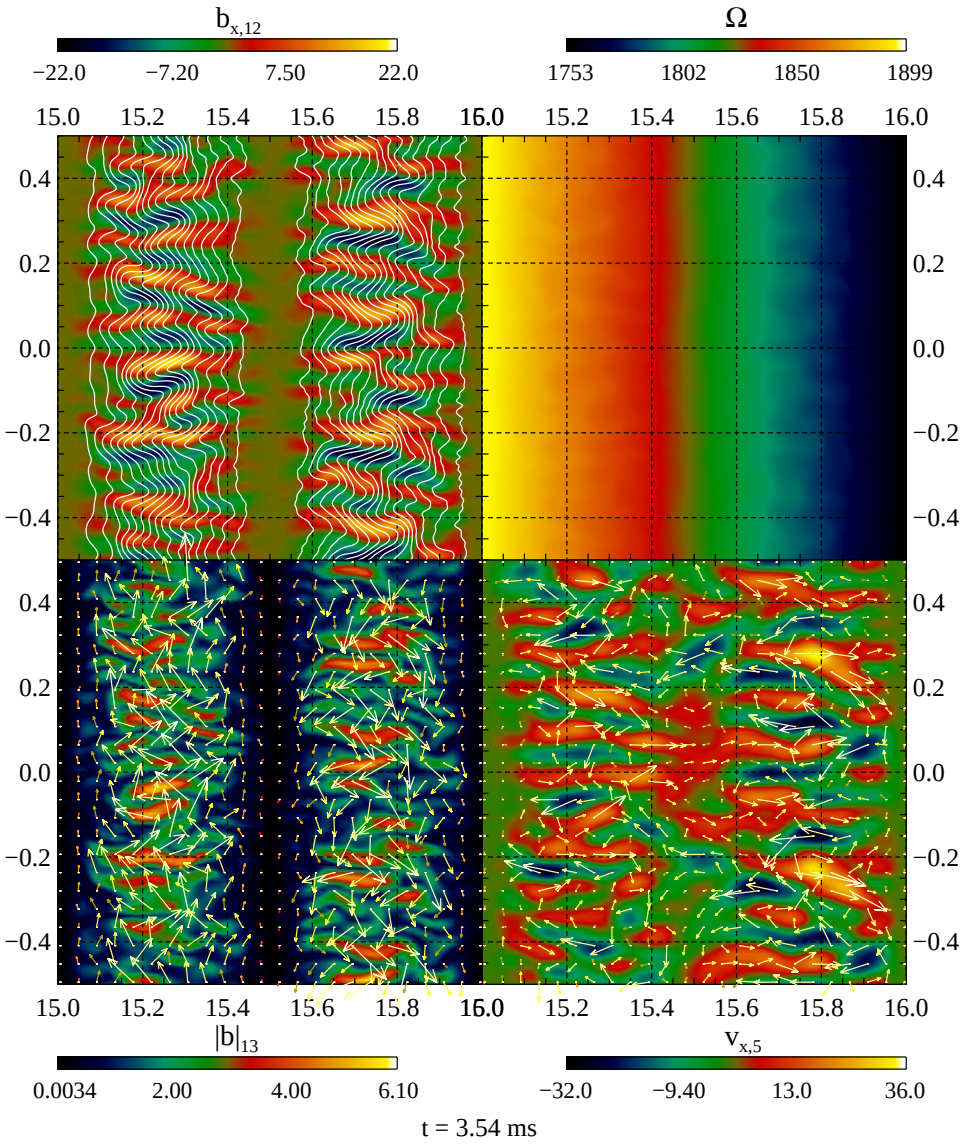

Figure 5.33: Same as Fig. 5.29, but for model Z2-3 at $t = 3.54\,\mathrm{ms}$.

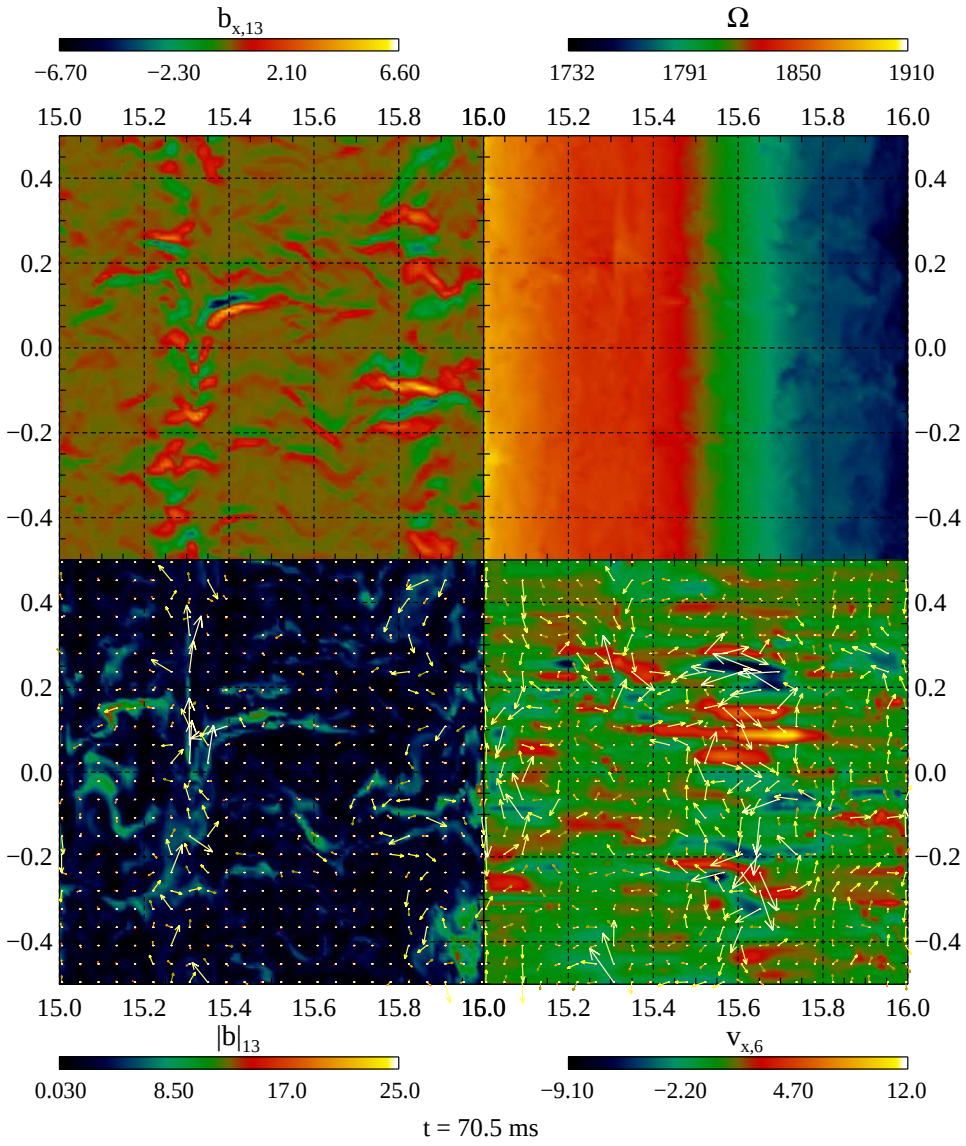

Figure 5.34: Same as Fig. 5.29, but for model Z2-3 at $t = 70.5\,\mathrm{ms}$. For clarity, we omitted the tangled magnetic field in the top left panel.

the post-collapse evolution of a supernova, i.e., a few 100 ms, the Maxwell stress has to be of the order of $\sim 10^{28}\,\mathrm{erg\,cm^{-3}}$. This corresponds to a field strength of $\sim 10^{14}\,\mathrm{G}$.

The stress value obtained from the above estimate appears to be in agreement with our simulations. Only uniform-field models achieve such high stresses when they develop channel flows. In this case, further amplification up to more than $10^{30}\,\mathrm{erg\,cm^{-3}}$ allows for a complete alteration of the rotation within a few milliseconds.

Although field strengths in excess of $10^{14}\,\mathrm{G}$ are quite common also in the other models, they do not give rise to such large stresses because of their lack of coherence. They, instead, show significant deviations from the initial rotational profile in localised regions within few tens of milliseconds as the mean Maxwell stress reaches the order of $10^{27}\,\mathrm{erg\,cm^{-3}}$. Because the spatial structure of the magnetic field is characterised by thin flux tubes, local variations of the rotational profile can be triggered by considerably weaker stresses than the ones typical for channel flows. For even weaker stresses, a slower, much more gradual modification of the rotational profile can be observed for $M_{\varpi\phi} \gtrsim 10^{27}\,\mathrm{erg\,cm^{-3}}$.

Influence of entropy gradients In a number of 2d simulations, we tried to investigate the influence of a thermal stratification on the MRI. We focused on models of series U2. Depending on their sign, entropy gradients may be either stabilising the MRI (if $\partial_\varpi s > 0$) or provide convective destabilisation (if $\partial_\varpi s < 0$). In both cases, the development of magneto-rotational modes may be significantly affected. The instability can be entirely suppressed by a convectively stable stratification. If the stabilisation does not suffice for a complete suppression, the geometry of the MRI modes will be affected: due to the influence of buoyancy, we do not expect them to cover large radial extents but rather to be squeezed into flat structures, if able to overcome the stabilisation at all. In a convectively unstable regime, on the other hand, the MRI will grow on larger spatial scales, resembling volume-filling hydrodynamic convection.

We simulated some of the models of series U2 with both positive and negative entropy gradients, $(1+S) \propto \varpi^{\alpha_s}$. We will refer to the corresponding models with $\alpha = 0$ as the "standard models" in the following.

Stabilisation For a slightly stable profile, $\alpha = 0.25$, and $\alpha = 0.5$ (models U2-7 and U2-8; the corresponding entropy gradients at $\varpi = 15\,\mathrm{km}$ are $\partial_\varpi s \approx 0.02\,\mathrm{km^{-1}}$ and $\partial_\varpi s \approx 0.04\,\mathrm{km^{-1}}$, respectively), we find that the MRI grows, though at a reduced rate: for model U2-8, we estimate a growth time of $\sim 14\,\mathrm{ms}$, corresponding to $\omega \sim 70\,\mathrm{s^{-1}}$, i.e., the growth is slower than in the corresponding model with a vanishing entropy gradient by a factor of 10 (Fig. Fig:Anw-MRI:U2-8–tevo). The maximum Maxwell stress reached by these model is reduced slightly w.r.t. the standard model. With increasing α, we observe less and less prominent radial channel-like flow structures. The MRI growth vanishes as α is increased up to $\alpha = 1$ (model U2-9, with an entropy gradient of $\partial_\varpi \approx 0.08\,\mathrm{km^{-1}}$). Such a stable gradient essentially suppresses the instability (see Fig. 5.36). We do not observe significant growth of the field or the velocity perturbation in this case. Instead, the initial perturbation is damped away quickly. At the end of the simulation, the magnetic field has not changed significantly: it is still mostly oriented in z direction and has the same strength as initially. The strong buoyant stabilisation essentially suppresses radial flows which are able to transform the z field into a radial one, which in turn could be wound up by differential rotation into a toroidal field. Hence, the toroidal component of the field is negligible. Initially, under the influence of the still relatively strong perturbation, a channel structure reminiscent of the standard case without thermal stratification develops in the ϖ component of the magnetic field. As the fluid

motion fades away, this pattern remains frozen in. The Maxwell stress quickly approaches zero, not inducing any large-scale angular-momentum transport.

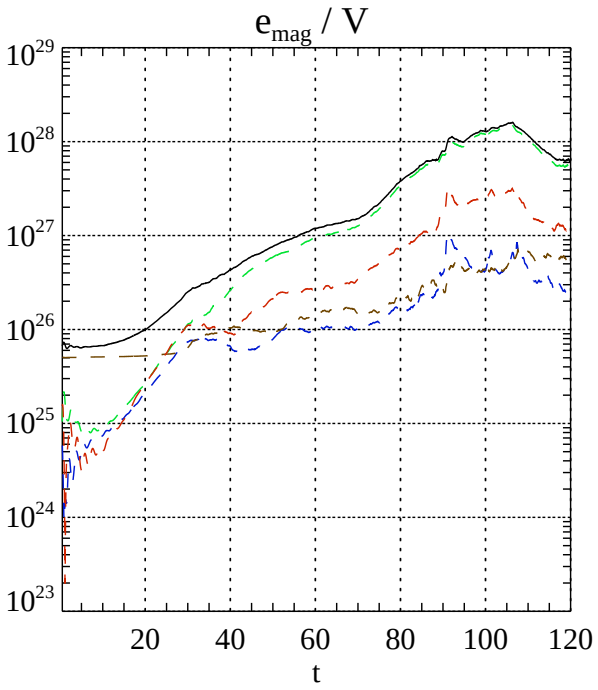

Figure 5.35: Same as Fig. 5.27, but showing the entire time evolution of model U2-8.

Convection In the opposite case of $\alpha < 0$, convection quickly sets in and leads to a fairly different evolution.

We have to make a few comments regarding BCs. Since they allow for radial transport of internal energy, shearing disc boundaries may, in principle, lead to artificial transport of entropy across the pseudo-periodic boundaries, thus modifying the initial entropy profile. In tests with comparing shearing disc with reflecting BCs, we verified that neither of these BC artificially suppresses the MRI, and that both lead to very similar results.

We start the discussion with models with an initially very weak field (10^4 G) and a relatively strong negative entropy gradient, $\partial_{\varpi} s = -0.1\mathrm{km}^{-1}$ (model U2-10). In this case, the MRI is far from being resolved numerically; hence, there is no back-reaction of the magnetic field onto the flow.

The initial perturbations are amplified very rapidly and convection sets in during the first two milliseconds. We find structures that are typical for convective flows: vortices surrounded by down-drafts of "cold", i.e., low-entropy, material and up-flows of "hot", i.e., entropy-rich, gas. After a few revolutions, the initially several small vortices merge to form a single coherent and very persistent structure, a large vortex. The rotational profile of the system, after being disorted by a certain amount during the first epoch with several small vortices, quickly relaxes to its initial state. Afterwards it does not change significantly. A further characteristic of the state is that the magnetic field strength is diminished inside the convection zone, and instead is accumulated near

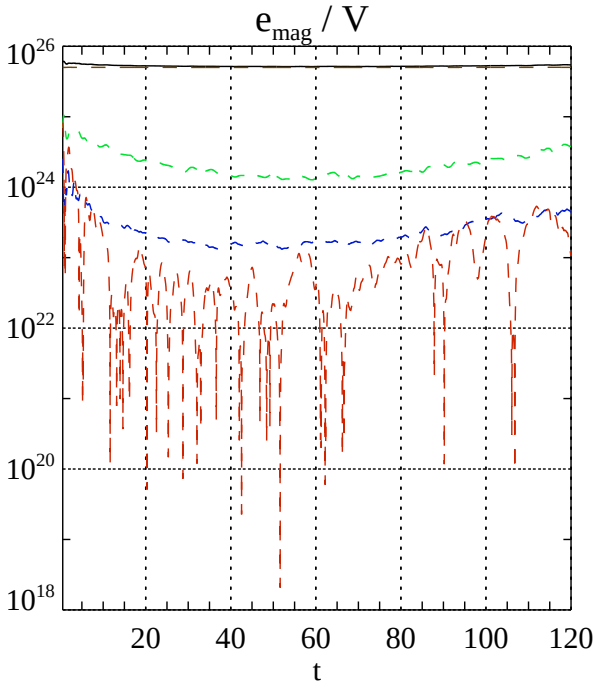

Figure 5.36: Same as Fig. 5.27, but showing the entire time evolution of model U2-9.

the inner and outer boundary. This phenomenon is reminiscent of the expulsion of magnetic flux from convection cells well-known from magneto-convection theory.

The intensity of convection depends on the magnitude of the entropy gradient. For a shallower gradient, the growth of the perturbations is much slower, and the formation of large-scale flow structures is delayed considerably. Furthermore, the development of the MRI in a convectively unstable system depends on the relative importance of the entropy gradients and the magnetic field.

Models with a rather shallow entropy gradient, e.g., model U2-11, behave very similar to models with no gradient at all, displaying only slight modifications to the MRI. Most findings of pure MRI models hold here, too. The MRI grows on a similar timescale as in the standard case, leading to angular-momentum transport and eventually to large-scale channel flows. In the final phase, both the entropy and the angular-velocity profiles are transformed into radially streaming channels.

In models with strong entropy gradients (e.g., model U2-12), on the other hand, convection dominates over the MRI. After a short initial phase during which a convective flow pattern is set up, starting from mushroom-like flows that merge into larger vortices, the entropy profile is flattened. The magnetic field shows a structure similar to the one described above: it is strongest at the edge of the vortices and only fairly weak in their interiors. Since most of the domain possess only a weak field (in our model $b_z \lesssim 10^{12}\,\mathrm{G}$, which tends to decrease), we do not observe any growth of the MRI despite the essentially unmodified Ω profile. Instead, the field energy and the Maxwell stress is depleted as convective motions expulse the field from the vortex.

Three-dimensional simulations

Though the previously discussed axisymmetric simulations demonstrate the possibility of MRI-driven field amplification in SN cores and provide some insight into the evolution of an MRI-unstable layer of a supernova core, to address the problem in full generality, we have to perform three-dimensional simulations. These are, however, computationally quite expensive. Thus, we are not able to perform as much simulations as we did in 2d. Instead, we have to focus on a few selected models.

Differences with axisymmetry Axisymmetry imposes severe restrictions to the dynamics of the magnetic and kinetic fields. The most important limitations are that, in axisymmetry, a toroidal field cannot be converted into a poloidal one, and that the disruption of the channel flows requires non-axisymmetric parasitic instabilities (Goodman & Xu 1994).

Models We simulated models with different field geometries and varied the initial field strength, the entropy profile, and the grid size. The models are summarised in Tab. 5.5.

model name	field geometry	grid size $[\mathrm{km}]\times[\mathrm{km}]\times[\mathrm{km}]$	Ω_0 $[\mathrm{s}^{-1}]$	α_Ω	S_0	$\partial_\varpi S$	b_0 $[10^{12}\,\mathrm{G}]$
U3-1	uniform b_z	$1\times1\times1$	1900	-0.25	0	0	4
U3-2	uniform b_z	$1\times1\times1$	1900	-0.25	0	0	10
U3-3	uniform b_z	$1\times1\times1$	1900	-0.25	0	0	20
U3-4	uniform b_z	$1\times4\times1$	1900	-0.25	0	0	4
U3-5	uniform b_z	$1\times4\times1$	1900	-0.25	0	0	10
U3-6	uniform b_z	$1\times4\times1$	1900	-0.25	0	0	20
U3-7	uniform b_z	$2\times8\times2$	1900	-0.25	0	0	10
U3-8	uniform b_z	$2\times8\times2$	1900	-0.25	0	0	20
U3-9	uniform b_z	$1\times4\times1$	1900	-0.25	0.2	-0.02	10
U3-10	uniform b_z	$1\times4\times1$	1900	-0.25	0.2	-0.04	10
Z3-1	b_z, zero flux	$1\times4\times1$	1900	-0.25	0	0	10
T3-1	uniform b_ϕ	$1\times4\times1$	1900	-0.25	0	0	40

Table 5.5: A list of our three-dimensional MRI models. The first column gives the name of the model. In the second column, the initial field geometry is listed. The next column gives the size of the grid. The last five columns show the initial conditions of the model: the parameters governing the initial angular velocity (Ω_0 and α_Ω), the parameters of the entropy profile (S_0 and α_S), and the initial field strength b_0.

Uniform b_z field

Models U3-1, U3-2, and U3-3: basic behaviour We start the discussion with uniform-field models. Comparing the linear growth phase of models U3-1, U3-2, and U3-3, we find a similar dependence of the growth rate on the field strength: if the MRI wave length is resolved well, the growth is fast and independent of b_0 (U3-2 and U3-3). Under-resolved models, such as U3-1, exhibit a slower growth of the MRI.

During early phases, the evolution is similar to the corresponding axisymmetric models: a number of radially aligned channels appear. The strong differential rotation causes significant wind-up of flow features leading to structures very elongated in ϕ direction. Hence, there is only a modest variation of the MHD variables with azimuthal angle in this stage. Sheet-like structures dominate the field geometry. The rotational profile begins to show distortions due to the transport of angular momentum by the Maxwell stress (see Fig. 5.37, showing the model at $t = 11.8\,\mathrm{ms}$).

Unlike in axisymmetry, the coherent channel flows do not persist in this model, but rather are modified by the parasitic instabilities identified by Goodman & Xu (1994) as the linear growth of the MRI terminates at the transition to the saturation phase. The resulting flow is more complex than the one at earlier times: though the presence of coherent structures such as flux sheets is still significant, their geometry is more tangled and twisted, and less anisotropic than earlier on. This indicates the turbulent disruption of the channels (see Fig. 5.38, showing the model at $t = 35.1\,\mathrm{ms}$).

This evolution from coherent channel flows to a more turbulent state is characteristic for all three-dimensional models of series U3. However, as pointed out by Sano & Inutsuka (2001), channel flows can develop from the turbulent state of such a model. Consequently, the magnetic field and the angular-momentum transport are amplified strongly. This is what we observe in model U3-3 at late times, $t \gtrsim 40\,\mathrm{ms}$ (see Figs. 5.39 and 5.40), when a strong channel flow is created. The model again enters a state of exponential growth, and a large part of its angular momentum is extracted by Maxwell stresses. The field strength reaches several $10^{15}\,\mathrm{G}$, and the mean Maxwell stress component $M_{\varpi\phi}$ exceeds $10^{30}\,\mathrm{erg\,cm^{-3}}$. Since our shearing disc boundaries allow for a loss of angular momentum, and thus for the total disruption of the differential rotation profile by transport through the radial boundaries, this stage represents the end of the evolution, just as it did in axisymmetry: the instability has used up its free-energy reservoir. Hence the later evolution only consists of violent oscillations of the channel mode. We do not observe this evolution in any of the other uniform-field models. However, since this process, evolving in a turbulent environment, possesses a random character, we suspect that the lack of a coherent channel flow is a mere coincidence, and that these models may as well develop such a channel mode during their later evolution.

Models U3-4 through U3-8: effects of the grid size We now discuss models U3-4, U3-5, and U3-6. These are identical to the models discussed previously, except for a four times larger grid extent in ϕ direction. We note that all models evolve similarly: an early linear phase during which multiple channel flows develop is superseded by a turbulent phase without notable channels. We do not observe late-time channel modes disrupting the flows. If we compare the saturation levels of the field strength, field energy and Maxwell stress, we note only a very weak dependence on the grid size.

In models U3-7 and U3-8, we doubled the grid size in each direction while keeping the number of grid cells fixed. We rather concentrate on the well-resolved models U3-7 and U3-8, and compare them to models with the same initial field but smaller grid, U3-5 and U3-6, respectively. In each of the two pairs (U3-5 and U3-7, and U3-6 and U3-8), we find very similar dynamics. We note, however, that the magnetic field energy and the Maxwell stress are larger by approximately a factor of 2. For their shearing sheet simulations, Sano et al. (2004) (and later also Pessah et al. (2007)) derived scaling laws according to which one expects stronger fields and stresses for larger grids. We note, however, that their results do not easily carry over to our simulations involving density and pressure stratification.

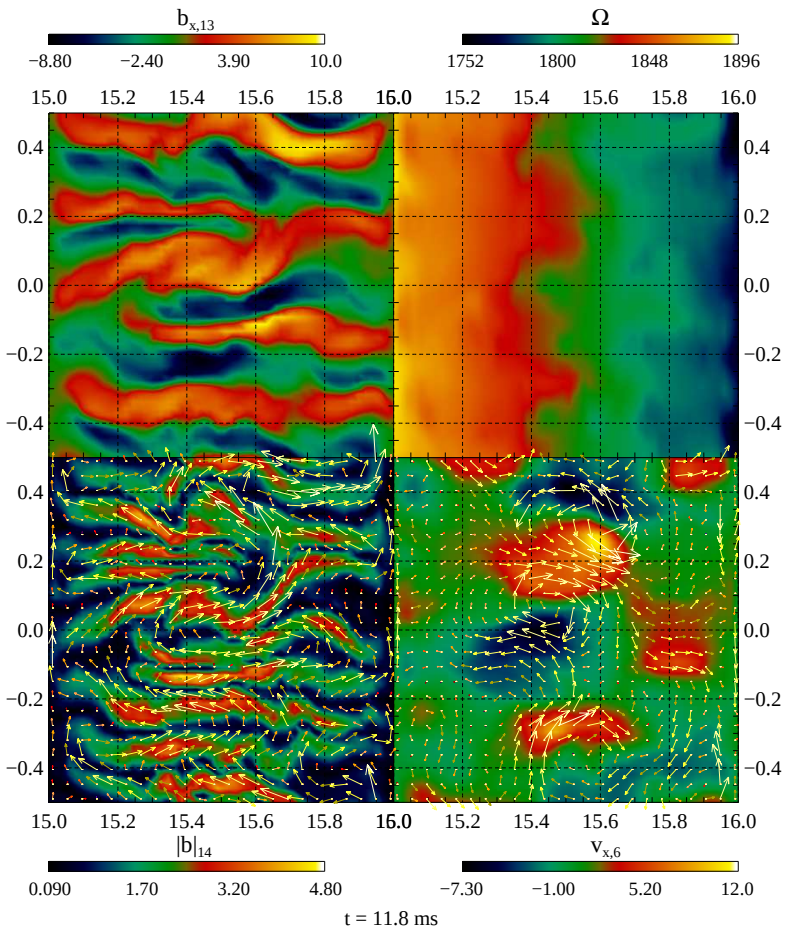

Figure 5.37: The flow and field state of model U3-3 at $t = 11.8\,\mathrm{ms}$. The top group of panels shows a cut through the model at a given ϕ coordinate. The b_ϖ component (in the plot denoted as b_x) of the magnetic field and the angular velocity are plotted in the top left and right panels, respectively. The panels in the second row show the magnetic field strength along with two-dimensional (i.e., (b_ϖ, b_z)) field vectors (left), and the v_ϖ (denoted as v_x in the plot) component of the velocity field along with two-dimensional velocity vectors (right). In the bottom panel, we show a volume rendering of the field strength, the red, green, and blue axis pointing into ϖ, ϕ, and z direction, respectively.

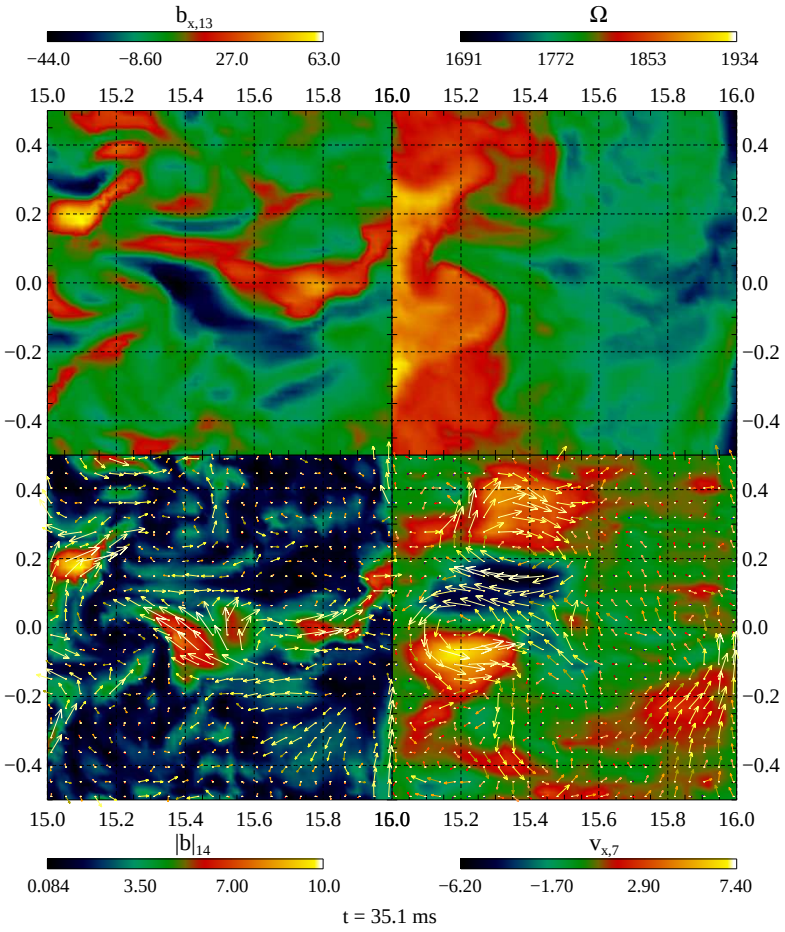

Figure 5.38: Same as Fig. 5.37, but at $t = 35.1\,\mathrm{ms}$.

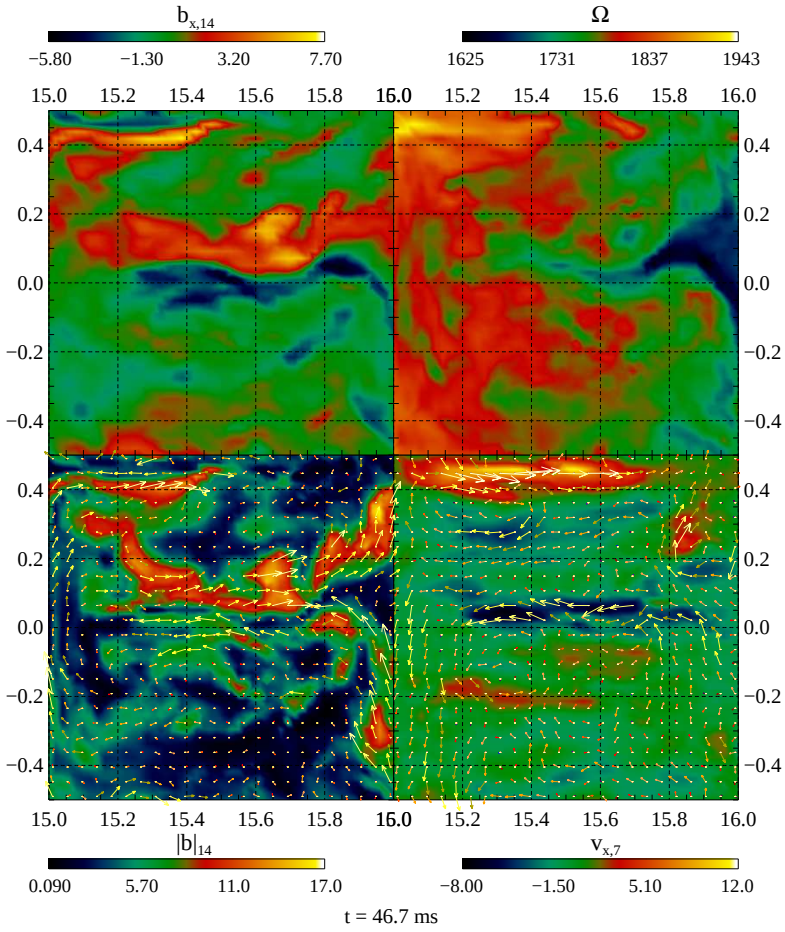

Figure 5.39: Same as Fig. 5.37, but at $t = 46.7\,\mathrm{ms}$.

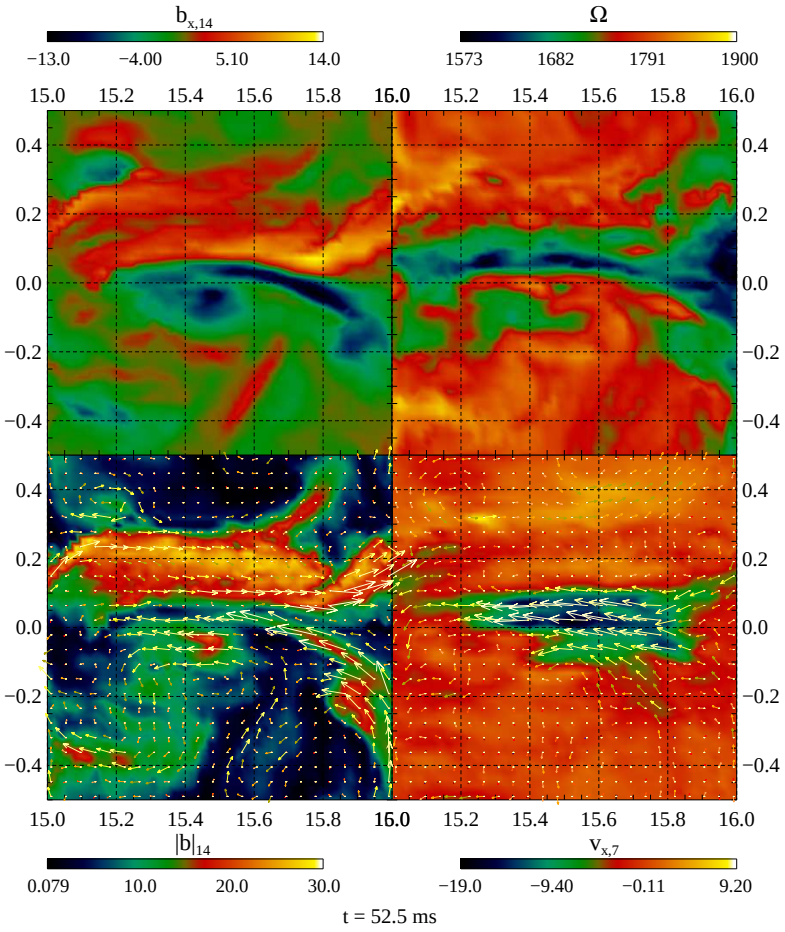

Figure 5.40: Same as Fig. 5.37, but at $t = 52.5\,\mathrm{ms}$.

Models U3-9 and U3-10: magneto-convection We continue our discussion with convectively unstable models U3-9 and U3-10. In these models, the entropy gradients are rather shallow ($\partial_{\varpi} s = -0.02\,\mathrm{km}^{-1}$ and $\partial_{\varpi} s = -0.04\,\mathrm{km}^{-1}$, respectively), allowing for the standard MRI scenario to apply without too drastic modifications. If we compare the two models with the corresponding ones without entropy gradients, we find fairly similar values of the saturation fields and Maxwell stresses. We find densely packed channel flows in the early phases. These flows modify both the rotation and the entropy profiles. Later, MRI saturation sets in, and the flow becomes turbulent (Fig. 5.41), leading to large values of the transport coefficients. The vigorous transport soon establishes a rather shallow entropy profile in most of the grid. In this region, the instability is to large degree a standard magneto-rotational one, whereas near the inner and outer radial boundary we find structures reminiscent of convective mushrooms.

A model with vanishing flux We also simulated one model (Z3-1) with an initial field in z direction but a vanishing magnetic flux. This model, after a linear growth phase, develops turbulence. At late times, we do not see any channel flows. Compared to uniform-field models of the same initial background profile and field strength, the magnetic energy and Maxwell stresses are somewhat lower, but the amplification leads to very strong fields in excess of $10^{14}\,\mathrm{G}$.

Toroidal initial fields We, finally, discuss model T3-1 having a uniform toroidal field initially. In this case, the instability is generically non-axisymmetric. In such models, the most unstable modes have a finite wave number in ϕ direction, but an infinite wave number in z direction. Thus, they are under-resolved on any grid. Consequently, we find a very slow growth of the instability in model T3-1 (Fig. 5.42). We reach saturation not before $t \approx 50\,\mathrm{ms}$. The saturation amplitude of the field and the magnetic stress is similar to uniform-field models with a considerably weaker initial field, more or less comparable to model U3-5. In this model, the dynamics is dominated by a turbulent flow. Coherent structures may develop similar to other three-dimensional models, but they neither reach the spatial extent nor the dynamical impact, e.g., of model U3-3.

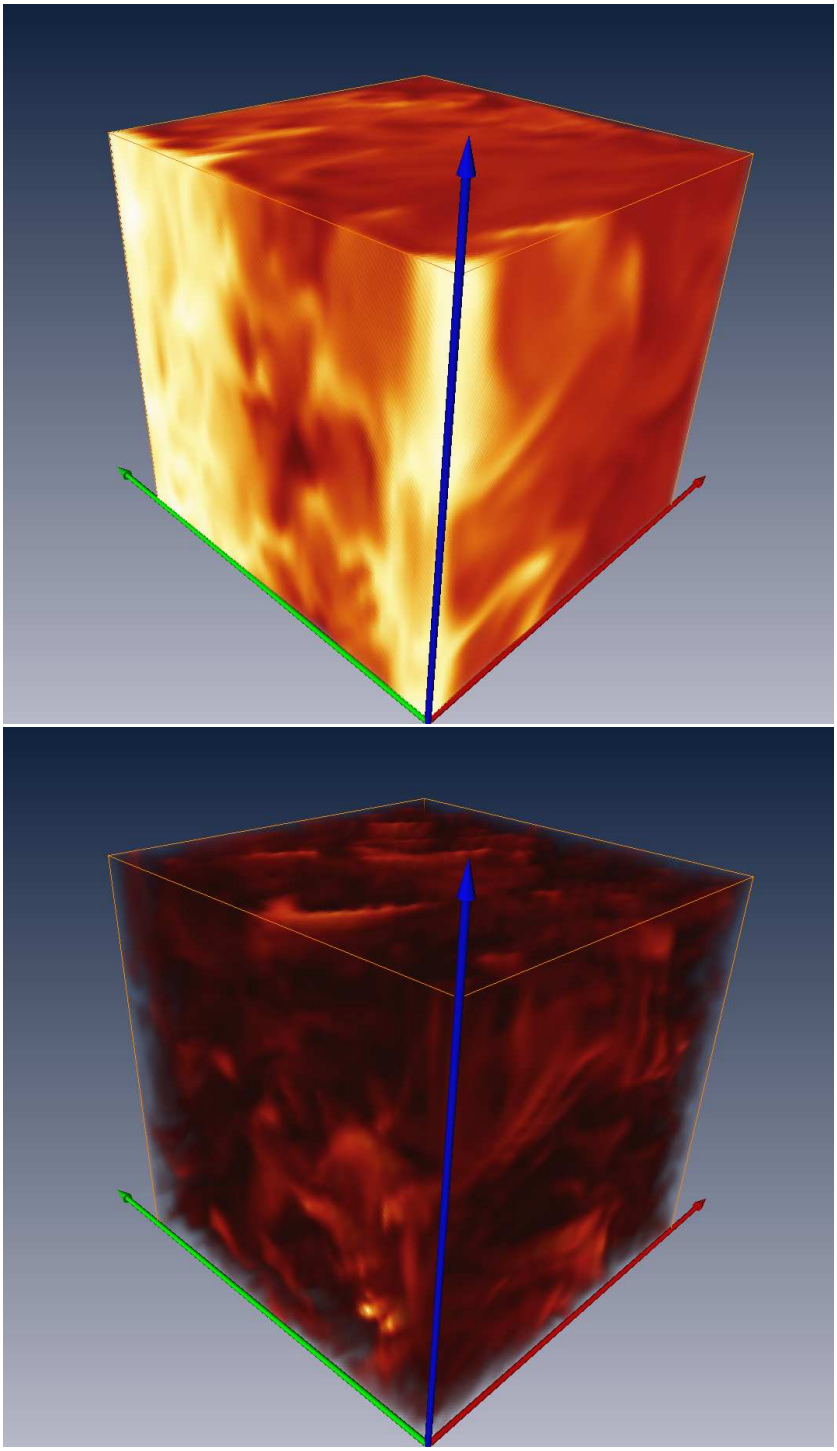

Figure 5.41: Model U3-10 at $t = 39.8\,\mathrm{ms}$. The top and bottom panels show a volume rendering of the entropy and the field strength, respectively. The arrows signify the ϖ (red), ϕ (green), and z (blue) directions.

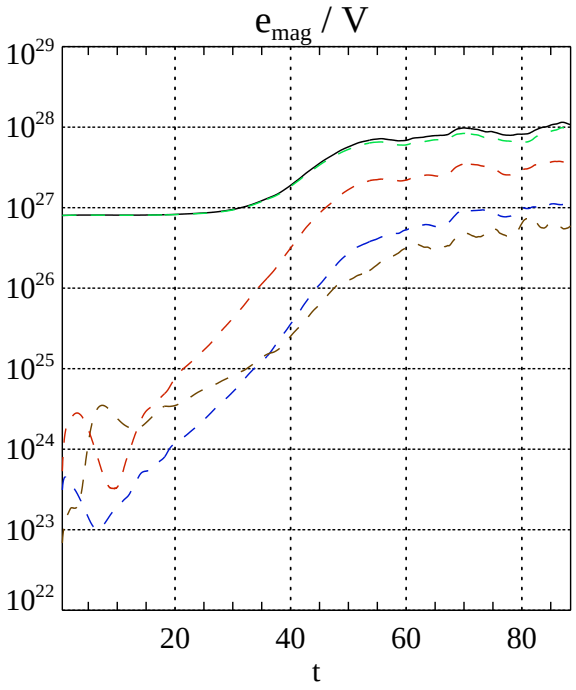

Figure 5.42: Same as Fig. 5.27, but for model T3-1.

Chapter 6

Summary and conclusions

> IF YOU FOLLOW REASON FAR ENOUGH IT ALWAYS LEADS TO CONCLUSIONS THAT ARE CONTRARY TO REASON.
>
> Samuel Butler

Development of a new radiation-MHD code The physics of compact astrophysical objects, their formation, evolution, and, finally, their catastrophic explosions is very rich and complex, including, e.g., general relativity, the dynamics of – potentially turbulent – fluids and magnetic fields, neutrino transport, nuclear reactions, and the *equation of state (EOS)* of nuclear matter. Not only are effects from very diverse fields of physics involved, but typically they are closely coupled, and thus cannot be addressed independently of each other. Therefore, the applicability of analytic approaches to these phenomena is limited, and instead numerical simulations have to be used to study most problems. Simulations, in principle, can follow the evolution of complex systems under very general conditions. Thus, they are a prime tool of theoretical astrophysics, and are applied to very different astrophysical problems, including compact objects and cosmic explosions.

Despite large numerical efforts and the rapid improvement of the computational power of supercomputers in recent years, the immense complexity of many problems still poses a problem to numerical methods. Therefore, important problems such as the notoriously difficult question of the explosion mechanism of core collapse supernovae still await solution. Thus, the development, implementation, testing, and application of new accurate and efficient numerical schemes for the solution of the equations governing the evolution of complex astrophysical systems is an active field of research in theoretical astrophysics.

In this thesis, we focus on methods for two important fields: *magnetohydrodynamics (MHD)* and *radiation hydrodynamics (RHD)*. Our efforts are, in part, motivated by the recent progress in the solution of hyperbolic systems of *partial differential equations (PDEs)* in general, and especially the MHD scheme. Many modern schemes for hyperbolic systems belong to the class of *high-resolution shock-capturing (HRSC)* schemes. Two key ingredients of these techniques are the reconstruction and the Riemann solver steps. Both steps are important in determining the order of accuracy and the stability of the method.

Typically, the design of a reconstruction method is a trade-off between accuracy and stability. It is possible to construct methods of a very high formal order of accuracy, but to ensure stability

these methods have to fulfil certain constraints. Many traditional MHD methods use the so-called piecewise-linear method reconstruction scheme based on the total variation diminishing constraint, resulting in 2^{nd}-order accuracy. Several years ago, different stability constraints were proposed, leading to stable reconstruction schemes with a higher order of accuracy, viz. the so-called *weighted essentially non-oscillatory (WENO)* (Liu et al. 1994) and *monotonicity preserving (MP)* (Suresh & Huynh 1997) schemes. Still not very widespread, these schemes have been applied for astrophysical flows only recently. To study their properties, we implemented both WENO and MP schemes in our new MHD code.

HRSC schemes rely on the solution of the Riemann problem at each interface of neighbouring grid zones, i.e., the problem of the evolution of two MHD states separated by a discontinuity. For a number of systems, including the MHD equations, it is possible to construct exact Riemann solvers which decompose the solution into characteristic waves, i.e., the eigenvectors of the Jacobian of the flux matrix. Depending on the complexity of the eigenspace of the Jacobian, these methods are usually fairly elaborate and computationally expensive. In many cases, one employs approximate Riemann solvers which do not require the construction of the full eigenspace, but, typically, are based only on a few eigenvalues. These methods are much faster than exact solvers, but are less accurate. They lead to additional numerical diffusion, i.e., they have a larger numerical viscosity than exact solvers. Recently, the *multi stage (MUSTA)* (Titarev & Toro 2005; Toro & Titarev 2006) class of Riemann solvers with reduced numerical viscosity was proposed. Based on standard approximate Riemann solvers, this method is computationally very cheap, but it can lead to results nearly as accurate as the ones obtained with an exact solver. We implemented and tested different MUSTA solvers.

The MHD equations are a hyperbolic system of PDEs. Thus, they can be solved using HRSC methods. However, one of their most important features, viz. the absence of magnetic monopoles, $\vec{\nabla} \cdot \vec{b} = 0$, precludes the unmodified application of these methods and requires a careful design of MHD schemes to prevent unphysical effects caused by the spurious development of magnetic monopoles due to numerical errors. Different methods exist to ensure a divergence-free numerical evolution of the magnetic field. Among these, our code uses the *constraint transport (CT)* method (Evans & Hawley 1988) based on a spatial discretisation of the magnetic field fully consistent with the induction equation and the divergence constraint. The divergence remains zero to machine precision during the simulations.

In CT schemes, the magnetic field and the fluid variables (density, momentum, and energy) are discretised in different ways, and the evolution equations of these two groups of variables are treated separately. On the other hand, both equations are tightly coupled: the velocity field enters the induction equation for the magnetic field, and the evolution of the fluid is affected by the magnetic field via the Lorentz force. The CT framework allows for different construction methods of the coupling terms, i.e., the electric field and the Lorentz force. To construct the electric field, we implemented the scheme of Pen et al. (2003) and a scheme based on the recently developed *upwind constraint transport (UCT)* methods (Londrillo & Del Zanna 2000; Londrillo & del Zanna 2004; Gardiner & Stone 2005) which computes the electric field consistently with the solution of the MHD Riemann problem. The computation of the Lorentz force involves spatial averaging of field components which we perform – following the UCT method – using high-order interpolation and taking into the divergence constraint.

We evaluated our implementation of the MHD equations using several standard tests for numerical MHD. Among these are the propagation of hydromagnetic waves, different Riemann problems involving discontinuities (e.g., shock waves), and problems testing aspects of turbulent flows. For all tests, the code reproduced the correct results, e.g., the correct locations and speeds of waves.

Strong discontinuities are resolved stably and accurately, with very little smearing of sharp fronts, and with only minor numerical oscillations. In a wave-propagation test, the code, depending on the reconstruction method, demonstrated an accuracy of 3rd to 4th order.

The transport of energy (and lepton number) by (neutrino) radiation through matter is a very complex problem unless certain simplifications are allowed by the physical conditions. If the reactions of the radiation with the gas can be neglected, the system is optically thin, and we can apply the free-streaming approximation. If, on the other hand, the reactions couple radiation and matter very tightly and the system is optically thick, the diffusion approximation provides a good description of the transport. In both approximations, the *radiative transfer (RT)* equation reduce to that of the 0th angular radiation moment, i.e., the evolution equation for the radiative energy.

In many systems such as supernovae, both regimes apply in different spatial regions separated by a transition zone where neither of the approximations is valid. In such a case, two different approaches are widely applied. In one approach one attempts to solve the RT equations exactly using Boltzmann solvers, and the other approach one relies on modifications of the diffusion approximations by introducing flux limiters (*flux-limited diffusion (FLD)* approximations) to provide an interpolation between the diffusion and the free-streaming limits. The first approach is fairly demanding and computationally very expensive, but its accuracy surpasses that of the simpler and faster FLD approach, where – like in standard diffusion – only the 0th moment equation is solved.

We implemented a transport scheme which belongs to the class of approximative methods, but evolves the 0th and 1st moments of the radiation intensity (i.e., radiation energy and momentum) rather than only the 0th moment (Pons et al. 2000; Audit et al. 2002; Audit & González 2006). Since a truncated series of moments equations does not form a closed system of equations, we need a closure relation. In two-moment transport, this closure is given by the *variable Eddington factor (VEF)*. Though typical VEFs are simple analytic or implicit functions of the radiation energy and momentum, they provide a good approximation of the radiation field in both the diffusion and the free-streaming limits as well as in the intermediate regime.

If the VEF fulfils certain constraints, the resulting two-moment system is hyperbolic, i.e., we can solve the system using HRSC schemes. In the radiative transfer part of our code, we implemented the same numerical methods we use for the HD equations, i.e., high-order reconstruction and MUSTA solvers.

Neutrino-matter reactions such as emission, absorption, and scattering couple radiation and matter. The resulting source terms do not interfere with the hyperbolic structure of the MHD and RT systems, and thus can be accounted for in a separate step. To use the code for supernova simulations, we implemented the emission and absorption of neutrinos by nuclei and free nucleons, and neutrino scattering off nuclei and nucleons. To simplify the test simulations, we did not take into account the spectral dependence of the radiation moments on the neutrino energy but rather evolved the grey system (i.e., integrated over neutrino energies).

We verified our RT scheme using a number of test problems by comparison with analytic results or existing numerical simulations. We find that the code is able to handle both the diffusion and the free-streaming limits accurately. In the intermediate regime, the results are in good agreement with reference simulations. We, furthermore, performed a RHD simulation of the spherically symmetric collapse and post-collapse evolution of the iron core of a star of $40 M_{\odot}$. Though it was not our goal to make detailed predictions concerning the explosion mechanism of massive stars, we verified that our code is able to handle this problem properly, and to produce results that are in qualitative agreement with more detailed simulations. In particular, we reproduced the deleptonisation of the core during collapse, the trapping of the neutrinos in the dense core, the creation, propagation, and

subsequent stall of the supernova shock wave, and the intense luminosity burst. No shock revival was observed, i.e., we do not find a prompt explosion.

Hydromagnetic instabilities We used our code to investigate the evolution of two hydromagnetic instabilities relevant to cosmic explosions: the MHD *Kelvin-Helmholtz (KH)* instability and the *magneto-rotational instability (MRI)*. Both instabilities can lead to turbulent flows varying on small length scales. Thus, our simulations profitted greatly from the use of high-resolution difference methods.

Kelvin-Helmholtz instability The merger of two neutron stars is one of the most promising models for short gamma-ray bursts. After a long inspiral phase, the neutron stars touch each other in a thin contact surface. Due to the combined orbital and rotational motion of the stars, a strong shear develops across the contact surface. The shear layer is KH unstable, and, thus, perturbations of the layer grow exponentially. Most NS possess a magnetic field which will be amplified by the instability. In merger simulations, Price & Rosswog (2006) found that the magnetic field strength increases to very large values exceeding 10^{15} G. They speculated about even stronger fields in equipartition with the kinetic or the thermal energy, corresponding to $10^{16...18}$ G.

To check these results using an independent numerical method, we performed local simulations of KH-unstable shear layers with magnetic fields. We performed two sets of simulations to gain insight into the physics of the KH instability in general, and its occurrence in the merger process in particular.

In two-dimensional simulations, we confirmed the basic picture established by Frank et al. (1996), Jones et al. (1997), and Jeong et al. (2000).

1. Non-magnetic shear layers are unstable against the KH instability. Perturbations of the shear interface grow exponentially until non-linear saturation sets in, and a circular vortex forms at the unstable interface between the fluids streaming in opposite directions. The vortex remains stable and coherent unless it is dissipated by (physical or numerical) viscosity.
2. A strong magnetic field (Alfvén number of the shear flow less than unity) suppresses the instability because the flow perturbations cannot bend the magnetic field lines due to the strong magnetic tension force. No vortex forms, and the shear flow exists until the end of the simulation.
3. Weaker magnetic fields cannot suppress the instability or modify its linear growth phase, but have a large influence on the non-linear saturation phase. Fields corresponding to Alfvén numbers around unity lead to a stabilisation in the non-linear phase.
4. The topology of the magnetic field is dominated by thin flux sheets. The main mechanism for field amplification is the stretching of flux sheets by the vortical motion. Due to the conservation of magnetic flux, the flux sheets become thinner during the stretching. Once their thickness approaches the width of a few grid cells, effects of the finite grid resolution become important, and further growth is inhibited by dissipation due to numerical resistivity: field lines reconnect, releasing magnetic into internal energy. Since the magnetic energy was previously amplified by the fluid motion, the magnetic field acts as a catalyst mediating the conversion of kinetic into internal energy, i.e., dissipation of kinetic energy. These processes are responsible for the dissipative dynamics of KH models identified by Jones et al. (1997) in models with very weak initial fields. In these models, the KH vortex remains coherent in the non-linear phase, but is subject to enhanced dissipation slowly extracting kinetic energy.

For slightly stronger fields, Jones et al. (1997) observed the disruption regime. If the magnetic field is in local equipartition with the kinetic energy when it reconnects, the dissipation of kinetic energy is sufficiently intense to change the dynamics globally: the vortex is disrupted quickly, and a broad transition layer dominated by flux sheets is established.
Our simulations, in particular investigations of the dependence of the border between dissipative and disruptive dynamics as a function of field strength and grid resolution, led us to the conclusion that the generic behaviour of weak-field models is the disruption of the vortex, and that the dissipative regime occurs due to insufficient resolution only.

5. An upper bound for the magnetic field strength of a model is given by local equipartition of magnetic and kinetic energy, i.e., it does not depend on the initial field strength. Whether or not this limit is actually reached in a simulation depends on both the initial field strength and the grid resolution: unless a sufficiently fine grid is used, or the initial field is sufficiently strong, the field amplification will terminate before equipartition is reached due to numerical dissipation. Since the amplification of the field occurs in increasingly thin flux sheets, a simulation will show the growth of the field by a large factor only if very fine structures can be resolved. Thus, to reach kinetic equipartition strength starting from a very weak field requires a sufficiently fine grid resolution.
6. If excess numerical resistivity caused by inadequate grid resolution does not prevent the field strength from growing to kinetic equipartition, the model will exhibit the disruptive behaviour.

Our simulations also include models with a supersonic shear. In this case, we demonstrated the importance of resonantly travelling shock waves for the evolution of the instability. Even without magnetic field, strong dissipation of kinetic energy occurs in supersonic shear flows due to shock heating. The evolution of the shear flow with weak magnetic fields is qualitatively similar to subsonic models.

We performed a few three-dimensional simulations of weak-field models which confirm the results by Ryu et al. (2000). The dynamics is similar to the two-dimensional case, but the dissipation of kinetic energy is enhanced w.r.t. the two-dimensional case due to the presence of generically three-dimensional instabilities.

In simulations with initial data motivated by the contact surface of merging NS, we confirm the results of Price & Rosswog (2006). The linear growth phase of the instability lasts for several tenths of a millisecond, and perturbations grow exponentially. Saturation sets in, and the KH vortex is disrupted by the reconnecting magnetic field whose energy reaches equipartition with the kinetic energy. The maximum field strengths exceed 10^{15} G, in some models even 10^{16} G. We do not find fields in equipartition with the internal energy, i.e., field strengths of the order of 10^{18} G.

Magneto-rotational instability We used our code to investigate the evolution of differentially rotating magnetised post-collapse cores of massive stars which, according to linear analysis, should be unstable against the MRI.

Established by Velikhov (1959) and Chandrasekhar (1960), the MRI was found to be crucial for the dynamics of accretion discs. If the angular velocity of a differentially rotating (e.g., Keplerian) magnetised disc has a negative radial gradient, the MRI will amplify any seed magnetic field exponentially, irrespective of the field strength. In the non-linear saturation phase, the MRI leads to turbulence and enhanced transport of angular momentum. Confirmed by an increasingly large number of local and global disc simulations, MRI-driven turbulent transport is now considered to explain the observed accretion rates of accretion discs (for a review, see Balbus & Hawley 1998).

In stars, general MHD instabilities including the MRI were investigated by, e.g., Acheson (1978). Later, Balbus (1995) generalised the MRI stability criterion to situations involving entropy gradients. The resulting criterion, replacing the Solberg-Høiland criterion, provides a rather general criterion for the rotational stability of stars. Although the MRI in stars may be relevant in many evolutionary stages, most previous studies on the MRI focused on accretion discs. There are a few important differences between discs and stars. Unlike discs, stars are supported against gravity mainly by pressure gradients and not (Keplerian) rotation. In stars, entropy gradients play a more important role than in discs, potentially leading to stabilisation (positive radial entropy gradient) of MRI unstable layers or to convective destabilisation (negative radial entropy gradient) of the system.

Akiyama et al. (2003) pointed out that the MRI might work as well in supernova cores,since they rotate differentially due to the conservation of angular momentum of individual fluid elements during the homologous collapse. They estimated the possible magnetic field strength that can be reached due to amplification by the MRI, assuming equipartition between magnetic and rotational energy. Analysing the conditions for MRI in non-magnetic one-dimensional simulations of spherical yet rotating cores, they found that the cores are MRI-unstable in large parts, and that the field should grow to $10^{15...16}$ G within a few revolutions of the core, i.e., a few milliseconds.

Later two-dimensional MHD simulations of the magneto-rotational collapse of simplified models of stellar cores (e.g., Obergaulinger et al. 2006b) confirmed these results by showing exponential field growth in regions of strongly negative angular velocity gradients. However, these collapse simulations suffered from a severe problem: the MRI has a preferred length scale associated with the distance an Alfvén wave travels during one rotation period. This scale sets the wavelength of the fastest growing mode (the so-called MRI wavelength). Modes with longer wavelengths are also unstable, but possess a much smaller growth rate. If a simulation is unable to resolve the MRI wavelength by several grid cells, it will strongly underestimate the growth of the MRI or even – for very poor resolution – miss it entirely. Since the MRI wavelength is proportional to the Alfvén velocity, it is smallest for the astrophysically most relevant case of weak initial fields. Thus, the predictive power of global simulations (i.e., simulations of the entire core) is limited by the grid resolution one can afford on current computers.

To study the evolution of the MRI in post-collapse cores, we performed two- and three-dimensional local simulations. We simulated a small part of the core, replacing its surroundings by boundary conditions. At a radius of approximately 15 km near the equatorial plane of the core, we constructed differentially rotating initial models in hydrostatic equilibrium between gravitational, centrifugal, and pressure forces. We endowed these models with an initially uniform field in z-direction, a field in z-direction with a vanishing net flux, or a uniform toroidal field. We used periodic boundary conditions in vertical and azimuthal directions, and shearing sheet boundary conditions in radial direction.

In all simulations the MRI grows within a few rotational periods, which, for our models, corresponded to less than a few milliseconds – if the MRI wavelength is resolved well. Otherwise, a considerably slower growth si observed. In axisymmetric models with a uniform initial field in z-direction, we recovered the channel solutions identified by Hawley & Balbus (1991), and investigated in detail by Goodman & Xu (1994). The instability develops coherent large-scale flows that merge into one up-flow and one down-flow. These flows are characteristic of the linear phase of the instability. In three dimensions, they are prone to non-axisymmetric instabilities, and break down into turbulence. Lacking these parasitic instabilities, the channel modes persist even at nonlinear saturation. As a result, the flows do not saturate until the rotational profile is completely disrupted. For a zero-flux initial field, we observe the development of turbulent flows without

coherent channel flows. Thus, in axisymmetry, the results from local disc simulations apply to the case of supernova cores as well. In particular, the growth times are of the order of the rotational period, as expected.

In three-dimensional simulations of models with uniform initial b_z, the channel flows of the linear growth phase are disrupted by parasitic instabilities, and the velocity and magnetic fields become turbulent. As a result, the magnetic fields and the Maxwell stress reach lower saturation values. The maximum field strengths are in the range of $10^{14..15}$ G, the toroidal field exceeding the poloidal components by a factor of 2...4, typically. Even in the turbulent state, coherent channel-like flows can develop. In one of our models, we observe the disruption of the rotational profile by a channel flow similar to the axisymmetric case. Varying the field geometry, we find that in supernova cores the MRI works both with an initial b_z field with vanishing net flux and a uniform toroidal field, the saturation fields being of the same order as in the uniform-field models.

Additional simulations involved systems with stabilising or destabilising entropy gradients. For strong positive gradients, no instability occurs at all, whereas for negative gradients we observe the development of convective flows, i.e., up- and down-flows of matter of high and low entropy, respectively. In such models, the initial entropy gradient is removed by convective overturns. In the resulting flat entropy profile, the MRI can lead to similar flows and similar field strength as in models with a flat initial entropy profile.

Outlook While our study of the KH instability already allows us to draw conclusions on the evolution of an interesting astrophysical system, viz. the contact surface of merging neutron stars, the MRI in supernova cores certainly deserves a further, more thorough investigation. Having demonstrated that the MRI indeed works in the case of stars, and particularly supernova cores, as expected from analytic considerations and from the analogy with disc simulations, subsequent studies can focus on the scaling of the saturation fields and stresses with the initial field strength. This should include simulations of weaker initial fields which require a considerably finer, grid and thus are computationally more demanding. Furthermore, the dependence of the saturated state on numerical parameters such as the grid size and resolution merits additional investigations. The ultimate goal of such investigations would be the development of a sub-grid model, i.e., a parametric description of the effects of the MRI below the grid resolution that can be used in global simulations. In turbulence theory, such (LES; large eddy simulation) models, typically based on turbulent viscosities and resistivities, are used with great success, but the precise formulation of a model for the MRI is not yet established.

Our code is a rather advanced and versatile tool, which can already be applied to various astrophysical systems. Nevertheless, one has to put more effort into additional code development in order to fulfil the requirements of certain more intricate problems. In particular, global two- or three-dimensional simulations of core-collapse supernovae, hypernovae and collapsars require an improvement of the treatment of the neutrino transport (possibly by using an energy-dependent transport scheme) and of the neutrino-matter interactions, as well as to implement an efficiently parallelised three-dimensional Poisson solver. Further simulations focusing on the fundamental physics of MHD instabilities, on the other hand, should include physical viscosities and resistivities.

Appendix A

Conservation laws in general coordinates

In this appendix, we will shortly summarise the formulation of tensorial conservation laws of the Gauss and Stokes types (Eqn. (2.2)) in general orthogonal coordinates, including Cartesian, spherical, and cylindrical ones. A more thorough discussion of these issues can be found, e.g., in the books by Mihalas & Weibel Mihalas (1984, appendix A) and Warsi (1993).

We consider three-dimensional space labelled by coordinates $\vec{\xi} = (\xi_1, \xi_2, \xi_3)$. We will use the symbols summarised in Tab. A.1; to distinguish between geometric terms in these coordinates, we will uses subscripts Ca, sp, and cy for Cartesian, spherical, and cylindrical coordinates, respectively.

Cartesian	(x, y, z)
Spherical	(r, θ, ϕ)
Cylindrical	(ϖ, ϕ, z)

Table A.1: The three orthogonal coordinates we implemented.

Metric and geometry elements We start with the metric tensor g describing the spatial distance associated with coordinate differences:

$$(\mathrm{d}s)^2 = g_{ij}\mathrm{d}\xi^i\mathrm{d}\xi^j. \tag{A.1a}$$

In general orthogonal coordinates, it reads

$$g = \mathrm{diag}(h_1, h_2, h_3), \tag{A.1b}$$

where h_i are functions of the coordinates. Because of the orthogonality, the metric is diagonal lacking cross products of coordinates. The specialisation to Cartesian, spherical, and cylindrical coordinates is given by

$$g_{\mathrm{Ca}} = \mathrm{diag}(1, 1, 1), \tag{A.2a}$$
$$g_{\mathrm{sp}} = \mathrm{diag}(1, r, r\sin\theta), \tag{A.2b}$$
$$g_{\mathrm{cy}} = \mathrm{diag}(1, \varpi, 1). \tag{A.2c}$$

From the metric, we can compute all kinds of geometry elements: the distance along a coordinate direction, the area of a surface orthogonal to one of the coordinates, and the volume of a spatial domain.

Line elements The general line element $\mathrm{d}\mathcal{L}_i$ is given by

$$\mathrm{d}\mathcal{L}_i = h_i \mathrm{d}\xi_i. \tag{A.3a}$$

In Cartesian, spherical, and cylindrical coordinates:

$$\mathrm{d}\mathcal{L}_x = \mathrm{d}x, \qquad \mathrm{d}\mathcal{L}_y = \mathrm{d}y, \qquad \mathrm{d}\mathcal{L}_z = \mathrm{d}z. \tag{A.3b}$$

$$\mathrm{d}\mathcal{L}_r = \mathrm{d}r, \qquad \mathrm{d}\mathcal{L}_\theta = r\,\mathrm{d}\theta, \qquad \mathrm{d}\mathcal{L}_\phi = r\sin\theta\,\mathrm{d}\phi. \tag{A.3c}$$

$$\mathrm{d}\mathcal{L}_\varpi = \mathrm{d}\varpi, \qquad \mathrm{d}\mathcal{L}_\phi = \varpi\,\mathrm{d}\phi, \qquad \mathrm{d}\mathcal{L}_z = \mathrm{d}z. \tag{A.3d}$$

Surface elements The general surface element is given by

$$\mathrm{d}\mathcal{A}_i = \prod_{j\neq i} h_j \mathrm{d}\xi_j. \tag{A.4a}$$

In Cartesian, spherical, and cylindrical coordinates:

$$\mathrm{d}\mathcal{A}_x = \mathrm{d}y\,\mathrm{d}z, \qquad \mathrm{d}\mathcal{A}_y = \mathrm{d}z\,\mathrm{d}x, \qquad \mathrm{d}\mathcal{A}_z = \mathrm{d}x\,\mathrm{d}y. \tag{A.4b}$$

$$\mathrm{d}\mathcal{A}_r = r^2\,\mathrm{d}(-\cos\theta)\,\mathrm{d}\phi, \qquad \mathrm{d}\mathcal{A}_\theta = \sin\theta\,\mathrm{d}\frac{r^2}{2}\,\mathrm{d}\phi, \qquad \mathrm{d}\mathcal{A}_\phi = \mathrm{d}\frac{r^2}{2}\,\mathrm{d}\theta. \tag{A.4c}$$

$$\mathrm{d}\mathcal{A}_\varpi = \varpi\,\mathrm{d}\phi\,\mathrm{d}z, \qquad \mathrm{d}\mathcal{A}_\phi = \mathrm{d}\varpi\,\mathrm{d}z, \qquad \mathrm{d}\mathcal{A}_z = \mathrm{d}\frac{\varpi^2}{2}\,\mathrm{d}\phi. \tag{A.4d}$$

Volume elements The volume surface element is given by

$$\mathrm{d}\mathcal{V} = \prod h_i \mathrm{d}\xi_i. \tag{A.5a}$$

In Cartesian, spherical, and cylindrical coordinates:

$$\mathrm{d}\mathcal{V} = \mathrm{d}x\,\mathrm{d}y\,\mathrm{d}z, \tag{A.5b}$$

$$\mathrm{d}\mathcal{V} = \mathrm{d}\frac{r^3}{3}\,\mathrm{d}(-\cos\theta)\,\mathrm{d}\phi, \tag{A.5c}$$

$$\mathrm{d}\mathcal{V} = \mathrm{d}\frac{\varpi^2}{2}\,\mathrm{d}(\phi)\,\mathrm{d}z. \tag{A.5d}$$

Covariant derivatives From the metric, we can compute the Christoffel symbols required to formulate the covariant derivatives. We will not list them here explicitly, but rather directly summarise the covariant derivatives of tensors of different ranks.

Gradient of a scalar In Cartesian, spherical, and cylindrical coordinates, the gradient of a scalar function f is given by

$$\vec{\nabla} f = \partial_x f \vec{e}_x + \partial_y f \vec{e}_y + \partial_z f \vec{e}_z, \tag{A.6a}$$

$$\vec{\nabla} f = \partial_r f \vec{e}_r + \frac{1}{r}\partial_\theta f \vec{e}_\theta + \frac{1}{r\sin\theta}\partial_\phi f \vec{e}_\phi, \tag{A.6b}$$

$$\vec{\nabla} f = \partial_\varpi f \vec{e}_\varpi + \frac{1}{\varpi}\partial_\phi f \vec{e}_\phi + \partial_z f \vec{e}_z. \tag{A.6c}$$

Divergence of a vector The divergence of a vector $\vec{v}$ in general orthogonal coordinates is given by

$$\vec{\nabla}\cdot\vec{v} = \sum_i \frac{1}{h_i}\partial_i h_i v^i. \tag{A.7a}$$

In Cartesian, spherical, and cylindrical coordinates, we have

$$\vec{\nabla}\cdot\vec{v} = \partial_x v_x + \partial_y v_y + \partial_z v_z, \tag{A.7b}$$

$$\vec{\nabla}\cdot\vec{v} = \frac{1}{r^2}\partial_r r^2 v_x + \frac{1}{r}\partial_\theta \sin\theta v_\theta + \frac{1}{r\sin\theta}\partial_\phi v_\phi, \tag{A.7c}$$

$$\vec{\nabla}\cdot\vec{v} = \frac{1}{\varpi}\partial_\varpi \varpi v_\varpi + \frac{1}{\varpi}\partial_\phi v_\phi + \partial_z v_z. \tag{A.7d}$$

Curl of a vector The curl of a (pseudo) vector $\vec{v}$ in general orthogonal coordinates is given by

$$\left(\vec{\nabla}\times\vec{v}\right)^i = \frac{1}{\sqrt{g}}\left(\partial_j v^k - \partial_k v^j\right). \tag{A.8a}$$

The coordinates of the curl in Cartesian, spherical, and cylindrical coordinates are listed below:

$$\left(\vec{\nabla}\times\vec{v}\right)^i = \frac{1}{\sqrt{g}}\left(\partial_j v^k - \partial_k v^j\right), \tag{A.8b}$$

$$\left(\vec{\nabla}\times\vec{v}\right)^r = \frac{1}{r\sin\theta}\left[\partial_\theta\left(\sin\theta v^\phi\right) - \partial_\phi v^\theta\right], \tag{A.8c}$$

$$\left(\vec{\nabla}\times\vec{v}\right)^\theta = \frac{1}{r}\left[\frac{1}{\sin\theta}\partial_\phi v^r - \partial_r r v^\phi\right], \tag{A.8d}$$

$$\left(\vec{\nabla}\times\vec{v}\right)^\phi = \frac{1}{r}\left[\partial_r r v^\theta - \partial_\theta v^r\right], \tag{A.8e}$$

$$\left(\vec{\nabla}\times\vec{v}\right)^\varpi = \frac{1}{\varpi}\partial_\phi v^z - \partial_z v^\phi, \tag{A.8f}$$

$$\left(\vec{\nabla}\times\vec{v}\right)^\phi = \partial_z v^\varpi - \partial_\varpi v^z, \tag{A.8g}$$

$$\left(\vec{\nabla}\times\vec{v}\right)^z = \frac{1}{\varpi}\left[\partial_\varpi\left(\varpi v^\phi\right) - \partial_\phi v^\varpi\right]. \tag{A.8h}$$

Divergence of tensor of rank 2 The covariant divergence of a tensor of rank 2, $\mathfrak{T}$, is given by

$$\nabla_j \mathfrak{T}^{ij} = \frac{1}{\sqrt{g}}\partial_j(\sqrt{g}\mathfrak{T}^{ij}) + \Gamma^i_{jk}\mathfrak{T}^{jk}. \tag{A.9a}$$

In Cartesian coordinates, Eqn. (A.9a) reads

$$\nabla_j \mathfrak{T}^{ij} = \partial_j \mathfrak{T}^{ij}. \tag{A.9b}$$

The expressions for spherical coordinates involve geometric source terms:

$$\nabla_j \mathfrak{T}^{rj} = \frac{1}{r^2}\partial_r r^2 \mathfrak{T}^{rr} + \frac{1}{r}\partial_\theta \sin\theta\ \mathfrak{T}^{r\theta} + \frac{1}{r\sin\theta}\partial_\phi \mathfrak{T}^{r\phi} - \frac{1}{r}\left[\mathfrak{T}^{\theta\theta} + \mathfrak{T}^{\phi\phi}\right], \tag{A.9ca}$$

$$\nabla_j \mathfrak{T}^{\theta j} = \frac{1}{r^2}\partial_r r^2 \mathfrak{T}^{\theta r} + \frac{1}{r}\partial_\theta \sin\theta\ \mathfrak{T}^{\theta\theta} + \frac{1}{r\sin\theta}\partial_\phi \mathfrak{T}^{\theta\phi} + \frac{1}{r}\left[\mathfrak{T}^{r\theta} - \cot\theta\ \mathfrak{T}^{\phi\phi}\right], \tag{A.9cb}$$

$$\nabla_j \mathfrak{T}^{\phi j} = \frac{1}{r^2}\partial_r r^2 \mathfrak{T}^{\phi r} + \frac{1}{r}\partial_\theta sin\theta\ \mathfrak{T}^{\phi\theta} + \frac{1}{r\sin\theta}\partial_\phi \mathfrak{T}^{\phi\phi} + \frac{1}{r}\left[\mathfrak{T}^{r\phi} + \cot\theta\ \mathfrak{T}^{\theta\phi}\right]. \tag{A.9cc}$$

In cylindrical coordinates, the result is:

$$\nabla_j \mathfrak{T}^{\varpi j} = \frac{1}{\varpi}\partial_\varpi\left(\varpi\mathfrak{T}^{\varpi\varpi}\right) + \frac{1}{\varpi}\partial_\phi\left(\mathfrak{T}^{\varpi\phi}\right) + \partial_z\left(\mathfrak{T}^{\varpi z}\right) - \frac{1}{\varpi}\mathfrak{T}^{\phi\phi}, \tag{A.9da}$$

$$\nabla_j \mathfrak{T}^{\phi j} = \frac{1}{\varpi}\partial_\varpi\left(\varpi\mathfrak{T}^{\phi\varpi}\right) + \frac{1}{\varpi}\partial_\phi\left(\mathfrak{T}^{\phi\phi}\right) + \partial_z\left(\mathfrak{T}^{\phi z}\right) + \frac{1}{\varpi}\mathfrak{T}^{\varpi\phi}, \tag{A.9db}$$

$$\nabla_j \mathfrak{T}^{zj} = \frac{1}{\varpi}\partial_\varpi\left(\varpi\mathfrak{T}^{z\varpi}\right) + \frac{1}{\varpi}\partial_\phi\left(\mathfrak{T}^{z\phi}\right) + \partial_z\left(\mathfrak{T}^{zz}\right). \tag{A.9dc}$$

Conservation laws We now can formulate the Gauss conservation laws for a scalar and a vector, and the Stokes conservation law for a vector in all three coordinate systems. If we insert the correct conserved variables (mass, momentum, energy, radiation moments; magnetic field) and the correct fluxes (mass and energy flux vectors, stress tensors, higher moments; electric field) and sources, we can read off from these equations the MHD and RT equations.

Scalar conservation law The conservation law for a scalar variable u with flux $\vec{f}$ and source s reads: in Cartesian coordinates:

$$\partial_t u + \partial_x f^x + \partial_y f^y + \partial_z f^z = s, \tag{A.5a}$$

in spherical coordinates:

$$\partial_t u + \frac{1}{r^2}\partial_r r^2 f^r + \frac{1}{r}\partial_\theta \sin\theta f^\theta + \frac{1}{r\sin\theta}\partial_\phi f^\phi = s, \tag{A.5b}$$

in cylindrical coordinates:

$$\partial_t u + \frac{1}{\varpi}\partial_\varpi \varpi f^\varpi + \frac{1}{\varpi}\partial_\phi f^\phi + \partial_z f^z = s. \tag{A.5c}$$

Gauss conservation law for a vector The Gauss-type conservation law for a vector variable $\vec{v}$ with symmetric flux tensor $\mathfrak{T}$ and source $\vec{s}$ reads in Cartesian coordinates:

$$\partial_t v^i + \partial_x \mathfrak{T}^{ix} + \partial_y \mathfrak{T}^{iy} + \partial_z \mathfrak{T}^{iz} = s^i, \tag{A.6a}$$

in spherical coordinates:

$$\partial_t v^r + \frac{1}{r^2}\partial_r r^2 \mathfrak{T}^{rr} + \frac{1}{r}\partial_\theta \sin\theta\, \mathfrak{T}^{r\theta} + \frac{1}{r\sin\theta}\partial_\phi\, \mathfrak{T}^{r\phi} = s^r + \frac{1}{r}\left[\mathfrak{T}^{\theta\theta} + \mathfrak{T}^{\phi\phi}\right], \tag{A.6b}$$

$$\partial_t v^\theta + \frac{1}{r^2}\partial_r r^2 \mathfrak{T}^{\theta r} + \frac{1}{r}\partial_\theta \sin\theta\, \mathfrak{T}^{\theta\theta} + \frac{1}{r\sin\theta}\partial_\phi\, \mathfrak{T}^{\theta\phi} = s^\theta - \frac{1}{r}\left[\mathfrak{T}^{r\theta} - \cot\theta \mathfrak{T}^{\phi\phi}\right], \tag{A.6c}$$

$$\partial_t v^\phi + \frac{1}{r^2}\partial_r r^2 \mathfrak{T}^{\phi r} + \frac{1}{r}\partial_\theta \sin\theta\, \mathfrak{T}^{\phi\theta} + \frac{1}{r\sin\theta}\partial_\phi\, \mathfrak{T}^{\phi\phi} = s^\phi - \frac{1}{r}\left[\mathfrak{T}^{r\phi} + \cot\theta \mathfrak{T}^{\theta\phi}\right], \tag{A.6d}$$

in cylindrical coordinates:

$$\partial_t v^\varpi + \frac{1}{\varpi}\partial_\varpi \varpi\, \mathfrak{T}^{\varpi\varpi} + \frac{1}{\varpi}\partial_\phi\, \mathfrak{T}^{\varpi\phi} + \partial_z \mathfrak{T}^{\varpi z} = s^\varpi + \frac{1}{\varpi}\mathfrak{T}^{\phi\phi}, \tag{A.6e}$$

$$\partial_t v^\phi + \frac{1}{\varpi}\partial_\varpi \varpi\, \mathfrak{T}^{\phi\varpi} + \frac{1}{\varpi}\partial_\phi\, \mathfrak{T}^{\phi\phi} + \partial_z \mathfrak{T}^{\phi z} = s^\phi - \frac{1}{\varpi}\mathfrak{T}^{\varpi\phi}, \tag{A.6f}$$

$$\partial_t v^z + \frac{1}{\varpi}\partial_\varpi \varpi\, \mathfrak{T}^{z\varpi} + \frac{1}{\varpi}\partial_\phi\, \mathfrak{T}^{z\phi} + \partial_z \mathfrak{T}^{zz} = s^z. \tag{A.6g}$$

Stokes conservation law for a vector The Stokes conservation law for a (pseudo) vector $\vec{u}$ with flux $\vec{F}$ and source $\vec{S}$ reads in Cartesian coordinates:

$$\partial_t u^x + [\partial_y F^z - \partial_z F^y] = S^x, \tag{A.7a}$$
$$\partial_t u^y + [\partial_z F^x - \partial_x F^z] = S^y, \tag{A.7b}$$
$$\partial_t u^z + [\partial_x F^y - \partial_y F^x] = S^z, \tag{A.7c}$$

in spherical coordinates:

$$\partial_t u^r + \frac{1}{r\sin\theta}\left[\partial_\theta \sin\theta F^\phi - \partial_\phi F^\theta\right] = S^r, \tag{A.7d}$$
$$\partial_t u^\theta + \frac{1}{r}\left[\frac{1}{\sin\theta}\partial_\phi F^r - \partial_r r F^\phi\right] = S^\theta, \tag{A.7e}$$
$$\partial_t u^\phi + \frac{1}{r}\left[\partial_r r F^\theta - \partial_\theta F^r\right] = S^\phi, \tag{A.7f}$$

in cylindrical coordinates:

$$\partial_t u^\varpi + \frac{1}{\varpi}\left[\partial_\phi F^z - \partial_z F^\phi\right] = S^\varpi, \tag{A.7g}$$
$$\partial_t u^\phi + \left[\partial_z F^\varpi - \partial_\varpi F^z\right] = S^\phi, \tag{A.7h}$$
$$\partial_t u^z + \frac{1}{\varpi}\left[\partial_\varpi \varpi F^\phi - \partial_\phi F^\varpi\right] = S^z. \tag{A.7i}$$

Appendix B

Multi-stage solvers

In this appendix, we will explain some technical details of the implementation of the MUSTA solvers. We will assume that the MUSTA scheme uses s steps and an arbitrary (approximate) Riemann solver.

We start with the cell averages of the conserved variables, u_i, the subscript i denoting the grid cell. We will refer to this grid as the original grid. The procedure is as follows:

1. Reconstruct the left and right zone-interface variables $u^{\mathrm{L,R}}_{i\pm\frac{1}{2}}$.
2. For each interface $i-\frac{1}{2}$ open the Riemann fan, i.e., evolve the Riemann problem defined by the left and right states according to the following recipe:
   (a) Define an equidistant grid of $2z$ zones from $-z$ to z (the *MUSTA grid*, see Fig. B.1); for simplicity, we set the cell width to unity. We will denote the variable on the MUSTA grid with ξ, and the grid index on the MUSTA grid with j, assuming that the cell interface with the index $j=\frac{1}{2}$ is located at $\xi=0$, and the zones $j=0$ and $j=1$ have the coordinates $\xi\in[-1;0]$ and $\xi\in[0;1]$, respectively. The centre of zone j is located at ξ_j.
   (b) Map the interface values onto the MUSTA grid (we will denote the variables on the MUSTA grid with w and the corresponding fluxes with v):
   $$w_j=\begin{cases} u^{\mathrm{L}}_{i-\frac{1}{2}} & \text{if } \xi_j<0 \\ u^{\mathrm{R}}_{i-\frac{1}{2}} & \text{if } \xi_j>0 \end{cases}. \tag{B.1}$$
   Here, i refers to the (fixed) zone interface of the original grid, and j refers to the zones of the MUSTA grid.
   (c) Reconstruct the MUSTA variables w to the interfaces of the MUSTA grid, obtaining $w^{\mathrm{L,R}}_{j\pm\frac{1}{2}}$. For this step, we use simple PCM reconstruction.
   (d) Compute the fluxes $v^{\mathrm{L,R}}_{j\pm\frac{1}{2}}=v(w^{\mathrm{L,R}}_{j\pm\frac{1}{2}})$.
   (e) Compute the final interface fluxes $v_{j\pm\frac{1}{2}}$ from the interface values of the MUSTA variables and fluxes using the (approximate) RS.
   (f) Define the MUSTA time step δt from the CFL condition on the MUSTA grid: $(\delta t)^{-1}=CFL\max(\lambda^{\mathrm{L,R}}_{j\pm\frac{1}{2}})$.
   (g) Evolve the MUSTA variables one step in time. We only take into account the fluxes, disregarding any sources terms, whether physical or geometrical:
   $$w_j=\delta t(v_{j+\frac{1}{2}}-v_{j-\frac{1}{2}}). \tag{B.2}$$

(h) Repeat steps 2b – 2g $(s-1)$ times, i.e., evolve the MUSTA variables s time steps.

(i) Return to the physical grid (the u variables): obtain the predictor values $u^{\mathrm{L,R}}_{i-\frac{1}{2}}$ from the MUSTA variables $w_{0;1}$:

$$u^{\mathrm{L}}_{i-\frac{1}{2}} = w_0, \tag{B.3}$$

$$u^{\mathrm{R}}_{i-\frac{1}{2}} = w_1. \tag{B.4}$$

3. Perform the corrector step:
   (a) compute the fluxes $f^{\mathrm{L,R}}_{i\pm\frac{1}{2}}$ from $u^{\mathrm{L,R}}_{i-\frac{1}{2}}$.
   (b) use the RS to compute the final fluxes from $f^{\mathrm{L,R}}_{i\pm\frac{1}{2}}$ and $u^{\mathrm{L,R}}_{i\pm\frac{1}{2}}$.

The number of zones on the MUSTA grid depends on the number of MUSTA steps. For a one-step scheme (MUSTA(1)), we only need $2z = 2$ zones. Larger numbers of steps require us to either use larger MUSTA grids or apply boundary conditions on the MUSTA grid. Taking into account the domain of dependence of the hyperbolic system (due to the CFL condition, a zone can only influence its immediate neighbours during one step). Since for most problems a one-step scheme is sufficient, we do not go into further detail here, referring the reader to Toro & Titarev (2006).

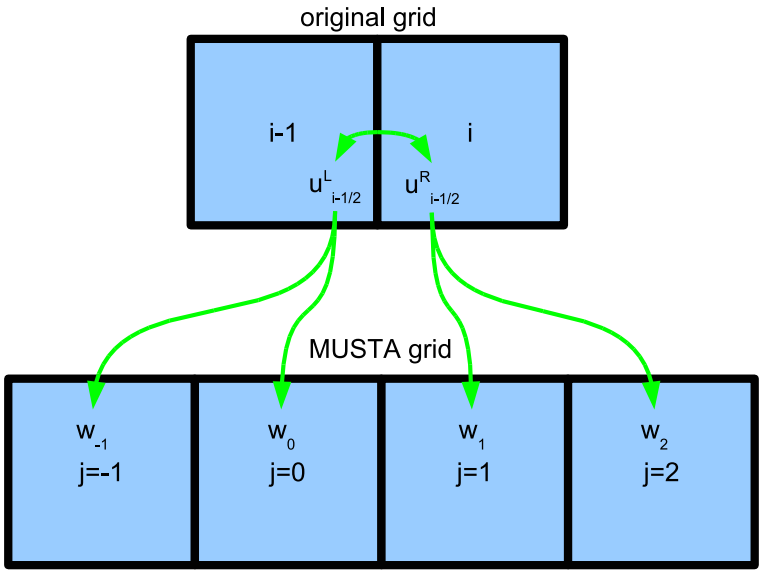

Figure B.1: A sketch of the correspondence between the original and the MUSTA grids. The left and right interface variables of the original grid, $u^{\mathrm{L,R}}_{i-\frac{1}{2}}$ are mapped to the MUSTA grid. We evolve the MUSTA variables for a few time steps and map the resulting variables back to the original grid.

Appendix C

Constraint transport: induction equation and Lorentz force

Here, we will discuss the technical details of our implementation of the CT method. Our basic variables are the HD state $u_{i,j,k}$ defined as volumetric zone averages[1] , and the components of the magnetic field, $\left(b^x_{i-\frac{1}{2},j,k}, b^y_{i,j-\frac{1}{2},k}, b^z_{i,j,k-\frac{1}{2}}\right)^T$, defined as surface averages over zone interfaces (see Fig. C.1). For the evolutionary equations, we have to compute the HD fluxes, f, and the electric field, $\vec{E} = -\vec{v}\times\vec{b}$ (For simplicity, we set $c = 1$ in this section.). Following our CT discretisation, the fluxes and the electric field are defined on zone surfaces and zone edges, respectively. By definition, both variables depend on both HD variables and the magnetic field. Their computation using HRSC schemes is not uniquely defined. We use the following steps:

1. Start with the discretised conserved variables $u_{i,j,k}$ and the "original" magnetic field components $\left(b^x_{i-\frac{1}{2},j,k}, b^y_{i,j-\frac{1}{2},k}, b^z_{i,j,k-\frac{1}{2}}\right)^T$.
2. Compute the zone averages of the magnetic field, $\vec{B}_{i,j,k}$, from the original zone-surface values using either (arithmetic) averaging or high-order reconstruction techniques.
3. To compute the fluxes in x direction (the *x sweep*):
   (a) Reconstruct the conserved variables $u_{i,j,k}$ and the transverse fields, $B^{y,z}_{i,j,k}$, to the zone surfaces at $x_{i\pm\frac{1}{2}}$, yielding left and right interface values. The divergence constraint implies that the longitudinal magnetic field (i.e., the x component in the x sweep) is continuous. In accordance with this continuity requirement, we do not reconstruct the x component of the field, but rather set $B^x_{i\pm\frac{1}{2},j,k} = b^x_{i\pm\frac{1}{2},j,k}$.
   (b) Compute the fluxes $(f^x)^{\mathrm{L,R}}_{i\pm\frac{1}{2},j,k}$ and the electric field components

$$\left(E^{x,x}_{i-\frac{1}{2},j,k}\right)^{\mathrm{L,R}} = 0, \tag{C.1a}$$

$$\left(E^{x,y}_{i-\frac{1}{2},j,k}\right)^{\mathrm{L,R}} = -\left(v^z B^x - v^x B^z\right)^{\mathrm{L,R}}_{i-\frac{1}{2},j,k}, \tag{C.1b}$$

$$\left(E^{x,z}_{i-\frac{1}{2},j,k}\right)^{\mathrm{L,R}} = -\left(v^x B^y - v^y B^x\right)^{\mathrm{L,R}}_{i-\frac{1}{2},j,k}. \tag{C.1c}$$

[1] Subscripts i, j, k refer to the x, y, z coordinates of grid zones. Integer indices denote zone centres and volume averages over the zones, and non-integer indices denote (averages over) zone interfaces

Here, the 1st and 2nd superscript of the electric field refer to the x sweep and the vector component of the electric field, respectively. Although it is not necessarily vanishing, we set the component $E^{x,x}$ to zero because we do not need this component in the scheme (since the induction equation involves the curl rather than the divergence of the electric field, i.e., there is no term involving $E^{x,x}$ in the x sweep).

(c) Compute the final interface fluxes $f^x_{i\pm\frac{1}{2},j,k}$ using a (MUSTA or non-MUSTA) RS. In the same step, compute the final interface values of the electric field, $E^{x,\cdot}_{i\pm\frac{1}{2},j,k}$, using the same RS. In case of a MUSTA scheme, this means that we have to perform at least one MUSTA predictor step for the magnetic field components as well, i.e., we have to evolve the left and right interface values of the magnetic field using the electric fields from Eqn. (C.1). Please note that the longitudinal magnetic field, $B^x_{i-\frac{1}{2},j,k}$, is not affected by the MUSTA predictor step(s), because there is no x derivative in the x component of the induction equation. Thus, the continuity requirement on b^x is fulfilled after the predictor step(s), too.

(d) The results of this procedure are the interface fluxes and the interface electric fields. We store the fluxes to compute the temporal change of the HD variables and the electric fields to compute the zone-edge electric fields from them in a later step. Store the zone-interface values of the fluid velocity, $v^{x,\cdot}_{i-\frac{1}{2},j,k}$ as well. We will need it to determine the upwind direction when computing the zone-edge electric fields.

4. Repeat step 3 for the y and z sweeps, yielding the interface fluxes $f^y_{i,j-\frac{1}{2},k}$ and $f^z_{i,j,k-\frac{1}{2}}$, the interface electric fields $E^{y,\cdot}_{i,j-\frac{1}{2},k}$ and $E^{z,\cdot}_{i,j,k-\frac{1}{2}}$, and the interface velocities $v^{y,\cdot}_{i,j-\frac{1}{2},k}$ and $v^{z,\cdot}_{i,j,k-\frac{1}{2}}$. In these and similar expressions in the following, the dot in the superscripts serves as a placeholder for vector indices, i.e., for x, y, and z.
5. Perform the x sweep of the computation of the zone-edge values of the electric fields:
   (a) Reconstruct the field components $E^{y,\cdot}_{i,j-\frac{1}{2},k}$ and the velocities $v^{y,\cdot}_{i,j-\frac{1}{2},k}$ to the zone edges, $x = x_{i\pm\frac{1}{2}}$, yielding left and right states $\left(E^{x,y,\cdot}_{i\pm\frac{1}{2},j-\frac{1}{2},k}\right)^{\mathrm{L,R}}$. Now, the additional superscript x refers to the x sweep of the construction of the E field.
   (b) From these, obtain unique edge fields $E^{x,y,\cdot}_{i\pm\frac{1}{2},j-\frac{1}{2},k}$ using an upwind solver (or any other RS).
   (c) Repeat these steps for the field components $E^{z,\cdot}_{i,j,k-\frac{1}{2}}$ to obtain $E^{x,z,\cdot}_{i\pm\frac{1}{2},j,k-\frac{1}{2}}$.
6. Repeat step 5 for the y and z directions to obtain $E^{y,x,\cdot}_{i-\frac{1}{2},j\pm\frac{1}{2},k}$, $E^{y,z,\cdot}_{i,j\pm\frac{1}{2},k-\frac{1}{2}}$, $E^{z,x,\cdot}_{i-\frac{1}{2},j,k\pm\frac{1}{2}}$, and $E^{z,y,\cdot}_{i,j-\frac{1}{2},k\pm\frac{1}{2}}$.
7. Using these fields, compute the edge fields $E^x_{i,j-\frac{1}{2},k-\frac{1}{2}}$ by averaging $E^{y,z,x}_{i,j-\frac{1}{2},k-\frac{1}{2}}$ and $E^{z,y,x}_{i,j-\frac{1}{2},k-\frac{1}{2}}$, and analogously for the other components.
8. Using the interface fluxes and the edge electric fields, compute the temporal change of u and $\vec{b}$.

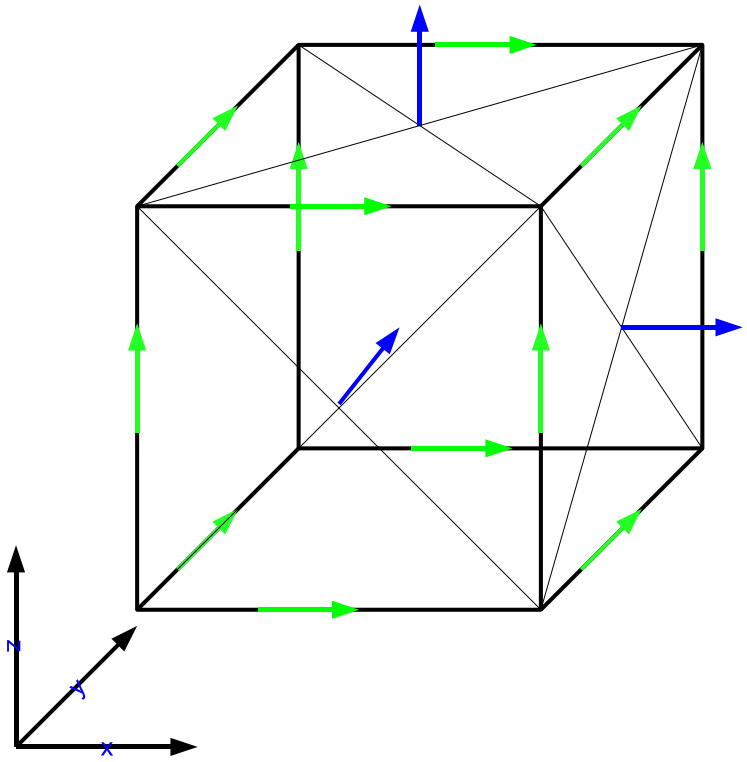

Figure C.1: A sketch of a cell of the MHD grid. The blue vectors indicate the collocation of the components of the magnetic field. Each field component lives on an orthogonal zone surface. The green vectors show the components of the electric field. They are collocated on zone edges. The left and right states of variables reconstructed in step 3a as well as the fluxes computed from these variables and the electric field components computed in step 3b live at the same location as the magnetic field does. In step 5a, the electric fields are reconstructed from the zone surfaces (blue) to zone edges (green).

Bibliography

Acheson, D. J. 1978, Royal Society of London Philosophical Transactions Series A, 289, 459

Agertz, O., Moore, B., Stadel, J., et al. 2007, MNRAS, 380, 963

Akiyama, S., Wheeler, J. C., Meier, D. L., & Lichtenstadt, I. 2003, ApJ, 584, 954

Ardeljan, N. V., Bisnovatyi-Kogan, G. S., & Moiseenko, S. G. 2005, MNRAS, 359, 333

Arlt, R. & Rüdiger, G. 2001, A&A, 374, 1035

Audit, E., Charrier, P., Chièze, J. ., & Dubroca, B. 2002, ArXiv Astrophysics e-prints

Audit, E. & González, M. 2006, in EAS Publications Series, ed. P. Stee, 115–128

Balbus, S. A. 1995, ApJ, 453, 380

Balbus, S. A. 2001, ApJ, 562, 909

Balbus, S. A. & Hawley, J. F. 1991, ApJ, 376, 214

Balbus, S. A. & Hawley, J. F. 1992a, ApJ, 400, 610

Balbus, S. A. & Hawley, J. F. 1992b, ApJ, 392, 662

Balbus, S. A. & Hawley, J. F. 1998, Reviews of Modern Physics, 70, 1

Balsara, D. 1999a, Journal of Quantitative Spectroscopy and Radiative Transfer, 61, 617

Balsara, D. 1999b, Journal of Quantitative Spectroscopy and Radiative Transfer, 61, 629

Bisnovatyi-Kogan, G. S., Popov, I. P., & Samokhin, A. A. 1976, Ap&SS, 41, 287

Brackbill, J. & Barnes, D. C. 1980, J. Comput. Phys., 35, 426

Brandenburg, A., Nordlund, A., Stein, R. F., & Torkelsson, U. 1995, ApJ, 446, 741

Buras, R., Rampp, M., Janka, H.-T., & Kifonidis, K. 2006, A&A, 447, 1049

Burrows, A., Dessart, L., Livne, E., Ott, C. D., & Murphy, J. 2007, ApJ, 664, 416

Burrows, A. & Lattimer, J. M. 1986, ApJ, 307, 178

Burrows, A. & Thompson, T. A. 2002, ArXiv Astrophysics e-prints

Cerdá-Durán, P., Font, J. A., & Dimmelmeier, H. 2007, A&A, 474, 169

Cernohorsky, J. & Bludman, S. A. 1994, ApJ, 433, 250

Cernohorsky, J. & van Weert, C. G. 1992, ApJ, 398, 190

Chandrasekhar, S. 1960, Proceedings of the National Academy of Science, 46, 253

Chandrasekhar, S. 1961, Hydrodynamic and hydromagnetic stability (International Series of Monographs on Physics, Oxford: Clarendon, 1961)

Dai, W. & Woodward, P. R. 1998, J. Comput. Phys., 142, 331

Del Zanna, L. & Bucciantini, N. 2002, A&A, 390, 1177

Del Zanna, L., Bucciantini, N., & Londrillo, P. 2003, A&A, 400, 397

Del Zanna, L., Zanotti, O., Bucciantini, N., & Londrillo, P. 2007, A&A, 473, 11

Dimmelmeier, H., Font, J. A., & Müller, E. 2002, A&A, 388, 917

Evans, C. R. & Hawley, J. F. 1988, ApJ, 332, 659

Font, J. 2003, Living Rev. Relativity, 6

Frank, A., Jones, T. W., Ryu, D., & Gaalaas, J. B. 1996, ApJ, 460, 777

Fromang, S., Hennebelle, P., & Teyssier, R. 2006, A&A, 457, 371

Fromang, S. & Papaloizou, J. 2007, ArXiv e-prints, 705

Fromang, S., Papaloizou, J., Lesur, G., & Heinemann, T. 2007, ArXiv e-prints, 705

Gardiner, T. A. & Stone, J. M. 2005, J. Comput. Phys., 205, 509

Goldreich, P. & Schubert, G. 1967, ApJ, 150, 571

Goodman, J. & Xu, G. 1994, ApJ, 432, 213

Harten, A., Enqguqist, B., Osher, S., & Chakravarthy, S. 1987, J. Comput. Phys., 71, 231

Hawley, J. F. 2000, ApJ, 528, 462

Hawley, J. F. & Balbus, S. A. 1991, ApJ, 376, 223

Hawley, J. F. & Balbus, S. A. 1992, ApJ, 400, 595

Hawley, J. F. & Balbus, S. A. 2002, ApJ, 573, 738

Hawley, J. F., Balbus, S. A., & Stone, J. M. 2001, ApJ, 554, L49

Hawley, J. F., Gammie, C. F., & Balbus, S. A. 1995, ApJ, 440, 742

Hawley, J. F., Gammie, C. F., & Balbus, S. A. 1996, ApJ, 464, 690

Janka, H.-T. 1991, PhD thesis, Technische Universität München, (1991)

Jeong, H., Ryu, D., Jones, T. W., & Frank, A. 2000, ApJ, 529, 536

Jiang, G.-S. & Shu, C.-W. 1996, J. Comput. Phys., 126, 202

Jiang, G.-S. & Wu, C. 1999, J. Comput. Phys., 150, 561

Jin, S. & Levermore, C. 1996, J. Comput. Phys., 126, 446

Jin, S., Pareschi, L., & Toscani, G. 2000, SIAM J. Num. Anal., 38, 913

Jones, T. W., Gaalaas, J. B., Ryu, D., & Frank, A. 1997, ApJ, 482, 230

Keil, W., Janka, H.-T., & Mueller, E. 1996, ApJ, 473, L111+

Keppens, R. & Tóth, G. 1999, Physics of Plasmas, 6, 1461

Keppens, R., Tóth, G., Westermann, R. H. J., & Goedbloed, J. P. 1999, Journal of Plasma Physics, 61, 1

Klahr, H. H. & Bodenheimer, P. 2003, ApJ, 582, 869

Kössl, D., Müller, E., & Hillebrandt, W. 1990, A&A, 229, 378

Kotake, K., Yamada, S., Sato, K., et al. 2004, Phys. Rev. D, 69, 124004

Kulikovskii, A. G., Pogorelov, N. V., & Semenov, A. Y. 2001, Chapman & Hall/CRC monography and surveys in pure and applied mathematics, Vol. 118, Mathematical aspects of numerical solutions of hyperbolic systems (Chapman & Hall/CRC Press)

LeVeque, R. J. 1992, Numerical Methods for Conservation Laws, 2nd edn., Lectures in mathematics - ETH Zürich (Birkhäuser)

LeVeque, R. J. 1998, in Saas-Fee Advanced Course 27: Computational Methods for Astrophysical Fluid Flow., 1

Levy, D., Puppo, G., & Russo, G. 1999, Mathematical Modelling and Numerical Analysis, 33, 547

Levy, D., Puppo, G., & Russo, G. 2000, SIAM J. Sci. Comput., 22, 656

Levy, D., Puppo, G., & Russo, G. 2002, SIAM J. Sci. Comput., 24, 480

Liu, X.-D., Osher, S., & Chan, T. 1994, J. Comput. Phys., 115, 200

Londrillo, P. & Del Zanna, L. 2000, ApJ, 530, 508

Londrillo, P. & del Zanna, L. 2004, J. Comput. Phys., 195, 17

Malagoli, A., Bodo, G., & Rosner, R. 1996, ApJ, 456, 708

Marek, A. 2007, PhD thesis, Technische Universität München

Marek, A., Dimmelmeier, H., Janka, H.-T., Müller, E., & Buras, R. 2006, A&A, 445, 273

Martí, J. & Müller, E. 2003, Living Rev. Relativity, 6

Masada, Y., Sano, T., & Shibata, K. 2007, ApJ, 655, 447

Masada, Y., Sano, T., & Takabe, H. 2006, ApJ, 641, 447

Meier, D. L., Epstein, R. I., Arnett, W. D., & Schramm, D. N. 1976, ApJ, 204, 869

Menou, K., Balbus, S. A., & Spruit, H. C. 2004, ApJ, 607, 564

Mignone, A. & Bodo, G. 2006, MNRAS, 368, 1040

Mihalas, D. & Weibel Mihalas, B. 1984, Foundations of radiation hydrodynamics (New York: Oxford University Press, 1984)

Müller, E. & Hillebrandt, W. 1979, A&A, 80, 147

Müller, E. & Steinmetz, M. 1995, Comp. Phys. Comm., 89, 45

Munier, A. & Weaver, R. 1985a, Comput. Phys. Rep.

Munier, A. & Weaver, R. 1985b, Comput. Phys. Rep.

Obergaulinger, M., Aloy, M. A., Dimmelmeier, H., & Müller, E. 2006a, A&A, 457, 209

Obergaulinger, M., Aloy, M. A., & Müller, E. 2006b, A&A, 450, 1107

Oechslin, R. & Janka, H.-T. 2006, MNRAS, 368, 1489

Oechslin, R., Janka, H.-T., & Marek, A. 2007, A&A, 467, 395

Oechslin, R., Rosswog, S., & Thielemann, F.-K. 2002, Phys. Rev. D, 65, 103005

Pen, U., Arras, P., & Wong, S. 2003, ApJS, 149, 447

Perucho, M., Hanasz, M., Martí, J.-M., & Miralles, J.-A. 2007, Phys. Rev. E, 75, 056312

Pessah, M. E., Chan, C.-k., & Psaltis, D. 2007, ApJ, 668, L51

Plewa, T. & Müller, E. 1999, A&A, 342, 179

Pons, J. A., Ibáñez, J. M., & Miralles, J. A. 2000, MNRAS, 317, 550

Powell, K. G. 1994, ICASE Report No.94-24

Price, D. J. & Monaghan, J. J. 2004a, MNRAS, 348, 123

Price, D. J. & Monaghan, J. J. 2004b, MNRAS, 348, 139

Price, D. J. & Monaghan, J. J. 2005, MNRAS, 364, 384

Price, D. J. & Rosswog, S. 2006, Science, 312, 719

Rahman, T. & Moore, R. B. 2005a, ArXiv Astrophysics e-prints

Rahman, T. & Moore, R. B. 2005b, ArXiv Astrophysics e-prints

Rampp, M. 2000, PhD thesis, Technische Universität München

Rampp, M. & Janka, H.-T. 2002, A&A, 396, 361

Rosswog, S. 2007, in Revista Mexicana de Astronomia y Astrofisica Conference Series, Vol. 27, Revista Mexicana de Astronomia y Astrofisica, vol. 27, 57–79

Rosswog, S. & Davies, M. B. 2002, MNRAS, 334, 481

Rosswog, S., Davies, M. B., Thielemann, F.-K., & Piran, T. 2000, A&A, 360, 171

Rosswog, S. & Liebendörfer, M. 2003, MNRAS, 342, 673

Rosswog, S. & Price, D. 2007, MNRAS, 379, 915

Rosswog, S., Ramirez-Ruiz, E., & Davies, M. B. 2003, MNRAS, 345, 1077

Ryu, D. & Jones, T. W. 1995, ApJ, 442, 228

Ryu, D., Jones, T. W., & Frank, A. 2000, ApJ, 545, 475

Ryu, D., Miniati, F., Jones, T. W., & Frank, A. 1998, ApJ, 509, 244

Sano, T. 2007, Ap&SS, 307, 191

Sano, T. & Inutsuka, S.-i. 2001, ApJ, 561, L179

Sano, T., Inutsuka, S.-i., Turner, N. J., & Stone, J. M. 2004, ApJ, 605, 321

Scheck, L., Kifonidis, K., Janka, H.-T., & Müller, E. 2006, A&A, 457, 963

Shakura, N. I. & Syunyaev, R. A. 1973, A&A, 24, 337

Shen, H., Toki, H., Oyamatsu, K., & Sumiyoshi, K. 1998, Progress of Theoretical Physics, 100, 1013

Shu, C.-W. 1990, SIAM J. Sci. Comput., 5, 127

Shu, C.-W. 1997, ICASE Report No.97-65

Shu, C.-W. & Osher, S. 1989, J. Comput. Phys., 83, 32

Stone, J. M., Hawley, J. F., Gammie, C. F., & Balbus, S. A. 1996, ApJ, 463, 656

Stone, J. M. & Pringle, J. E. 2001, MNRAS, 322, 461

Suresh, A. & Huynh, H. 1997, J. Comput. Phys., 136, 83

Sweby, P. K. 1984, SIAM J. Num. Anal., 21, 995

Symbalisty, E. M. D. 1984, ApJ, 285, 729

Tadmor, E. 1998, in Advanced Numerical Approximate of Nonlinear Hyperbolic Equations. Lecture notes in Mathematics 1697, 1997 C.I.M.E. course in Cetraro, Italy, June 1997 (A. Quarteroni ed.) (Springer Verlag), 1

Tassoul, J. 1978, Theory of rotating stars (Princeton Series in Astrophysics, Princeton: University Press, 1978)

Tchekhovskoy, A., McKinney, J. C., & Narayan, R. 2007, MNRAS, 379, 469

Thompson, C. & Duncan, R. C. 1993, ApJ, 408, 194

Titarev, V. A. & Toro, E. F. 2005, International Journal for Numerical Methods in Fluids, 49, 117

Toro, E. 1997, Riemann Solvers and Numerical Methods for Fluid Dynamics (Berlin: Springer)

Toro, E. F. & Titarev, V. A. 2006, J. Comput. Phys., 216, 403

Velikhov, E. 1959, Sov. Phys. JETP, 36, 995

Warsi, Z. 1993, Fluid dynamics : theoretical and computational approaches (CRC Press, Boca Raton)

Woodward, P. & Colella, P. 1984, Journal of Computational Physics, 54, 115

Woosley, S. E., Heger, A., & Weaver, T. A. 2002, Reviews of Modern Physics, 74, 1015

Yamada, S. & Sawai, H. 2004, ApJ, 608, 907

Zachary, A. L., Malagoli, A., & Collela, P. 1994, SIAM J. Sci. Comput., 15, 263

Zhang, B. & Mészáros, P. 2004, International Journal of Modern Physics A, 19, 2385

Zhang, W. & MacFadyen, A. I. 2006, ApJS, 164, 255

Zwerger, T. & Müller, E. 1997, A&A, 320, 209

Acronyms

BC	boundary condition
BH	black hole
CFL	Courant-Friedrichs-Levy
CT	constraint transport
ENO	essentially non-oscillatory
EOS	equation of state
FD	finite difference
FLD	flux-limited diffusion
FV	finite volume
GRB	gamma-ray burst
HD	hydrodynamics
HLL	Harten-Lax-van Leer
HRSC	high-resolution shock-capturing
KH	Kelvin-Helmholtz
LTE	local thermodynamic equilibrium
LxF	Lax-Friedrichs
LxW	Lax-Wendroff
MHD	magnetohydrodynamics
MP	monotonicity preserving
MRI	magneto-rotational instability
MUSTA	multi stage
NS	neutron star
ODE	ordinary differential equation

PCM	piecewise-constant method
PDE	partial differential equation
PLM	piecewise-linear method
PNS	proto-neutron star
RHD	radiation hydrodynamics
RK	Runge-Kutta
RM	radiation moments
RME	radiation-moments equation
RS	Riemann solver
RT	radiative transfer
RTE	radiative-transfer equation
ShD	shearing disc
ShS	shearing sheet
SN	supernova
SPH	smoothed particle hydrodynamics
TMT	two-moment transport
TVD	total variation diminishing
UCT	upwind constraint transport
VEF	variable Eddington factor
WENO	weighted essentially non-oscillatory

Nomenclature

The following symbols were used. We list symbols used across different sections of the thesis. Symbols which are only "local" to one specific section are not necessarily included.

Constants

c	vacuum speed of light
$M_\odot$	solar mass, $= 1.98 \times 10^{30}\,\mathrm{g}$
ρ_{nuc}	nuclear density, $\rho_{\mathrm{nuc}} \sim 2 \times 10^{14}\ \mathrm{g\ cm^{-3}}$

Geometry

$\mathcal{A}$	area
$\mathcal{L}$	length
$\mathcal{V}$	volume

MHD variables

$\vec{B}$	magnetic field
$\vec{b} = \frac{\vec{B}}{\sqrt{4\pi}}$	magnetic field
ε	internal energy density
$\vec{E}$	electric field
e_{kin}	kinetic energy density
e_{mag}	magnetic energy density
e_{tot}	total energy density
$\mathscr{E}$	volume-integrated energy
S	entropy
Γ	adiabatic index
$\vec{j}$	electric current density
$\mathscr{M}$	volume-integrated mass

$\vec{\mathscr{P}}$	volume-integrated momentum
Ω	angular velocity
$P_{\rm mag}$	magnetic pressure
$P_\star$	total pressure
φ	gravitational potential
Re	hydrodynamic Reynolds number
$\mathsf{Re}_{\rm m}$	magnetic Reynolds number
ρ	gas density
$c_{\rm s}$	sound speed
$\mathfrak{T}$	stress tensor
T	gas temperature
$\vec{v}$	gas velocity
Y_e	electron fraction

RT variables

η	radiative emissivity
$\mathfrak{f}$	flux factor
χ	opacity
κ	True opacity
τ	optical depth
Pe	Peclet number
$\mathfrak{E}, \bar{\mathfrak{E}}$	radiation energy density
$\mathfrak{I}$	specific radiation intensity
$\mathfrak{F}, \vec{\bar{\mathfrak{F}}}$	radiation flux density
$\mathfrak{P}, \bar{\mathfrak{P}}$	radiation pressure tensor
$\mathfrak{p}$	variable Eddington factor

List of Tables

List of Figures

List of selected equations

Index

Danksagung

> DEN GÖTTERN VERDANKE ICH, DASS ICH GUTE GROSSVÄTER, GUTE ELTERN, EINE GUTE SCHWESTER, GUTE LEHRER, GUTE HAUSGENOSSEN, VERWANDTE, FREUNDE, ÜBERHAUPT FAST NUR GUTE MENSCHEN UM MICH HATTE.
>
> Marcus Aurelius Antoninus, *Selbstbetrachtungen*, I, 17[1]

Wenn – falls – dieses ganze Unternehmen einen guten Ausgang genommen hat, so verwundert mich das immer wieder; es wird verständlicher, wenn ich bedenke, daß ich in all dem nicht allein auf mich gestellt war, sondern vielfältige Unterstützung von allen Seiten erfahren habe. Daher will ich an dieser Stelle einer ganzen Reihe von Weggefährten danken.[2]

Meinem Betreuer Ewald Müller danke ich sehr herzlich für die Themenstellung und die stets gute und freundliche Betreuung. Besonders die recht große Freiheit, die ich genießen durfte, war mir in gleichem Maße Ansporn und Verpflichtung, wie sie dazu beitrug, daß mir die Arbeit Freude machte.

Leider gibt es für das wissenschaftliche Schreiben noch kein *constraint-transport*-Schema. Daher treten in einer solchen Arbeit unvermeidlich Divergenzen auf: zwischen verschiedenen Aussagen, zwischen dem Text und den Abbildungen, zwischen dem gemeinten und dem geschriebenen, zwischen dem geschriebenen und der englischen Sprache, ... Zum Glück bietet das Verfahren des *magneto-hermeneutischen Diskurses* (MHD) mit einem aufmerksamen Leser verschiedene Möglichkeiten, diese Divergenzen abzubauen. Dafür, daß sie diesen aufwendigen Prozeß übernommen haben, bin ich den Korrekturlesern – Ewald, Robert Buras und Thomas Mädler – sehr dankbar.

Bei der Anfertigung dieser Arbeit hatte ich das Vergnügen, mit vielen Kollegen zusammenzuarbeiten; von noch mehr durfte ich lernen. Es sei hier – neben Ewald – insbesondere Miguel Angel Aloy, Pablo Cerdá-Durán, Harry Dimmelmeier, Thomas Janka, Konstantinos Kifonidis, Andi Marek und Henk Spruit gedankt. Ein besonderer Dank gebührt Rainer Moll, dem – außer mir selber – wagemutigen ersten Anwender meines Codes. Manche Fehler kamen erst bei seinen Tests und Simulationen ans Licht und manche Erweiterung habe ich erst auf seinen Anstoß hin eingebaut.

Dem Max-Planck-Institut für Astrophysik (MPA), an dem ich nun schon über vier Jahre mein Unwesen treibe, möchte ich für die freundliche Aufnahme und die immer gute Arbeitsbedingungen danken.

Allen, die dazu beigetragen haben, daß diese Jahre nicht nur arbeitsreich, sondern vor allem einfach eine sehr schöne Zeit waren, danke ich sehr herzlich. Insbesondere danke ich allen, mit denen ich das Büro geteilt habe: Almudena, Mattia, Pierre, Fei, Reiner, Markus, Roland, Robert

[1] Herausgegeben und übertragen von Arno Mauersberger, 1997, Bechtermünz Verlag

[2] Wenn der Ausgang doch kein so guter gewesen sein sollte, so gelten die Danksagungen natürlich trotzdem.

und Andi. Alle anderen, denen ich danken möchte, aufzuzählen, würde den Rahmen sprengen und darüberhinaus die Gefahr bergen, jemanden zu vergessen; daher versuche ich es gar nicht erst, sondern fasse mich (zur Abwechslung einmal) kurz: ich danke allen aus der Hydro-Gruppe, allen tapferen Mensagängern und allen ausdauernden Kaffeepausierern. Für das wöchentliche Fußballspiel danke ich den Kickern von MPA, MPE und IPP und allen anderen Spielern. Unter den Kollegen von anderen Instituten möchte ich mich besonders bei Veronika bedanken.

Die Entwicklung des numerischen Codes und die Durchführung und Auswertung der Simulation erfolgte auf Rechnern des MPA und des Rechenzentrums Garching (RZG) der MPG. Den Systembetreuern beider Institute bin ich dankbar dafür, daß sie mir stets hilfsbereit zur Seite standen, wenn Probleme auftraten. Daneben sei ausdrücklich Ewald und Volker Springel gedankt, die sich für die Anschaffung des sehr leistungsfähigen und zuverlässigen OPA-Clusters eingesetzt haben, auf dem die meisten der größeren Rechnungen aus dieser Arbeit liefen.

Meinen Eltern schließlich verdanke ich, daß ich diesen Weg überhaupt einschlagen konnte. Ihnen sei dafür ein herzliches *Vergelt's Gott* gesagt.